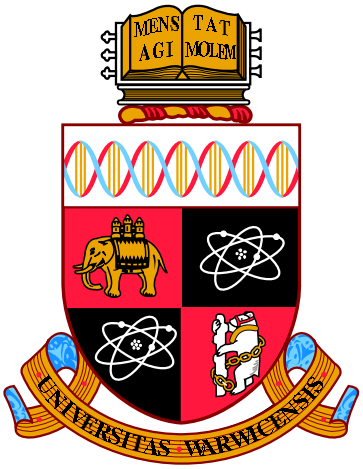

Computational Modelling of Diastole for Human Ventricle

by

Arnab Palit

Thesis

submitted in partial fulfillment of the requirements for

the degree of

Doctor of Philosophy

WMG

September 2015

THE UNIVERSITY OF WARWICK

Contents

List of Tables

List of Figures

List of Abbreviations

BSREC	Biomedical and Scientific Research Ethics Committee.
BV	Bi-ventricle.
CMRI	Cardiac Magnetic Resonance Imaging.
CVD	Cardiovascular Disease.
DTMRI	Diffusion Tensor Magnetic Resonance Imaging.
ED	End Diastole.
EDP	End Diastolic Pressure.
EDPVR	End Diastolic Pressure Volume Relation.
EDV	End Diastolic Volume.
EF	Ejection Fraction.
ErD	Early Diastole.
ErDV	Early Diastolic Volume.
ES	End Systole.
ESV	End Systolic Volume.
FE	Finite Element.
GA	Genetic Algorithm.
LV	Left ventricle.
RSM	Response Surface Method.
RV	Right Ventricle.
SSFP	Steady State Free Precession.
SV	Stroke Volume.
UHCW	University Hospitals Coventry and Warwickshire Trust.

Acknowledgements

I take this opportunity to express my earnest gratitude to Prof. Mark Williams and Prof. Theodoros Arvanitis for their continuous guidance, encouragement and enthusiasm throughout the course of PhD study. They have guided me to the right pathway of conducting the research, presenting the results and writing journal papers, that particularly motivated me to build my research portfolio. I am also indebted to Dr. Sunil Bhudia for his unflinching support and assistance in understanding the medical and clinical aspects of cardiac mechanics.

I would like to convey my special thanks to Dr. Pasquale Franciosa for sharing his unbounded experience in FE modelling throughout my doctoral work. My sincere thanks are also due to my friends Nilanjan, Debajyoti and Abhishek for their illimitable assistance on numerous occasions. Dr. Glen Turley deserves a special mention for his enormous help in arranging all the software required for the research. I would also like to thank Prof. Vinesh Raja to provide the opportunity in carrying out my PhD on this subject. My sincere gratitude goes to all the staffs at the WMG and radiologists at Coventry and Warwickshire NHS Trust (UHCW) for helping me to fulfil the study. The continuous encouragement from Prof. Manoj Tiwari of IIT Kharagpur, India is also much appreciated. In addition, delicate concerns from Paranjayee, Supratik, Hillol, Bramha, Anup, Manoj and Saurin deserve an honourable mention. I am grateful to the WMG for awarding me the prestigious studentship without which this research would never have been accomplished.

Last but not the least, I express my deepest gratitude to my parents and elder brother. They have provided more than generous understanding throughout my years of education and have given me the freedom to develop whilst also showing unwavering support. My life over the past four years has transformed beyond all recognition because of one person, my wife Debasmita Palit. She has shown remarkable patience and faith in me of the like I have never experienced. I am looking forward with excitement to my life ahead with her beyond the PhD.

Declarations

I declare that all work described within this report was undertaken by myself unless otherwise acknowledged within the text. This thesis is presented in accordance with the regulations for the degree of Doctor of Philosophy. This work has not been previously submitted for any other academic degree or qualification

List of Publications

Journal Publications :

1. **Palit, A.**, Bhudia, S. K., Arvanitis, T. N., Turley, G. A., Williams, M. A. Computational modelling of left-ventricular diastolic mechanics: effect of fibre orientation and right-ventricle topology, Journal of Biomechanics, DOI : http://dx.doi.org/10.1016/j.jbiomech.2014.12.054

2. **Palit, A.**, Bhudia, S. K., Arvanitis, T. N., Turley, G. A., Williams, M. A., Subject-specific orthotropic passive material property of myocardium and their effect on diastolic mechanics, submitted

3. **Palit, A.**, Bhudia, S. K., Arvanitis, T. N., Turley, G. A., Williams, M. A., Subject-specific diastolic simulation of human ventricle, draft paper has been prepared and to be submitted

Conference Publications :

1. **Palit, A**., Turley, G. A., Bhudia, S. K., Wellings, R.,Williams, M. A., 2014. Assigning Myocardial Fibre Orientation to a Computational Biventricular Human Heart Model. in Goh, J.(ed), The 15th International Conference on Biomedical Engineering. 43 Springer International Publishing.144-147.

2. **Palit, A**., Bhudia, S. K., Arvanitis, T. N., Sherwood, V., Wayte, S., Turley, G. A., Williams, M. A., Effect of Fibre Orientation on Diastolic Mechanics of Human Ventricle 37th IEEE EMBC 2015 proceedings

Abstract

Diastolic heart failure (DHF) with normal systolic pump function has been typically observed in the majority of HF patients. DHF changes regular diastolic behaviour of left-ventricle (LV), and increases the ventricular wall stress. Therefore, normalisation of increased LV wall stress is the cornerstone of many existing and new therapeutic treatments. However, information regarding such regional stress-strain distribution for human LV is extremely limited in the literature. Thus, the study aimed at estimating the normal range and regional variation of diastolic stress-strain field in healthy human LVs, and exploring the influence of fibre structure, geometrical heterogeneity and material properties on passive inflation of LV. It is envisaged that such information could be used as targets for future in-silico studies to design optimised HF treatments.

FE modelling of passive diastolic mechanics was carried out using personalised ventricular geometry, that was constructed from magnetic resonance imaging (MRI), and structure-based orthotropic constitutive law. Laplace-Dirichlet-Region growing-Finite element (LDRF) algorithm was developed in order to assign the myocardium fibre map on ventricular geometry. The effect of right ventricle (RV) deformation, that has not been taken into account by the majority of researchers due to modelling simplification, was investigated for the first time by comparing the results predicted by bi-ventricle (BV) and single LV models, constructed from the aforementioned MRI data. In addition, personalised in-vivo measurement of fibre structure, that might be different in individual subjects and diseased conditions, is still an open question. Therefore, the sensitivity of LV diastolic mechanics to the details of the fibre structure was accomplished for the first time using eight different fibre orientations. In-vivo passive orthotropic myocardium properties for healthy human myocardium, indispensable for personalised LV wall stress estimation, was identified, and subsequently, the regional variations of LV wall stress-strain were investigated by incorporating geometrical heterogeneity, personalised myocardium properties and LV base movements in the FE models.

RV deformation increased average fibre and sheet stress-strain in LV wall during diastole, and therefore, the effect should always be included in cardiac biomechanics study. Any pathological remodelling, that increased the amount of transmural fibre angle, led to an additional LV inflation. The study indicates that a change in fibre orientation may contribute to the heart failure with preserved ejection fraction (HFpEF) development. Future therapeutic intervention should consider the effect of altered fibre orientation for better outcome. Due to the ill-posed nature of the inverse optimisation problem, the average myocardial stiffness was extracted by identifying the normal ranges of the parameters. A novel method was developed by combining FE modelling, response surface method (RSM) and genetic algorithm (GA) to identify the passive orthotropic myocardium properties for healthy human myocardium using routinely used clinical data. These myocardium properties can directly be utilised in future computational studies. Although the regional stress-strain distribution of the LV wall was highly heterogeneous amongst the individuals, it was observed that the inner wall of the LV experienced higher fibre stress compared to the outer wall. The LV wall near the base and the lateral region received greater stress-strain compared to the other regions. The incorporation of LV base movement (not addressed in the literature) improved the FE model predictions, and therefore, it is recommended to be considered in later studies. In addition, normal ranges of various stress-strain components in different regions of LV wall were reported for five healthy human ventricles considering RV deformation, LV base movement, and subject-specific myocardium properties. This information could be used as a reference map for future studies.

The study revealed that the FE modelling can be employed to analyse the effect of geometry, fibre-structure and material properties on normal ventricular mechanics, and therefore, can provide a greater insight into the underlying mechanics of failing heart and plan for optimised surgical intervention. Hence, the research has impacts on computational cardiac biomechanics as well as clinical cardiac physiology fields.

Chapter 1

Introduction

1.1 Motivation

Cardiovascular disease (CVD) is the foremost modern health problem leading to death worldwide, accounting 40% of all human mortality (Go et al., 2013), with an estimation of nearly 196 billion euro spent per year on heart related medical treatments in Europe only (Nichols et al., 2012). Heart Failure (HF) remains one of the significant causes of CVD (Wallen and Rao, 2010). Within the year of admission of HF, statistical data reveals 32% death of patients in the UK (Cleland et al., 2010), and 5-year mortality rate of 50% worldwide (Krumholz et al., 2000). Epidemiological studies reported that more than half of the patients diagnosed with HF have left-ventricular (LV) diastolic dysfunction, albeit with normal systolic pump function (Wang et al., 2009). In general, the LV remodelling process, associated with such diastolic HF, is identified to be driven by an increase in LV wall stress that results in reduced cardiac output, increased risk of cardiac arrest, and insufficient blood supply to the rest of the body (Walker et al., 2005; Wall et al., 2006). The LV remodelling is, there-

fore, increasingly recognised as a potential target for therapeutic interventions, which include the use of hydrogel injection (Lee et al., 2013a), anisotropic reinforcement (Fomovsky et al., 2012), and cardiac support devices (Wenk et al., 2013; Lee et al., 2014a). The main objective of such surgical interventions is to reduce the myofibre stress of LV wall to the normal range at end diastole (ED). However, stress in the left ventricle (LV) cannot be measured directly (Huisman et al., 1980). Finite element (FE) modelling, in combination with new cardiac imaging modalities and advanced simulation tools, can be used to analyse the diastolic mechanics of healthy heart and identify the normal ranges of stress-strain distribution in LV wall. Such information will provide a greater insight of the physiology and pathophysiology of healthy heart as well as HF patients, and thereby, predict their responses to surgical interventions.

1.2 Research Scope

Ventricular geometry, fibre orientations and passive myocardium properties of healthy human subjects are the critical aspects for an accurate stress-strain prediction from the FE model of ventricle. The majority of earlier FE models assumed that the LV had an axisymmetric or non-axisymmetric idealised geometry such as truncated ellipsoid, spheroid, and cylinder (Guccione et al., 1995; Usyk et al., 2000). With the advancement in imaging modalities, subject-specific ventricular geometry was used in FE modelling. However, the majority of past studies considered the geometry of left ventricle only, without considering the right ventricle (RV) due to its complex structure. Therefore, use of bi-ventricular (BV) geometry in FE modelling of diastole is extremely limited. As a result, the effect of RV deformation was not included in those studies

and was outlined as a research limitation (Sun et al., 2009; Wang et al., 2013a; Mojsejenko et al., 2015; Nikou et al., 2015). Myocardial fibre orientation plays a critical role in ventricular mechanics (Buckberg et al., 2008; Wang et al., 2013a). Although transmural variation in fibre orientation is histologically similar for human hearts, differences exist in fibre angle between individual subjects and diseased hearts (Buckberg et al., 2008). As indicated by Rohmer et al. (2007); Bayer et al. (2012) and Genet et al. (2014), measurement of in-vivo subject-specific fibre orientation is still an open question. Therefore, sensitivity of LV diastolic mechanics to the details of the fibre structure is an important issue and has never been considered for bi-ventricular model. Passive orthotropic proprieties of healthy human myocardium is scarcely available in literature, and in-vivo estimation of such properties using routine clinical data is one of the primary challenges in cardiac biomechanics (Wang et al., 2009; Xi et al., 2013). In-vivo estimation of passive myocardial properties for human ventricle using non-invasive techniques would lead to improved understanding of the global and regional ventricular mechanics (Guccione et al., 1995; Augenstein et al., 2005; Wang et al., 2009), which results better planning for diagnosis and treatments. The majority of passive diastolic models of human ventricle considered one subject only, and therefore, the effect of geometrical heterogeneity was not considered on the wall stress strain distribution. Furthermore, normalisation of ventricular stress is the cornerstone for many therapeutic treatments as outlined in Section 1.1. Thus, identification of the normal range of regional stress strain at end diastole (ED) would be very useful for future surgical modelling and planning. Based on the aforementioned research scopes, the definition of the research problem and objectives are outlined in the following section.

1.3 Definition of the Research Problem

As stated in Section 1.2, the scope of the research is focused on the passive diastolic mechanics of LV. The research question and the objectives for this study are detailed below.

"How to predict the normal range of LV wall stress-strain at end diastole and to identify the influence of ventricular geometry, myocardial fibre-orientation, and myocardium material properties on passive inflation of healthy human ventricle."

- **Objective 1:** To examine the effect of RV topology on (a) stress-strain distribution of LV wall during diastole, and (b) end diastolic pressure volume relation (EDPVR) of LV.

- **Objective 2:** To investigate the effect of fibre orientation on (a) fibre stress-strain distribution of LV wall during diastole, and (b) end diastolic pressure volume relation (EDPVR) of LV.

- **Objective 3:** To estimate the in-vivo passive orthotropic properties of healthy human myocardium using routinely used non-invasive clinical data, and to explore the effect of geometry, fibre orientation and end diastolic pressure on the estimated properties.

- **Objective 4:** To investigate the change in stress-strain distribution amongst the different wall locations and regions for five normal human ventricles at ED due to the change in ventricular geometry and base movements, and subsequently, to provide a reference map of stress-strain values in healthy LV wall at ED for future computational studies.

A detailed description on identifying these research objectives, based on the research gap in the existing literature, is given in Chapter 2.

1.4 Research Contributions

A brief overview of the research contributions, obtained in order to address the research objectives, is summarised as follows.

[Objective 1] Effect of RV on LV passive inflation: The assumption of single LV model in the literature was interrogated for the first time by identifying the effect of RV deformation on LV diastole. The study showed that RV deformation (a) increased the average fibre and sheet stress and strain of LV wall as well as changed the stress-strain distribution pattern, and (b) increased LV inflation moderately. Therefore, RV should be considered in computational model to obtain more accurate results in future studies. The findings elucidated in Chapter 4 and published in a journal article (Palit et al., 2015a).

[Objective 2] Effect of fibre orientation on LV diastolic mechanics: (a) The high fibre stress field gradually reduced from endocardium to mid-wall and shifted more towards endocardium with the reduction in fibre angle, especially near the equatorial location. (b) Any pathological remodelling of the fibre orientation that increased the amount of transmural fibre angle led to additional LV inflation. Such effects was more notable if the fibre angle was higher towards endocardium. The study indicates that change in fibre orientation may contribute to the heart failure with preserved ejection fraction (HFpEF) development. Besides, future therapeutic intervention should

consider the effect of altered fibre orientation while planning for surgery, and as a consequences, identification of subject-specific fibre-orientation is very important. These findings were obtained from the study detailed in Chapter 4 using pig myocardium properties, and Chapter 6 using human myocardium properties. The work involving pig myocardium proprieties was published in a journal article (Palit et al., 2015a) and that relating to human myocardium properties was disseminated in a conference proceedings (Palit et al., 2015b).

[Objective 3] Estimation of passive myocardium properties of healthy human ventricle: (a) A new method was developed by combining FE modelling, response surface (RS) and Genetic Algorithm (GA) to non-invasively estimate the average values of passive orthotropic myocardium proprieties of healthy human ventricle using routinely employed clinical data. Additional subject-specific information, such as LV wall strain from MRI tagging and pressure-volume relation, could easily be incorporated in the developed method to estimate more accurate personalised myocardium properties. (b) The effect of ventricular geometry, fibre orientation and EDP on estimated parameters values were explored and reported in this study. This myocardium properties can be directly used in future computational studies of human heart to develop new patch or injectable material or design personalised therapeutic treatments for diastolic HF patients. The contribution is detailed in Chapter 5 and is submitted in a journal (Palit et al., 2015d).

[Objective 4] Change in stress-strain distribution amongst the different wall locations and regions of healthy LV wall at ED: (a) Although the stress-strain distribution of the LV wall was highly heterogeneous due to the geometrical heterogeneity, it was observed that the inner wall of LV experi-

enced higher fibre stress compared to the outer wall. The LV wall near the base location received greater stress and strain with respect to the middle and apical locations. In general, the lateral LV wall underwent higher stress distribution in comparison to the other three regions. This information would help the cardiac surgeon to design location and region based therapeutic treatments. (b) The detailed measurement of normal range of LV wall stress-strain at ED, reported in the study, could be used as targets for in-silico design of therapeutic interventions for diastolic heart failure treatments. (c) Inclusion of LV longitudinal base movement, that was disregarded in the literature, improved the FE model predictions and also increased the average fibre stress-strain. Additionally, it is concluded that only EDV based validation, carried out in the literature, would not be sufficient enough to provide an accurate model estimation. All the results are illustrated in Chapter 6 and to be submitted in a journal (Palit et al., 2015c).

In addition, two more research contributions were achieved in course of the study.

Development of rule-based algorithm to automatically assign the fibre orientation on ventricular mesh geometry: A novel Laplace-Dirichlet-Region growing-FEM (LDRF) based algorithm was developed to assign fibre orientation on computational ventricular mesh geometry (biventricle or single LV). The algorithm was developed based on the method suggested by Wong and Kuhl (2014) with a major amendment in identifying the surface domains automatically to define the Dirichlet boundary conditions. This work has been detailed in Chapter 3 and published in a conference proceeding (Palit et al., 2014).

Summarised all the analytical expressions required for the validation of the FE implementation of Holzapfel-Ogden law: Complete expressions of the stress tensor and related mathematical descriptions of Holzapfel-Ogden constitutive law for the passive myocardium under various test cases were included in Chapter 3. These analytical expressions are very useful to validate the FE implementation of Holzapfel-Ogden material model, and therefore, could be employed in future computational study.

The detailed discussion of the research findings is given in the respective chapters (3, 4, 5 and 6) with an overall conclusion in Chapter 7.

1.5 Organisation of the Thesis

The structure of this thesis is shown in Figure 1.1. Following this, a brief description of each chapter is provided to give a general outline of the present study.

This chapter has presented the motivation to the research problems, research objectives aimed at addressing the research problem, followed by research contributions and thesis outline.

Chapter 2: Literature Review - The literature review details the background information, research gap, and derivation of research objectives as stated in Section 1.3. The Literature is categorised into eight different themes- (a) overview of ventricular structure and function, (b) fibre architecture of myocardium, (c) different type of in-vivo imaging modalities used in the literature to construct ventricular geometry, (d) overview of rule-based algorithms to as-

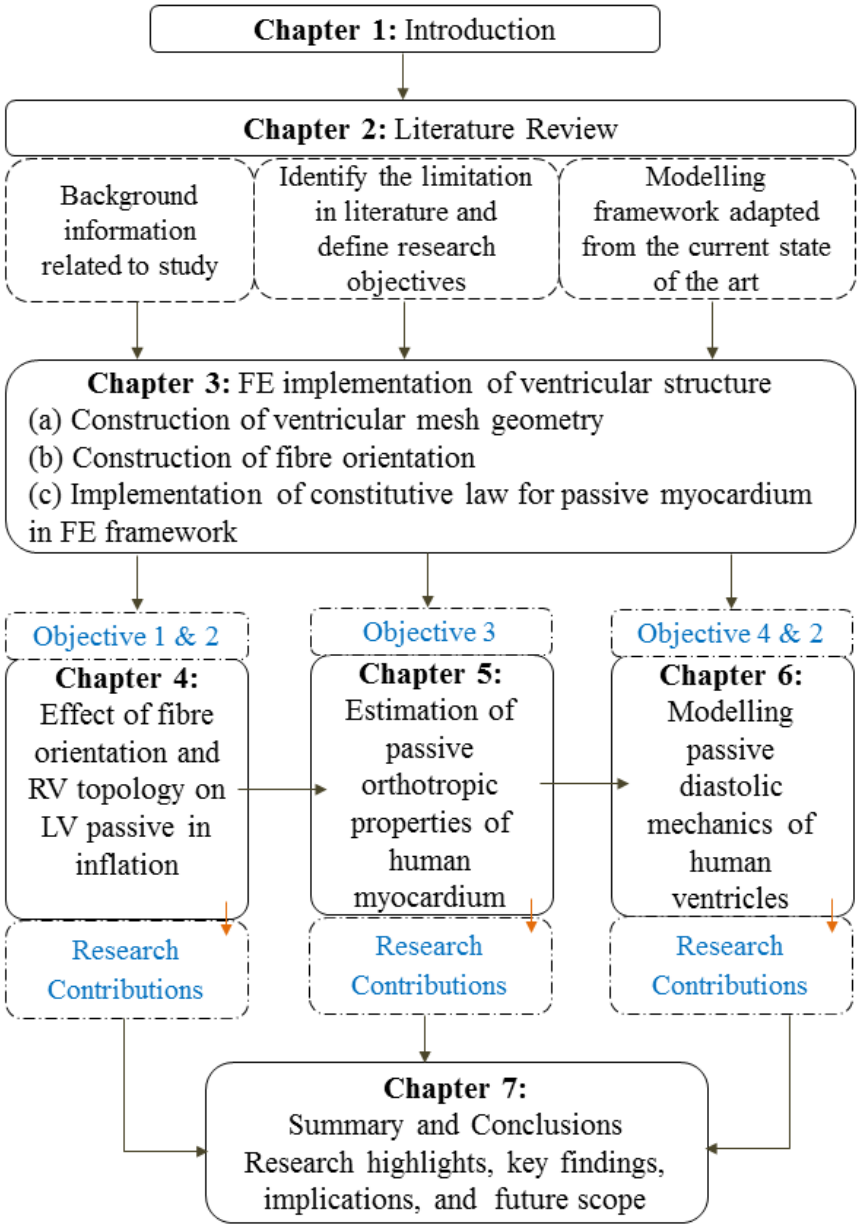

Figure 1.1: Schematic of the thesis structure

sign the fibre structure on ventricular mesh geometry, (e) passive properties of myocardium and related assumptions in FE modelling, (f) review on existing constitutive laws to select the best one, (g) methods to estimate the constitutive parameters and existing problem till date, (h) a brief overview of the

existing FE models of LV to identify the research limitations.

Chapter 3: FE Implementation of Ventricular Structure - Three prerequisites are to be accomplished for FE modelling of ventricle - (a) construction of ventricular mesh geometry, (b) assignment of myocardial fibre structure on it, and (c) implementation of passive myocardial material law in FE framework. In this chapter, the procedures to implement these prerequisites in FE framework will be described.

Chapter 4: Effect of Fibre Orientation and RV Topology on LV Passive Inflation - This chapter will address the first two objectives i.e. effect of RV topology and fibre orientation on LV diastolic mechanics (objective 1 and 2). The contributions to the knowledge will be highlighted at the end of this chapter.

Chapter 5: Estimation of Passive Orthotropic Properties of Human Myocardium - This chapter will present an inverse optimisation procedure using FE modelling, response surface methods (RSM) and genetic algorithm (GA) to non-invasively estimate the passive orthotropic properties (i.e. parameters of Holzapfel-Ogden law) of human myocardium using non-invasive routine clinical data (objective 3). Furthermore, the effect of fibre orientation, geometry and end diastolic pressure (EDP) on estimated values of the parameters will be outlined, and therefore, the range of the parameters for passive healthy human myocardium will be identified. The key findings will be summarised at the end of this chapter.

Chapter 6: Modelling Passive Diastolic Mechanics of Human Ventricles - In this chapter, passive diastolic mechanics of human LV for five

healthy subjects will be accomplished to explore the regional stress-strain distribution at ED (objective 4). The effect of geometrical heterogeneity and base movement (not addressed in the literature) will be explored and a reference map for regional stress strain components will be reported. Moreover, Chapter 4 addressed the effect of fibre orientation using single geometry with pig myocardium properties. Therefore, the effect of fibre orientation using human myocardium porosities for two subjects, identified in Chapter 5, will be again illustrated in this chapter to get a robust and generalised conclusion. All the research contributions will be summarised at the end of this chapter.

Chapter 7: Summary and Conclusions - Although each chapter includes the key findings, this chapter will summarise the research work by highlighting the methods and techniques used throughout the study, the key contributions to the knowledge with its implications, and future scope.

Chapter 2

Literature Review

2.1 Introduction

Anatomically realistic ventricular geometry is critical in computational model to produce physiological motion. The underlying fibre-sheet orientation of ventricular wall (myocardium) plays an important role for both regional and global ventricular mechanisms. Therefore, the chapter starts with an overview of ventricular anatomy and cardiac cycle (Section 2.2), followed by the fibre-sheet architecture of myocardium (Section 2.3). The construction of subject-specific three dimensional (3D) ventricular mesh geometry requires in-vivo imaging. A summary of such imaging modalities, used in recent computational studies, is stated in Section 2.4 and the best imaging modality for the study is identified followed by the identification of first research objective (Objective 1). Besides, implementation of fibre-sheet structure on computational mesh geometry is a major challenge and very crucial for realistic computational results. A brief overview of the existing methods and their limitations to assign fibre orientation on ventricular mesh geometry is illustrated in Section

2.5 to find out the best rule based algorithm, which would be used and modified in the study to overcome its limitations (Section 3.3 of Chapter 3). Also, this section highlights the reason for carrying out the research objective 2. State-of-the-art of passive myocardium properties, used in computational model, is outlined in Section 2.6, followed by an overview of available constitutive laws, used to define the mechanical behaviour of myocardium (Section 2.7). These critical reviews are carried out to select the modelling framework, the constitutive law, and the assumptions required for the study (Chapters 3, 4, 5 and 6). Estimation of the constitutive parameters for specific species (animal or human) is very critical to generate accurate stress-strain prediction from the computational model. A summary of the methods used in estimating material parameters are included in Section 2.8 to identify the research gap, that helps to define objective 3. There after, the computational models of the left ventricle (LV) required for simulating cardiac mechanics are outlined in Section 2.9 along with the current limitations, which help to deduce last research objectives of the study (Objective 4).

2.2 Ventricular Structure and Function

2.2.1 Anatomy of the Human Heart

The heart is a hollow chambered muscular organ of vertebrates that pumps blood received from veins throughout the blood vessels by repeated, rhythmic contractions and dilatations and thereby maintaining the blood flow through the entire circulatory system. Human heart is divided into right and left sections by a muscular wall called the interventricular septum (Figure 2.1). Also each section is divided into upper and lower components known as atria and ventricle respectively. Hence, the anterior of human heart is divided into four pumping chambers. The upper two chambers are called left and right atria while the other two lower chambers are called left and right ventricles. The LV wall is thicker than the RV wall because of the physiological adjustment to the higher pressure against which it must pump blood (Guyton and Hall, 2011). The shape of the LV can be approximated as a truncated prolate spheroid, with the tip of the long-axis known as the apex.

The wall of the heart consists of three layers: epicardium, myocardium, and endocardium. The epicardium is the outermost layer with the thickness of the order 100 µm consisting of epimysial collagen and some elastin which gives the surface of the heart a smooth, slippery texture. The endocardium is inner most lining of the interior surface and cavities with thickness approximately 100 µm. It covers heart valves and tendons and is continuous with endothelium that lines the major blood vessels that attach to heart. It consists of epimysial collagen, a layer of endothelial cells and elastin. The middle layer is the myocardium. Myocardium mainly consists of cardiac muscle cell

or myocyte which occupies 70% of the ventricular wall volume under normal condition. Cardiac myocytes are $50-150\,\mu m$ long in length and $10-20\,\mu m$ in diameter although their dimensions vary depending on age, position in cardiac wall and species (Gilbert et al., 2007). The cardiac muscle fibres are connected by electrical synapses (gap junctions) which allow muscle action potentials to spread from fibre to fibre. Several blood vessels called coronary arteries are responsible to supply the oxygen and nutrients to myocardium. The arrangement of individual cardiac cells throughout the myocardium plays a significant role in the deformation of the ventricular wall. Histological studies reported that the myocytes are assembled in an axial fashion that gives rise to a distinct direction, termed as the fibre direction which have significant influence on ventricular mechanics and electrical conduction. A brief overview of the fibre orientation is described in Section 2.3.

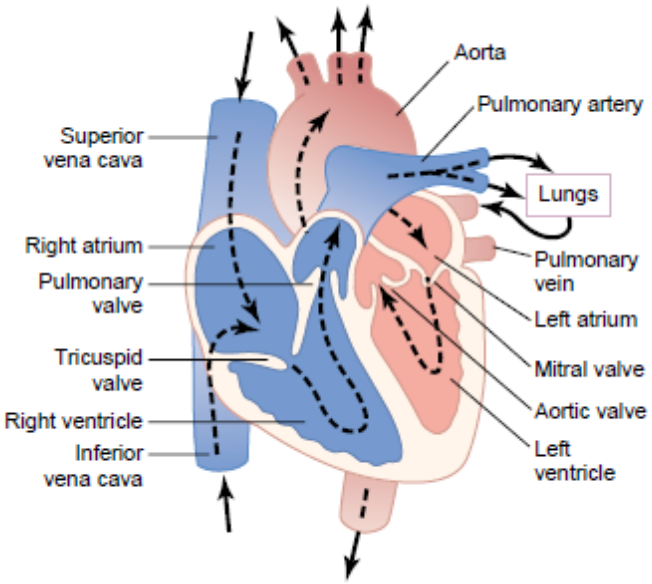

Figure 2.1: Anatomy of the human heart (Guyton and Hall, 2011)

The heart is contained within a special sac called the pericardium. The pericardium is an extremely tough membrane that protects the heart. It composed of three layers; the outer fibrous pericardium, middle parietal pericardium and inner visceral pericardium. The fibrous pericardium has a smooth and well lubricated lining which protects against infection, fastens the heart within the chest, and allows the heart to move freely inside the sac. The parietal pericardium adheres to the fibrous pericardium. The visceral layer, also called epicardium, adheres to the heart. Both parietal and visceral layer are made of serous membranes. The space between the visceral pericardium and the parietal pericardium is called pericardial cavity. This cavity filled with small amount of pericardial fluid that is secreted by the serous membrane. This fluid serves as a shock absorber by reducing friction between the pericardial membranes.

The direction of blood flow, and its passage between the chambers into the great vessels, is controlled by four valves. Two antrioventricular or cuspid valves (tricuspid and mitral valves) which prevent back-flow of blood from ventricles to atrium and two semilunar valves (aortic and pulmonary) which separate the ventricle from its great artery and prevent back flow of blood from arteries to ventricles. Mitral valve controls the flow of oxygen-rich blood from the left atrium to the left ventricle. It is also called bicuspid valve and has two cusps. Tricuspid valve allows the flow of oxygen-poor blood from the right atrium to the right ventricle. Aortic valve controls flow of oxygen-rich blood from the left ventricle to the aorta whereas pulmonary valve allows flow of oxygen-poor blood from the right ventricle to the pulmonary artery. The heart valves in turn are controlled and operated by pressure changes in the

ventricles as well as by the papillary muscles which are part of the myocardium.

2.2.2 Cardiac Cycle

A cardiac cycle is defined from the beginning of one heartbeat to the beginning of the next. Each cycle is initiated by spontaneous generation of an action potential in the sinus node. The cardiac cycle consists of two major phases : diastole during which the heart fills with blood, followed by a period of contraction called systole (Guyton and Hall, 2011). Diastolic phase can further be subdivided into three phases: rapid inflow, diastasis, and atrial systole whereas systolic phase has three sub-phases: isovolumic contraction (IVC), ejection, and isovolumic relaxation (IVR) (Figure 2.2). Each phase of the cardiac cycle can be characterised by changes in ventricular pressure and volume (Figure 2.3). During diastole (Phase D), the LV fills with blood, which increases cavity pressure that results myofibres stretching. This event is clinically termed as ventricular preloaded that can be determined by the LA pressure, LV end diastolic volume (EDV) and LV end diastolic pressure (EDP). LV systole starts with isovolumic contraction (phase A) when LV pressure increases rapidly without any change in LV volume due to closure of both the mitral and aortic valves. The ejection phase (phase B) occurs when LV pressure exceeds the aortic pressure (afterload), and subsequently, the blood is ejected into the aorta. The afterload is determined by the mean arterial pressure. The LV pressure increases, and then, gradually drops towards the end of ejection. After the closure of the aortic valves, the LV undergoes isovolumic relaxation (phase C) and the LV cavity pressure decreases.

The end diastolic pressure volume relation (EDPVR) represents the

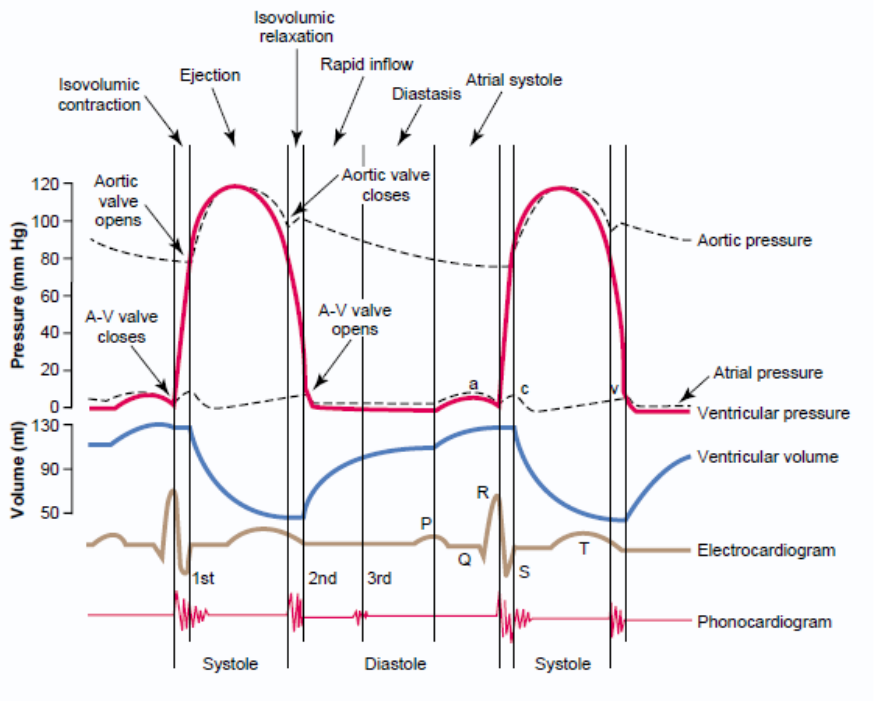

Figure 2.2: Events of the LV cardiac cycle, showing changes in left atrial pressure, LV pressure, aortic pressure, ventricular volume, the electrocardiogram, and the phonocardiogram (Guyton and Hall, 2011)

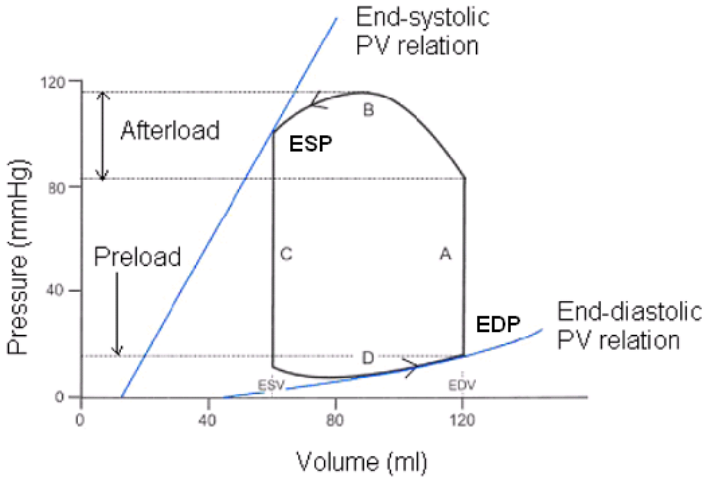

Figure 2.3: LV pressure-volume relation. A: IVC, B: ejection; C: IVR; D: diastole (Fonseca, 2004)

length-tension relation of passive myocardium. During diastolic filling phase, ventricular wall (myocardium) stretches that eventually increases the passive tension of the wall as well as cavity pressure. The end systolic pressure volume relation represents (ESPVR) the active length-tension relation for myocardium. Changes in preload and afterload have a considerable effect on the shape of the pressure-volume relation of LV.

The ventricular myocardium is the main functional tissue of the heart with complex fibre structure, which is very critical in cardiac mechanics. Therefore, a brief overview of myocardial fibre structure is included in a separate section (Section 2.3). Electrical activity of the heart and micro-structure of the ventricular wall were not included as it was not within the scope of the study.

2.3 Structure of the Human Myocardium

As discussed in the previous section, the human heart wall composes of three layers: inner endocardium, outer epicardium and a thick middle layer called myocardium. The myocardium consists of cardiomyocytes that are laid out in bundles called muscle fibre. This fibre orientation changes spatially within the myocardium.

Streeter and Basset (1966) verified the hypothesis that there existed distinct muscle fibres which exhibited a helical fibre pattern from the apex to base within the myocardium of pig's heart. Later, Streeter et al. (1969) performed the fibre direction measurement across the left ventricular wall of 18 dog hearts with the use of a light microscope. The section of a full specimen is shown in Figure 2.4 which is obtained from Streeter et al. (1969) where α is helix or fibre angle with respect to the local circumferential direction (v). The results from their study indicated two key information : (a) fibre angle changed smoothly from about $+60^{\circ}$ at the endocardium to about -60° on the epicardium (Streeter and Hanna, 1973); (b) the fibre angle remained almost same during cardiac cycle i.e. from systole to diastole despite of 28% increase in myocardial wall thickness.

However, Streeter in his later work identified that fibres were not always parallel to the epicardium plane, instead some fibres were inclined with the epicardial surface. The extra angle was termed as inclination angle or imbrication angle or transverse angle (Dorri, 2004; Rijcken et al., 1999) which was nothing but the deviation of the fibres from a plane parallel to the epicardium. Figure 2.5 shows the helix angle (α_h) and transverse angle (α_t) in a through

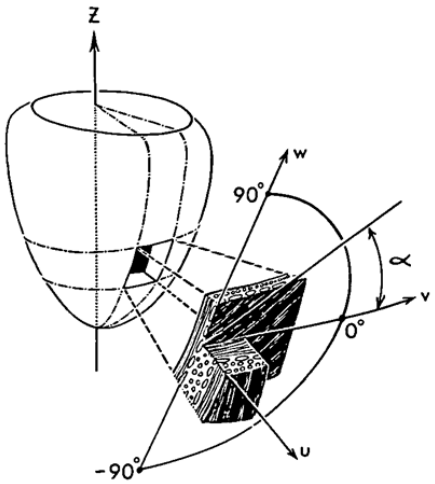

Figure 2.4: Schematic diagram of the LV representing the through wall block specimen with fibre angle (α) with respect to the local circumferential direction (v) (Streeter et al., 1969)

wall myocardial block taken from LV wall. Helix angle (α_h or simply α) is the angle between regional circumferential direction ($\mathbf{e_c}$) and the projection of $\mathbf{f}$ on the plane perpendicular to the regional transmural or radial direction ($\mathbf{e_n}$) (Rijcken et al., 1999). Transverse angle, (α_t) (also termed as imbrication angle or inclination angle) is the angle between the regional circumferential direction ($\mathbf{e_c}$) and the projection of the fibre direction on the plane perpendicular to the regional longitudinal direction ($\mathbf{e_z}$) (Rijcken et al., 1999). However, it was identified that the inclination angle remained very small in the myocardial wall with the order of few degrees (Dorri, 2004). Thus all computational models of fibre orientation considered no transverse angle ($\alpha_t = 0$) in order to simplify the mathematical construction. This assumption was used in this study (Section 3.3 of Chapter 3)

The idea of a continuous fibre orientation of the myocardium of the left ventricular wall was popular for more than two decades after the work of

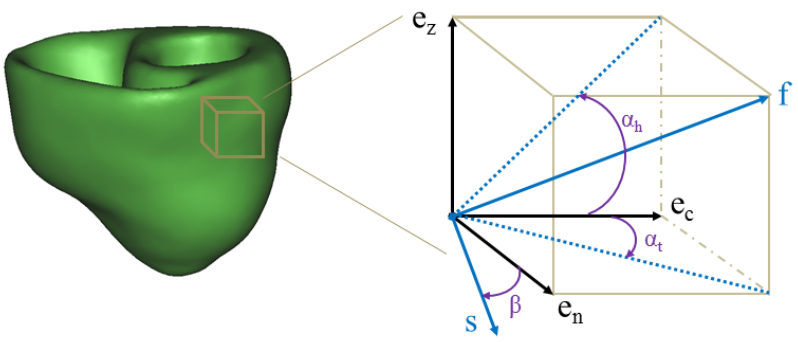

Figure 2.5: Schematic representation of fibre-sheet angles used in computational model

Streeter and co-worker. However, their works failed to identify the existence of any layered organisation of the left ventricular wall. LeGrice et al. (1995b) examined the three-dimensional structure of ventricular myocardial muscle cells and corresponding extracellular connective tissue matrix in four dog hearts using electron microscopy. They observed that all specimens had consistent laminar arrangement of myocytes with significant cleavage plane between muscle layers. From the longitudinal-transmural sections of the specimens shown in Figure 2.6a, it was found that the arrays of distinct muscle layers ran across the wall of the ventricle from the endocardium to the epicardium in an approximately radial direction. Additionally, from the longitudinal-circumferential sections (Figure 2.6b), it was identified that the layers coincided with the local myocytes direction and the progressive change of the layers orientation in the successive sections was consistent with the known variation of muscle fibre angle.

Legrice et al. (1997) and LeGrice et al. (2001) proposed the three distinct material axes (S,F,N) based on the laminar structure of the myocardium

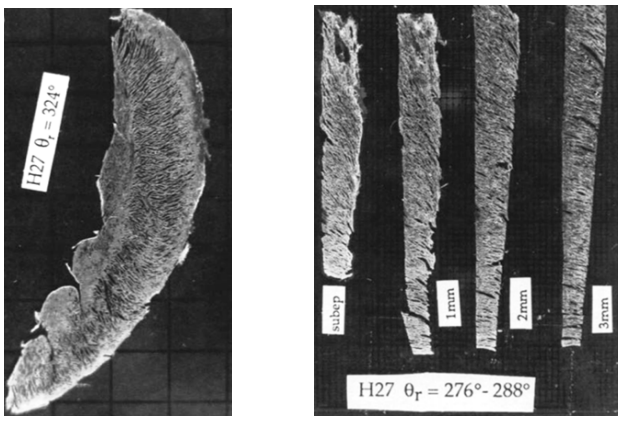

(a) L-T section (b) L-C section

Figure 2.6: (a) Micrograph of longitudinal-transverse (L-T) section of a dog LV showing the alignment of the layers in radial direction; (b) longitudinal-circumferential (L-C) section of LV showing the layered alignment with transmural variation of fibre angle (LeGrice et al., 1995b)

(Figure 2.7). The **F** represented the fibre direction. The **S** represented the sheet direction which was in plane of the sheet but perpendicular to **F**. The **N** was orthonormal to both S and F. Along with this, definition of fibre (α_h) and sheet angles (β) are also important in order to generate fibre orientation in a computational heart geometry. It was considered that the α_h varied transmurally approximately $-50°$ to $-70°$ in the sub-epicardium and right ventricular septal endocardium to almost $0°$ in the mid-wall to $+50°$ to $+70°$ at sub-endocardium and right ventricular free wall endocardium (Streeter et al., 1969; Holzapfel and Ogden, 2009). The sheet angle (β) is the angle between the sheet-axis with the local radial or transverse axis (Figure 2.5). This definitions are used in rule-based algorithms, reviewed in Section 2.5, to assign fibre-orientation in ventricular mesh geometry. Detailed mathematical description and implementations of the fibre orientations and fibre angle are described in Section 3.3 of Chapter 3.

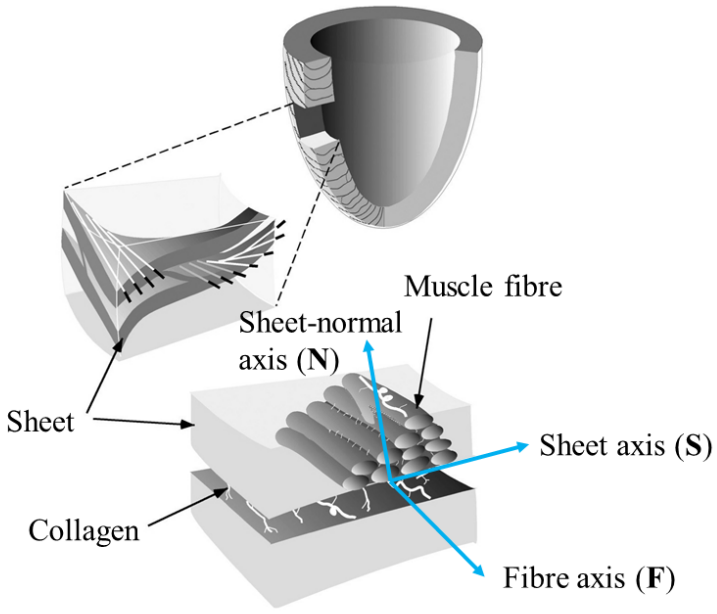

Figure 2.7: Schematic representation of fibre-sheet microstructure of myocardium with local coordinate system adapted from Smaill et al. (2004)

From the schematic representation in Figure 2.7, it is observed that the myocytes are organised in a sheet which extend radially through the ventricular wall. Also, the muscle fibre angle varied transmurally from epicardium to endocardium. Endomysial (around individual myocytes) collagen was shown in adjacent muscle fibre where as perimysial collagen (associated with groups of myocytes) connected neighbour sheets. These observations suggested that the mechanical behaviour of the ventricular myocardium are orthotropic rather than transversely isotropic. To date, various microscopy techniques (Pope et al., 2008) and use of diffusion tensor magnetic resonance imaging (DTMRI) have provided another means to investigate these structures in the intact heart. A brief review of myocardial laminar sheet architecture, resulted from various image and experimental techniques, was detailed in Gilbert et al. (2007).

2.4 In-vivo Imaging and Ventricular Geometry

Although the shape of LV can be can be approximated as a truncated prolate spheroid, thin-walled cylinder, or thick-walled axisymmetric truncated ellipsoid (Guccione et al., 1995; Costa et al., 1996; Usyk et al., 2000; Guccione et al., 2001a; Dorri, 2004; Goktepe et al., 2011; Eriksson et al., 2013), the geometrical heterogeneity can only be incorporated in the model by using subject-specific geometry of LV, which is now possible due to the advancement of in-vivo imaging modalities. Mostly three type of imaging data were used in the literature to construct mesh geometry of ventricle as follows : (a) echocardiography, (b) cardiac computed tomography (cardaic CT) and (c) cardiac magnetic resonance imaging (CMRI).

Echocardiography was used by few researchers for modelling LV (Dang et al., 2005a,b) as it is essential for cheap, easy and real time preliminary diagnosis. Cardiac CT uses x-ray machine to capture images and provides high spatial resolution. However, very few studies used cardiac CT to model ventricular mechanics (Peters et al., 2009; Xi et al., 2011b) as it requires the use of harmful ionizing radiation and potentially risky contrast agents. Cardiac magnetic resonance imaging (CMRI) is based on the same basic principles as MRI but with optimisation for compatibility in the cardiovascular system. One of the optimisation technique uses ECG gated MRI to capture the whole cardiac cycle with 2D image stack. CMRI becomes gold standard method for the characterisation of cardiac anatomy, functions and diseased muscle with a good temporal resolution (Axel, 2002; Petitjean and Dacher, 2011). Recently,

most of the studies used CMRI to construct subject-specific geometry of ventricles (Walker et al., 2005; Wang et al., 2009, 2013a; Genet et al., 2014). The contrast agent is required in CT scan to reliably separate the image of the heart myocardial wall from the blood in the chamber as the soft tissue resolution of CT scan is not as good as MRI (Axel, 2002). Moreover, the temporal resolution of cardiac CT scanning is not as good as compared to cardiac MRI . Beside, MRI is more precise and reliable method for measuring LV mass and functionalities for clinical evaluation of the individual patient compare to the information can be captured from echocardiography (Bottini et al., 1995; Stuckey et al., 2008).

Therefore, subject-specific CMRI (ECG gated, breathe hold, steady state free precession (SSFP) cine CMRI) was used in this study to construct ventricular mesh geometry. Details of the CMRI acquisition protocol and geometry construction are illustrated in Section 3.2 of Chapter 3.

A brief overview of different geometry used in FE models of LV is summarised in Table 4.1. As shown in Table 4.1, the majority of earlier FE models of ventricle used axisymmetric or non-axisymmetric idealised geometry such as truncated ellipsoid, spheroid, cylinder. With the advancement in imaging modalities (i.e. MRI), subject-specific ventricular geometry was utilised in FE modelling. Customised programming, script or commercial software packages were used in literature to construct the geometry from in-vivo images of ventricle. As highlighted in Table 4.1, the majority of studies considered only LV geometry without considering the right ventricle (RV). As RV myocardium is thinner than LV myocardium, segmentation of the RV myocardium is difficult. Therefore, only LV geometry was considered for simplification. Bi-ventricular

(BV) geometry of human heart for FE modelling of diastole is very limited due to its complex structure, and as a result, the effect of RV deformation was not included in those studies (Table 4.1). However, RV deformation might have a considerable effect on LV diastolic mechanics, and it was outlined as limitation in many studies (Sun et al., 2009; Wang et al., 2013a; Mojsejenko et al., 2015; Nikou et al., 2015). Hence, the first objective of the research was

- **Objective 1:** To examine the effect of RV topology on (a) stress-strain distribution of LV wall during diastole, and (b) end diastolic pressure volume relation (EDPVR) of LV.

Objective 1 is addressed in Chapter 4 by comparing the model prediction from single LV and bi-ventricular (BV) model.

2.5 Implementation of Fibre Orientation on Ventricular Mesh Geometry

The fibre-sheet architecture of the myocardium produces material orthotropy which plays an important role in cardiac mechanics, and an accurate reconstruction of the myocardium fibre architecture in a computational model is very critical for realistic cardiac simulation. However, implementing smooth varying cardiac muscle fibre orientation on the created mesh geometry remains one of the major challenges in cardiac mechanics (Wong and Kuhl, 2014). Common approaches include image-based and rule-based methods (Bayer et al., 2012; Wong and Kuhl, 2014). The widely used image based approaches utilise Diffusion Tensor Magnetic Resonance Imaging (DTMRI) which provides three-dimensional information on fibre architecture in a non-destructive process. However, DTMRI can be best performed ex-vivo (Bayer et al., 2012). Rohmer et al. (2007) explored that the acquisition time was approximately 60 hrs for capturing in-vivo DTMRI of the human heart on a 1.5 Tesla clinical scanner using a standard diffusion tensor acquisition protocol. Although recent studies reported the feasibility of in-vivo DTI (Toussaint et al., 2013), the densification of such sparse data is still an open question, and modified scanners with specific scanning sequences are required (Genet et al., 2014). Alternative approach, which included rule-based methods, were introduced by many researchers to map histologically measured fibre orientation on the ventricular mesh geometry created from subject-specific in-vivo image data. Due to the unavailability of DTI data, rule-based fibre orientation implementation was adapted in this research. A brief description of various rule-based approaches are described below. The methodologies to implement

fibre structure from DTMRI are not included here because it is out of scope of the present study.

Nielsen et al. (1991) described fibre orientation using two nodal parameters of each element in the mesh geometry. The fibre orientation between endocardium and epicardium was then interpolated linearly with transmural variation provided by cubic Hermite basis functions.

Bovendeerd et al. (1992) defined muscle fibre orientation by the helix angle which was defined as a function of normalised radial coordinate, and it varied linearly in mid-wall layers and quadratically in the subendocardial and subepicardial layers.

Many researchers used best fit method to incorporate fibre orientation in a irregular geometry. The irregular mesh geometry was first projected to a prolate spheroid coordinate system to map it onto an idealised geometry and created a mathematical model of fibre direction (Costa et al., 1996; Vetter and McCulloch, 2000).

Potse et al. (2006) introduced a new algorithm by parametrised the minimal distance in the transmural direction from endocardium to epicardium and defined the direction from base to apex parallel to the long axis of the LV. They defined a thickness parameter which was related to helix angle of fibre direction by a hypothetical equation. The algorithm developed by Potse et al. (2006) was adapted by many researchers (Bishop et al., 2009; Bernabeu et al., 2008; Bishop et al., 2010; Wang et al., 2013a) in subsequent years. However, one of the crucial step of the algorithm was to discriminate different surfaces such as epicardial, RV endocardial and LV endocardial surfaces in

the mesh geometry. Bishop et al. (2010) focused on this and introduced a method to overcome the issue. They performed a secondary segmentation of the MRI images to obtain the epicardial, RV and LV endocardial surfaces and then mapped them onto the final ventricular mesh using a nearest neighbor mapping algorithm.

Takayama et al. (2008) introduced a sketch based approached to implement layered fibre structure on ventricular geometry. They used feature based interpolation by using Laplacian smoothing. The fibre orientation was specified on each layer of mesh geometry by drawing strokes on them using computer mouse.

Bayer et al. (2012) developed Laplace-Dirichlet Rule-Based (LDRB) algorithm to assign fibre-sheet architecture on a mesh geometry of a canine ventricle. They solved the interpolation within the myocardium by a bi-directional spherical linear interpolation (bislerp) algorithm.

Wong and Kuhl (2014) implemented fibre orientation by using Poisson interpolation (PI) which reduced to Laplace interpolation for a given Dirichlet boundary conditions. They used the featured based interpolation concept described in Takayama et al. (2008). The Poisson interpolation was solved using a standard linear finite element technique for scalar-valued second-order boundary value problems and instigated the feature to be interpolated as a global unknown.

There are several drawbacks in using best fit approach (Costa et al., 1996; Vetter and McCulloch, 2000) to define fibre orientation. Difficulties arise while mapping a real ventricular geometry onto an idealised geometri-

cal (ellipsoid) representation of the heart. Furthermore, the real ventricular geometries do not look like ellipsoid and singularity may be inherited when mapping ventricles onto idealised ellipsoid (Wong and Kuhl, 2014). The minimal distance parametrisation methods (Potse et al., 2006; Bishop et al., 2009; Bernabeu et al., 2008; Bishop et al., 2010; Wang et al., 2013a) can not assure the absence of singularities in the minimal distance function throughout the myocardium wall thickness specially in septum region (Bayer et al., 2012). The sketch-based approach proposed by Takayama et al. (2008) defined the fibre angle using computer mouse stroke which had the drawbacks of introducing manual error. To the best of our knowledge, LDRB and Poisson interpolation (PI) based approached are the most efficient. However, PI based approach did not require any transmural depth normalisation, which was used in LDRB algorithm to define fibre and sheet angles. Also, the Poisson interpolation was solved by FE techniques which took into account the element shape function to ensure best approximating solution whereas bislerp lacked the features in LDRB. In addition, PI based algorithms is easy to interpret and implement in computational coding. Hence, PI based algorithm was selected in the work to implement fibre orientation. PI algorithms required boundary condition on epicardial, LV and RV endocardial surfaces. Identification of different surfaces without manual intervention is a challenge. In this work, we focused on that issue and modified the PI based algorithm, proposed by Wong and Kuhl (2014), by introducing region growing and distance based approach, detailed in Section 3.3 of Chapter 3.

Histological studies confirmed that the myocardial fibre angle varies from -50° to -70° in the sub-epicardial to almost 0° in the mid-wall, to $+50^\circ$

to $+70^{\circ}$ at sub-endocardial with respect to the local circumferential direction of the LV (Section 2.3). The widely used image based approach to determine fibre-sheet orientation utilised DTMRI (Bayer et al., 2012; Rohmer et al., 2007; Dorri, 2004; Geerts et al., 2002). As discussed, DTMRI can be best performed ex-vivo (Bayer et al., 2012; Rohmer et al., 2007) and the feasibility of in-vivo DTI is still an open question (Genet et al., 2014). Moreover, researchers assigned fibre orientation derived from DTMRI of a ventricle on a separate ventricular geometry, which might not have the same fibre orientation (Section 2.9). Alternative approach is the implementation of rule-based algorithm which can yield fibre-sheet architecture that are reasonably close to those derived from DTMRI, yet discrepancies exist between them (Bishop et al., 2009). Even though the fibre-sheet orientation is histologically similar for human hearts, differences exist in fibre angle between individual subjects (Buckberg et al., 2008). In addition, the fibre-sheet architecture may also alter in diseased hearts, such as in myocardial infarction due to tissue remodelling (Buckberg et al., 2008). Therefore, sensitivity of LV diastolic mechanics to the details of fibre structure is an important issue and has not been carried out for bi-ventricular model as shown in Table 4.1 of Chapter 4. Therefore, one of the objectives of the research was

- **Objective 2:** To investigate the effect of fibre orientation on (a) fibre stress-strain distribution of LV wall during diastole, and (b) end diastolic pressure volume relation (EDPVR) of LV.

Objective 2 was first explored using pig's myocardial properties as illustrated in Chapter 4. Later, the effect was investigated again in Chapter 6 using human myocardium properties.

2.6 Mechanical Behaviour of the Passive Myocardium

Almost all biological soft tissues are viscoelastic, heterogeneous, anisotropic and nearly incompressible in nature and undergo finite deformation in-vivo under normal and diseased conditions (Weiss et al., 1996; Dorri, 2004). However, for the simplicity of the simulation and computation limitations, some assumptions were considered by different researchers in order to define myocardial properties. A brief description of these assumptions has been described below.

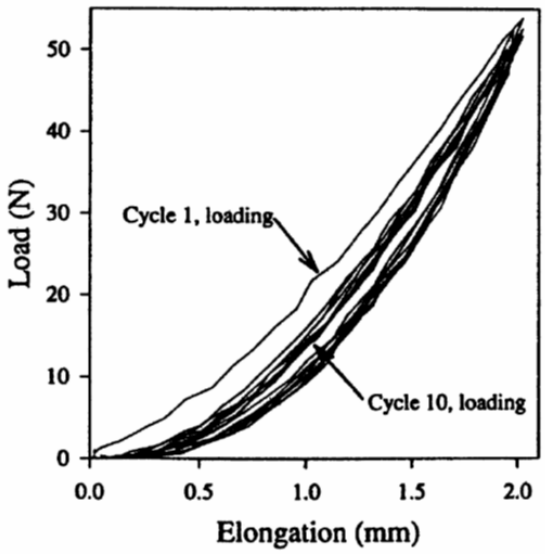

Figure 2.8: Load-elongation behaviour of human fascia lata tested along the fibre direction (Weiss, 1994; Weiss et al., 1996)

From the biaxial test of excised sheet of canine myocardium, Demer and Yin (1983) reported that the passive myocardium exhibited both nonlinear elastic and viscoelastic behaviour. Due to the viscoelastic behaviour, the load-elongation curves during loading and unloading showed hysteresis

which is loss of energy (Demer and Yin, 1983). However, after a number of repeated loading-unloading, the hysteresis stabilised and reached a 'preconditioned' state as observed from the load elongation experiment of human fascia (Figure 2.8) (Weiss, 1994; Weiss et al., 1996). As a result, in the preconditioned state, the viscoelastic property can be considered as one elastic material under loading and another elastic material under unloading condition. Several authors denoted this procedure as 'pseudoelastic' approximation and thus myocardium was frequently modelled as a finite hyperelastic material (Yin et al., 1987; Weiss et al., 1996; Costa et al., 2001) which allowed numerical modelling for finite deformation and anisotropy. Additionally, there are very limited data on the viscoelastic properties of passive myocardium in the shear modes of deformation (Schmid et al., 2008). Moreover, viscoelastic modelling is not important because the mechanical simulation on the time scale of cardiac cycle is very short compare to the relaxation time of viscoelastic response (Holzapfel and Ogden, 2009).

Myocardium shows direction dependent passive property due to its fibrous architecture (Demer and Yin, 1983; Yin et al., 1987; Costa et al., 2001). Figure 2.9, which is extracted from the Figure 4 of Yin et al. (1987), shows the representative biaxial stress-strain data of a passive canine myocardium. The Figure 2.9 clearly indicates the highly non-linear and anisotropic properties of myocardium muscle. Details of the biaxial experiment protocols and the mechanical properties of passive myocardium were described in the quantitative studies of Demer and Yin (1983); Yin et al. (1987) and Novak et al. (1994). Although the myocardium was mentioned anisotropic in these studies, the biaxial tests suggested that the myocardium is transversely isotropic (Holzapfel

and Ogden, 2009).

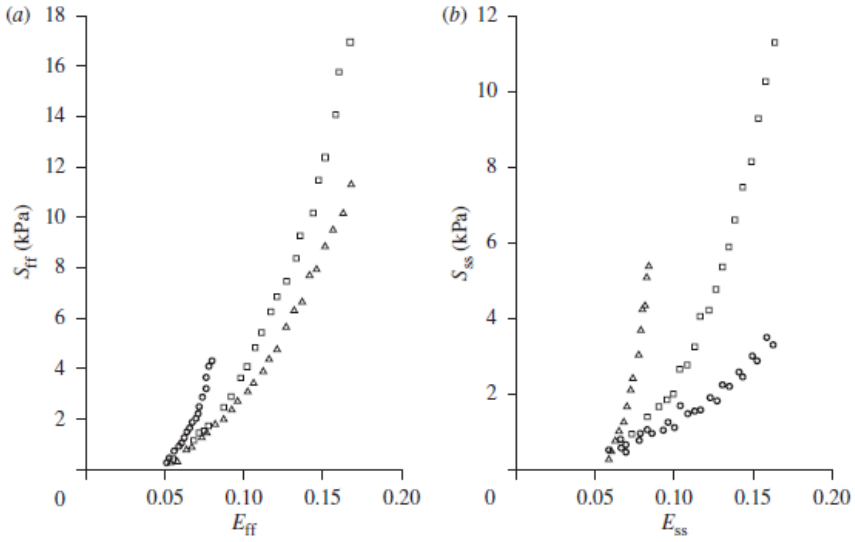

Figure 2.9: Second Piola-Kirchhoff stress along fibre (S_{ff}) and sheet (S_{ss}) directions were plotted with Green-Lagrange strain in fibre (E_{ff}) and sheet (E_{ss}) directions respectively for three different biaxial loading protocols of a canine LV myocardium (Yin et al., 1987). The three sets of data in each figure correspond to constant strain ratios as follows: E_{ff}/E_{ss} equal to 2.05 (triangles), 1.02 (squares) and 0.48 (circles)

Dokos et al. (2002) performed simple shear tests on the passive myocardium of six pig hearts. Their experiments clearly exhibited that the shear properties were orthotropic with respect to three mutually principle material directions (**f**, **s**, **n**). This orthotropic nature is explained in Figure 2.10, which is originally based on the Figure 6 of Dokos et al. (2002). The ordering of the labels fn and fs in Figure 6 of Dokos et al. (2002) were switched in the Figure 2.10 by Holzapfel and Ogden (2009) to make it consistent with the data shown in the other figures of Dokos et al. (2002). Figure 2.10 shows highly non-linear response with relatively low hysteresis and direction dependent (orthotropic) shear properties. The shear modes are defined as (ij) to specify the

shear in the j direction in the ij plane, where $i, j \in \{\text{f, s, n}\}$. Therefore, the first index (i) denoted the normal direction of the face which was translated by the shear, and the second index (j) was the direction of the translation. For example, (fs) represented the shear deformation of the face (fibre-sheet plane) which is normal to fibre direction (f) towards the sheet direction (s). Figure 2.10 exhibits that the passive myocardium is least resistant to simple shear deformation in the planes which are perpendicular to n for shear in s and f direction (ns and nf shear modes respectively) whereas it is most resistant that extend myocyte or fibre axis f (fs and fn shear modes respectively). It was deduced that the stiffness in the **f**, **s** and **n** directions would be ordered according to $f > s > n$ so that the order of shear responses in six shear modes would follow as (fs) > (fn) > (sf) > (sn) > (ns), (nf). The recent study by Sommer et al. (2015b) on human myocardium reported the similar characteristics.

Although inclusion of muscle fibre and sheet architecture into the simulation model generates significant material heterogeneity, another approximated assumption for the computational model was to consider myocardial material as homogeneous when described with respect to the locally varying structural axes defined by fibre and sheet direction (Usyk et al., 2000).

The myocardial tissue could be considered as incompressible based on the experimental results of Vossoughi et al. (1980). They measured volumetric strains of tissue specimen under hydrostatic stresses and concluded that the myocardium was incompressible. Therefore, most hyperelastic constitutive cardiac models considered the deformation as volume-preserving (Vetter and McCulloch, 2000; Holzapfel and Ogden, 2009). However, this incompress-

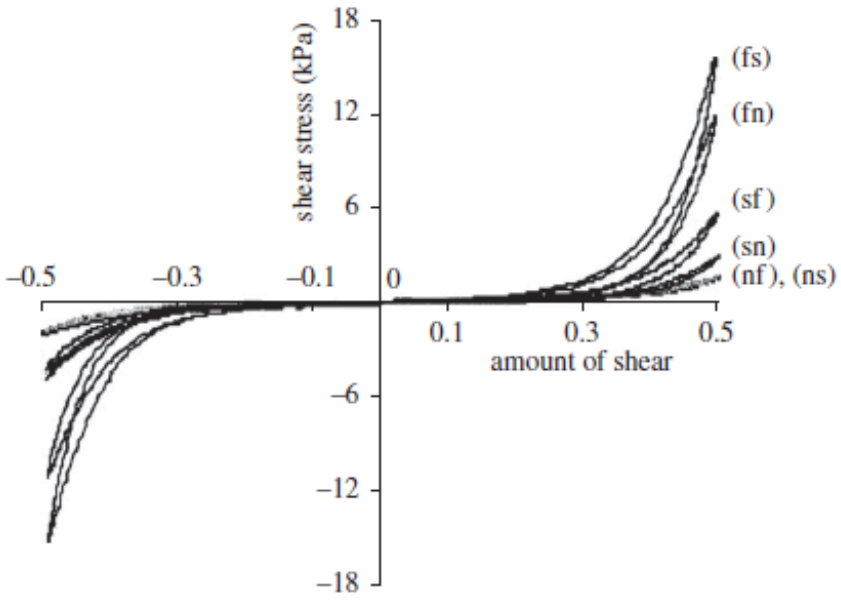

Figure 2.10: Representative stress-strain plot for simple shear tests on a cube of a typical myocardial specimen of a pig LV myocardium (Dokos et al., 2002; Holzapfel and Ogden, 2009)

ibility assumption may not be justified specially for myocardium due to the presence of vascular network that continues about 10-20% of the total volume of the myocardial wall (Goktepe et al., 2011). Yin et al. (1996) reported that the volume change in LV wall may range in between 5-10%. Hence, further experimental research is required to find a conclusive remark regarding the incompressibility of myocardium (Goktepe et al., 2011). Nevertheless, computational treatment of passive myocardium is accomplished by classical three-field, pressure-dilatation-displacement FE formulation of quasi-incompressibility to overcome the locking problems exhibited by the purely displacement based FE formulations of incompressibility (Goktepe et al., 2011; Wang et al., 2013a; Eriksson et al., 2013). The quasi-incompressibility is imposed by decomposing the deformation gradient into volumetric and isovolumic parts and using

a high bulk modulus for the volumetric deformation (Goktepe et al., 2011; Wang et al., 2013a; Genet et al., 2014).

Another aspects of myocardial tissue is that unloaded myocardium experiences residual stress. Omens and Fung (1990) conducted an experiment on five potassium-arrested rat hearts and concluded the residual stress existed in unloaded myocardium. Costa et al. (1997) measured the 3D residual strain in the mid-anterior free wall of a canine LV. The residual strain distribution from the experiment suggested fibre tension in epicardium and fibre compression in endocardium in the unloaded LV. Growth and remodelling may be responsible for generating such residual stress (Holzapfel and Ogden, 2009). Thus, residual stress-strain may have a crucial influence on the myocardial stiffness in physiological condition. For example, inclusion of residual stress may reduce fibre stress distribution predicted by the models which did not consider it. However, 3D residual stresses are very difficult to measure and thus their inclusion in the model must be treated carefully.

This section highlighted the mechanical behaviour of the passive myocardium, observed from various experimental studies, and the assumptions made while carrying out the FE model of ventricle. It was concluded that the passive left ventricular myocardium should be considered as non-linear hyperelastic, orthotropic, quasi-incompressible (or incompressible), and homogeneous material to develop the FE modelling of ventricles. This modelling framework was used throughout the study as detailed in Chapters 3, 4, 5 and 6.

2.7 Review of Constitutive Models

As described in Section 2.6, the myocardium is considered as hyperelastic material for FE modelling of ventricle. The stress is calculated from strain energy function (constitutive law) for a hyperelastic material model. Several constitutive laws have been proposed by various researchers over the past. Two different approaches were used in order to incorporate the directional dependency of the deformation into the strain energy function (Weiss et al., 1996; Dorri, 2004) as follows : (a) strain based constitutive law defined in local coordinate system, and (b)invariant based constitutive law defined in global coordinate system. Each category can be further subdivided into two subcategories: transversely isotropic model and orthotropic model. Brief description of each categorisation with corresponding constitutive laws are discussed in subsequent sections.

2.7.1 Strain Based Constitutive Law in Local Coordinate System

This approach was very popular when investigators started to define constitutive models for soft tissue, and it is still widely used. The key idea behind this approach is derived from the fact that a local coordinate system can be defined in each point of the anisotropic material to align one of the axes of the local coordinate system to the direction of the anisotropy. In this local coordinate system, a quadratic function can then be defined as a function of the component of Green-Lagrange (GL) strain tensor. Therefore, all the numerical calculations must be calculated in local coordinate system in this approach. The strain based constitutive laws can be divided into two categories: (A)

transversely isotropic model, and (B) orthotropic model.

A. Transversely Isotropic Constitutive Law

Chuong and Fung (1986) proposed the Fung-type strain energy function (Eq. (2.1)) to describe the mechanical properties of arteries with orthotropic symmetry, where Q is a quadratic function of three principal strain components and C is a user defined constant whose value can be chosen suitably (Hafner et al., 2002; Dorri, 2004). The term is subtracted by 1 to ensure that the strain energy density function becomes zero in the reference configuration (where Q=0) (Schmid et al., 2006).

$$W = \frac{1}{2}C(e^{Q} - 1) \tag{2.1}$$

Guccione et al. (1991) presented an explicit form for the Q mentioned in Eq. (2.1) to define a cylindrical model of LV geometry with transversely isotropic structure. They define a local coordinate system (X_r, X_f, X_c) which was orthogonal in the stress-free state. X_r was aligned with radial direction, X_f represented the fibre direction in the plane normal to the X_r axis. X_c was directed towards the cross-fibre direction. The form of the Q is

$$\begin{aligned} Q = {} & 2b_1(E_{rr} + E_{ff} + E_{cc}) + b_2E_{ff}^2 \\ & + b_3(E_{cc}^2 + E_{rr}^2 + E_{cr}^2 + E_{rc}^2) + b_4(E_{rf}^2 + E_{fr}^2 + E_{fc}^2 + E_{cf}^2) \end{aligned} \tag{2.2}$$

where E_{ij} are the components of the Green-Lagrange strain tensor in the local coordinate system and five coefficients C and b_1 to b_4 are material constants which can be determined from the measurement and numerical experiment.

Bovendeerd et al. (1992) defined an orthonormal local coordinate system (X_1, X_2, X_3) where X_3 is fibre direction and X_1 and X_2 are cross-fibre directions, and expressed Q as follows:

$$Q = a_1(I_E)^2 + a_1 II_E + a_3 E_{33}^2 + a_4(E_{31}^2 + E_{32}^2) \tag{2.3}$$

where, E_{ij} are the components of GL strain tensor in the local coordinate system. I_E and II_E are the two strain invariants.

Guccione et al. (1995) modified the definition of Q defined in (2.2) by excluding the $(E_{rr} + E_{ff} + E_{cc})$ term as

$$Q = b_f E_{11}^2 + b_t(E_{22}^2 + E_{33}^2 + E_{23}^2 + E_{32}^2) + b_{fs}(E_{12}^2 + E_{21}^2 + E_{13}^2 + E_{31}^2) \tag{2.4}$$

where, E_{11} is fibre strain, E_{22} is cross-fibre strain, E_{33} is radial strain, E_{23}, E_{12}, and E_{13} are shear strain in transverse plane, fibre-cross fibre plane, and fibre-radial plane respectively.

Emery et al. (1997); Okamoto et al. (2000); Vetter and McCulloch (2000); Guccione et al. (2001a,b); Walker et al. (2005); Sun et al. (2009); Wenk et al. (2011a,b, 2012) used the expression of the Q defined by the Eq. (2.4) in order to simulate various cardiac functionalities.

Huyghe et al. (1991a) proposed one of the few models that characterise the passive viscoelastic response of the myocardium. They considered the myocardium as sponge-like material and treated it as a biphasic (fluid-solid) model based on the quasi-linear viscoelastic law. To the best of our knowledge, this is the only biphasic model of the myocardium documented in the

literature. The model was implemented in FE framework to simulate diastole of a canine LV (Huyghe et al., 1992). Although, the author referred the model as orthotropic, it was observed from the Eq. (B8) in the appendix of Huyghe et al. (1992) that it was transversely isotropic (Holzapfel and Ogden, 2009).

B. Orthotropic Constitutive Law

Recent studies described the laminar architecture of the myocardium forming local orthotropic material axes within it (LeGrice et al., 1995a,b, 2001). This orthotropic behaviour of myocardium was also evident from the simple shear test of pig's (Dokos et al., 2002) and human myocardium (Sommer et al., 2015a). Detailed description of orthotropic laminar structure was described in Section 2.3. Motivated from these facts, the definition of Q was modified in order to implement the orthotropic behaviour.

Usyk et al. (2000); Costa et al. (2001) defined orthonormal local co-ordinate system (X_f, X_s, X_n) where X_f represents the fibre direction, X_s indicates sheet direction which is perpendicular to fibre direction and X_n is normal to the sheet plane. Then they defined Q with six material parameters to incorporate the orthotropic properties as

$$\begin{aligned} Q = {} & b_{ff}E_{ff}^2 + b_{ss}E_{ss}^2 + b_{nn}E_{nn}^2 + b_{fs}(E_{fs}^2 + E_{sf}^2) \\ & + b_{fn}(E_{fn}^2 + E_{nf}^2) + b_{ns}(E_{ns}^2 + E_{sn}^2) \end{aligned} \tag{2.5}$$

where, E_{ij} are the components of the Green-Lagrange strain and b_{ij} are material constants. Here, $E_{ij} = E_{ji}$ and thus the Q can be re-written as

$$Q = b_{ff}E_{ff}^2 + b_{ss}E_{ss}^2 + b_{nn}E_{nn}^2 + 2b_{fs}E_{fs}^2 + 2b_{fn}E_{fn}^2 + 2b_{ns}E_{ns}^2 \tag{2.6}$$

Nash and Hunter (2000) proposed a pole-zero formulation to describe a fully orthotropic constitutive law for passive myocardium that directly related to its micro-structure. The key idea for the formulation was that the stress-strain behaviour along one axis was nearly independent of the degree of lateral stretch. The functional form of the pole-zero strain energy follows as

$$W = \frac{k_{ff}E_{ff}^2}{|a_{ff} - |E_{ff}||^{b_{ff}}} + \frac{k_{fn}E_{fn}^2}{|a_{fn} - |E_{fn}||^{b_{fn}}} + \frac{k_{nn}E_{nn}^2}{|a_{nn} - |E_{nn}||^{b_{nn}}} + \frac{k_{fs}E_{fs}^2}{|a_{fs} - |E_{fs}||^{b_{fs}}} + \frac{k_{ss}E_{ss}^2}{|a_{ss} - |E_{ss}||^{b_{ss}}} + \frac{k_{ns}E_{ns}^2}{|a_{ns} - |E_{ns}||^{b_{ns}}} \tag{2.7}$$

where, a_{ij},b_{ij} and k_{ij} are material constants. a_{ij} is termed as limiting strains or poles. b_{ij} is related to the curvature of the uniaxial stress-strain relationship. Lastly, the k_{ij} represents the weight which contributes to the corresponding mode of deformation to the total strain energy of the material. Stevens et al. (2003) implemented the model and concluded that the pole-zero law should be reformulated to make a better separation of material parameters.

Schmid et al. (2006) defined a new Fung-type model called 'separated Fung-type law' (SFL). In this model, the single exponential form of Eq. (2.5) was decoupled with 12 parameters. They also proposed a tangent model based on pole-zero formulation (Schmid et al., 2006). However, to the best of our knowledge, nobody used SFL or tangent model based constitutive law till date for ventricular modelling.

2.7.2 Invariant Based Constitutive Law in Global Coordinate System

The second approach is mainly based on microstructure of myocardium. The strain energy function has been defined in terms of the invariants of the deformation and the fibre direction by using the theory of continuum mechanics of fibre-reinforced composites (Spencer, 1984; Weiss et al., 1996; Dorri et al., 2006). In the case of transversely isotropic model, it has been assumed that the strain-energy function depends on five scalars I_1, I_2, I_3, I_4, I_5 i.e.

$$W = W[I_1(C), I_2(C), I_3(C), I_4(C,N), I_5(C,N)] \tag{2.8}$$

where where, $\mathbf{C}$ is right Cauchy-green deformation tensor and $\mathbf{N}$ is the unit vector field for anisotropic fibre direction (Weiss et al., 1996). For the purpose of modelling, it has been assumed that the fibre bundles are embedded in a homogeneous ground matrix with which the fibres interact. I_1 I_2, and I_3 are first, second and third invariant respectively. The fourth invariant, I_4 is represented by the Eq. (2.9)

$$I_4(\mathbf{C}, \mathbf{N}) = \mathbf{N} \cdot \mathbf{C} \cdot \mathbf{N} \tag{2.9}$$

The dependency on I_5 has been discarded because of less experimental data as well its less influence on the whole energy function (Weiss, 1994; Weiss et al., 1996; Dorri, 2004). However, the invariant based formulation can be also subdivided into two categories: A.transversely isotropic and B. orthotropic.

A. Transversely Isotropic Constitutive Law

The first invariant based transversely isotropic model which consider the fibre structure was proposed by Humphrey and Yin (1987b,a, 1989). They expressed

the strain energy function as the summation of two exponential functions, one with I_1 and one with I_4 respectively with four material parameters c, b, A and a. The specific form of the strain energy function is

$$W = c(e^{b(I_1-3)} - 1) + A(e^{a(\sqrt{I_4}-1)^2} - 1) \tag{2.10}$$

Few years later, Humphrey et al. (1990b) proposed a new form of polynomial strain energy function with 5 material parameters starting from c_1 to c_5. The energy function has the form

$$\begin{aligned} W = c_1(\sqrt{I_4} - 1)^2 + c_2(\sqrt{I_4} - 1)^3 + c_3(I_3 - 3) \\ + c_4(I_3 - 3)(\sqrt{I_4} - 1) + c_5(I_3 - 3)^2 \end{aligned} \tag{2.11}$$

Lin and Yin (1998) proposed a new form of strain energy function based on the biaxial tests of passive and activated myocardium of a rabbit heart. They stated that the simplest strain energy function, which fitted with the biaxial test data of excised passive myocardium, required fourteen (14) parameters. In order to minimise the number of parameters, they proposed the following form of strain energy instead of polynomial form

$$W(I_1, I_4) = C_1(e^Q - 1) \tag{2.12}$$

where,

$$Q = C_2(I_1 - 3)^2 + C_3(I_1 - 3)(I_4 - 1) + C_4(I_4 - 1)^2 \tag{2.13}$$

For the first time, they performed similar test on activated thin sheet of myocardium by using barium perfusion or rapid pacing in the presence of ryanodine. They proposed the following strain energy function for active myocardium

$$\begin{aligned} W(I_1, I_4) = C_0 + C_1(I_1 - 3)(I_4 - 1) + C_2(I_1 - 3)^2 \\ + C_3(I_4 - 1)^2 + C_4(I_1 - 3) + C_5(I_4 - 1) \end{aligned} \tag{2.14}$$

Dorri et al. (2006) used the active energy function model defined by Eq. (2.14) to simulate active contraction on a cadaver human heart.

Kerckhoffs et al. (2003) described a new form of energy function with six material parameters. The total energy function was consisted of three separate energy function: (a) the first terms is related to isotropic component, W_i which represents tissue shape change, (b) the second term, W_f relates with extra stiffness along the myocardial fibre direction and (c) the last term, W_v is related to volume changes i.e. they considered it as compressible material. The strain energy functions are as below:

$$W_p = W_i + W_f + W_v \tag{2.15}$$

with

$$W_i = a_0(e^{a_1\overline{I}_1^2 + a_2\overline{I}_2} - 1) \tag{2.16}$$

$$W_f = a_3(e^{a_4 E_f^2} - 1) \tag{2.17}$$

$$W_v = a_5(det(\mathbf{F}^T \cdot \mathbf{F} - 1)^2) \tag{2.18}$$

where E_{ff} is the Green-Lagrange strain in the fibre direction. The invariants $\overline{I}_1$ and $\overline{I}_2$ are related to principal invariants I_1 and I_2 of $\mathbf{C}$. The $\mathbf{F}$ is the deformation gradient and $\mathbf{F}^T$ represents transpose of it.

Yang et al. (2008) used modified Mooney-Rivlin model to incorporate anisotropy with 6 material parameters. The form of the strain energy function is as follows:

$$\begin{aligned} W = {} & c_1(I_1 - 3) + c_2(T_2 - 3) + D_1[\exp(D_2(I_1 - 3)) - 1] \\ & + \frac{K_1}{2K_2}[\exp[K_2(I_4 - 1)^2 - 1] \end{aligned} \tag{2.19}$$

They used this energy function to simulate right ventricular functionalities in their subsequent work (Tang et al., 2010, 2011)

B. Orthotropic Constitutive Law

To the best of our knowledge, the first invariant based orthotropic strain energy function was proposed by Holzapfel and Ogden (2009). The energy function has eight (8) parameters as follows

$$W = \frac{a}{2b}\exp[b(I_1 - 3)] - 1 + \sum_{i=f,s} \frac{a_i}{2b_i}\left\{\exp[b_i(I_{4i} - 1)^2] - 1\right\} + \frac{a_{fs}}{2b_{fs}}[\exp(b_{fs}I_{8fs}^2) - 1] \tag{2.20}$$

The first term of the energy function in Eq. (2.20) represents the isotropic ground matrix material. The remaining terms relate the structural contribution of myocytes and the families of collagen fibre embedded in the tissue. Fibre and sheet directions are denoted by f, and s respectively and I_{4f}, I_{4s}, and I_{8fs} are fibre, sheet, and fibre-sheet invariants respectively. Goktepe et al. (2011); Wang et al. (2013a); Eriksson et al. (2013) used the structure based orthotropic model to simulate diastolic cardiac simulation. Goktepe et al. (2011) modified the strain energy function in order to incorporate the quasi-incompressible condition.

A brief review of existing constitutive laws is summarised in Table 2.1. From that Table 2.1, it can be easily identified that most of the researchers carried out the ventricular modelling considering myocardium as transversely isotropic - be it a strain based or invariant based formulations. However, as detailed in Section 2.3, it is now confirmed that the myocardium is orthotropic in nature (LeGrice et al., 1995a,b, 2001; Dokos et al., 2002). One problem in developing accurate orthotropic model is lack of experimental data. Early contribution of the experimental data were contained in the work of Demer and Yin (1983) and Yin et al. (1987). They obtained the experimental data

Table 2.1: Review of existing constitutive models

Equation Number	Strain Based Constitutive Law: Transversely Isotropic	Strain Based Constitutive Law: Orthotropic	Material Parameters
(2.1),(2.2)	Guccione et al. (1991)		6
(2.1),(2.3)	Bovendeerd et al. (1992)		5
(2.1),(2.4)	Guccione et al. (1995) Emery et al. (1997) Okamoto et al. (2000) Vetter and McCulloch (2000) Guccione et al. (2001a) Guccione et al. (2001b) Sun et al. (2009) Wenk et al. (2011a,b, 2012)		4
(2.1),(2.5)		Usyk et al. (2000)	7
(2.1),(2.5)		Costa et al. (2001)	
(2.7)		Nash and Hunter (2000) Stevens et al. (2003)	18
	Invariant Based Constitutive Law		
	Transversely Isotropic	**Orthotropic**	
(2.10)	Humphrey and Yin (1987b) Humphrey and Yin (1989)		4
(2.11)	Humphrey et al. (1990b)		5
(2.15)	Kerckhoffs et al. (2003)		6
(2.19)	Yang et al. (2008)		6
(2.19)	Tang et al. (2010, 2011)		6
(2.20)		Holzapfel and Ogden (2009) Goktepe et al. (2011) Wang et al. (2013a) Eriksson et al. (2013)	8

from biaxial testing of canine myocardium. However, only biaxial test data is not sufficient enough to characterise the orthotropic nature of myocardium (Holzapfel and Ogden, 2009). Dokos et al. (2002) examined the passive shear properties of pig hearts which enables the researchers to develop orthotropic model accurately. Pole-zero law (Eq. (2.7)) proposed by Nash and Hunter (2000) should be redefined to get better understanding of the material parameters (Stevens et al., 2003). Modified Fung-type law (Eq. (2.5)) was introduced to incorporate material orthotropy (Usyk et al., 2000; Costa et al.,

2001). However, in all the Fung-type material models, the material parameters were merely used as weighting factors, rather than providing any physical importance (Goktepe et al., 2011). Besides, some of the material parameters were highly correlated in Fung-type law (Wang et al., 2013a; Goktepe et al., 2011; Holzapfel and Ogden, 2009). Recently, Holzapfel and Ogden (2009) developed a constitutive law (Eq. (2.20)) that considered the locally orthotropic tissue architecture and the parameters of this model were closely related to the characteristic micro-structure of myocardium (Goktepe et al., 2011; Eriksson et al., 2013). Moreover, a recent study by Nikou et al. (2015) reported that the the structurally orthotropic Holzapfel-Ogden constitutive law is capable of generating a more physiological EDPVR in the ventricle. Therefore, Holzapfel-Ogden constitutive law was used in the study to define the characteristics of myocardium. Details of the Holzapfel-Ogden constitutive law and its implementation in FE framework are discussed in Section 3.4 of Chapter 3.

2.8 Estimation of Passive Myocardial Material Parameters

As discussed in Section 2.7, various constitutive laws were proposed by the researchers over the past to define the mechanical behaviour of the myocardium. The estimation of material parameters, associated with the strain energy function, for human myocardium are very critical for FE modelling of cardiac mechanics. A brief overview of the estimating material parameters is described in the following sections.

The traditional method of estimating the values of material parameters was to fit the model parameters to match the ex-vivo experimental results. As detailed in Section 2.6, several experimental studies were carried out to identify the properties of myocardium, harvested from a specific heart. Such studies included the the biaxial tests of canine myocardium (Demer and Yin, 1983; Yin et al., 1987; Humphrey et al., 1990a; Novak et al., 1994) and simple shear test of pig's (Dokos et al., 2002) and human myocardium (Sommer et al., 2015b). Schmid et al. (2006, 2008); Holzapfel and Ogden (2009); Goktepe et al. (2011); Wang et al. (2013a) fitted the model parameters to match the simple shear test results of pig's myocardium. However, these traditional methods involved invasive, ex-vivo operations, that resulted the destruction of the myocardium tissues (as a result of sectioning samples) and therefore, are not suitable for in-vivo clinical measurement (Dokos et al., 2000). Moreover, ex-vivo experiments using cadaver hearts may not be the true representative of the in vivo passive properties due to tissue homoeostasis (Wang et al., 2009). An extensive literature survey showed that all ex-vivo experimental data were

measured from animal heart, (except the recent publications by Sommer et al. (2015a,b)) and, therefore, data for passive human myocardium were largely missing. Consequently, the computational models of human LV, using such animal data, were unable to produce expected passive inflation for human heart (Wang et al., 2013a; Eriksson et al., 2013; Baillargeon et al., 2014).

Several work was accomplished to assess the passive material properties in isolated hearts with FE analysis (Omens et al., 1993; Emery et al., 1997; Okamoto et al., 2000; Augenstein et al., 2005, 2006; Nair et al., 2007). Omens et al. (1993); Emery et al. (1997) measured 2D strain in isolated rat heart subject to passive loading. FE analysis was then accomplished to estimate material parameters so that the predicted strain matched with the experimental results. Okamoto et al. (2000) utilised suction apparatus to generate shear deformation, 3D tagged MRI and FE modelling to estimate myocardial properties in isolated arrested canine hearts using. Augenstein et al. (2005, 2006) used SPAtial Modulation of Magnetization (SPAMM) MRI and FE modelling and sequential quadratic programming (SQP) to estimate the material properties in arrested pig hearts that underwent passive inflation. Nair et al. (2007) utilised genetic algorithm, FE modelling to estimate the parameters by matching it with previously measured epicardial strain at 2 points on the surface of an isolated rabbit heart. All of them used Fung-type transversely isotropic constitutive model with animal heart.

FE modelling, in combination with CMRI or MRI tagging, was carried out by few researchers to estimate passive myocardial properties in a non-invasive manner (Walker et al., 2005; Wang et al., 2009; Xi et al., 2011b,a; Wenk et al., 2011b; Xi et al., 2013; Genet et al., 2014; Gao et al., 2015).

Walker et al. (2005) used FE modelling to scale the pressure parameters of Fung-type law by matching it with LV EDV. Wang et al. (2009) used FE modelling, MRI tagging, DTMRI derived fibre orientation and SQP to estimate the passive properties of a canine ventricle. Xi et al. (2011b) used reduced-order Unscented Kalman Filter (rUKF) to estimate human myocardium properties. Xi et al. (2011a, 2013) also used MRI tagging, DTMRI and the method of parameter sweeps to estimate passive properties in a healthy and two diseased human ventricles. Genet et al. (2014) used FE modelling to estimate material parameters by matching it with empirical Klotz curve. They reduced the material parameters to two by replacing cross-fibre parameters with 40% of fibre parameter. All the method used Fung-type transversely isotropic constitutive model. Recently, (Krishnamurthy et al., 2013) used the transversely isotropic part of Holzapfel-Ogden model to estimate the 4 parameters for five diseased human ventricles. Gao et al. (2015) estimated the orthotropic parameters of Holzapfel-Ogden model recently using FE modelling of LV. Sun et al. (2009) and Wenk et al. (2011b) estimated the active properties of myocardium using FE modelling and genetic algorithm based heuristic search. Stevens et al. (2003); Remme et al. (2004) identified the material parameters of the pole-zero law using FE modelling and synthetic data. Due to high intercorrelation amongst the parameters, only 3 parameters out of 18 were estimated.

All the study regarding material parameter estimation is summarised in Table 5.2. Although, animal and human myocardium material parameters were estimated mostly using Fung-type transversely-isotropic law, estimation of orthotropic material proprieties using Fung-type or Holzapfel-Ogden law is limited till date as is evident from Table 5.2. On the other hand, it was

discussed in Section 2.7 that the Holzapfel-Ogden law is used in the study due to its several advantages over Fung-type law. In-vivo estimation of Holzapfel-Ogden material parameters for healthy human myocardium is still limited. An inverse estimation method, which is typically formulated as a non-linear optimisation problem to minimize the differences in the measurements with respect to the unknown parameters, could be used to quantify constitutive parameters of Holzapfel-Ogden material law for healthy human myocardium. Due to the highly non-linear nature of the inverse optimisation problem, large design space, and correlation amongst the material parameters, it is non-trivial to inversely estimate those parameters accurately and uniquely using limited clinical data. The trade-off is that, while fewer clinical data make the inverse problem more ill-posed, requirement of more subject-specific data (i.e. MRI tagging and in-vivo ventricular pressure) leads to more complex and invasive clinical measurements with longer processing times, which is not always possible. Only necessary measurements (cine CMRI) are performed routinely for patients. Therefore, one of the major challenges in that study was to use standard clinical data to extract the human myocardial stiffness by identifying the normal range of the parameters value, rather than finding unique solution. Therefore another objective of the study was as follows

- **Objective 3:** To estimate the in-vivo passive orthotropic properties of healthy human myocardium using routinely used non-invasive clinical data, and to explore the effect of geometry, fibre orientation and end diastolic pressure on the estimated properties.

The objective is addressed in Chapter 5.

2.9 Computational Models of Ventricle

Computational models of human ventricle are only feasible with extremely limiting assumptions. Complex constitutive behaviour of passive and active myocardium, complicated geometries and intricate in-vivo conditions of the ventricles have to be treated accurately in order to get reliable computational results. During the last forty years, there were a number approaches involving analytical and FE analysis in conjunction with experimental measurements including in-vivo imaging to formulate advanced computational models of the ventricles. A short critical review of the published finite element models of the ventricles and their results is discussed in the following.

2.9.1 Thin-walled and Thick-walled Models

In early studies of heart modelling, the assumption of axisymmetric LV geometry was very popular and provided basic understanding of the heart functions. In thin-walled models, the wall stress can be calculated analytically as a function of chamber pressure and geometrical curvature. Therefore, few researchers approximated LV geometry as thin-walled sphere (Burch et al., 1952), cylinder (Burch et al., 1952), or ellipsoid (Sandler and Dodge, 1963). The results form these studies could be considered as a first approximation of the mean stress-strain of the ventricular wall. A more detailed review of thin walled models was described in Vinson (1977).

The next improvement was the incorporation of more complex models by considering LV as thick-walled ellipsoid (Wong and Rautaharju, 1968; Ghista and Sandler, 1969; Streeter et al., 1970), sphere (Janz, 1980), or cylin-

drical model (Tozeren, 1983). Most of the researchers used cineangiocardiography in their models for invasive measurements. A more extensive review of thick walled models was detailed in Grewal (1988).

Stress distribution within the vessel wall, calculated using thick-walled model, contributed relatively little to the understanding of ventricular mechanics due to the geometric simplifications.The simplifications of the LV geometry was usually associated by other assumptions with respect to the material behaviour. In earlier (1960s and 1970s) studies of ventricular modelling, assumptions like isotropy and linear elasticity of the material were widely used. Analytic methods were only possible with various limiting assumptions. A more advance method was required to incorporate realistic geometry, inhomogeneity, anisotropy and non-linear material properties. The finite element (FE) method, developed in the late 1950s, was ideal for this sort of problem. The only drawback of the FE method was the high computational time required to solve the problem. Due to this reason, analytical tool was widely used rather than FE. However, the rapid increase from the mid 1980s in affordable computing power negated this issue and FE method became the popular tool for this sort of modelling. A brief review of the FE model of ventricle is described in the following section.

2.9.2 FE models

The Finite Element (FE) method became an obvious choice for ventricular modelling, as it is suited to incorporate non-linear constitutive properties, irregular asymmetric ventricular geometries, tissue anisotropy and complex

boundary conditions (Dorri, 2004; Walker et al., 2005; Tang et al., 2010). This part of the review will concentrate on FE modelling of LV to explore the cardiac mechanics. Electrical or electrochemical modelling of human heart were not the scope of the study and therefore, were not included in this section .

Janz and Grimm (1972) and Gould et al. (1972), who previously used thick-walled model, developed the LV FE model using ring shaped element for the first time. The geometric data was obtained from cross-sections of post-mortem rat hearts (Janz and Grimm, 1972) or cine-angiography (Gould et al., 1972). Gould et al. (1972) showed that transmural stress was depended on the local wall curvature of the LV. Later, Janz and Grimm (1973); Janz et al. (1974) showed, for the first time, the importance of use finite deformation theory instead of classical infinitesimal deformation theory for FE formulation of ventricular diastolic mechanics.

Hunter (1975) developed the non-axisymmetric FE model of a canine LV for the first time. The geometry was developed from the physical measurements of the epicardium and endocardium radial coordinate of silicon-filled hearts mounted on a rig. The fibre distributions, reported by Streeter et al. (1969), was also include in the model. The modelling framework was furtherer modified by Nielsen et al. (1991) to develop a mathematical model of 3D geometry of the LV and fibre architecture which can be fitted with experimental measurement.

Pao et al. (1976) developed true cross-sectional shape of an isolated canine heart from multiplanar roentgenographic to simulate in-plane stress analysis for early and end diastolic phase and compared with the results derived

from symmetric cylindrical model. They showed that varying wall thickness and wall curvature influenced the distribution of wall stress significantly even for an isotropic and linear elastic material.

Panda and Natarajan (1977) incorporated myocardium material anisotropy in their linear elastic model along with a non-symmetric layered geometry created from cine-angiography of human. They demonstrated that anisotropy had a considerable influence on the stress distribution of a LV chamber during cardiac cycle.

Vinson et al. (1979) modelled the diastolic phase of the human LV as a passive structure with internal ventricular pressure being considered as variable load to study the effect of regional heterogeneity material properties using nonsymmetric geometry.

Arts et al. (1982) used a thick walled symmetric cylindrical anisotropic model for the myocardium which was assumed to be composed of contractile fibre structure embedded in an incompressible fluid matrix. They identified that fibre stress and fibre shortening might be uniformly distributed across the LV wall.

Yettram et al. (1983) demonstrated the effect of myocardial fibre orientation on the mechanical behaviour of the LV during diastole by using LV geometry which was constructed using cine-angiographic images. They identified that more realistic fibre arrangement reduced the LV deformation and direct stresses.

Perl et al. (1986) and Horowitz et al. (1986) created a non-symmetric 3D geometry of the LV which was based on the geometric data derived by Ritman and co-worker from computed tomography (CT). They implemented fibre orientation using truss element in FE environment. They concluded that the material non-linearity and mechanical active force were evidently the most significant factor affecting the ventricular deformation. Nevertheless, the material anisotropy, the geometric non-linearity also played a considerable role in the ventricular deformation and stress pattern.

Humphrey and Yin (1989) presented a new approach by considering myocardium as a hyperelastic material and employed a constitutive law with thick-walled cylindrical geometry. They modelled the diastolic phase and the stress-strain pattern was identified in the equatorial region only of the cylindrical model.

Huyghe et al. (1991b) introduced a two phase axisymmetric FE model using X-ray tomography of LV. They expressed passive myocardium properties using an anisotropic quasi linear viscoelastic constitutive law which was developed by Huyghe et al. (1991a). They only simulated diastolic phase and explored that ventricular stiffness increased with the intercoronary blood volume. Furthermore, they included end systolic phase simulation in their subsequent work using the same axisymmetric FE model (Huyghe et al., 1992) and identified that systolic active fibre stress was very sensitive to transmural fibre orientation.

Bovendeerd et al. (1992) examined the dependence of local LV wall mechanics on myocardial fibre angle by considering LV as a thick walled trun-

cated ellipsoid.They reported that muscle fibre stress and strain distribution across the LV wall was very sensitive to the transmural distribution of the fibre orientation which agreed with the findings by Huyghe et al. (1992). In their subsequent work, they introduced the transverse angle (see definition in Section 2.5 and Figure 2.5) along with helix angle in the model (Bovendeerd et al., 1994) and observed that the pressure-volume loop of LV was hardly influenced by inclusion of non-zero transverse angle whereas active muscle stress, sacromere length change and shear deformation at circumferential-radial plane were significantly affected by it.

Guccione et al. (1995) carried out a 3D FE analysis to explore the transmural distribution of fibre stress during ED and ES of a beating dog heart. They used the axisymmetric geometric model proposed by Nielsen et al. (1991). They recognised that there was significant regional heterogeneity of fibre stress and strain in the normal left ventricle associated regional variation in fibre orientation and shape.

Vetter and McCulloch (2000) carried out a FE analysis to estimate only the passive material properties of an intact rabbit heart and validated their result with measured epicardial strain. They identified that the fibre strain was larger than cross-fibre strain which agreed excellently with the observation found in dog and rat myocardium.

Nash and Hunter (2000) introduced a new strain energy function termed as pole-zero constitutive law to describe the orthotropic property of passive myocardium. Furthermore, active muscle fibre properties based on isolated muscle experiment was introduced to predict the transmural distribution of

principle strain at the end-systolic phase. They found that 3-D principal strains and pressure-volume relations predicted by the model were similar with experimental observations. Stevens et al. (2003) computed the material parameter sensitivity with the respect to the fibre-sheet material strain and heart shape in end-diastole of a pig heart by using the 'pole-zero' constitutive law proposed by Nash and Hunter (2000). However, they concluded that the pole-zero law should be reformulated to make a better separation of material parameters.

Usyk et al. (2000) used prolate spheroidal geometry to model LV and incorporated measured transmural distributions of fibre and sheet angles at the base and apex. They compared the orthotropic model with transversely isotropic model and observed that the orthotropic model provided improved agreement with measured end-diastolic strains. Also they recognised that inclusion of cross-fibre active stress with the active fibre stress yielded significant agreement between modelled and measured transverse shear-stain.

Guccione et al. (2001a) used MRI, invasively measured ventricular pressure and FE model of ovine LV to study the mechanism underlying mechanical dysfunction in the BZ region of LV aneurysm. They reported that the dysfunction occurred mainly due to the myocardial contractile dysfunction rather than higher wall stress. In the same year, Guccione et al. (2001b) explored that the effect of residual stress, produced by LV volume reduction surgery, on LV function was not significant. They considered thick-walled axisymmetric truncated ellipsoid as LV geometry for the study.

Moustakidis et al. (2002) measured regional wall stress using FE modelling of 8 Dorsett sheep and observed that the change in LV geometry increased the wall stress and its temporal distribution in the border zone of aneurysm area. However, the assumed myocardium was linearly elastic isotropic material which was not appropriate for heart modelling.

Dang et al. (2005a) carried out FE modelling of infarct LV of sheep to test the hypothesis that akinetic myocardium contains contracting myocytes using Fung-type law. Also, Dang et al. (2005b) performed FE modelling to explore the effect of patch size and stiffens in surgical ventricular restoration. They used 2D echocradigraphy to construct the LV geometry in both the studies.

Walker et al. (2005) developed MRI-based FE modelling of LV aneurysm for five sheep. They reported that 24% increase in fibre stress and 115% increase in cross-fiber stress at the border zone relative to remote regions, which may contribute to LV remodelling. Later, Walker et al. (2008) evaluated the effect of linear repair of LV aneurysm on end systolic stress using FE modelling of sheep LV and identified that the ES stress was reduced due to infarct plication.

Dorri et al. (2006) demonstrated a FE analysis to explore the local wall stress based on the deformation pattern observed during systolic contraction using ex-vivo DTMRI derived fibre orientation on a LV geometry created from the scanning of a cadaver heart. They found that only active stress along fibre direction was not sufficient enough to reproduce the various deformation patterns generated during systolic contraction.

Sun et al. (2009) developed a genetic algorithm based formal optimisation to scale the active properties of LV myocardium with aneurysm at remote and border zone. In subsequent year, Sun et al. (2010) evaluated that Dor procedure could not improve the borderzone contractility of a dyskinetic anteroapical myocardial infarction, although it was able to redue the ED and ES stress. The same research group identified the effect of adjustable passive material on the LV dilation (Jhun et al., 2010), mechanical effect of injected material into a LV with MI (Wenk et al., 2011a), regional LV stress in a poster-basal MI, (Wenk et al., 2011b) in subsequent years. Later Lee et al. (2013a) developed patient-specific FE model to explore effect of SVR + CABG on ventricular mechanics.

Wang et al. (2009) carried out a FE analysis to simulate passive ventricular mechanics during diastole to estimate the values of the parameters of Fung-type law for canine myocardium. They used in-vivo tag-MRI to create 3D geometry of a canine LV and implemented fibre orientation from ex-vivo DTMRI. Later, they scaled the active properties of myocardium (Wang et al., 2010).

Wang et al. (2013a) carried out an FE analysis of a human LV to explore quantitative and qualitative information on heart function using the structure-based constitutive law proposed by Holzapfel and Ogden (2009). The LV geometry of a human was derived from MRI images and fibre orientation was quantitative using a rule-based approach. Also, they performed a comparative analysis between two constitutive models : Costa-law (Fung-type) based model (Costa et al., 2001) or holzapfel-law based (Holzapfel and Ogden, 2009) and explored that there were large differences between the stress-strain pre-

dicted by the two models even when the material parameters were fitted in the same experimental data. Furthermore, they identified that changes in sheet orientation had relatively little effect on the model predicted results whereas the results were quite sensitive to fibre orientation.

Eriksson et al. (2013) explored the influence of heterogeneity in fibre-sheet orientations on ventricular contraction using an electro-mechanically coupled models of ellipsoid LV . The fibre-sheet architecture was implemented using two models: (a) a homogeneous orthotropic model developed using a rule-based fibre-sheet architecture information and (b) a heterogeneous model created based on experimental data. They found that although the pressure-volume loop and mechanical functions were quantitatively and qualitatively similar and agreed well with experimental data, the predicted deformations were largely different between these models, particularly when torsion was considered.

Genet et al. (2014) reported the distribution of myofibre stress at ED and ES which for in silico design of heart failure treatments. They used five subjects and used MRI tagging, Fung-type transversely isotropic law in their study. In the following year, they explored the effect of residual stress on ventricular mechanics (Genet et al., 2015) and concluded that residual stress could reduce the myocardium stiffens by 40% at during passive filling. However, Wang et al. (2014) reported that the effects of such initial (residual) stresses are relatively small in late diastole when pressure is higher.

A more recent study by Nikou et al. (2015) compared Fung-type and Holzapfel-Ogden law by carrying out FE modelling of diastole. They reported

that Holzapfel-Ogden law is capable of producing more physiological EDPVR in the ventricle.

Epidemiological studies reported that more than half of the patients diagnosed with heart failure (HF) have left-ventricular (LV) diastolic dysfunction with normal systolic pump function (Wang and Nagueh, 2009). In general, the LV remodelling process, associated with such diastolic HF, was identified to be driven by an increase in LV wall stress (Wall et al., 2006; Lee et al., 2014a,b). The LV remodelling is, therefore, increasingly recognized as a potential target for therapeutic interventions to reduce the myofibre stress of LV wall to the normal range at end diastole (ED). As outlined in Section 2.9, most of the FE models of diastole used Fung-type transversely isotropic constitutive law (Guccione et al., 1995; Costa et al., 1996; Vetter and McCulloch, 2000; Wang et al., 2009; Genet et al., 2014). However, simple shear test of pig (Dokos et al., 2002) and human myocardium (Sommer et al., 2015b) clearly exhibited that myocardium is orthotropic in nature (Section 2.6 and Figure 2.10). Modified Fung-type (Usyk et al., 2000; Costa et al., 2001) and pole-zero law (Stevens et al., 2003) were used in diastolic simulation to incorporate such material orthotropy. However, the material parameters in those orthotropic models were merely used as weighting factors, rather than any physical significance (Goktepe et al., 2011), and some of these parameters were highly correlated (Wang et al., 2013a). Holzapfel-Ogden constitutive law (Holzapfel and Ogden, 2009) considered the locally orthotropic tissue architecture and the parameters of this model were closely related to the characteristic microstructure of myocardium. However, all the diastolic FE studies of human LV using Holzapfel-Ogden law used experimental data of animal myocardium

which resulted in too stiff stress-strain relation in patient-specific model and thereby unable to produce expected LV inflation through simulation (Wang et al., 2013a; Baillargeon et al., 2014; Palit et al., 2015a). As our previous objective (Objective 3 in Section 2.8) was to estimate the constitutive parameters of Holzapfel-Ogden model for human myocardium, the calibrated values could be used in diastolic modelling to get more realistic stress-strain distribution of human ventricle. Moreover, all the previous diastolic simulation model of human LV used only one subject except the study conducted by Genet et al. (2014) which had the limitations of using single LV model and transversely isotropic material law (Table 6.1). Besides, in most of the FE models of LV diastole, kinematic constraints were typically used to fix longitudinal basal movement in order to avoid any rigid body displacement and allowed the apex to move freely (Walker et al., 2008; Genet et al., 2014; Eriksson et al., 2013; Wang et al., 2013a). However, as suggested by Wang et al. (2009) and observed from CMRI, the apex of the heart did not move considerably during diastole, as opposed to the mitral valve plane (Figure 6.2). Therefore, the last objective, which is addressed in Chapter 6, of the study as follows

- **Objective 4:** To investigate the change in stress-strain distribution amongst the different wall locations and regions for five normal human ventricles at ED due to the change in ventricular geometry and base movements, and subsequently, to provide a reference map of stress-strain values in healthy LV wall at ED for future computational studies.

2.10 Summary

This chapter outlined the derivation of the research objectives and state-of-the-art of the following topics, which are essential for FE modelling of ventricles: (a) anatomy and cardiac cycle of ventricle (Section 2.2), (b) fibre-sheet architecture of myocardium (Section 2.3) which should be implemented in computational model to incorporate material orthotropy, (c) overview of different imaging modalities, mesh geometry construction and subsequently identification of research objective 1 (Section 2.4), (d) available rule-based algorithm to assign fibre-sheet structure on ventricular mesh geometry, selection of best method and its limitation and subsequently derivation of research objective 2 (Section 2.5), (d) passive properties of myocardium and related assumptions to carry out the computational modelling (Section 2.6), (e) constitutive laws to define myocardium characteristics (Section 2.7), (f) invasive and non-invasive method to estimate the constitutive parameters for animal and human myocardium (Section 2.8) and related research gap to address objective 3, and (g) a brief overview of the mechanical FE modelling of ventricles and indemnification of research objective 4 of the study (Section 2.9).

Chapter 3

FE Implementation of Ventricular Structure

3.1 Introduction

Three prerequisites are essential for FE modelling of ventricle as follows: (a) construction of ventricular mesh geometry, (b) assignment of myocardial fibre structure on it, and (c) implementation of passive myocardial material law in FE framework. The aim of this chapter is to vividly explain the procedures to implement these prerequisites in FE framework. The construction of three-dimensional (3D) mesh geometry from subject-specific cardiac images is the first step to FE modelling, a detailed description of which is discussed in Section 3.2. The second step is to incorporate the fibre-sheet architecture of the myocardium, that produces material orthotropy and therefore plays an important role in cardiac mechanics. However, implementing smoothly varying cardiac muscle fibre orientation on the created mesh geometry remains one of the major challenges in cardiac mechanics (Section 2.5 of Chapter 2).

Therefore, a fully automated rule based algorithm, built on the method proposed by Wong and Kuhl (2014), is developed to assign fibre-sheet orientation on ventricular mesh geometry (Section 3.3). In order to implement the third prerequisite, Holzapfel-Ogden hyperelastic material law was selected to define the passive myocardium properties of ventricle. Accurate implementation of this material law in FE framework is crucial, and therefore, is discussed in detail with several validation procedures in Section 3.4. The following chapters will describe the procedure to integrate all these prerequisites with proper boundary conditions to model ventricular passive inflation.

3.2 Construction of Ventricular Mesh Geometry

Construction of personalised 3D ventricular mesh geometry from in-vivo cardiac images is the initial step towards FE modelling of ventricle. Cardiac magnetic resonance imaging (CMRI) has become gold standard method for characterising cardiac anatomy, functions and diseased muscle with a good temporal resolution (see Section 2.4 of Chapter 2). Therefore, CMRI was used in this study to construct the ventricular mesh geometry. The image acquisition protocol is detailed in Section 3.2.1. Typically problem occurs when assessing the LV cavity volume created from the stack of short-axis image data only. Due to the through-plane motion of the basal slice, it is difficult to identify the basal-atrium intersection accurately throughout the cardiac cycle from short-axis images only (Thiele et al., 2002). As a result of which, the geometry created from just short-axis image stack exhibits partial volume error due to either inclusion or exclusion of an extra short-axis image slice in the volume. A method is proposed in Section 3.2.2 to circumvent such partial volume error while constructing ventricular mesh geometry from in-vivo CMRI data. The results and validations of the meshed model are discussed in Section 3.2.3.

3.2.1 In-vivo Image Acquisition

In the present study, ECG gated, breathe hold, steady state free precession (SSFP) cine cardiac magnetic resonance imaging (CMRI) was used to capture the images of normal human hearts in a dedicated MRI suite in 'University Hospitals Coventry and Warwickshire Trust' (UHCW), Coventry, UK.

'Biomedical and Scientific Research Ethics Committee' (BSREC) ethics approval (REGO-2012-032) and patients consents were obtained to carry out the research on anonymised CMRI data of human ventricle.

SSFP cine CMRI was captured using a 1.5T wide bore (450W) GE scanner. A set of short-axis and long-axis images were acquired according to the following criterion - the long-axis plane was orthogonal to the true short-axis image plane and intersected the centroid of the LV (Figure 3.1). The long-axis of the LV remains same while capturing both short and long-axis images (Figure 3.1). A series of short-axis images were captured covering both the ventricles from the base to the apex. An additional set of long-axis images were obtained by rotating the long-axis plane in 60° increments around the anatomical LV long axis according to the above mentioned criterion. A short-axis and a four chamber long-axis CMRI data are depicted in Figure 3.2. The details of typical scanning parameters for short-axis and long-axis images are summarised in Table 3.1. The short-axis slice thickness varied between 5-8 mm with no gap (Table 3.1). After scanning of the human ventricles, the SSFP cine MRI data was anonymised and exported in DICOM file format. Only demographic information such as gender, and age were kept.

3.2.2 Construction of Geometric Model

OsiriX (Mac) was used to read the SSFP CMRI data in order to identify the early-diastole (ErD), end-diastole (ED) and end-systole (ES) phase. The image frames corresponding to the start and end of each cardiac phase were defined from a long-axis image in which the mitral valve plane motion was clearly visible in cross-section (e.g. 4 chamber long-axis image shown in Figure 3.2b).

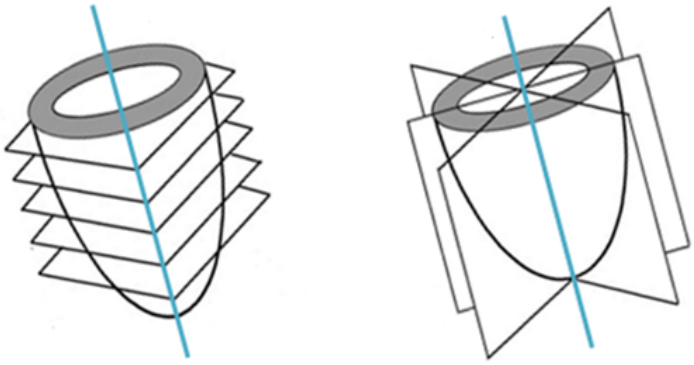

(a) Short-axis slices position (b) Long-axis slices position

Figure 3.1: Schematic representation of the short-axis and long-axis image planes while scanning human LV. The centre lines for both short and long-axis pass through the LV centroid and apex. Long-axis planes are true orthogonal to short-axis plane and intersect the centroid of the LV

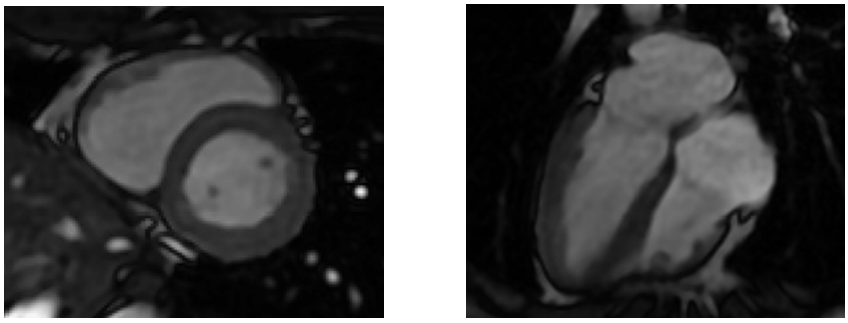

(a) SAX MRI (b) 4 chamber LAX MRI

Figure 3.2: Typical short-axis and long-axis SSFP cine CMRI data of human ventricle

The frame at which the mitral valve opened was defined as the start of a cardiac cycle (i.e. ErD), and the frame at which the mitral valve closed was described as ED. The identification of different phase in CMRI was verified by experienced radiologists and cardiac surgeons from UHCW.

At first, the short-axis image stack of early diastolic (ErD) time frame (e.g. 12th frame of each short-axis slice) were selected and imported to Mimics

Table 3.1: Typical scanning parameters for SSFP cine CMRI sequences

	Short axis	Long-axis
Acquisition matrix	192 × 200 pixels	200 × 200 pixels
Reconstructed image matrix	512 × 512 pixels	512 × 512 pixels
Flip angle	50°	50°
Bandwidth	325.5 Hz/pixel	325.5 Hz/pixel
TR	4.4 ms	3.5 ms
TE	1.6 ms	1.5 ms
Slice thickness	5-8 mm	8 mm
Slice gap	0 mm	0 mm
Frames per cardiac cycle	30	30
Field of View (FOV)	User adjustable (depends on patient size); typically ∼ 37 cm square	User adjustable (depends on patient size); typically ∼ 37 cm square

16.0 (Materialise, Belgium). Those images were then segmented by a semi-automatic procedure and preliminary three dimensional (3D) bi-ventricular geometry was construed in Mimics. The long-axis images of the same ventricle as well as of the same time frame (in this case, ErD time frame) were also segmented in Mimics. 3D bi-ventricular geometry, construed from short-axis image stack, and segmented point cloud of the long-axis images were exported to 3-matic 8.0 (Materialise, Belgium) and both were assembled together. As the LV long-axis was kept in the same position during both (i.e. long and short-axis) types of image acquisition, no further alignment was required during assembling. The long-axis images were then employed to identify the basal-atrium intersection accurately as opposed to the short-axis images, relative position of which changed due to the through plane motion of the ventricle from diastole to systole. Three top points from the three different long-axis images were selected to create a plane (Figure 3.3b). The 3D bi-ventricular geometry was then dissected by this plane in the actual basal-atrium inter-

section to remove the partial volume error introduced during the creation of 3D geometry only from short axis image stack (Figure 3.3). Surface smoothing and wrapping operation in 3-matic 8.0 was then performed to make the geometry usable for FE analysis. Finally the ventricular mesh geometry with linear tetrahedral elements was constructed in 3-matic 8.0 and exported in *.inp format (Abaqus input file format). The same procedure was employed to construct end-diastolic (ED) and end-systolic (ES) geometries.

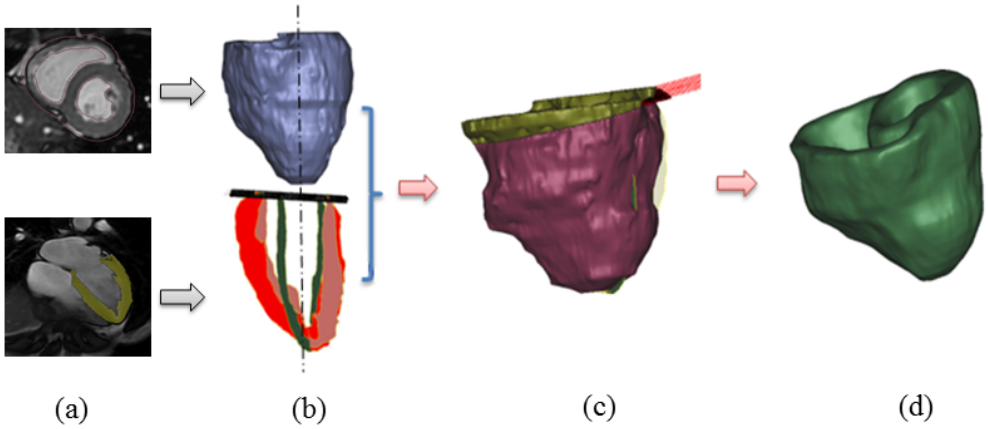

Figure 3.3: Procedure to create bi-ventricular mesh geometry from CMRI; (a) short-axis (above) and long-axis (below) CMRI at ErD and segmentation of the myocardium using semi-automatic procedure; (b) create geometry from stack of short-axis images and locate basal-atrium intersection using long-axis images; (c) assemble both together and remove extra volume by cutting it with the basal-atrium intersection plane; (d) final mesh geometry after smoothing

The volume of the LV cavity was calculated by constructing LV closed cavity geometry (3D) in 3-matic from the geometry of ventricle as shown in Figure 3.4. The point cloud of the constructed BV geometry was produced in 3-matic and there after the LV endocardium point cloud was extracted by removing all other points (Figure 3.4b and 3.4c respectively). The endocardium surface was then constructed in 3-matic from the point cloud of LV open cav-

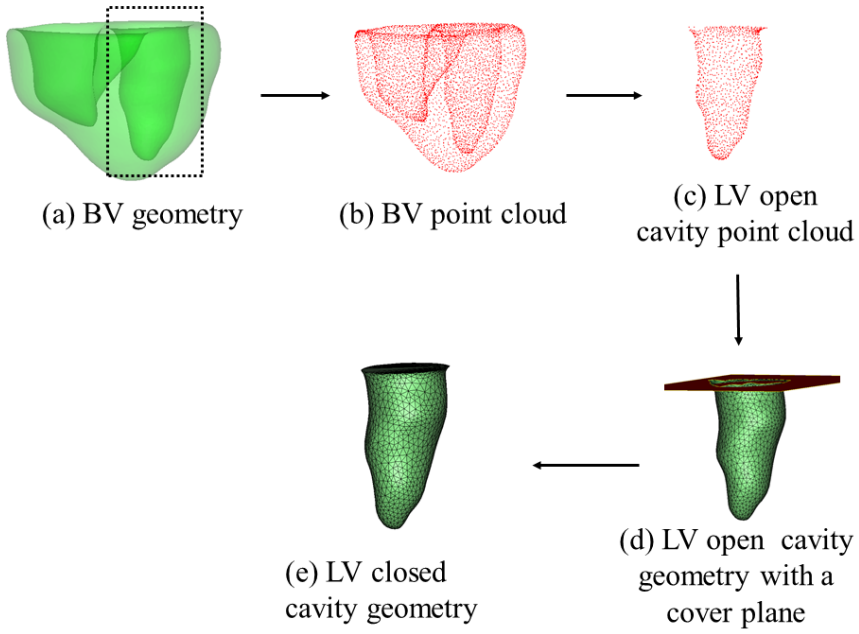

Figure 3.4: Creation of LV closed cavity geometry to calculate the LV cavity volume for different cardiac phases

ity. The base of the LV open cavity was then enclosed by a plane to convert it into a closed geometry (Figure 3.4d and 3.4e). The volume of the closed LV cavity geometry was then calculated in 3-matic. Using the same procedure for each phase (i.e. ErD, ED and ES), early diastolic volume (ErDV), end-diastolic volume (EDV), end-systolic volume (ESV) and subsequently the Stroke Volume (SV) and the Ejection Fraction (EF) were calculated. The LV cavity geometry was also utilised as validation parameter for the results predicted from simulation (see Section 6.4.1 of Chapter 6).

3.2.3 Results and Validation

Identification of different phases (i.e. ErD, ED and ES) from CMRI data of human ventricles was verified by experienced radiologists and cardiac sur-

geons from the UHCW. Segmented area of myocardium muscle in short-axis and long-axis images was also inspected by the same radiologist and surgeons. The verification of constructed geometry was carried out by LV cavity volume and segmented mask area based test. The LV cavity volume, constructed from the BV mesh geometry in 3-matic, was compared with the LV cavity volume, reported by the radiologists. It was found that the difference in LV cavity volume was in the range of 2-3%. The differences were introduced due to several factors such as human interventions, wrapping and smoothing operations required for creating usable FE mesh geometry, and most importantly the use of long-axis images to reduce partial volume error in LV cavity. The method included 3 to 5% muscle on BV geometry than the one created only from short-axis images. Thereafter, a segmented mask area based paired t-test ($\alpha = 0.05$) was conducted to study the changes in the mean mask area before and after the creation of ventricular geometry. The 'original' mask area, segmented semi-automatically in the CMRI, was exported for each of the 2D-slices of a complete short-axis image stack. The mask area in the same 2D-slice position was then calculated from the 3D geometry, created from the same short-axis images. The calculation of the mask area was carried out in Mimics and paired t-test was then performed in excel. It was observed that there was no significant difference between the mean segmented mask area before and after 3D geometry creation at 95% confidence level only when the slice thickness is below 8 mm with no gap.

3.3 Construction of Fibre Orientation

The fibre-sheet architecture of the myocardium produces material orthotropy which plays an important role in cardiac mechanics, and an accurate reconstruction of the myocardium fibre architecture in computational model is very critical for realistic cardiac simulation. The widely used image based approach to determine fibre-sheet orientation utilises Diffusion Tensor Magnetic Resonance Imaging (DTMRI) in ex-vivo heart (Bayer et al., 2012; Rohmer et al., 2007; Dorri, 2004; Geerts et al., 2002). However, obtaining such data in-vivo still remains an open question (Bayer et al., 2012; Genet et al., 2014). Alternative approach uses rule-based algorithm which can yield fibre-sheet architecture that are reasonably close to those derived from DTMRI. Details of different rule-base methods, used in literature, were summarised in Section 2.5 of Chapter 2. An automated rule-based algorithm, built on the method of Wong and Kuhl (2014), is introduced in this section to incorporate fibre-sheet orientation on the constructed mesh geometry. Figure 3.5 illustrates three orthonormal axes related to the characteristic micro-structure of fibre-sheet orientation in the heart: (1) the fibre axis ($\mathbf{f}$), (2) the sheet axis ($\mathbf{s}$) which is along with the laminar sheet and perpendicular to $\mathbf{f}$, and (3) sheet-normal ($\mathbf{n}$) which is orthogonal to both $\mathbf{f}$ and $\mathbf{s}$. The definitions of fibre helix angle (α_h), transverse angle (α_t) and sheet angle (β) were described in details in Section 2.3 of Chapter 2. Histological data showed that α_h varied transmurally by approximately -50° to -70° in the sub-epicardium and right ventricular septal endocardium to almost 0° in the mid-wall to $+50^\circ$ to $+70^\circ$ at sub-endocardium and right ventricular free wall endocardium (Streeter et al., 1969; Holzapfel and Ogden, 2009). The histological data for α_t is very limited till date and

remains very small with the order of a few degrees (Dorri, 2004). As a result, $\alpha_t = 0$ was considered for mathematical simplification (Dorri, 2004; Wong and Kuhl, 2014; Genet et al., 2014). Details of the rule-based algorithm, its implementation and results with validation are described in the following sections.

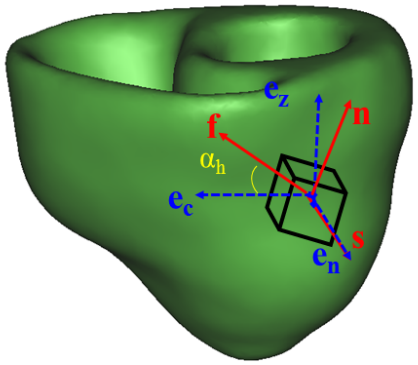

Figure 3.5: Schematic representation of material axes and local cardiac coordinate axes of the ventricle. Material axes **f**, **s** and **n** represent fibre, sheet and sheet-normal axes respectively. Local cardiac coordinate axes $\mathbf{e_n}$, $\mathbf{e_c}$ and $\mathbf{e_z}$ represent local radial or transmural, circumferential and longitudinal axes. α_h is helix angle

3.3.1 Rule-based Algorithm

Laplace-Dirichlet-Region growing-FEM (LDRF) based algorithm was formulated to assign fibre-sheet orientation on ventricular mesh geometry automatically. The LDRF algorithm was principally built based on the method proposed by Wong and Kuhl (2014) with a major amendment in identifying the different surface domains automatically. In this approach, it was assumed that the fibres in the endocardium, the inner wall, and epicardium, the outer wall, were parallel to the respective surface (i.e. $\alpha_t = 0$) (Dorri, 2004). Without loss of generality, it was considered that **s** was aligned with local radial direction

($\mathbf{e_n}$) (Eriksson et al., 2013; Wong and Kuhl, 2014). Figure 3.5 shows the definition of fibre-sheet direction with respect to local circumferential ($\mathbf{e_c}$), radial ($\mathbf{e_n}$) and longitudinal axis ($\mathbf{e_z}$) used in LDRF algorithm.

The main feature of the LDRF algorithm is to produce a smooth coordinate free fibre interpolation, adopted from feature based interpolation used in computer graphics (Takayama et al., 2008; Wong and Kuhl, 2014). The following Laplace equation is solved for the scalar-valued feature Φ,

$$\Delta\Phi = 0 \quad \text{, in domain } \Omega \tag{3.1}$$

for given Dirichlet boundary conditions (DBC),

$$\Phi = \overline{\Phi} \text{ , on } \partial\Omega \tag{3.2}$$

Therefore, for the scalar valued feature Φ, Laplace equation, $\Delta\Phi = 0$ generates a smooth linear interpolation across the cardiac domain Ω when Dirichlet boundary condition is defined on $\partial\Omega$. FEM based approach was used to solve this partial differential Eq. (3.1). In the present study, the domain Ω was discretised with four node tetrahedral elements and solved with the given Dirichlet boundary conditions (DBC), defined on $\partial\Omega$, considering the scalar valued feature Φ as the primary unknown. The LDRF consisted of three functions with three inputs as detailed below.

(A) LDRF Input

Three inputs were required for LDRF as follows

1. Three dimensional (3D) bi-ventricular geometry with finite element mesh

2. Point cloud of the plane parallel to the short-axis image plane just below the basal-atrium intersection

3. Fibre angle definition from the histological data

   It was assumed that fibres on epicardium ($\partial\Omega_{epi}$) and RV septal endocardium ($\partial\Omega_{rvsep}$) were inclined with $-\alpha_1$ and fibres on LV endocardium ($\partial\Omega_{lvendo}$) and RV free wall endocardium ($\partial\Omega_{rvfree}$) were inclined with $+\alpha_2$ with respect to the local circumferential direction of the LV. If it is assumed that $\alpha_1 = 60^\circ = \alpha_2$, then

$$\alpha_h = \begin{cases} -\alpha_1 = -60^\circ & \text{on } \partial\Omega_{epi} \text{ and } \partial\Omega_{rvsep} \\ +\alpha_1 = +60^\circ & \text{on } \partial\Omega_{lvendo} \text{ and } \partial\Omega_{rvfree} \end{cases} \tag{3.3}$$

Based on the helix angle definition in Eq. (3.3), the Dirichlet boundary conditions i.e. the fibre and sheet directions on domain $\partial\Omega$ would be defined using function 2.

(B) LDRF Functions

Three functions were used to generate fibre map on the bi-ventricular mesh geometry as detailed below.

Function 1: Automatic Separation of $\partial\Omega_{\mathbf{epi}}$, $\partial\Omega_{\mathbf{lvendo}}$, $\partial\Omega_{\mathbf{rvfree}}$ and $\partial\Omega_{\mathbf{rvsep}}$

The outer and inner surfaces ($\partial\Omega$) were identified from the whole mesh domain (Ω) based on the idea that there was no shared face between the elements on the surface domain $\partial\Omega$. Following the separation of $\partial\Omega$ from Ω, the basal part of the geometry was cut by the plane (PL) created from the imported point

cloud (i.e. input 2). The region growing algorithm (Franciosa and Gerbino, 2008), was then applied to identify $\partial\Omega_{epi}$, $\partial\Omega_{lvendo}$ and RV inner surface separately. A brief overview of the region growing methodology is described below.

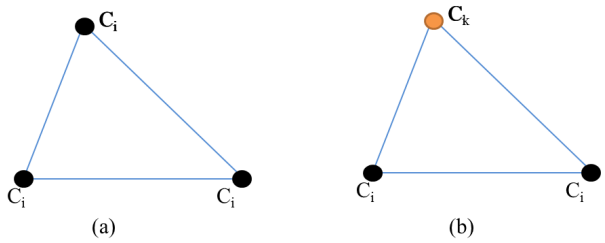

Figure 3.6: Schematic representation of (a) 'Seed' , and (b) 'non-seed' triangle; C_i or C_k is the centroid of cluster (Franciosa and Gerbino, 2008)

The region growing procedure was carried out by propagating the 'child' triangles around the 'seed' ones. If all the vertices of a triangle belonged to the same cluster, the triangle was considered as 'seed' (Figure 3.6). A triangle was considered as 'child' if it held the flowing conditions : (1) it must associate with same cluster, (C_i where, C_i is the centroid of cluster), i.e. it would be a 'seed' triangle as well, and (2) it must have an adjacent edge i.e. two common vertices with the related 'seed' triangle.

The region growing method is depicted in Figure 3.7. The growing operation started with the detection of a 'seed' triangle. The growing procedure stopped when no 'seed' triangle was available. 'Child' triangles were detected and subsequently the connected region was propagated (allocated triangles) until there was no 'child' or un-allocated triangle. An example of region growing procedure is explained in Figure 3.8 which is taken from Franciosa and Gerbino (2008). The region was grown around 'seed' triangles towards the edge of the borders. Typically, border edges were not 'seed' triangles, and

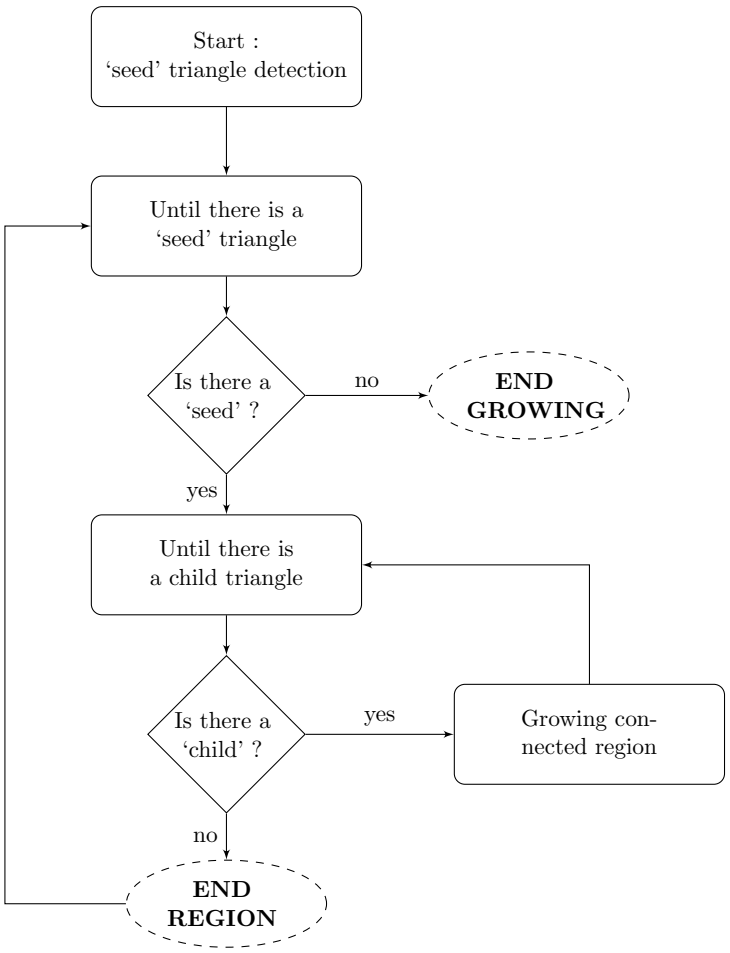

Figure 3.7: Work flow for region growing method (Franciosa and Gerbino, 2008)

therefore, the growing was stopped near them.

Using region growing method, three domains (i.e. $\partial\Omega_{lvendo}$, $\partial\Omega_{lvendo}$ and RV inner surface) were identified (Figure 3.9). The lowest point in $\partial\Omega_{lvendo}$ from the base was automatically recognised by evaluating the maximum perpendicular distance between the plane PL and every node in $\partial\Omega_{lvendo}$. The long-axis of LV was defined by the line perpendicular to PL and passing through the lowest point of $\partial\Omega_{lvendo}$. The same procedure was applied to

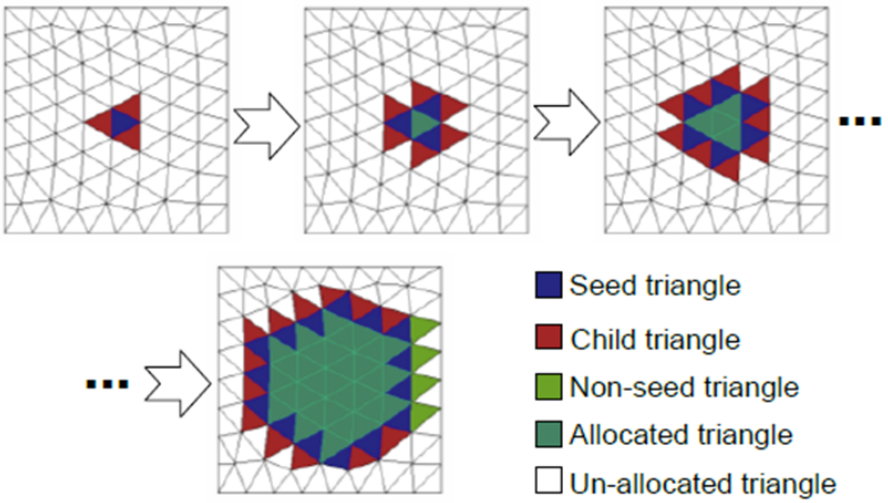

Figure 3.8: Schematic representation of region growing mechanism (Franciosa and Gerbino, 2008)

get the lowest point on RV inner surface and subsequently RV long-axis. RV and LV long axes were parallel to each other as both were perpendicular to plane PL. The perpendicular distance between every node in RV inner surface and LV long axis was measured, and using the perpendicular distance ($daxis_{LVRV}$) between LV and RV long axes as threshold values, the $\partial\Omega_{rvfree}$ and $\partial\Omega_{rvsep}$ were separated.

Function 2: Define Dirichlet Boundary Conditions (DBC)

The local coordinates ($\mathbf{e_n}$, $\mathbf{e_c}$, $\mathbf{e_z}$) were defined in every node on $\partial\Omega$. It was assumed that $\mathbf{e_z}$ would be parallel to the long-axis of LV, which was identified in function 1. The nodal normal $\mathbf{e_n}$ was calculated using area weighted facet-normal averaging algorithm (Wong and Kuhl, 2014). Facet-normal is the cross product of two edge vectors of the respective facet. Local $\mathbf{e_n}$ was then defined by the average of all the facet normals connected at that particular node. The nodal normal was automatically area averaged as the magnitude of the cross

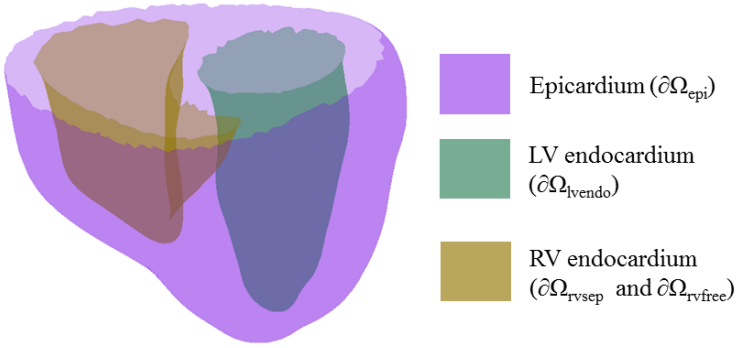

Figure 3.9: Output from region growing algorithm used in Function 1 to separate epicardium ($\partial\Omega_{epi}$), LV endocardium ($\partial\Omega_{lvendo}$) and RV endocardium surface ($\partial\Omega_{rvfree}$ and $\partial\Omega_{rvsep}$)

product was proportional to the area of the corresponding facet (Wong and Kuhl, 2014). Local circumferential $\mathbf{e_c}$ was the weighted cross product of $\mathbf{e_n}$ and $\mathbf{e_z}$ in order to ensure proper orientation of $\mathbf{e_c}$ on the $\partial\Omega_{epi}$.

$$\mathbf{e_c} = \begin{cases} +(\mathbf{e_z} \times \mathbf{e_n}) & \text{on } \partial\Omega_{epi} \text{ and } \partial\Omega_{rvsep} \\ -(\mathbf{e_z} \times \mathbf{e_n}) & \text{on } \partial\Omega_{lvendo} \text{ and } \partial\Omega_{rvfree} \end{cases} \tag{3.4}$$

It was assumed that the sheet direction was aligned with outward facing nodal normal ($\mathbf{e_n}$ or local transmural or radial direction) on $\partial\Omega$. Hence, $\mathbf{s}$ was calculated as,

$$\mathbf{s} = \begin{cases} +\mathbf{e_n} & \text{on } \partial\Omega_{epi} \text{ and } \partial\Omega_{rvsep} \\ -\mathbf{e_n} & \text{on } \partial\Omega_{lvendo} \text{ and } \partial\Omega_{rvfree} \end{cases} \tag{3.5}$$

The outward normal $\mathbf{e_{cz}}$ with respect to local e_c-e_z plane was calculated as,

$$\mathbf{e_{cz}} = \mathbf{e_c} \times \mathbf{e_z} \tag{3.6}$$

Fibres were assumed to be distributed at an angle of α_h with local $\mathbf{e_c}$. The projection ($\mathbf{p}$) of the fibre direction on e_c-e_z plane with respect to $\mathbf{e_c}$ at an angle α_h was,

$$\mathbf{p} = \mathbf{e_c}\cos(\alpha_h) + \mathbf{e_z}\sin(\alpha_h) \tag{3.7}$$

The fibre direction ($\mathbf{f}$) was defined by rotating $\mathbf{p}$ from the e_c-e_z plane back into the sheet plane tangent to the surface.

$$\mathbf{f} = \mathbf{s} \times (\mathbf{p} \times \mathbf{e_{cz}}) \tag{3.8}$$

At this point, all the Dirichlet boundary conditions (DBC) over the domain $\partial\Omega$ were defined.

Function 3: Solving Laplace Interpolation using FEM

In order to get smooth interpolated fibre distribution, $\mathbf{f}$ and $\mathbf{s}$ were interpolated over the whole cardiac domain Ω by considering each component of the vectors as a scalar valued feature Φ and the corresponding Laplace equation was solved. The shape function of the mesh element was calculated and used for defining the total sparse stiffness matrix (L_k) of the whole domain. The Dirichlet boundary conditions (DBC) were then applied as hard constraints and the equation was solved as,

$$\Phi = (L_k)DBC^{-1} \tag{3.9}$$

After Laplace interpolation, the $\mathbf{f}$ and $\mathbf{s}$ directions were defined for each node of the whole ventricular mesh (Ω). Using element shape function, fibre and

sheet directions could be interpolated to integration point or element centroid which would be useful while using in any FE software packages. In order to maintain the sheet direction to be orthonormal with fibre direction, Eq. (3.10) could be used

$$\overline{\mathbf{s}} = [\mathbf{f} \times \mathbf{s}] \times \mathbf{f} \tag{3.10}$$

After calculating $\mathbf{f}$ and $\mathbf{s}$, $\mathbf{n}$ was calculated using vector cross product (i.e. $\mathbf{n} = \mathbf{f} \times \mathbf{s}$). After that, all the $\mathbf{f}$, $\mathbf{s}$, and $\mathbf{n}$ vectors, defined at the centre of the mesh, were normalised for further use in FE modelling. A brief overview of the LDRF work flow is depicted in Figure 3.10.

3.3.2 Implementation

The LDRF algorithm was implemented in Matlab (Matlab, R2012b, The Mathworks, USA) (Appendix C). First, the ventricular mesh geometry, consisting of linear tetrahedral elements, was constructed from CMRI using Mimics and 3-matic as described in Section 3.2.2. The constructed mesh geometry was then exported from 3-matic in $*.inp$ (Abaqus input file) format which was the first input of LDRF algorithm. The plane (PL), which was the second input of LDRF algorithm, was created manually in 3-matic and exported in $*.asc$ format. The third input (i.e. fibre angle) was defined from the histological data. The $*inp$ file was used in Matlab to calculate the stiffness matrix of the whole geometry (Ω) using the shape function of the tetrahedral element. The boundary surface ($\partial\Omega$) was then identified using $TriRep()$ and $freeBoundary()$ functions in Matlab. The boundary surface was then cut by the plane PL such that there would be no connections among the epi-

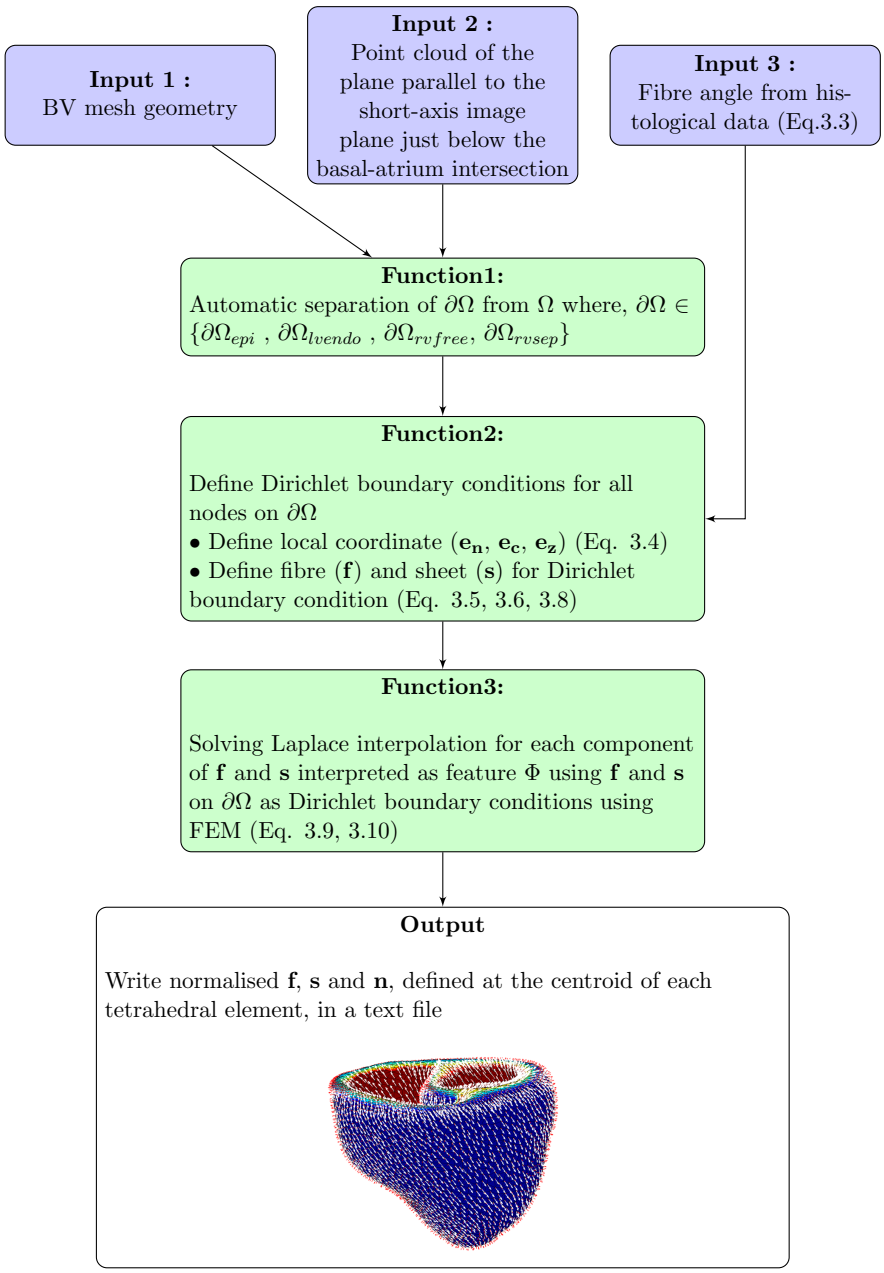

Figure 3.10: Work flow of LDRF algorithm

cardium, LV endocardium and RV endocardium surfaces. Three boundary surfaces ($\partial\Omega_{epi}$, $\partial\Omega_{lvendo}$, and RV endocardium) were then identified using the region growing algorithm. After that, the distance based method, as explained

in Function 1 of LDRF algorithm, was implemented to separate the RV endocardium surface into $\partial\Omega_{rvfree}$ and $\partial\Omega_{rvsep}$. Function 2 was implemented according to the mathematical descriptions to define the Dirichlet boundary conditions (DBC) on the $\partial\Omega_{epi}$, $\partial\Omega_{lvendo}$, $\partial\Omega_{rvfree}$ and $\partial\Omega_{rvsep}$ surfaces. The FE interpolation was carried out using the stiffness matrix of the whole geometry (calculated at the first of LDRF coding) and Dirichlet boundary conditions (produced in function 2) to define the fibre and sheet directions at each node of the mesh geometry. Finally, the interpolated fibre and sheet directions, defined at each node, were further interpolated to define the directions at the centroid of each tetrahedral elements in the mesh geometry. The mutual orthogonality of the $\mathbf{f}$ and $\mathbf{s}$ was maintained using Eq. (3.10). The sheet-normal ($\mathbf{n}$) was then calculated by carrying out cross product of $\mathbf{f}$ and $\mathbf{s}$ for each element. The vectors (i.e. $\mathbf{f}$, $\mathbf{s}$ and $\mathbf{n}$) were then normalised and written in a text file along corresponding element number for future use in FE software.

3.3.3 Results and Validation

Figure 3.11 shows the LDRF results providing a smooth continuum distribution of fibre angle (α_h) across the pre-defined Dirichlet boundary sets. The colour map represents the transmural variation of α_h from endocardium to epicardium. In Figure 3.11, the green in the colour bar represents $\alpha_h = 0$ radian. The green colour, which appeared in the middle of the ventricle wall, agreed excellently with the histological data and served as a validation for the algorithm. Figure 3.12 shows $\mathbf{f}$ and $\mathbf{s}$ directions throughout the ventricles. In the vicinity of the apex, a challenging region for smooth fibre map, appeared to be reasonably smooth. The results were also similar with the results of Wong

and Kuhl (2014). Further validation of the implemented fibre-orientation was carried out by using it in diastolic modelling of LV, and subsequently, comparing the FE predicted stress results with the published work. Details of that study will be described in Section 4.4.2 of Chapter 4.

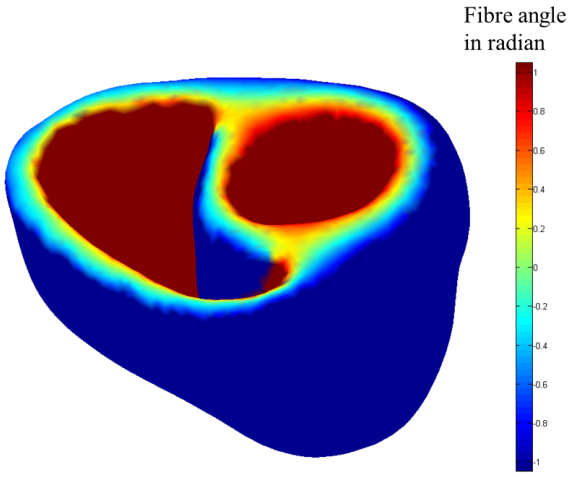

Figure 3.11: Transmural distribution of fibre angle (α_h) generated from LDRF algorithm. In this particular case, α_h was assumed to vary from $-60°$ to $+60°$

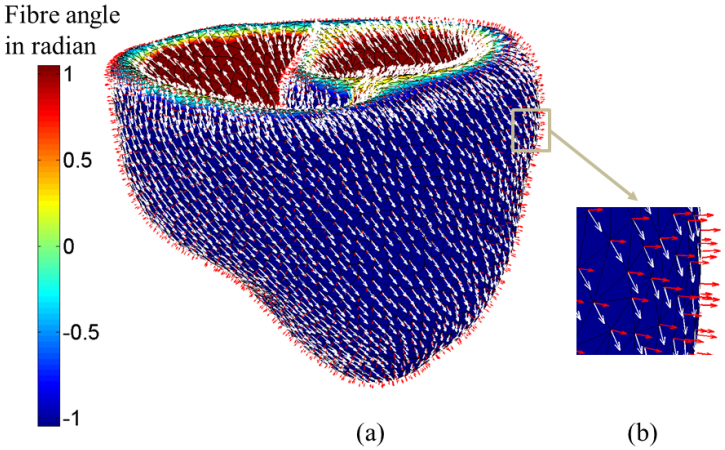

Figure 3.12: Fibre ($\mathbf{f}$) and sheet ($\mathbf{s}$) directions generated from LDRF algorithm. White and red arrows represent $\mathbf{f}$ and $\mathbf{s}$ directions respectively.

3.4 Constitutive Law for Passive Myocardium

Several constitutive laws had been proposed by various researchers considering myocardium tissue as hyperelastic material as detailed in Section 2.7 of Chapter 2. Holzapfel-Ogden material model (Holzapfel and Ogden, 2009) was elected in the study because of its several advantages compared to other orthotropic constitutive law as discussed in the Section 2.7. Details of the constitutive law, its numerical implementation in FE framework and validation methods with results are discussed in subsequent sections.

3.4.1 Holzapfel-Ogden Material Model

Most hyperelastic constitutive cardiac models considered the myocardium deformation as volume-preserving. However, this incompressibility assumption is not justified specially for myocardium due to the presence of vascular network that contributes to 10-20% of the total volume of the myocardial wall. Yin et al. (1996) reported that the volume change in ventricular wall may range in between 5-10% . Thus, the strain energy function developed by Holzapfel and Ogden (2009) was extended by Goktepe et al. (2011) and Eriksson et al. (2013) to include the multiplicative decomposition of deformation gradient. Using decoupled volumetric-isochoric formulation of finite elasticity, the deformation gradient ($\mathbf{F}$) is multiplicatively decomposed into a volumetric part (dilatational) $\mathbf{F_{vol}}$ and an isochoric part (volume preserving or distortional part) $\overline{\mathbf{F}}$ as,

$$\mathbf{F} = \overline{\mathbf{F}}\,\mathbf{F_{vol}} \quad \text{where} \quad \mathbf{F_{vol}} = J^{1/3}\,\mathbf{I} \quad \text{and} \quad \overline{\mathbf{F}} = J^{-1/3}\,\mathbf{F} \tag{3.11}$$

such that $J = \det(\mathbf{F_{vol}})$ and $\det(\mathbf{F}) = 1$. The left and right Cauchy-Green tensors are defined as $\mathbf{b} = J^{2/3}\ \overline{\mathbf{b}}$ and $\mathbf{C} = J^{2/3}\ \overline{\mathbf{C}}$ respectively, where, $\overline{\mathbf{b}} = \overline{\mathbf{F}}\ \overline{\mathbf{F}}^{\mathbf{T}}$ and $\overline{\mathbf{C}} = \overline{\mathbf{F}}^{\mathbf{T}}\ \overline{\mathbf{F}}$ denote the modified tensor quantities. The myocardium tissue is an orthotropic material with the fibre, sheet and sheet-normal directions denoted by $\mathbf{f_0}$, $\mathbf{s_0}$, $\mathbf{n_0}$ respectively in the Lagrangian framework. The strain energy function Ψ per unit reference volume is additively decomposed into volumetric ($\Psi_{vol}(J)$) and isochoric ($\overline{\Psi}$) parts,

$$\Psi = \Psi_{vol}(J) + \overline{\Psi}\ (\overline{I}_1, \overline{I}_{4f}, \overline{I}_{4s}, \overline{I}_{8fs}) \tag{3.12}$$

where, $\Psi_{vol}(J)$ and $\overline{\Psi}$ are given scalar valued function of J and the isochoric invariants $\overline{I}_1$, $\overline{I}_{4f}$, $\overline{I}_{4s}$, $\overline{I}_{8fs}$ respectively. The definition of isochoric invariants are

$$\overline{I}_1 = \mathrm{Tr}(\overline{\mathbf{C}}), \quad \overline{I}_{4f} = \mathbf{f_0} \cdot (\overline{\mathbf{C}}\mathbf{f_0}), \quad \overline{I}_{4s} = \mathbf{s_0} \cdot (\overline{\mathbf{C}}\mathbf{s_0}), \quad \overline{I}_{8fs} = \mathbf{f_0} \cdot (\overline{\mathbf{C}}\mathbf{s_0}) \tag{3.13}$$

The volumetric function $\Psi_{vol}(J)$ is defined as

$$\Psi_{vol}(J) = K\left(\frac{J^2 - 1}{2} - \ln J\right) \tag{3.14}$$

where, K is the user specified bulk modulus and serves as a penalty parameter to incorporate material incompressibility. The material tends to be more incompressible with the increase of K. The volume preserving function ($\overline{\Psi}$) consists of two parts - an isotropic part ($\overline{\Psi}_{iso}$) and an anisotropic part ($\overline{\Psi}_{aniso}$). The isotropic volume preserving part $\overline{\Psi}_{iso}$ depends only on $\overline{\mathbf{I}}_1$ and represents the contribution of an isotropic ground matrix of the myocardial material and described as

$$\overline{\Psi}_{iso} = \frac{a}{2b} \exp[b(\overline{I}_1 - 3)] \tag{3.15}$$

The anisotropic part $\overline{\Psi}_{aniso}$ correspond to the contributions from the myocytes and families of collagen fibre embedded within the ground matrix. The function is described as

$$\overline{\Psi}_{aniso} = \sum_{i=f,s} \frac{a_i}{2b_i} \left\{ \exp[b_i(\overline{I}_{4i} - 1)^2] - 1 \right\} + \frac{a_{fs}}{2b_{fs}} [\exp(b_{fs}\overline{I}_{8fs}^2) - 1] \tag{3.16}$$

As the collagen fibres do not support compression and to maintain strong ellipticity of the strain energy, the term containing the directionally dependent invariants are included in Eq. (3.16) only if $\overline{\mathbf{I}}_{4f} > 1$ and $\overline{\mathbf{I}}_{4s} > 1$ is fulfilled (Holzapfel and Ogden, 2009). There are total eight non-negative material parameters in the strain energy function (a, b, a_f, b_f, a_s, b_s, a_{8fs}, b_{8fs}) along with an extra bulk modulus (K). Hence the total strain energy function used in the study is

$$\begin{aligned} \Psi = K \left(\frac{J^2 - 1}{2} - \ln J \right) + \frac{a}{2b} \exp[b(\overline{I}_1 - 3)] \\ + \sum_{i=f,s} \frac{a_i}{2b_i} \left\{ \exp[b_i(\overline{I}_{4i} - 1)^2] - 1 \right\} + \frac{a_{fs}}{2b_{fs}} [\exp(b_{fs}\overline{I}_{8fs}^2) - 1] \end{aligned} \tag{3.17}$$

where, a and b parameters represent the response of isotropic ground matrix; a_f and b_f characterise the response of myocardial fibres; a_s and b_s denote the contribution of sheet; and a_{fs} and b_{fs} account for the shear effects in the sheet-plane. All a_i ($i = f,\ s,\ fs$) and a represent the dimension of stress in kPa and the unit-less parameter b_i ($i = f,\ s,\ fs$) and b represent the non-linear behaviour of the corresponding structure.

The second Piola-Kirchhoff stress tensor $\mathbf{S} = 2\partial\Psi/\partial\mathbf{C}$ is also divided

into a purely volumetric part ($\mathbf{S}_{vol}$) and a purely isochoric ($\overline{\mathbf{S}}$) part i.e. $\mathbf{S} = \mathbf{S}_{vol} + \overline{\mathbf{S}}$. The volumetric part is

$$\mathbf{S} = Jp_h\mathbf{C}^{-1} \quad \text{where,} \quad p_h = \frac{d\Psi_{vol}}{dJ} = K\left(\frac{J^2-1}{J}\right) \tag{3.18}$$

and the isochoric part is

$$\begin{aligned}\overline{\mathbf{S}} = 2J^{-2/3}\Big[&\overline{\Psi}_1\mathrm{DEV}(\mathbf{I}) + \overline{\Psi}_{4f}\mathrm{DEV}(\mathbf{f_0}\otimes\mathbf{f_0}) + \overline{\Psi}_{4s}\mathrm{DEV}(\mathbf{s_0}\otimes\mathbf{s_0}) \\ &+ \frac{1}{2}\overline{\Psi}_{8fs}\mathrm{DEV}(\mathbf{f_0}\otimes\mathbf{s_0} + \mathbf{s_0}\otimes\mathbf{f_0})\Big]\end{aligned} \tag{3.19}$$

where, $\mathbf{I}$ is identity tensor and

$$\mathrm{DEV}(\bullet) = (\bullet) - \frac{1}{3}[(\bullet) : \mathbf{C}]\mathbf{C}^{-1} \tag{3.20}$$

is the deviatoric operator in the Lagrangian description so that $\mathrm{DEV}(\partial\overline{\Psi}/\partial\overline{\mathbf{C}}) : \mathbf{C} = 0$. Furthermore, in Eq. (3.19), the following definitions are used.

$$\overline{\Psi}_1 = \frac{\partial\overline{\Psi}}{\partial\overline{I}_1} = \frac{a}{2}\exp[b(\overline{I}_1 - 3)]\ , \tag{3.21}$$

$$\overline{\Psi}_{4i} = \frac{\partial\overline{\Psi}}{\partial\overline{I}_{4i}} = a_i(\overline{I}_{4i} - 1)\exp[b_i(\overline{I}_{4i} - 1)^2]\ , \quad i = \mathrm{f,\ s}, \tag{3.22}$$

$$\overline{\Psi}_{8fs} = \frac{\partial\overline{\Psi}}{\partial\overline{I}_{8fs}} = a_{fs}\overline{I}_{8fs}\exp[b_{fs}\overline{I}_{8fs}^2]\ , \tag{3.23}$$

3.4.2 FE Implementation of Holzapfel-Ogden Material Law

The Holzapfel-Ogden constitutive law for passive myocardium was implemented using a user-defined subroutine 'Hypela2' in MSC-Marc Mentat (MSC Software Corporation, California, US) (Appendix B). 'Total Lagrange Frame-

work' was used in 'Hypela2'. Instead of using complex analytical expression to calculate material elasticity tensor in Lagrangian description, the 'finite-difference' approach was adopted in 'Hypela2'. The fibre-sheet orientation field for a given mesh, generated using LDRF algorithm (Section 3.3.1), were saved in a text file and subsequently used in 'Hypela2' to incorporate material orthotropy. Classic three field formulation (i.e. pressure-dilatation-displacement) was used in MSC Marc using 'FEATURE 3402' to overcome the locking problems exhibited by purely displacement-based FE formulation (Goktepe et al., 2011). The validation of the material model implementation was carried out by comparing the FE results with the analytical solutions as detailed in Section 3.4.3 and 3.4.4.

3.4.3 Analytical Expression of the Stress Tensor for Analytical Test Cases

When a new material model/constitutive law is implemented in FE framework, the numerical implementation needs to be validated by comparing the simulation results with the analytical solutions. For this reason, analytical expression of the stress tensor for the Holzapfel-Ogden material model under standard analytical test cases is presented here. Expressions are presented for the following standard test cases : (1) uniaxial stretch, (2) biaxial stretch, (3) simple shear, (4) uniaxial compression. Also, to check the implementation of material orthotropy in FE framework, (5) simple shear test expression is included when undeformed fibre and sheet directions are not aligned with global X and Y axis respectively.

A unit cube specimen of Holzapfel-Ogden material (myocardium tissue)

with orthogonal material directions is considered. If not stated otherwise in the following, the undeformed fibre ($\mathbf{f_0}$), sheet ($\mathbf{s_0}$) and sheet-normal ($\mathbf{n_0}$) directions of the cube element are assumed to coincide with the global cartesian coordinate system (X, Y, Z), and therefore, $[\mathbf{f_0}] = [\ 1,\ 0,\ 0\ ]^{\mathrm{T}}$, $[\mathbf{s_0}] = [\ 0,\ 1,\ 0\ ]^{\mathrm{T}}$, $[\mathbf{n_0}] = [\ 0,\ 0,\ 1\ ]^{\mathrm{T}}$. Furthermore, it is assumed that the material is incompressible and under plane stress state.

(A) Uniaxial Stretch Test

The deformation gradient ($\mathbf{F}$) and right Cauchy green tensor ($\mathbf{C}$) for uniaxial stretch λ_{ff} in the $\mathbf{f_0}$ direction are

$$[\mathbf{F}] = \begin{bmatrix} \lambda_{ff} & 0 & 0 \\ 0 & 1/\sqrt{\lambda_{ff}} & 0 \\ 0 & 0 & 1/\sqrt{\lambda_{ff}} \end{bmatrix}, \quad [\mathbf{C}] = \begin{bmatrix} \lambda_{ff}^2 & 0 & 0 \\ 0 & 1/\lambda_{ff} & 0 \\ 0 & 0 & 1/\lambda_{ff} \end{bmatrix}, \tag{3.24}$$

It is stated in the definition of Holzapfel-Ogden model that the terms related to the fibre and sheet direction in the strain energy function are only active when they are in tension. For that reason, $\Psi_{4s} = 0$ as $\lambda_{ss} < 1$ in this case. The components of Cauchy stress are

$$\sigma_{11} = \lambda_{ff}^2 a \exp[b(\lambda_{ff}^2 + \frac{2}{\lambda_{ff}} - 3)] + 2\lambda_{ff}^2(\lambda_{ff}^2 - 1)a_f \exp[b_f(\lambda_{ff}^2 - 1)^2] \tag{3.25}$$

$$\sigma_{22} = \sigma_{33} = \sigma_{12} = \sigma_{13} = \sigma_{23} = 0 \tag{3.26}$$

(B) Biaxial Stretch Test

For biaxial stretch, λ_{ff} and λ_{ss} in the $\mathbf{f_0}$ and $\mathbf{s_0}$ directions respectively, the deformation gradient ($\mathbf{F}$) and right Cauchy Green tensor ($\mathbf{C}$) are

$$[\mathbf{F}] = \begin{bmatrix} \lambda_{ff} & 0 & 0 \\ 0 & \lambda_{ss} & 0 \\ 0 & 0 & 1/(\lambda_{ff}\lambda_{ss}) \end{bmatrix}, \quad [\mathbf{C}] = \begin{bmatrix} \lambda_{ff}^2 & 0 & 0 \\ 0 & \lambda_{ss}^2 & 0 \\ 0 & 0 & 1/(\lambda_{ff}\lambda_{ss})^2 \end{bmatrix}, \quad (3.27)$$

The components of Cauchy stress tensor are

$$\sigma_{11} = 2\Psi_1(\lambda_{ff}^2 - 1/\lambda_{ff}^2\lambda_{ss}^2) + 2\Psi_{4f}\lambda_{ff}^2 \quad (3.28)$$

$$\sigma_{22} = 2\Psi_1(\lambda_{ss}^2 - 1/\lambda_{ff}^2\lambda_{ss}^2) + 2\Psi_{4s}\lambda_{ss}^2 \quad (3.29)$$

$$\sigma_{33} = p_h + 2\Psi_1(1/\lambda_{ff}^2\lambda_{ss}^2) = 0 \quad (3.30)$$

$$\sigma_{12} = \sigma_{13} = \sigma_{23} = 0 \quad (3.31)$$

where,

$$\Psi_1 = \frac{a}{2}\exp[b(\lambda_{ff}^2 + \lambda_{ss}^2 + 1/\lambda_{ff}^2\lambda_{ss}^2 - 3)] , \quad (3.32)$$

$$\Psi_{4f} = a_f(\lambda_{ff}^2 - 1)\exp[b_f(\lambda_{ff}^2 - 1)^2] , \quad (3.33)$$

$$\Psi_{4s} = a_s(\lambda_{ss}^2 - 1)\exp[b_s(\lambda_{ss}^2 - 1)^2] , \quad (3.34)$$

p_h is calculated from Eq. (3.30) and inserted into Eq. (3.28) and (3.28).

(C) Simple Shear Test

Six possible modes of simple shear test can be carried out based on the material directions ($\mathbf{f_0}$, $\mathbf{s_0}$, $\mathbf{n_0}$), aligned in the global cartesian coordinate (X, Y, Z) system (Figure 3.13). In order to distinguish amongst the six different shear modes, the notation employed by Dokos et al. (2002), Holzapfel and Ogden

(2009) and Goktepe et al. (2011) is used. The shear modes are defined as (ij) to specify the shear in the j direction in the ij plane where $i, j \in \{\text{f, s, n}\}$. Therefore, the first letter in shear mode (ij) denotes the normal vector of the face that is displaced by the simple shear and the second letter indicates the direction of the deformation. For example, the modes in which the fibres are stretched are (fn) and (fs). It should be noted that the order of the indices i and j in (ij) (i.e. with parenthesis), which defines shear mode, is important. On the other hand, the order of i and j in ij (i.e. without parenthesis), which refers plane, is not relevant. The Cauchy stress components for each shear mode is detailed in the following section.

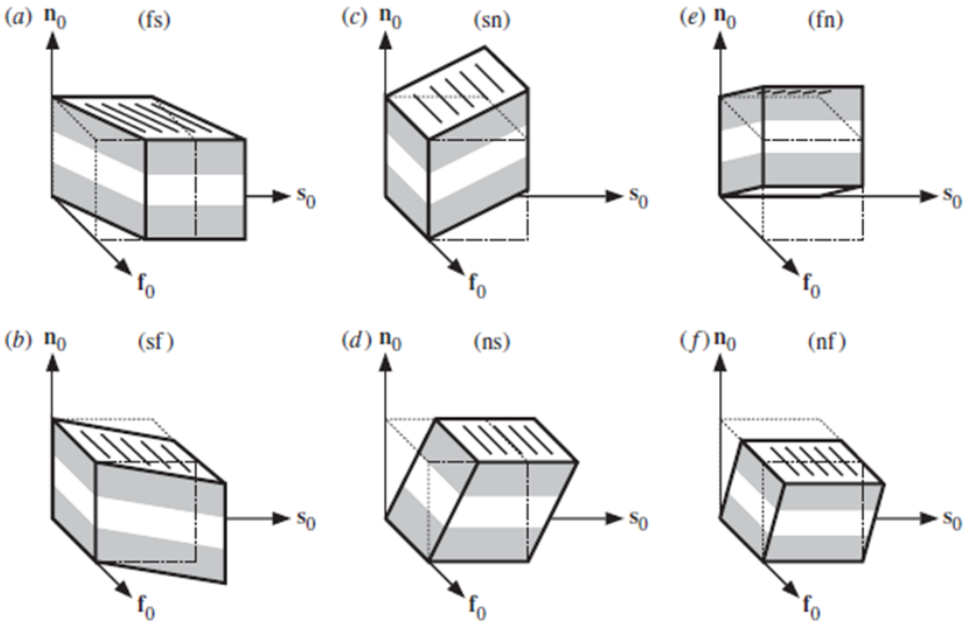

Figure 3.13: Schematic diagram of six possible simple shear modes for a cube (myocardium) defined with respect to the fibre ($\mathbf{f_0}$), sheet ($\mathbf{s_0}$) and sheet-normal ($\mathbf{n_0}$) directions. The shear modes are defined as (ij) to specify the shear in the j direction in the ij plane where $i, j \in \{\text{f, s, n}\}$; the diagram was taken from Holzapfel and Ogden (2009)

1. **Shear Mode (fs)**

   Shear mode (fs) refers to shear γ in $\mathbf{s_0}$ direction in fs plane (Figure 3.13a). The deformation gradient ($\mathbf{F}$) and right Cauchy Green tensor ($\mathbf{C}$) are

$$[\mathbf{F}] = \begin{bmatrix} 1 & 0 & 0 \\ \gamma & 1 & 0 \\ 0 & 0 & 1 \end{bmatrix}, \quad [\mathbf{C}] = \begin{bmatrix} 1+\gamma^2 & \gamma & 0 \\ \gamma & 1 & 0 \\ 0 & 0 & 1 \end{bmatrix}, \tag{3.35}$$

   The components of Cauchy stress tensor are

$$\sigma_{11} = 2\gamma^2 a_f \exp[\gamma^4 b_f] \tag{3.36}$$

$$\sigma_{22} = \gamma^2 a \exp[\gamma^2 b] + 2\gamma^4 a_f \exp[\gamma^4 b_f] + 2\gamma^2 a_{fs} \exp[\gamma^2 b_{fs}] \tag{3.37}$$

$$\sigma_{12} = \gamma a \exp[\gamma^2 b] + 2\gamma^3 a_f \exp[\gamma^4 b_f] + \gamma a_{fs} \exp[\gamma^2 b_{fs}] \tag{3.38}$$

$$\sigma_{33} = \sigma_{13} = \sigma_{23} = 0 \tag{3.39}$$

2. **Shear Mode (fn)**

   Shear mode (fn) refers to shear γ in $\mathbf{n_0}$ direction in fn plane (Figure 3.13e). The deformation gradient ($\mathbf{F}$) and right Cauchy Green tensor ($\mathbf{C}$) are

$$[\mathbf{F}] = \begin{bmatrix} 1 & 0 & 0 \\ 0 & 1 & 0 \\ \gamma & 0 & 1 \end{bmatrix}, \quad [\mathbf{C}] = \begin{bmatrix} 1+\gamma^2 & 0 & \gamma \\ 0 & 1 & 0 \\ \gamma & 0 & 1 \end{bmatrix}, \tag{3.40}$$

The components of Cauchy stress tensor are

$$\sigma_{11} = 2\gamma^2 a_f \exp[\gamma^4 b_f] \tag{3.41}$$

$$\sigma_{33} = \gamma^2 a \exp[\gamma^2 b] + 2\gamma^4 a_f \exp[\gamma^4 b_f] \tag{3.42}$$

$$\sigma_{13} = \gamma a \exp[\gamma^2 b] + 2\gamma^3 a_f \exp[\gamma^4 b_f] \tag{3.43}$$

$$\sigma_{22} = \sigma_{12} = \sigma_{23} = 0 \tag{3.44}$$

3. **Shear Mode (sf)**

Shear mode (sf) refers to shear γ in $\mathbf{f_0}$ direction in sf plane (Figure 3.13b). The deformation gradient ($\mathbf{F}$) and right Cauchy Green tensor ($\mathbf{C}$) are

$$[\mathbf{F}] = \begin{bmatrix} 1 & \gamma & 0 \\ 0 & 1 & 0 \\ 0 & 0 & 1 \end{bmatrix}, \quad [\mathbf{C}] = \begin{bmatrix} 1 & \gamma & 0 \\ \gamma & 1+\gamma^2 & 0 \\ 0 & 0 & 1 \end{bmatrix}, \tag{3.45}$$

The components of Cauchy stress tensor are

$$\sigma_{11} = \gamma^2 a \exp[\gamma^2 b] + 2\gamma^4 a_s \exp[\gamma^4 b_s] + 2\gamma^2 a_{fs} \exp[\gamma^2 b_{fs}] \tag{3.46}$$

$$\sigma_{22} = 2\gamma^2 a_s \exp[\gamma^4 b_s] \tag{3.47}$$

$$\sigma_{12} = \gamma a \exp[\gamma^2 b] + 2\gamma^3 a_s \exp[\gamma^4 b_s] + \gamma a_{fs} \exp[\gamma^2 b_{fs}] \tag{3.48}$$

$$\sigma_{33} = \sigma_{13} = \sigma_{23} = 0 \tag{3.49}$$

4. **Shear Mode (sn)**

Shear mode (sn) refers to shear γ in $\mathbf{n_0}$ direction in sn plane (Figure 3.13c). The deformation gradient ($\mathbf{F}$) and right Cauchy Green tensor

(**C**) are

$$[\mathbf{F}] = \begin{bmatrix} 1 & 0 & 0 \\ 0 & 1 & 0 \\ 0 & \gamma & 1 \end{bmatrix} \quad , \quad [\mathbf{C}] = \begin{bmatrix} 1 & 0 & 0 \\ 0 & 1+\gamma^2 & \gamma \\ 0 & \gamma & 1 \end{bmatrix} \quad , \tag{3.50}$$

The components of Cauchy stress tensor are

$$\sigma_{22} = 2\gamma^2 a_s \exp[\gamma^4 b_s] \tag{3.51}$$

$$\sigma_{33} = \gamma^2 a \exp[\gamma^2 b] + 2\gamma^4 a_s \exp[\gamma^4 b_s] \tag{3.52}$$

$$\sigma_{23} = \gamma a \exp[\gamma^2 b] + 2\gamma^3 a_s \exp[\gamma^4 b_s] \tag{3.53}$$

$$\sigma_{11} = \sigma_{12} = \sigma_{13} = 0 \tag{3.54}$$

5. **Shear Mode (nf)**

Shear mode (nf) refers to shear γ in $\mathbf{f_0}$ direction in nf plane (Figure 3.13f). The deformation gradient (**F**) and right Cauchy Green tensor (**C**) are

$$[\mathbf{F}] = \begin{bmatrix} 1 & 0 & \gamma \\ 0 & 1 & 0 \\ 0 & 0 & 1 \end{bmatrix} \quad , \quad [\mathbf{C}] = \begin{bmatrix} 1 & 0 & \gamma \\ 0 & 1 & \\ \gamma & \gamma & 1+\gamma^2 \end{bmatrix} \quad , \tag{3.55}$$

The components of Cauchy stress tensor are

$$\sigma_{11} = \gamma^2 a \exp[\gamma^2 b] \tag{3.56}$$

$$\sigma_{33} = 0 \tag{3.57}$$

$$\sigma_{13} = \gamma a \exp[\gamma^2 b] \tag{3.58}$$

$$\sigma_{22} = \sigma_{12} = \sigma_{23} = 0 \tag{3.59}$$

6. **Shear Mode (ns)**

Shear mode (ns) refers to shear γ in $\mathbf{s_0}$ direction in ns plane (Figure 3.13d). The deformation gradient ($\mathbf{F}$) and right Cauchy Green tensor ($\mathbf{C}$) are

$$[\mathbf{F}] = \begin{bmatrix} 1 & 0 & 0 \\ 0 & 1 & \gamma \\ 0 & 0 & 1 \end{bmatrix}, \quad [\mathbf{C}] = \begin{bmatrix} 1 & 0 & 0 \\ 0 & 1 & \gamma \\ 0 & \gamma & 1+\gamma^2 \end{bmatrix}, \tag{3.60}$$

The components of Cauchy stress tensor are

$$\sigma_{22} = \gamma^2 a \exp[\gamma^2 b] \tag{3.61}$$

$$\sigma_{33} = 0 \tag{3.62}$$

$$\sigma_{23} = \gamma a \exp[\gamma^2 b] \tag{3.63}$$

$$\sigma_{11} = \sigma_{12} = \sigma_{13} = 0 \tag{3.64}$$

Derivation of the Cauchy stresses for the six specific shear modes leads to the following explicit expressions of shear stress in terms of the material parameters and the amount of shear γ as follows

$$\sigma^{(fs)} = \gamma a \exp[\gamma^2 b] + 2\gamma^3 a_f \exp[\gamma^4 b_f] + \gamma a_{fs} \exp[\gamma^2 b_{fs}] \tag{3.65}$$

$$\sigma^{(fn)} = \gamma a \exp[\gamma^2 b] + 2\gamma^3 a_f \exp[\gamma^4 b_f] \tag{3.66}$$

$$\sigma^{(sf)} = \gamma a \exp[\gamma^2 b] + 2\gamma^3 a_s \exp[\gamma^4 b_s] + \gamma a_{fs} \exp[\gamma^2 b_{fs}] \tag{3.67}$$

$$\sigma^{(sn)} = \gamma a \exp[\gamma^2 b] + 2\gamma^3 a_s \exp[\gamma^4 b_s] \tag{3.68}$$

$$\sigma^{(nf)} = \gamma a \exp[\gamma^2 b] \tag{3.69}$$

$$\sigma^{(ns)} = \gamma a \exp[\gamma^2 b] \tag{3.70}$$

(D) Compression Test

The unit cube is subjected to an active stress S_a, which results contraction, in the fibre ($\mathbf{f_0}$) (or global X) direction. The cube is assumed to be incompressible and as a result, the cube will expand in the sheet ($\mathbf{s_0}$) (or global Y) and sheet-normal ($\mathbf{n_0}$) (or global Z) directions due to the active stress S_a in fibre ($\mathbf{f_0}$) (or global X) direction. Due to the active compression, the stretch in fibre, sheet and sheet-normal directions are λ_f, λ_s and λ_n respectively and the deformation gradient ($\mathbf{F}$) is

$$[\mathbf{F}] = \begin{bmatrix} \lambda_f & 0 & 0 \\ 0 & \lambda_s & \gamma \\ 0 & 0 & \lambda_n \end{bmatrix} \tag{3.71}$$

where $\lambda_f < 1$, $\lambda_s > 1$ and $\lambda_n > 1$. Each components of the Cauchy stress tensor is zero at equilibrium as the cube can freely deform. The Lagrange multiplier p_h can be calculated using the relation $\sigma_{33} = 0$. Using volume-preserving incompressible material ($J = \det\mathbf{F} = 1$) condition, the following set of non-linear equations are obtained as

$$\sigma_{11} = 2\Psi_1(\lambda_f^2 - \lambda_n^2) + 2\Psi_{4f}\lambda_f^2 + S_a = 0 \tag{3.72}$$

$$\sigma_{22} = 2\Psi_1(\lambda_s^2 - \lambda_n^2) + 2\Psi_{4s}\lambda_s^2 = 0 \tag{3.73}$$

$$\lambda_f\lambda_s\lambda_n = 1 \tag{3.74}$$

where,

$$\Psi_1 = \frac{a}{2}\exp[b(\lambda_f^2 + \lambda_s^2 + \lambda_f^n - 3)]\,, \tag{3.75}$$

$$\Psi_{4f} = a_f(\lambda_f^2 - 1)\exp[b_f(\lambda_f^2 - 1)^2]\,, \tag{3.76}$$

$$\Psi_{4s} = a_s(\lambda_s^2 - 1)\exp[b_s(\lambda_s^2 - 1)^2]\,, \tag{3.77}$$

In this particular case, $\Psi_{4f} = 0$ as $\lambda_f < 1$ (explained in Section 3.4.1 and (Holzapfel and Ogden, 2009)) due to compression in fibre direction. The set of Eq. (3.72) to (3.74) can be solved to find the values of λ_f, λ_s and λ_n for a given value of the active stress S_a.

(E) Simple Shear Test when Material Directions are not Aligned with Global Axes

In order to check the accurate implementation of the material orthotropy in FE framework, one complex analytical case of simple shear is considered. In this case, the undeformed fibre ($\mathbf{f_0}$) and sheet ($\mathbf{s_0}$) directions are assumed to be aligned with an angle α with respect to the global X axis in global XY plane (Figure 3.14).

Therefore, the fibre ($\mathbf{f_0}$), sheet ($\mathbf{s_0}$) and sheet-normal ($\mathbf{n_0}$) directions are

$$[\mathbf{f_0}] = \begin{bmatrix} \cos\alpha \\ \sin\alpha \\ 0 \end{bmatrix}\,, \quad [\mathbf{s_0}] = \begin{bmatrix} -\sin\alpha \\ \cos\alpha \\ 0 \end{bmatrix}\,, \quad [\mathbf{n_0}] = \begin{bmatrix} 0 \\ 0 \\ 1 \end{bmatrix} \tag{3.78}$$

Simple shear γ in the XY Plane in X direction i.e. shear mode (YX) is considered. Therefore, the deformation gradient ($\mathbf{F}$) and right Cauchy Green tensor

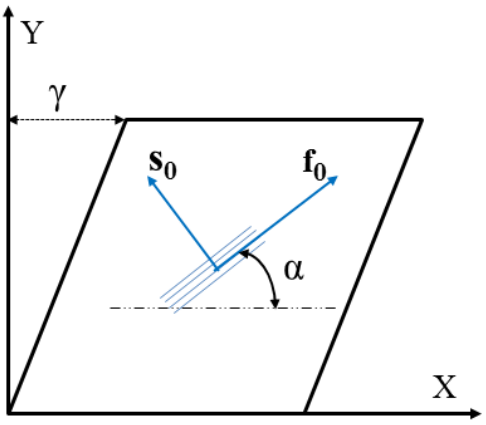

Figure 3.14: Simple shear (γ) test of a unit cube in the XY plane and in the X direction. The fibre ($\mathbf{f_0}$) direction is aligned at an angle α with respect to the global X axis in XY plane. The sheet ($\mathbf{s_0}$) axis is perpendicular to the fibre axis. The global Z axis is perpendicular to the page

($\mathbf{C}$) are

$$[\mathbf{F}] = \begin{bmatrix} 1 & \gamma & 0 \\ 0 & 1 & 0 \\ 0 & 0 & 1 \end{bmatrix} , \quad [\mathbf{C}] = \begin{bmatrix} 1 & \gamma & 0 \\ \gamma & 1+\gamma^2 & 0 \\ 0 & 0 & 1 \end{bmatrix} , \tag{3.79}$$

Using $s = \sin\alpha$ and $c = \cos\alpha$, the components of Cauchy stress tensor are expressed as

$$\sigma_{11} = 2[\Psi_1\lambda^2 + \Psi_{4f}(c+\lambda s)^2 + \Psi_{4s}(-s+\lambda c)^2 + \Psi_{8fs}(c+\lambda s)(-s+\lambda c)] \tag{3.80}$$

$$\sigma_{22} = 2(\Psi_{4f}s^2 + \Psi_{4s}c^2 + \Psi_{48fs}sc) \tag{3.81}$$

$$\sigma_{12} = 2[\Psi_1\lambda + \Psi_{4f}s(c+\lambda s) + 2\Psi_{4s}c(-s+\lambda c)] + \Psi_{8fs}(2\lambda sc + 2c^2 - 1) \tag{3.82}$$

$$\sigma_{33} = \sigma_{13} = \sigma_{23} = 0 \tag{3.83}$$

where,

$$\Psi_1 = \frac{a}{2}\exp(b\lambda^2)\ , \tag{3.84}$$

$$\Psi_{4f} = a_f(I_{4f}-1)\exp[b_f(I_{4f}-1)^2]\ , \tag{3.85}$$

$$\Psi_{4s} = a_s(I_{4s}-1)\exp[b_s(I_{4s}-1)^2]\ , \tag{3.86}$$

$$\Psi_{8fs} = a_{8fs}I_{8fs}\exp[b_{fs}I_{8fs}^2] \tag{3.87}$$

and,

$$I_{4f} = c^2 + 2\lambda sc + s^2(1+\lambda^2)\ , \tag{3.88}$$

$$I_{4s} = s^2 - 2\lambda sc + c^2(1+\lambda^2)\ , \tag{3.89}$$

$$I_{8fs} = -sc + \lambda c^2 - \lambda s^2 + sc(1+\lambda^2)\ , \tag{3.90}$$

3.4.4 Results and Validation

The numerical implementation of Holzapfel-Ogden material model in MSC Marc using 'Hypela2' was validated by comparing the simulation results with the analytical test case solutions, described in Section 3.4.3. The parameters' value of the Holzapfel-Ogden material model, used in those tests, are summarised in Table 3.2. Details of the validation results are described below.

Table 3.2: The parameter values of the Holzapfel-Ogden material model used for validation

Tests	a (kPa)	b	a_f (kPa)	b_f	a_s (kPa)	b_s	a_{fs} (kPa)	b_{fs}
Uniaxial	0.24	10.81	20.04	14.15	3.72	5.16	0.41	11.3
Biaxial	0.10	0.50	2.50	2.0	1.50	1.0	0.50	0.5
Simple Shear	0.24	10.81	20.04	14.15	3.72	5.16	0.41	11.3
Compression	0.24	10.81	20.04	14.15	3.72	5.16	0.41	11.3

(A) Uniaxial and Biaxial Stretch Tests using Unit Element

Uniaxial and biaxial stretch tests were carried out in MSC Marc using single cube element with unit length (e.g. 1 meter) (Figure 3.19a). For uniaxial or biaxial stretch tests, required axial displacements were given by varying it linearly from 0 to 0.2 along with proper boundary conditions. FE produced results matched excellently with the analytical results as summarised in Figure 3.15.

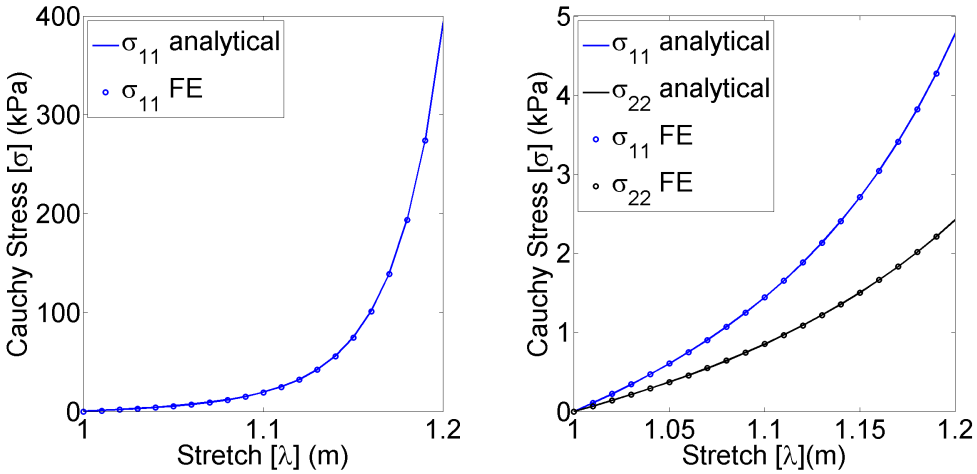

(a) Uniaxial stretch test

(b) Biaxial stretch test

Figure 3.15: Comparison between analytical and numerical (FE) results of the uniaxial and biaxial stretch tests

(B) Simple Shear Tests using Unit Element

Out of six shear modes, four modes ((fs), (fn), (sf) and (sn)) were selected for the validation procedure. The shear displacement was applied by varying it from 0 to 0.5 and the proper boundary conditions were applied for each shear mode. The corresponding Cauchy stress components for each of the tests were measured from MSC Marc and compared with the analytical results.The

FE test results, summarised in Figure 3.16, showed good agreement with the analytical solution.

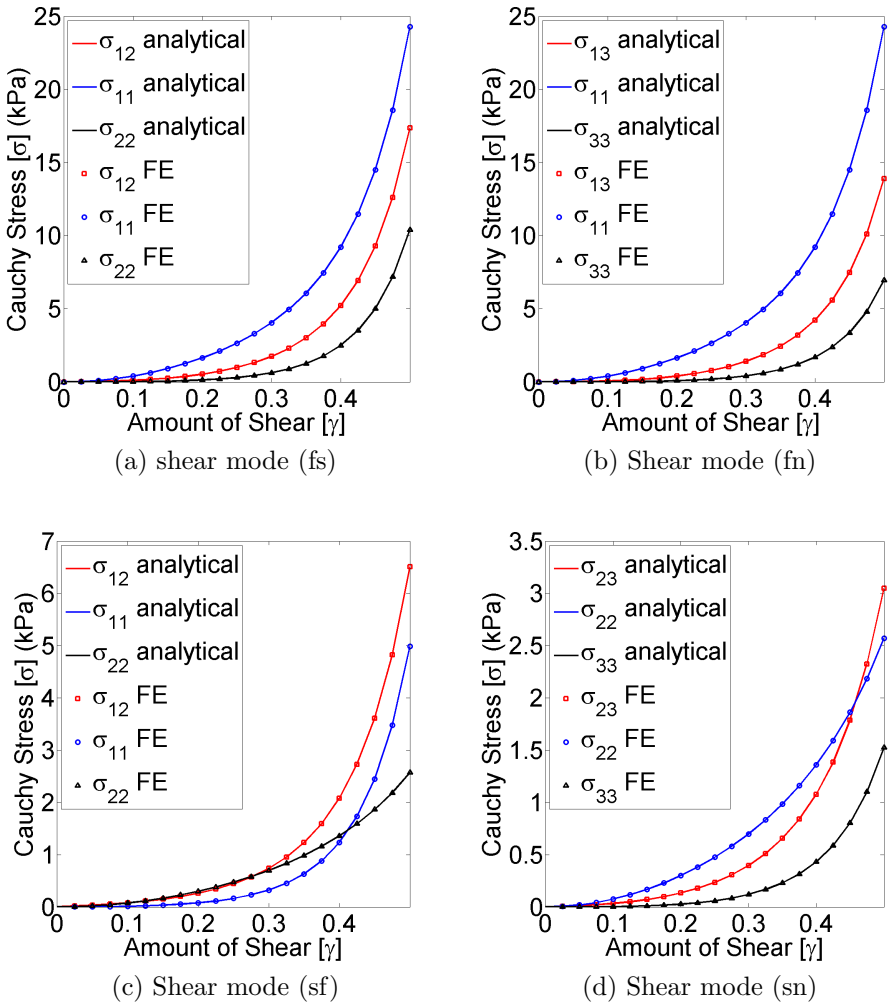

(a) shear mode (fs)

(b) Shear mode (fn)

(c) Shear mode (sf)

(d) Shear mode (sn)

Figure 3.16: Comparison between analytical and numerical (FE) results of the simple shear tests; shear modes (fs), (fn), (sf) and (sn) are shown here

(C) Compression Test using Unit Element

In order to carry out the compression test, active stress (S_a), varying linearly from 0 to 2 kPa, was applied in the fibre direction. After simulation, the displacements in fibre (λ_f), sheet (λ_s) and sheet-normal (λ_n) directions were

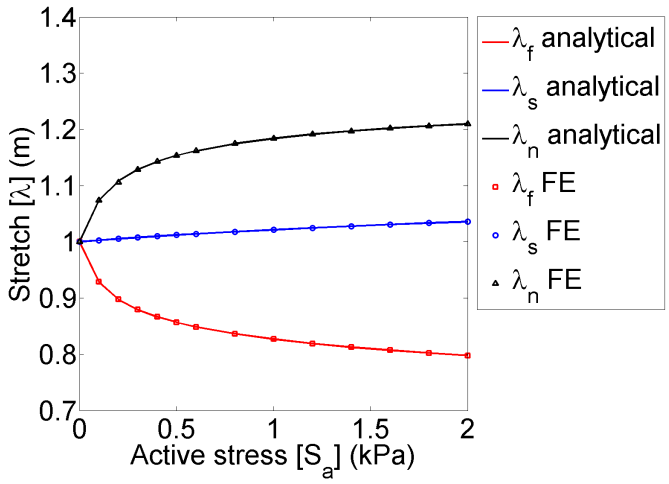

Figure 3.17: Comparison between analytical and numerical (FE) results of the compression test

measured from MSC Marc. The analytical displacements (λ_f, λ_s, λ_n) due to same active stress (S_a) were calculated by solving the set of non-linear Eq. (3.72) to (3.74) using Matlab function $fsolve()$ (Matlab, R2012b, The Mathworks, USA). The numerical results agreed excellently with the analytically calculated displacements (Figure 3.17).

(D) Shear Test using Unit Element when Material Directions are not aligned with Global Axes

In order to check the accurate implementation of material orthotropy in FE framework, (YX) shear mode was considered where the undeformed fibre ($\mathbf{f_0}$) and sheet ($\mathbf{s_0}$) directions were assumed to be aligned with an angle α with respect to the global X axis in global XY plane (Section 3.4.3 and Figure 3.14). Four (YX) shear tests were carried out in MSC Marc considering $\alpha =$ 60°, 30°, 45° and 0°. The analytical Cauchy stress components for each of the α value were calculated using Eq. (3.80) to (3.83). From Figure 3.18, it

is observed that the numerical results show good agreement with analytical solution for each α value. When $\alpha = 0°$ (i.e. when material directions aligned with global axes), it became the shear mode (sf). Therefore, Figure 3.18d and 3.16c are same.

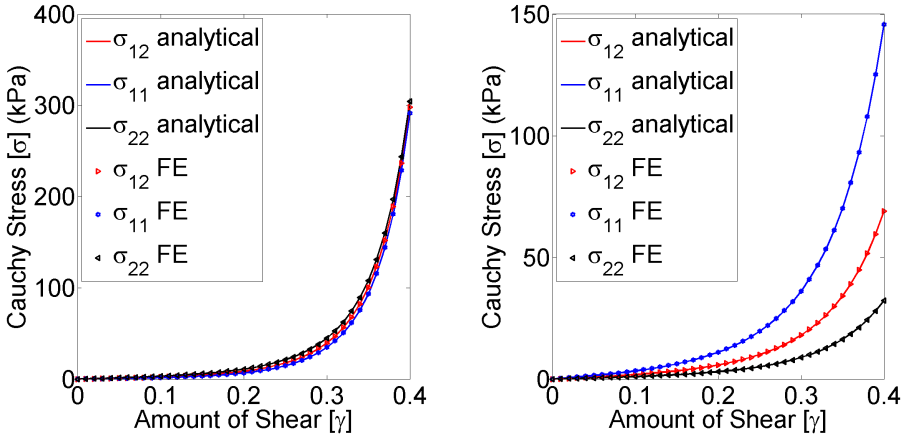

(a) shear mode (YX) when $\alpha = 60°$ (b) shear mode (YX) when $\alpha = 30°$

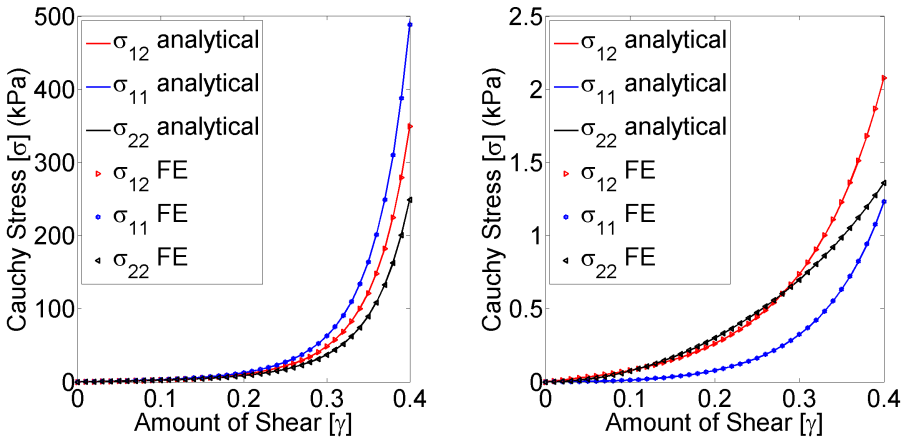

(c) shear mode (YX) when $\alpha = 45°$ (d) shear mode (YX) when $\alpha = 0°$

Figure 3.18: Comparison between analytical and numerical (FE) results of the simple shear mode (YX) when material directions are not aligned with global axes; $\mathbf{f_0}$ and $\mathbf{s_0}$ directions are assumed to be aligned with an angle α with respect to the global X axis in global XY plane

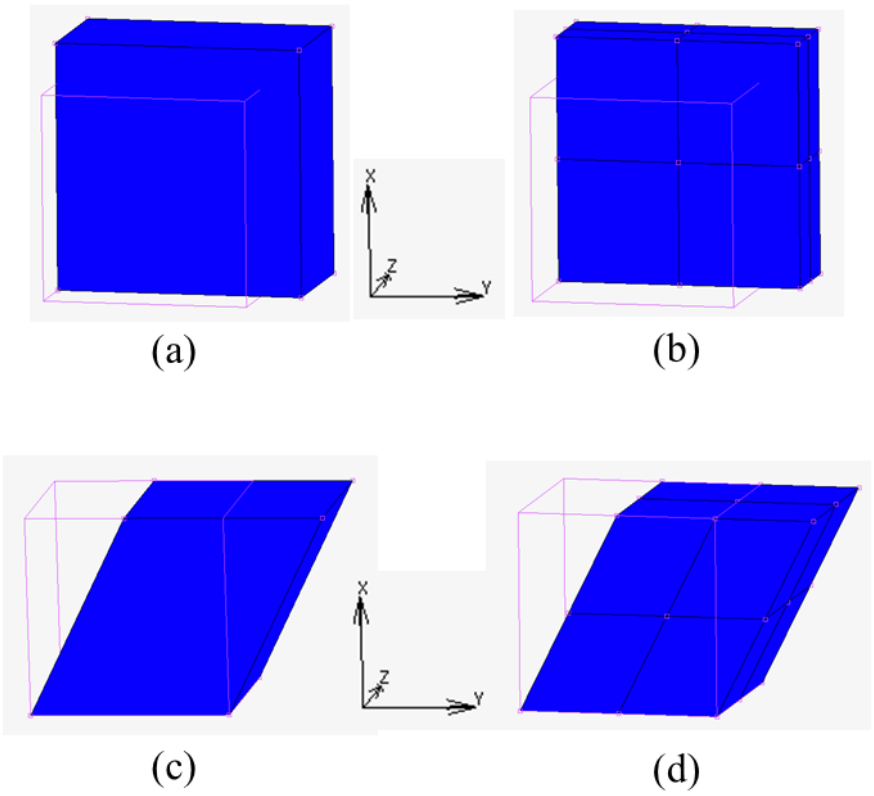

Figure 3.19: Schematic diagram of unit and multi-element biaxial and shear tests; (a) and (b) represent biaxial stretch test using unit and multi-element respectively; (c) and (d) represent simple shear test using unit and multi elements respectively

(E) Biaxial and Simple Shear Tests using Multi-element

Biaxial stretch and three simple shear (modes) tests were performed using multi-element to validate the general implementation of FE code. Eight small cube elements were combined properly using 'servo link' in MSC Marc so that they would behave as a single cube (Figure 3.19b). The material directions of all eight cubes were considered to be aligned with global cartesian coordinate. (fs), (fn) and (sn) shear modes were considered for the multi-element test. The multi-element FE results showed good agreement with the analytical solution (Figure 3.20).

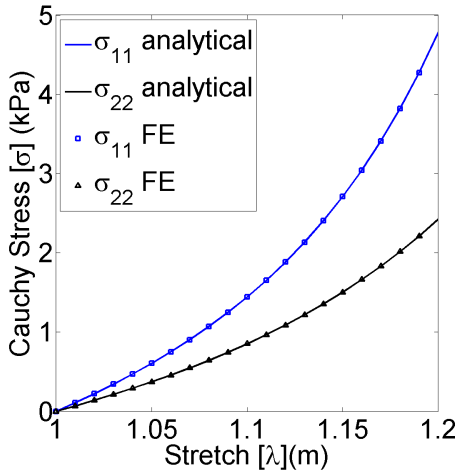

(a) Biaxial multi-elelement test

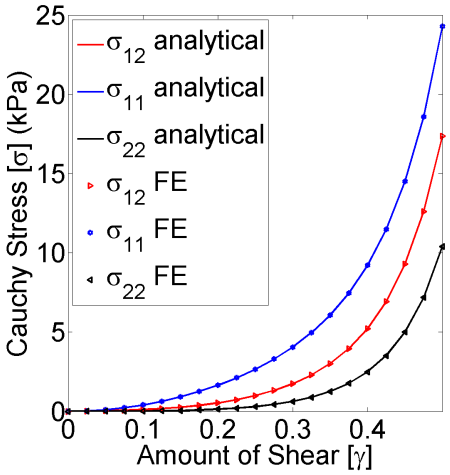

(b) shear mode (fs) multi-elelement test

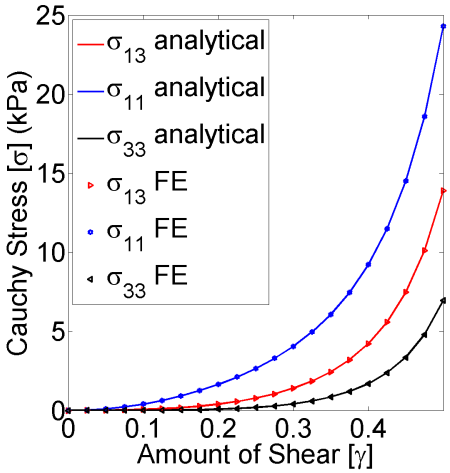

(c) shear mode (fn) multi-elelement test

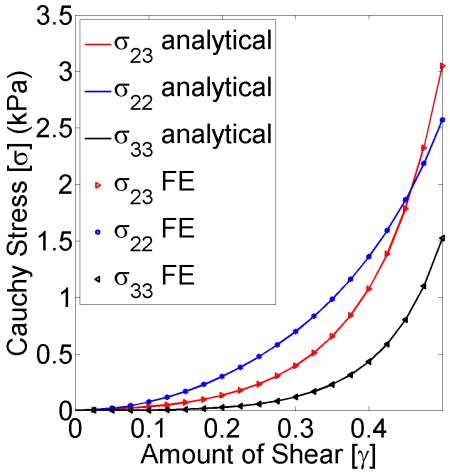

(d) shear mode (sn)multi-elelement test

Figure 3.20: Comparison between analytical and numerical (FE) results of the biaxial and three simple shear modes using multi-element FE model

The simulation results using single and multi-element models matched excellently with the analytical solutions. It was inferred that the orthotropic Holzapfel-Ogden constitutive law was accurately implemented in FE framework and could be used further to construct the ventricular model.

3.5 Research Contributions

The key research contributions from this chapter are summarised below.

- **Development of LDRF algorithm to automatically assign fibre map on ventricular mesh geometry:**

  A novel Laplace-Dirichlet-Region growing-FEM (LDRF) based algorithm was proposed to define fibre map on computational ventricular mesh geometry. The algorithm was developed based on the method suggested by Wong and Kuhl (2014) with a major amendment in identifying the surface domains automatically to define the Dirichlet boundary conditions. The identification of different surface domains, required to assign boundary values, was carried out using the region growing algorithm (Franciosa and Gerbino, 2008) and distance based approach. With three inputs and three functions, the algorithm can generate fibre and sheet orientations on either LV or BV mesh geometries automatically which can be used in future FE modelling.

- **Summarised all the analytical expression for FE implementation of Holzapfel-Ogden law:**

  The complete expressions of the stress tensor and related mathematical descriptions of Holzapfel-Ogden constitutive law for the passive myocardium under various test cases were elaborately summarised in Chapter 3. Such analytic expressions are very useful to validate the FE implementation of Holzapfel-Ogden material model, and therefore, could be useful in future computation study.

3.6 Summary

This chapter included the implementation of three aspects, required for FE modelling of human ventricles, as follows : (1) construction of ventricular mesh geometry from CMRI (Section 3.2), (2) assignment of fibre orientation on ventricular mesh geometry (Section 3.3), and (3) implementation of Holzapfel-Ogden material law in FE framework (Section 3.4). The construction of ventricular geometry used short and long-axis images in order to reduce the partial volume error, which was incorporated in LV geometry when constructing it from the stack of short axis images only. The LDRF algorithm to assign fibre orientation on ventricular mesh geometry modified the method of Wong and Kuhl (2014) by automatically identifying the different surface domains using the region growing and distance based approach. The chapter also included the implementation of the Holzapfel-Ogden constitutive law in FE framework which was utilised to define the myocardial material characteristics. Proper validations were carried out for each of the implemented prerequisites by comparing it with literature, analytical results or thorough inspection by experienced radiologists. An integration of all three aspects together with proper boundary conditions would lead to the FE modelling of ventricular mechanics as discussed in the subsequent chapters.

Chapter 4

Effect of Fibre Orientation and RV Topology on LV Passive Inflation

4.1 Introduction

In Chapter 1, it was mentioned that FE modelling, in combination with new cardiac imaging modalities and advanced simulation tools, could be used for improved understanding of the diastolic mechanics of the left ventricle (LV) under normal and pathological conditions. In order to develop the FE modelling of ventricle, the ventricular geometry, fibre-orientation and myocardial material properties are the necessary prerequisites as mentioned in the Chapter 3. Existing LV diastolic models considered only single LV geometry and ignored the effects of right ventricle (RV) topology (Section 2.4 of Chapter 2). On the other hand, measuring subject-specific in-vivo myocardial fibre orientation is still an open question, and therefore, sensitivity of LV diastolic mechanics to

the details of fibre structure is an important issue and has not been carried out for bi-ventricular (BV) model (Section 2.5 of Chapter 2). Therefore, this chapter aims to answer the following research objectives, raised in Sections 2.4 and 2.5 of Chapter 2

Objective 1: To examine the effect of RV topology on (a) stress-strain distribution of LV wall during diastole, and (b) end diastolic pressure volume relation (EDPVR) of LV.

Objective 2: To investigate the effect of fibre orientation on (a) fibre stress-strain distribution of LV wall during diastole, and (b) end diastolic pressure volume relation (EDPVR) of LV.

The limitation in the literature, and subsequently, identification of the above research objectives are briefly encapsulated in Section 4.2. Details of the modelling approach (i.e. integration of three prerequisites and boundary conditions) and investigation strategies to perform the research objectives are outlined in Section 4.3 followed by the validation approaches. Mesh convergence study was performed in order to identify the minimum number of FE elements required to achieve reliable simulation results before final study (Section 4.3.6). Results and discussion of the two research objectives are described in Section 4.4 and 4.5 respectively. The research contributions from the study are abridged in Section 4.6.

4.2 Brief Literature Review

As shown in Table 4.1, the majority of passive simulations, carried out in earlier studies, were based on either animal heart or idealised geometry (Guccione

et al., 1995; Costa et al., 1996; Usyk et al., 2000; Guccione et al., 2001a; Dorri, 2004; Goktepe et al., 2011; Eriksson et al., 2013). With the advancement in imaging modalities over the years, subject-specific human heart geometry, created from MRI images, was used for the FE modelling (Wang et al., 2013a; Genet et al., 2014). However, using bi-ventricular geometry of human heart for FE modelling of diastole is very limited due to the complex structure of RV (Table 4.1). In addition, RV deformation seems to have a significant effect on EDPVR of LV and fibre stress-strain distribution of LV wall (Sun et al., 2009; Wang et al., 2013a; Mojsejenko et al., 2015; Nikou et al., 2015). Therefore, objective 1 was carried out to identify the effect of RV on LV passive inflation. The study would provide the validity of the assumption often made during ventricular modelling by considering only LV geometry without including the effect of RV.

The myocardium is the functional tissue of the ventricle. Recent studies with a higher level of magnification introduced the concept of fibre-sheet (laminar) architecture of the myocardial wall (LeGrice et al., 1995b; Hunter et al., 1998) (Section 2.3 of Chapter 2). Histological studies confirmed that the myocardial fibre angle varied from -50° to -70° in the sub-epicardial to almost 0° in the mid-wall, to $+50^{\circ}$ to $+70^{\circ}$ at sub-endocardial with respect to the local circumferential direction of the LV (Holzapfel and Ogden, 2009). The widely used image based approach to determine fibre-sheet orientation utilised Diffusion Tensor Magnetic Resonance Imaging (DTMRI) in ex-vivo heart (Bayer et al., 2012; Rohmer et al., 2007; Dorri, 2004; Geerts et al., 2002). However, obtaining such data in-vivo still remains an open question (Bayer et al., 2012; Genet et al., 2014). Alternative approach used rule-based

algorithm, which can yield fibre-sheet architecture that are reasonably close to those derived from DTMRI, yet discrepancies exist between them (Bishop et al., 2009). Even though the fibre-sheet orientation is histologically similar for human hearts, differences exist in fibre angle between individual subjects (Buckberg et al., 2008). In addition, the fibre-sheet architecture may also alter in diseased hearts, such as in myocardial infarction due to tissue remodelling (Buckberg et al., 2008). Therefore, sensitivity of LV diastolic mechanics to the details of fibre structure is an important issue (Objective 2) and has not been carried out for BV model (Table 4.1).

As summarised in Table 4.1, majority of the researchers used Fung-type transversely isotropic constitutive law (Costa et al., 1996; Guccione et al., 1995; Vetter and McCulloch, 2000). In contrast, simple shear test of pig's myocardium (Dokos et al., 2002) clearly exhibited its orthotropic nature. Diastolic modelling were carried out using modified Fung-type law (Usyk et al., 2000) and pole-zero law (Stevens et al., 2003) to incorporate material orthotropy. The material parameters in these orthotropic models are merely used as weighting factors, rather than any physical significance (Goktepe et al., 2011), and some of these parameters are highly correlated (Wang et al., 2013a). Recently, Holzapfel and Ogden (2009) developed a constitutive law that considered the locally orthotropic tissue architecture and the parameters of this model were closely related to the characteristic micro-structure of myocardium. As summarised in Table 4.1, Holzapfel-Ogden orthotropic law and bi-ventricular geometry were used to carry out the research objectives.

Table 4.1: A brief overview of the literature to identify the research gap and scope of the study

<table>
<tr><th colspan="2" rowspan="2"></th><th rowspan="2">Single LV</th><th rowspan="2">Bi-ventricle</th><th colspan="2">Effect of RV deformation on</th></tr>
<tr><th>Stress-strain</th><th>EDPVR</th></tr>
<tr><td colspan="2">Animal ventricle/Idealised geometry</td><td>Horowitz et al. (1986)
Humphrey and Yin (1989)
Guccione et al. (1995)
Costa et al. (1996)
Vetter and McCulloch (2000)
Usyk et al. (2000)
Wang et al. (2009)</td><td>Stevens et al. (2003)</td><td></td><td></td></tr>
<tr><td colspan="2">Transversely isotropic</td><td>Horowitz et al. (1986)
Humphrey and Yin (1989)
Guccione et al. (1995)
Costa et al. (1996)
Vetter and McCulloch (2000)
Wang et al. (2009)</td><td></td><td></td><td></td></tr>
<tr><td colspan="2">Orthotropic</td><td>Wang et al. (2013a)
Usyk et al. (2000)</td><td>Stevens et al. (2003)</td><td colspan="2" rowspan="4">Research Gap</td></tr>
<tr><td colspan="2">Human heart</td><td>Wang et al. (2013a)
Genet et al. (2014)</td><td></td></tr>
<tr><td rowspan="2">Effect of fibre-sheet orientation on</td><td>Stress-strain</td><td>Wang et al. (2013a)</td><td></td></tr>
<tr><td>EDPVR</td><td></td><td></td></tr>
</table>

4.3 Materials and Methods

4.3.1 Construction of Ventricular Mesh Geometry

In the present study, ECG gated, breathe hold, steady state free precession (SSFP) cine cardiac magnetic resonance imaging (CMRI) was used to capture the images of a normal human heart in a dedicated MRI suite in University Hospitals Coventry and Warwickshire Trust (UHCW), Coventry, UK. BSREC ethics approval (REGO-2012-032) (Appendix A) was obtained to carry out the research on anonymised human data. The $12th$ frame of the CMRI data was considered early diastole (ErD) phase whereas the $30th$ frame corresponded to the end diastole (ED) phase. Mimics and 3-matic (Materialise, Belgium) were used to construct the ventricular mesh geometry at ErD with linear tetrahedral elements as detailed in Section 3.2. Figure 4.1 shows the BV and LV mesh geometries constructed from same early diastolic CMRI image stack .

4.3.2 Construction of Rule-based Fibre Orientation

Laplace-Dirichlet-Region growing-FEM (LDRF) based algorithm, detailed in Section 3.3 of Chapter 3, was used to assign myocardial fibre sheet architecture on ventricular mesh geometry. The algorithm was developed based on the method proposed by Wong and Kuhl (2014), with the amendment in identifying the different surface domains automatically. It was assumed that fibres on epicardium ($\partial\Omega_{epi}$) and RV septal endocardium ($\partial\Omega_{rvsep}$) were inclined with $-\alpha_1$ and fibres on LV endocardium ($\partial\Omega_{lvendo}$) and RV free wall endocardium ($\partial\Omega_{rvfree}$) were inclined with $+\alpha_2$ with respect to local circumferential direction of LV. The values of α_1 and α_2 would be defined from histological data.

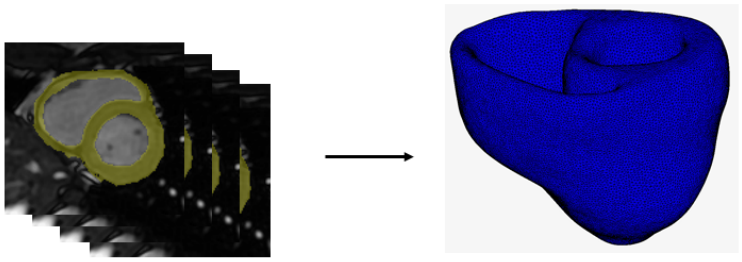

(a) Short-axis CMRI stack at ErD (b) BV mesh geometry at ErD

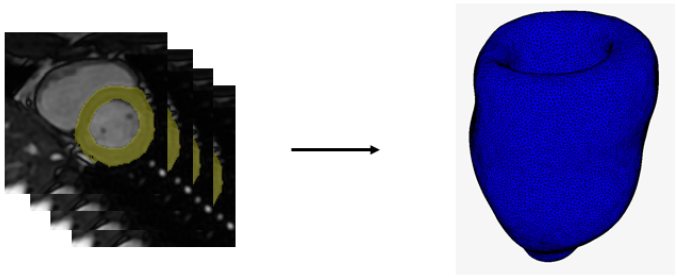

(c) Short-axis CMRI stack at ErD (b) LV mesh geometry at ErD

Figure 4.1: Graphical representation of two mesh geometries constructed from same CMRI at ErD; (a) Segmentation of both LV and RV, (b) BV mesh geometry, (c) Segmentation of only LV, and (d) LV mesh geometry

Figure 4.2 shows the same fibre orientation on BV and single LV model when α_1 and α_2 both are 60°.

4.3.3 FE Model of LV Passive Inflation

The early-diastolic (ErD) mesh geometry, composed of four node tetrahedral elements, was created from the early diastolic (ErD) CMRI of human heart. Early-diastole was considered as initial stress free configuration since the ventricular pressure was lowest at this point and therefore stress was minimum (Usyk et al., 2000; Sun et al., 2009; Wenk et al., 2011a; Genet et al., 2014). The longitudinal movement of the base nodes and the circumferential displacement of the epicardial wall at the base were suppressed in order to avoid undesirable

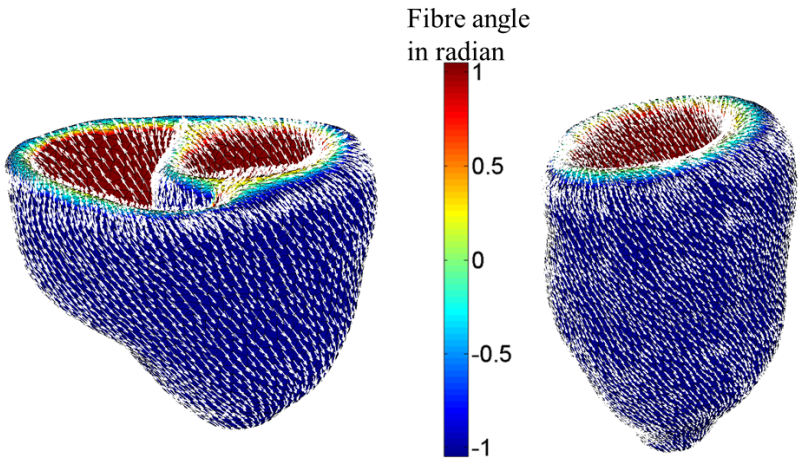

Figure 4.2: Pictorial representation of same fibre orientation on (a) BV and (b) single LV mesh geometries using LDRF algorithm. α_1 and α_2 both are considered 60° and the contour plot shows the fibre angle in radian

rigid body displacement (Eriksson et al., 2013; Wenk et al., 2012; Sun et al., 2009; Genet et al., 2014). The rest of the ventricular wall including apex was left free. The physiological LV end diastolic pressure (EDP) was considered as 10 mmHg due to the unavailability of subject-specific EDP which requires invasive measurements (Wang et al., 2013a; Lee et al., 2013a; Genet et al., 2014). Therefore, LV filling pressure, linearly varying from 0 to 10 mmHg, was applied on the endocardial surface of LV. For a simplified model, RV pressure was assumed to be one third of LV pressure so that it could produce physiologically observed RV filling pressure. A sensitivity study showed that the change in RV pressure within normal range did not modify the conclusion of the study.

$$\begin{aligned}\Psi = K\left(\frac{J^2-1}{2} - \ln J\right) + \frac{a}{2b}\exp[b(\overline{I}_1 - 3)] \\ + \sum_{i=f,s}\frac{a_i}{2b_i}\left\{\exp[b_i(\overline{I}_{4i} - 1)^2] - 1\right\} + \frac{a_{fs}}{2b_{fs}}[\exp(b_{fs}\overline{I}_{8fs}^2) - 1]\end{aligned} \tag{4.1}$$

Ventricular myocardium was characterised by Holzaphel-Ogden constitutive law (Eq. (4.1)), which was implemented using a user-defined subroutine 'Hypela2' in MSC-Marc (MSC Software Corporation, California, US) utilising Total Lagrange framework. Details of the constitutive law, its FE implementation and validation procedures were discussed in Section 3.4 of Chapter 3.

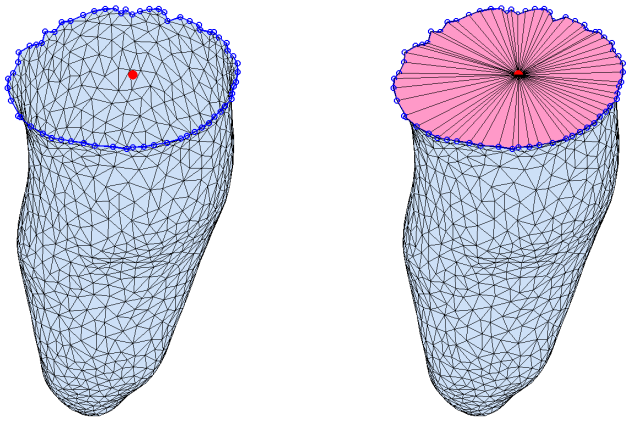

(a) LV open cavity (b) LV closed cavity

Figure 4.3: Construction of LV closed cavity from LV open cavity using Matlab and Python scripting in MSC Marc. The blue nodes represent the nodes on circumferential boundary of LV endocardial surface. The red node (CN) is constructed by calculating the mean positions of all the blue nodes. The triangular faces are created by joining the red node with the two blue nodes which are immediate neighbour to each other.

To measure LV cavity volume during simulation, 3D closed LV cavity was constructed in MSC Marc. From LDRF algorithm, the LV endocardial faces were identified (Figure 4.3a). The LV endocardial surface had an open and approximately circular boundary towards LV base. The nodes on the circumferential boundary were located along with their relative positions with each other, using user defined Matlab functions (Figure 4.3a). A new node (CN) was defined by calculating the mean of the coordinates of all the circum-

ferential boundary nodes. Therefore, the new node (CN) was approximately situated at the centre of the circular boundary (Figure 4.3a). A customised 'Python' script was then used in MSC Marc to construct a set of triangular faces that joined the newly constructed centre node (CN) with two nodes, which were immediate neighbour to each other and located on the circumferential boundary of LV cavity (Figure 4.3b). As a result, the LV open cavity was covered by the newly constructed triangular faces and was transformed into a closed cavity (Figure 4.3). All the triangular faces (endocardial faces as well as LV cavity cover faces) were then converted into 'cavity surface element' (element id 173) in MSC Marc using in-built toolbox. The LV cavity volume was measured throughout the simulation using 'Ucav' subroutine in MSC Marc.

4.3.4 Investigation Strategies

The value of K (Eq. (4.1)) was chosen as 200kPa (Vetter and McCulloch, 2000). The values of eight material parameters (a, b, a_i, b_i in Eq. (4.1) where $i = f$, s, fs) used in this study were taken from Wang et al. (2013a). All the values of material parameters are summarised in Table 4.2.

Table 4.2: Values of Holzapfel-Ogden passive material parameters used in this study (Wang et al., 2013a; Vetter and McCulloch, 2000)

a (kPa)	b	a_f (kPa)	b_f	a_s (kPa)	b_s	a_{fs} (kPa)	b_{fs}	K (kPa)
0.236	10.81	20.037	14.154	3.724	5.164	0.411	11.3	200

In order to study the stress strain distribution of the LV wall during passive inflation, three short-axis slices were considered as follows: (a) basal

slice positioned 5 mm below the base, (b) equatorial slice located 20 mm below the basal slice and (c) apical slice positioned 20 mm above the apex. In addition, two long axis slices were defined for the study. The *s-l* slice, passing through the septum and lateral wall, divided the both RV and LV geometry in the middle. The *a-p* slice, passing through anterior and posterior wall, divided the LV cavity in the middle. Figure 4.4 shows the locations of the slices. A brief overview of the investigation strategies to carry out the two research objectives are discussed in the following sections.

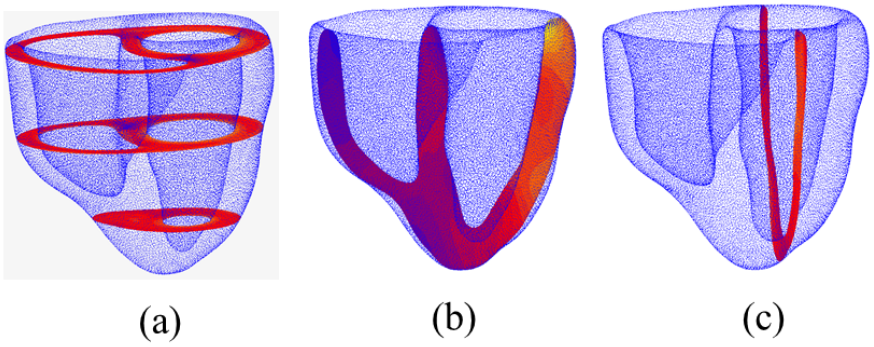

Figure 4.4: Position of different slices used in the study to analyse the stress strain distribution of the LV wall during passive inflation; (a) basal, equatorial and apical short-axis slices from top to bottom; (b) *s-l* long axis slice; (c) *a-p* long axis slice

(A) **Effect of Fibre-Orientation**

Six different fibre-structures were considered in the study as follows: fibre $[\alpha]$ represents a linear variation of helix angle from $-\alpha^{\circ}$ at epicardium ($\partial\Omega_{epi}$) and RV septal endocardium ($\partial\Omega_{rvsep}$) to $+\alpha^{\circ}$ at LV endocardium ($\partial\Omega_{lvendo}$) and RV free wall endocardium ($\partial\Omega_{rvfree}$), where, $\alpha = 30$, 40, 50, 60, 70 and 80. Explicit definitions of each fibre set are defined in Table 4.3. The sheet angle was assumed to be 0° i.e. the sheet directions were aligned with lo-

cal radial directions (see Section 3.3.1) in all the cases as it had very little effect on passive stress-strain distribution of LV wall (Wang et al., 2013a). Simulation of passive inflation of LV was carried out for each set of fibre-orientation (Figure 4.5) while keeping the mesh geometry, boundary and loading conditions same for all sets. The end diastolic pressure volume relation (EDPVR), fibre stress (Cauchy) and fibre strain (logarithmic) were measured for each simulation to identify the variation amongst them due to the change in fibre orientation.

Table 4.3: Different types of fibre orientation considered in the study

Fibre set	$\partial\Omega_{epi}$ and $\partial\Omega_{rvsep}$	$\partial\Omega_{lvendo}$ and $\partial\Omega_{rvfree}$
fibre 30	-30°	$+30^{\circ}$
fibre 40	-40°	$+40^{\circ}$
fibre 50	-50°	$+50^{\circ}$
fibre 60	-60°	$+60^{\circ}$
fibre 70	-70°	$+70^{\circ}$
fibre 80	-80°	$+80^{\circ}$

(B) **Effect of RV**

Two mesh geometries were considered - (a) single LV geometry and (b) BV geometry (Figure 4.1). Both the geometries were construed from same CMRI data using the procedure detailed in Section 3.2.2 of Chapter 3. In order to check the similarities between the LV part of BV geometry and the single LV geometry, two comparisons were carried out. Firstly, the LV cavity volumes, extracted from both geometries as detailed in Section 3.2.2, were compared . Secondly, the part comparison analysis was performed in 3-matic using the LV cavity geometries, extracted from LV and BV geometries. The geometries were ready to use only when the differences between the LV cavity

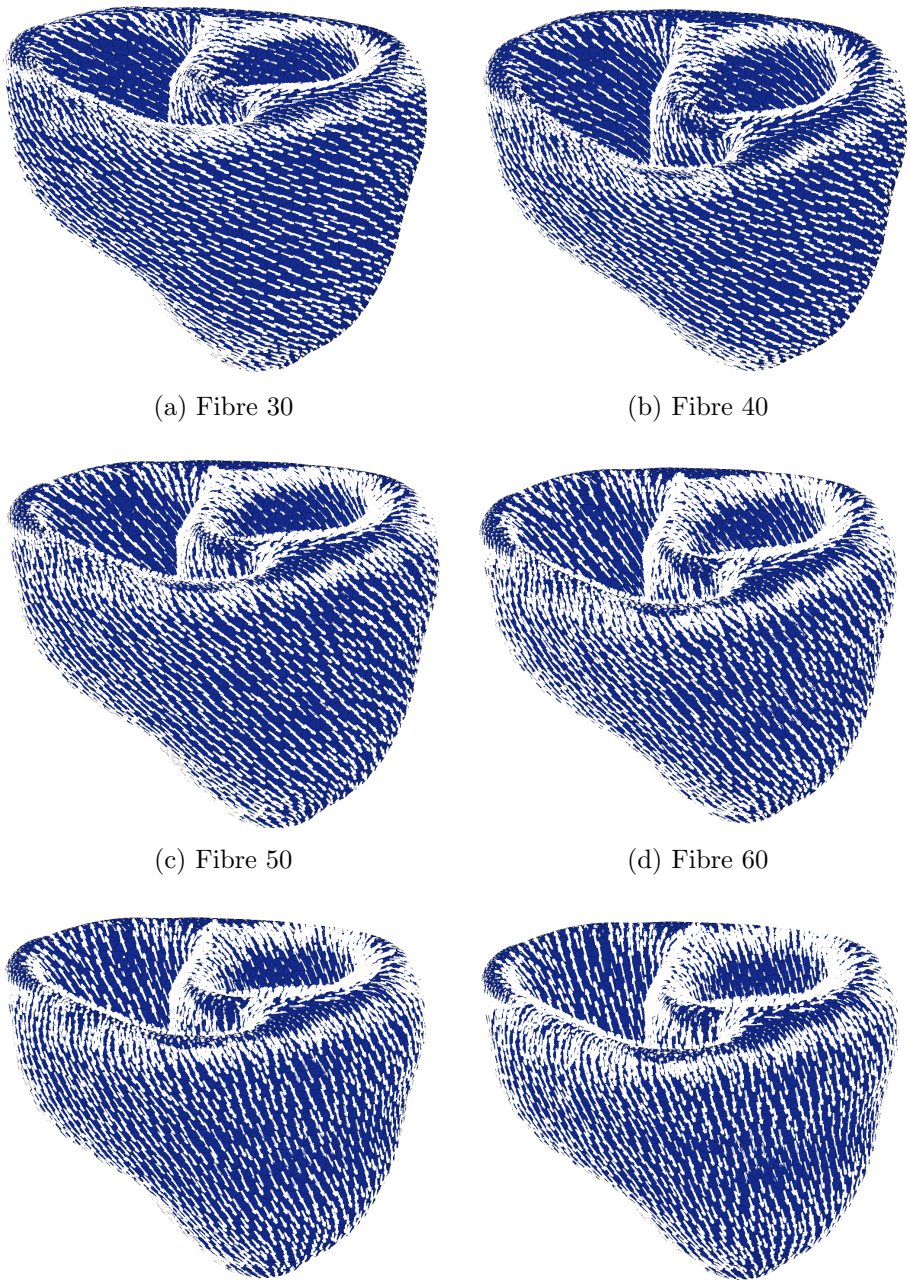

(a) Fibre 30 (b) Fibre 40

(c) Fibre 50 (d) Fibre 60

(e) Fibre 70 (f) Fibre 80

Figure 4.5: Graphical representation of six different fibre sets used in this study

volume and geometrical shape were less than 1% and 1% respectively. For each mesh geometry, six simulations were carried out using six different fibre

sets. The EDPVR, fibre and sheet stresses (Cauchy), and strains (logarithmic) were measured for each simulation to identify the effect of RV on passive LV inflation for a particular fibre orientation.

4.3.5 Validation Strategies

The validations of the three prerequisites i.e. construction of ventricular mesh geometry, fibre orientation and FE implementation of Holzapfel-Ogden material model were described in Chapter 3. The validation of the passive diastolic inflation of BV and single LV model was carried out by comparing the pressure-normalise volume (PV_n) relation calculated by our model to the experimental measurement of ex-vivo human heart by Klotz et al. (2006). The validation method was adapted from Wang et al. (2013a). The normalised volume (EDV_n) was calculated as

$$EDV_n = \frac{EDV - V_0}{V_{30} - V_0} \tag{4.2}$$

in which, V_0 and V_{30} are the volume of LV cavity at pressure 0 mmHg and 30 mmHg. EDV is the volume of LV for a particular LV diastolic pressure. The simulation was carried out for each fibre orientation up to 40 mmHg and EDV_n was calculated according to Eq. (4.2). The simulation predicted pressure-normalise volume (PV_n) was then compared with the the experimental measurement of Klotz et al. (2006). Although the simulation was continued up to 40 mmHg, the EDP of the LV was still assumed 10 mmHg as stated in Section 4.3.3. Also, the effect of different fibre orientations on fibre stress distribution of LV wall during passive inflation was identified using single LV model. The results were then qualitatively compared with the effect of fibre orienta-

tion reported by Wang et al. (2013a). Such qualitative validation was used to check the proper implementation of fibre orientation and FE modelling of ventricular diastole. Thus, different validation approaches were implemented for each step of the study in order to produce reliable results.

4.3.6 Mesh Convergence Study

Mesh convergence study was performed in order to identify the minimum number of elements and nodes required in a mesh geometry to achieve reliable simulation results. The BV geometry (Figure 4.1b) was considered for the study. In 3-matic, the number of linear tetrahedral elements (tet4) in a mesh geometry can be controlled by changing the maximum edge length of the elements. Reducing the maximum edge length for a particular aspect ratio would increase the number of tet4 elements in mesh geometry. Six cases were considered by varying the tet4 elements number in BV mesh geometry as shown in Table 4.4. For each case, passive inflation of LV was simulated using the boundary conditions mentioned in Section 4.3.3. The maximum displacement, maximum and minimum Cauchy stress and logarithmic strain in fibre direction, predicted from each case, were compared to identify the optimal element number to be used in the final study.

Table 4.4: Element and node number used for mesh convergence study

	Element Number	Node Number
Case 1	∼400,000	∼75,000
Case 2	∼500,000	∼85,000
Case 3	∼600,000	∼98,000
Case 4	∼700,000	∼110,000
Case 5	∼800,000	∼120,000
Case 6	∼900,000	∼140,000

4.4 Results

4.4.1 Mesh Convergence Study

Figure 4.6 shows the relative differences in predicted results from the mesh convergence study. The percentage change for each parameter (i.e. max displacement, max and min fibre stress and strain) was calculated with the corresponding results from the finest mesh (i.e. case 6). It was observed that the relative difference between the predicted parameter values became less than 3% and 2% when the element number was more than 700,000 (case 4) and 800,000 (case 5) respectively (figure 4.6). Therefore, in all the subsequent study in the thesis, the minimum element number in a BV mesh geometry was considered to be ∼750,000. As RV was not present in the single LV geometry, the minimum element number was assumed ∼450,000for single LV geometry.

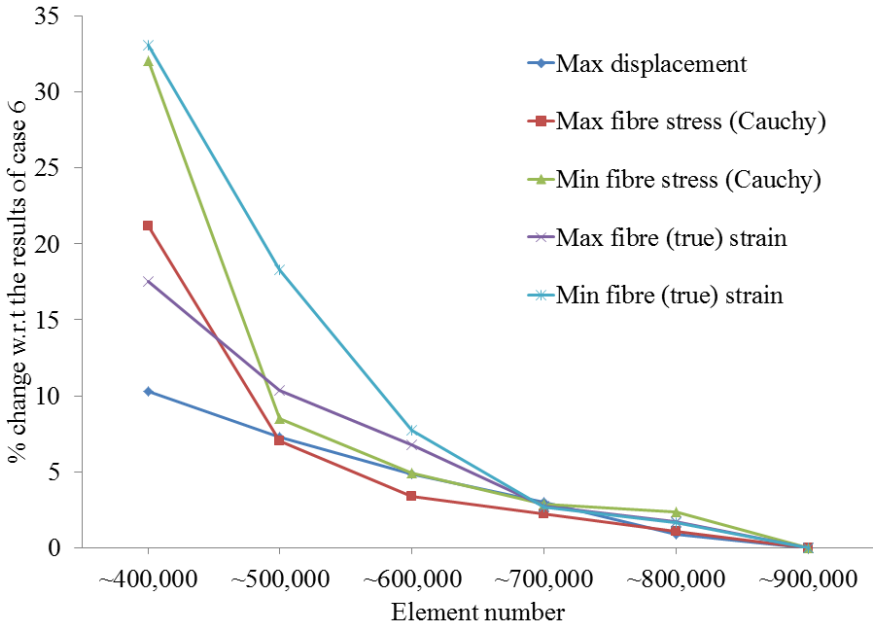

Figure 4.6: Results from the mesh convergence study. The percentage change for each of the predicted parameter values is calculated with respect to the values obtained from case 6

4.4.2 Validation of the Model

As explained in Section 4.3.5, validation of the passive diastolic inflation of BV and single LV model was carried out by comparing the pressure-normalise volume (PV_n) predicted from the model to the experimental measurement of ex-vivo human heart by Klotz et al. (2006). The PV_n was calculated by using Eq.(4.2) for both BV and LV models. Figure 4.7 and 4.8 show the pressure-normalised volume (PV_n) relationship predicted from BV and LV model respectively with different fibre orientations. Both the model predictions showed good agreement with the human experimental data (Klotz et al., 2006). However, when fibre angle was 30°, 70° and 80°, the closeness of the predicted PV_n with the experimental data was more. In addition, the pressure-normalised volume relation for different fibre orientations followed the hypothesis that the volume-normalised EDPVRs have a common shape, irrespective of different species and diseased ventricles (Klotz et al., 2006) (Figure 4.7 and 4.8).

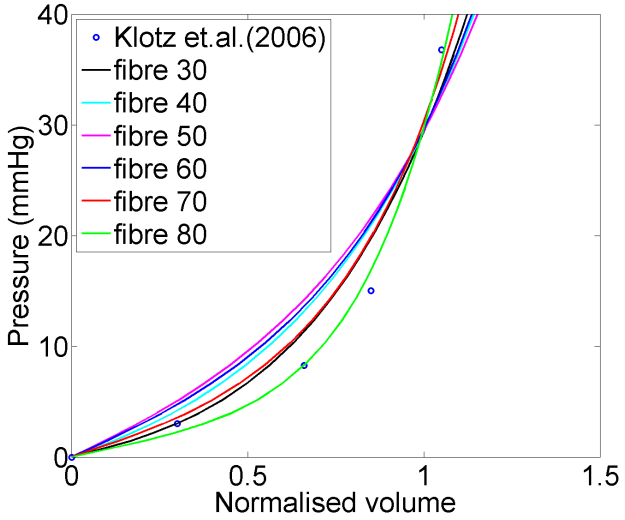

Figure 4.7: Comparison of pressure-normalised volume (PV_n) relationship calculated from the BV model with different fibre orientations and experimental measurement from ex-vivo human heart by Klotz et al. (2006)

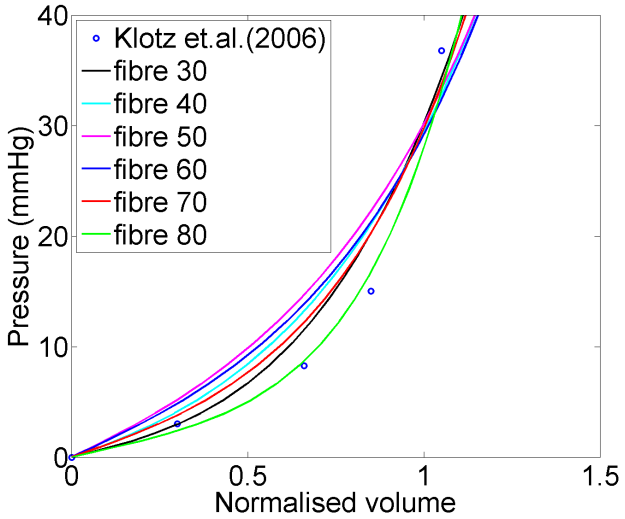

Figure 4.8: Comparison of pressure-normalised volume (PV_n) relationship calculated from the single LV model with different fibre orientations and experimental measurement from ex-vivo human heart by Klotz et al. (2006)

Figure 4.9 shows the effect of fibre orientation on fibre stress distribution of LV wall at 10 mmHg LV pressure, predicted from single LV model at three different locations. The results were only used to validate our model with the literature. For fibre angle 80° and 70°, the inner (endocardium) and the outer (epicardium) wall experienced less fibre stress than the mid-wall. On the other hand, the endocardium and the epicardium experienced higher fibre stress compared to the mid-wall for fibre angle less than 60°. The same observation was reported by 'path 1' and 'path 4' plots of Figure 10, reported in Wang et al. (2013a). The basal and equatorial locations, used in this study, were equivalent to 'path 1' and 'path 4' respectively. Such qualitative agreement indicated the correct implementation of the ventricular FE modelling and fibre orientation in this study. Detailed quantitative comparison of the simulation results with the literature did not seem to be merited due to the different factors such as differences in geometry, and constitutive parameters (Section

4.5.1). Moreover, the exact location of the 'path', shown in Figure 10 of Wang et al. (2013a), was not explicitly mentioned, and therefore, comparing the stress values in such 'path' was not possible.

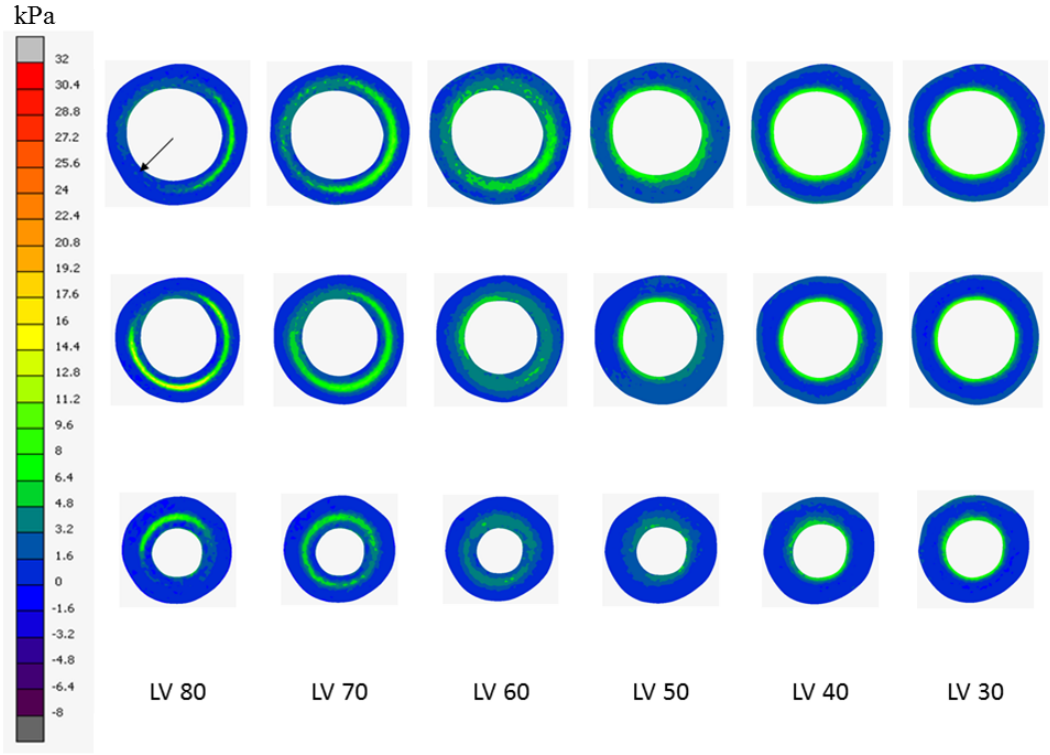

Figure 4.9: Effect of different fibre orientations on the fibre stress (Cauchy) distribution during passive inflation of LV at 10 mmHg LV cavity pressure; first, second and third row in each column represent basal, equatorial and apical slices respectively; The arrow depicts the location of septum

4.4.3 Effect of Fibre Orientations on EDPVRs of LV

Figure 4.10 and 4.11 represent the effect of fibre orientation on EDPVRs of LV, predicted from BV and single LV model respectively. With the increase in fibre angle from 50°, the volume change was more with respect to same LV cavity pressure. The EDPVRs for 30° and 40° were quite different from the EDPVRs of the rest of the fibre structure for both BV and single LV models.

The change in volume increased with the increment in fibre angle from 50° towards 80° and from 3% to 11.5% respectively at 10 mmHg LV pressure for BV model. The minimum LV EDV was achieved for fibre angle 50° for both models. However, it was observed that the relative differences in EDPVRs for different fibre directions generated from BV model was somewhat different from the results of single LV model. The differences were more notable when fibre angle was in between 30° and 60° and LV pressure was less than 10 mmHg. These observations are discussed in detail in Section 4.4.5.

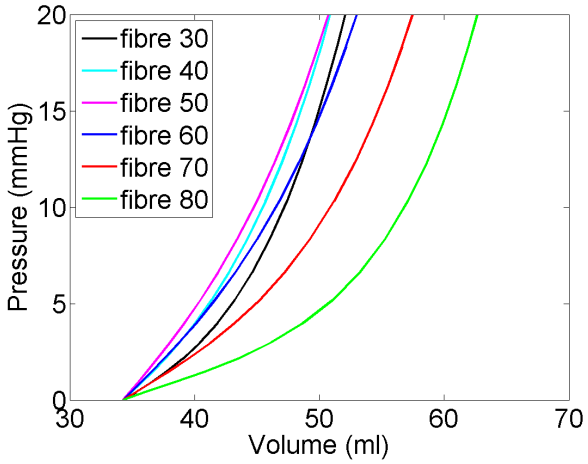

Figure 4.10: Effect of fibre orientation on the EDPVRs of LV, generated from BV model

4.4.4 Effect of Fibre Orientation on Stress Strain Distribution of LV Wall

Figure 4.12 and 4.13 compare the Cauchy stress and true strain distribution in fibre direction respectively at a LV pressure of 10 mmHg for three short axis positions (i.e. base, equatorial and apex). From Figure 4.12, it is observed that the variation in fibre stress distribution from the base to the apex is notable

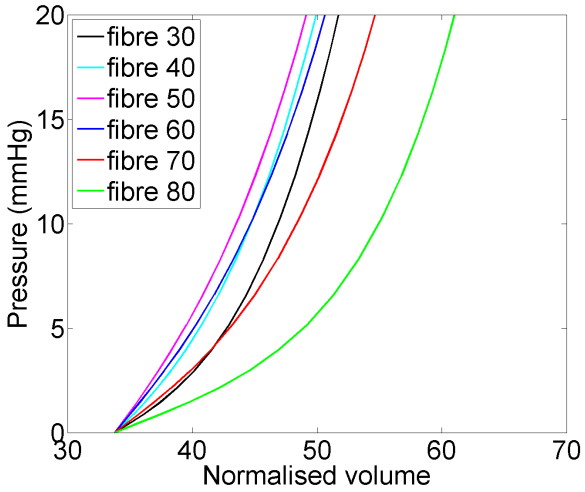

Figure 4.11: Effect of fibre orientation on the EDPVRs of LV, generated from single LV model

for fibre orientation 80°-60°. However, these changes were very little for small fibre angle (i.e. for 30° to 40°). The fibre stress in the epicardium and the endocardium was less compared to stress occurred in the middle of the wall, especially in the lateral and the posterior regions for fibre orientation 60°-80°. In contrast, the fibre stress for fibre orientation 30°-50° was decreasing from the endocardium, reaching minimum in the mid-wall and then gradually increasing again towards the epicardium. In addition, the variation in fibre stress distribution for fibre-angle 30°-50° was not significant.

Figure 4.13 shows that the mid-wall of the LV experiences maximum fibre strain whereas the fibre strain in the endocardium and the epicardium are comparatively less for fibre angle 70°-80°. In contrast, the endocardium received the greated fibre strain compared to the mid-wall for fibre distribution 30°-40°. Tensile fibre-strain was experienced mostly in the basal and the equatorial locations except for fibre angle 80° and 30°.

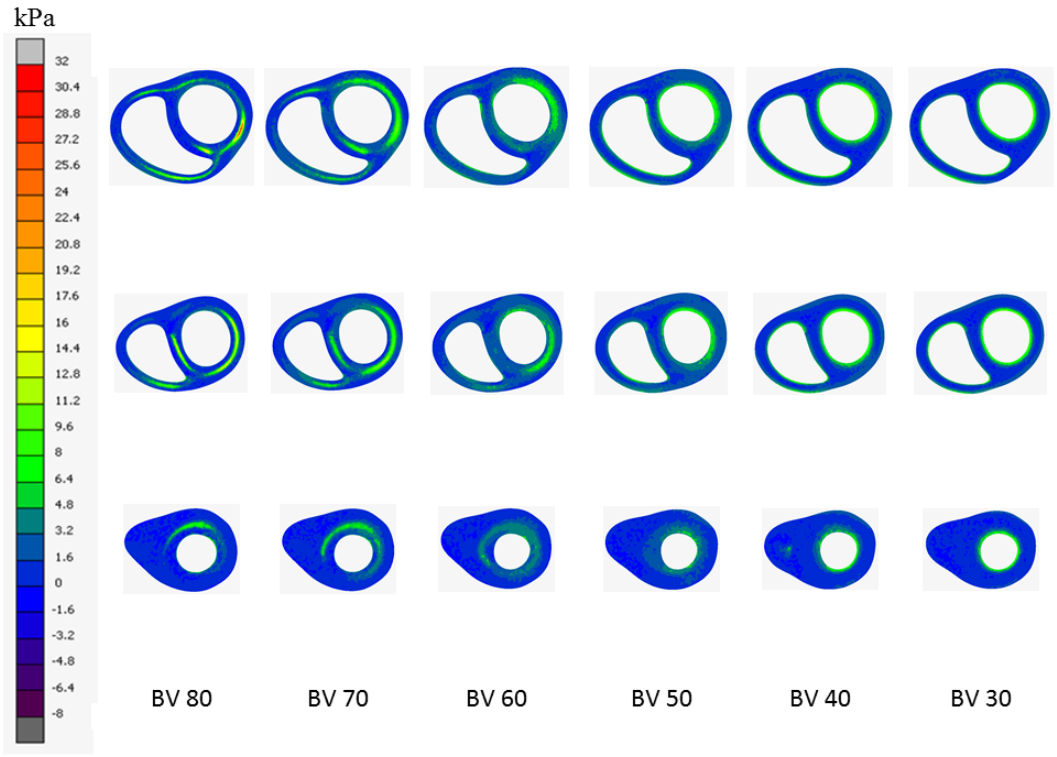

Figure 4.12: Effect of different fibre orientation on the Cauchy stress in fibre direction during passive inflation of LV at 10 mmHg LV cavity pressure; first, second and third row in each column represent basal, equatorial and apical slices respectively

4.4.5 Effect of RV on EDPVRs of LV

In order to study the effect of RV deformation, BV and single LV geometries were constructed from same CMRI. The difference in LV cavity volume and geometrical shape between the geometries was less than 1%, which induced from wrapping and smoothing procedure in 3-matic. Figure 4.14 represents the comparison of the EDPVRs calculated from BV model and single LV model for different fibre orientation. Interestingly, BV model produced more volume change compare to the volume change in single LV model with respect to the same pressure change. In BV model, RV pressure had two effects on LV inflation - (1) pressure on RV septal wall tried to suppress LV inflation and

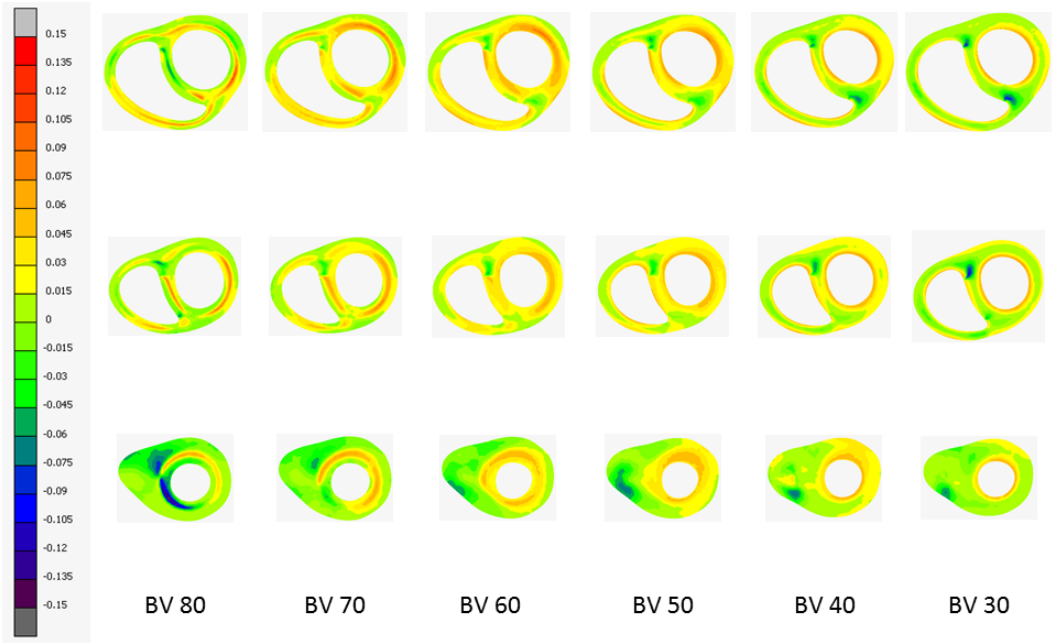

Figure 4.13: Effect of different fibre orientation on the true strain in fibre direction during passive inflation of LV at 10 mmHg LV cavity pressure; first, second and third row in each column represents basal, equatorial and apical slices respectively

(2) pressure on RV free wall helped in LV inflation. In addition, RV geometry provided structural supports to LV and thus provided greater inertia against the LV inflation. From the results, it was concluded that the net effect of RV geometry and pressure supported the LV to inflate more. The increase in LV inflation due to the RV deformation was approximately in the range of $3 - 5\%$ of LV volume, calculated from single LV model at LV EDP of 10 mmHg. Increment in LV inflation was more when fibre angles were $60°$ and $70°$.

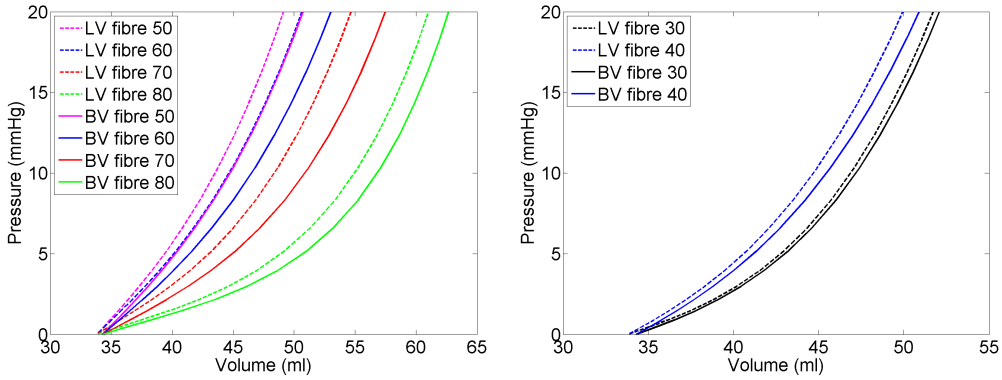

(a) (b)

Figure 4.14: Comparison between the EDPVRs computed using bi-ventricular model and single LV model for different fibre structures; (a) for fibre 50 to fibre 80, and (b) for fibre 30 to fibre 40

4.4.6 Effect of RV on Stress Strain Distribution of LV Wall

Figure 4.15 shows the effect of RV deformation on fibre stress-strain distribution of LV wall at 10 mmHg LV pressure when fibre orientation is 60°. The average stress and strain in fibre and sheet directions with standard deviation were calculated in anterior (A), lateral (L), posterior (P) and septum (S) regions of the basal, equatorial and apical positions from both the models, and a detailed quantitative comparison is shown in figure 4.16.

In basal slice, the high stress was experienced in the posterior and partially on the septum region for single LV model whereas it shifted towards the lateral region for BV model (Figure 4.15a and 4.16). That was also evident from the long-axis images in *s-l* position. In the equatorial, high fibre stress acted on the anterior wall for single LV model. In contrast, the high fibre stress occurred in the mid-wall of the posterior region of the equatorial position in

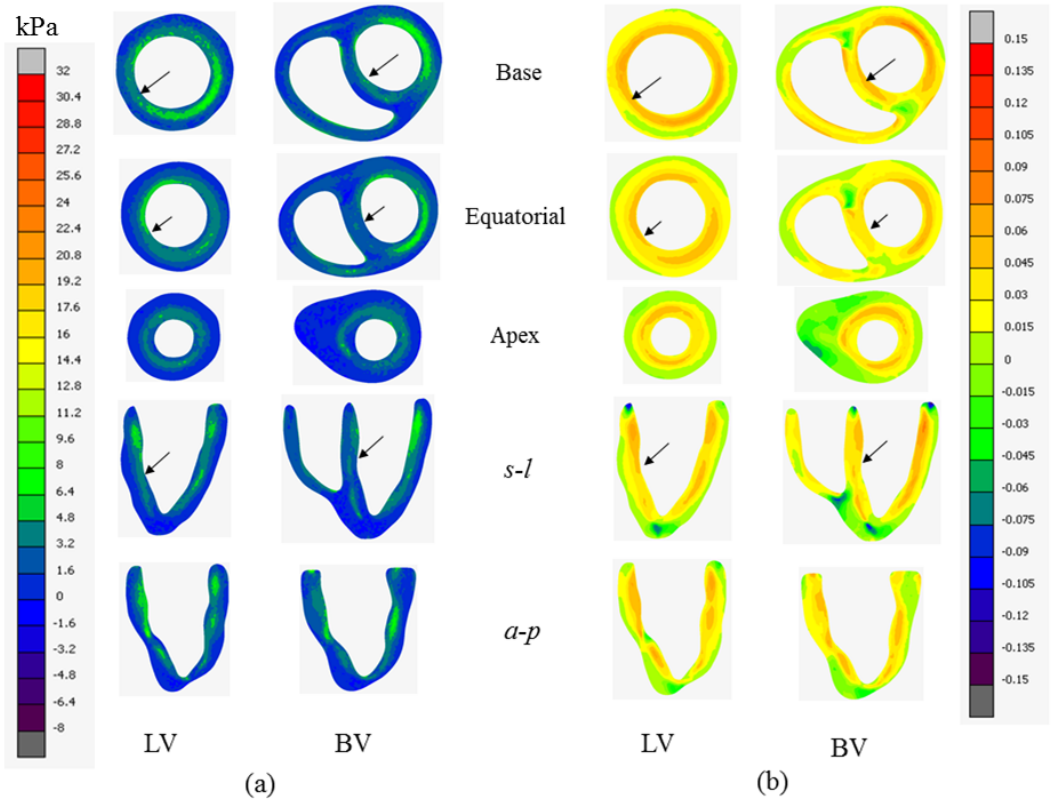

Figure 4.15: Comparison between (a) stress and (b) strain results in fibre direction computed using BV and single LV model for fibre angle 60° at LV cavity pressure of 10 mmHg; arrows represent the location of septum

BV model. In addition, *s-l* position shows that the single LV model predicts higher fibre stress in the anterior region of the basal and the equatorial positions which is completely in contrast with the fibre stress, generated in the same region from BV model. Fibre-stress prediction was different in septum (*s-l* position) from the single LV and the BV model.

In the basal position, high tensile fibre strain was experienced in the endocardium to the mid-wall for all four regions in single LV model. Low compressive fibre strain was experienced in the lateral, the posterior and partially the septum regions, and towards the epicardium (Figure 4.15b). In

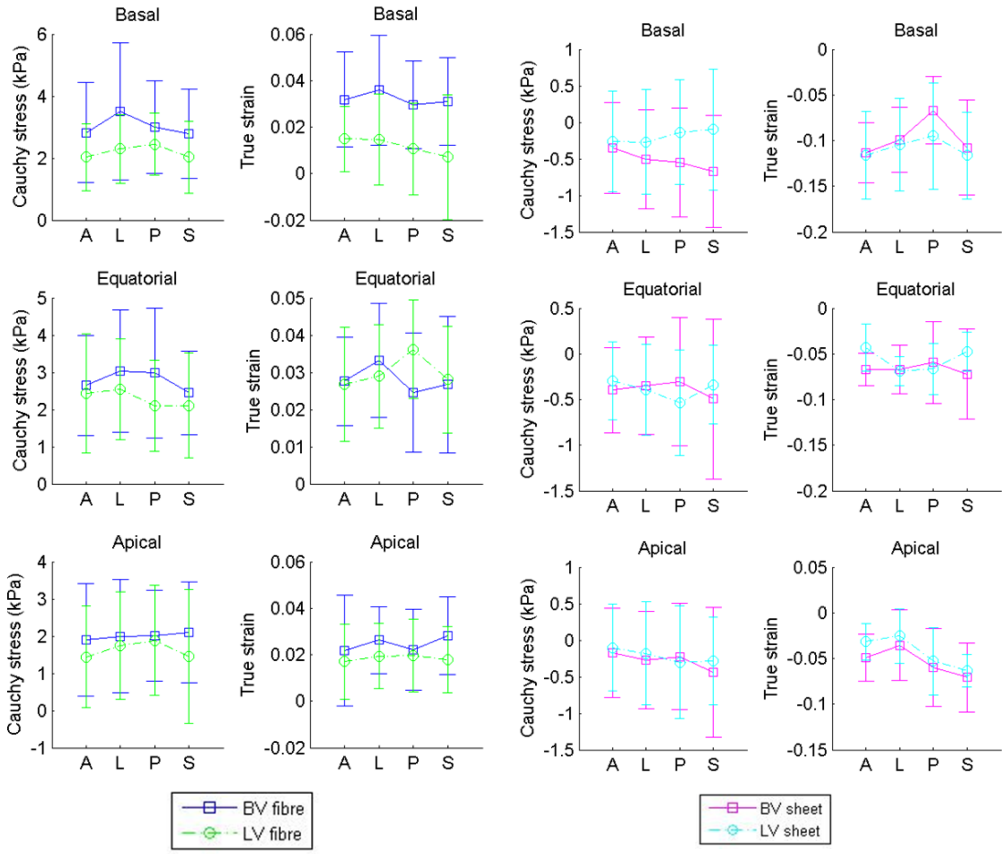

(a) (b)

Figure 4.16: Comparison between the stress-strain results predicted from BV and single LV model for fibre angle 60; the average stress and strain with standard deviation are calculated in anterior (A), lateral (L), posterior (P) and septum (s) regions of basal, equatorial and apical elements; (a) comparison of fibre stress and fibre strain; (b) comparison of sheet stress and sheet strain

contrast, BV model computed high tensile strain in the the lateral region of the endocardium and the mid-wall. The septum of the LV model experienced compressive fibre strain mainly from the equatorial to the apex, whereas no compressive force was experienced by the septum in the BV model.

The mean fibre stress and sheet stress predication by the BV model was more in all the regions of LV, especially near the basal area (figure 4.16). There

was notable difference in sheet stress prediction by the models in the lateral, the posterior and especially in the septum regions in the basal area. The fibre and sheet strain and sheet stress were almost identical in apical region for both the models. The variations in fibre and sheet stresses were higher for the BV model compared to the single LV model.

4.5 Discussion

4.5.1 Validation of the Model

The validation of the constructed BV and LV mesh geometries from CMRI data were shown in Section 3.2.3 of Chapter 3. The structure-based orthotropic Holzapfel-Ogden constitutive law was implemented in FE framework and validated with the analytical results as shown in Section 3.4.4 of Chapter 3. The volume-normalized EDPVRs (PV_n) resulted from the simulation model was validated with the experimental measurement from ex-vivo human heart. The same validation method was adopted by Wang et al. (2013a). In addition, the volume-normalised EDPVRs for different fibre orientation followed the hypothesis that volume-normalized EDPVRs should have a common shape, irrespective of different species and diseased ventricles (Klotz et al., 2006). The effect of fibre structure on fibre stress distribution for single LV model wall was qualitatively agreed with the simulation results reported in Wang et al. (2013a). Such qualitative validation indicated that the LDRF algorithm as well as the FE modelling of ventricle were accurate. The quantitative validation did not seem to be merited due to the following factors. (a) The model was reconstructed from human CMRI data and thus the geometry was not as regular as for some models used previously (Stevens et al., 2003; Nash and Hunter, 2000). This, in turn, affected the stress-strain distributions. (b) The single LV geometry was different amongst the studies as they were constructed from different CMRI data. (c) Due to the local heterogeneity between two LV geometries, the implemented fibre orientation for a particular helix angle was not exactly same. (d) The exact location from where the stress-strain values were reported was not explicitly mentioned in the literature, and therefore,

comparing the stress-strain values in such locations were not possible.

4.5.2 Effect on EDPVRs of LV

The study indicated that the fibre-angle distribution had large impact on the EDPVRs during LV diastole. The passive LV inflation was more, when the fibre-direction shifted more towards LV longitudinal axis. In addition, the change in volume was very close to each other when the fibre-angle varied in the range of 30° to 60°. This suggests that any pathological remodelling of the fibre structure, which increases the volume change more than the normal condition, indicates increment in fibre-angle. Although the effect of fibre-distribution was carried out by few researchers on LV diastole (Wang et al., 2013), the influence of fibre distribution on EDPVRs of LV was not explored. Such effects were investigated for the first time in this study and have introduced the novelty of the research. Increases in the LV mass, LV fibrosis, and cardiomyocyte stiffness had been shown to contribute to heart failure with preserved ejection fraction (HFpEF) (Paulus and Tschpe, 2013). The present results suggested that changes in the fibre direction in LV wall may contribute to the HFpEF development. These findings will be helpful in medical practice to diagnose the condition of the LV in diastole with known fibre structure. Besides, it can lead to development of new drugs which can alter fibre-structure in order to control the inflation of LV in diseased conditions.

Interestingly, RV deformation eventually helped the LV to inflate more although it provided additional geometrical constraint against LV. The reason was that the pressure on RV free wall supported the LV to inflate more compared to the pressure acted on RV septum, which tried to suppress the LV

expansion. This indicates the importance of including RV geometry and pressure condition for any LV modelling in future studies. In addition, previous studies (Dorri et al., 2006) simplified the effect of RV by providing RV pressure only on the septum wall of a single LV model. However, this was not suitable to identify the overall effect of RV deformation on LV diastolic mechanics as illustrated in this study.

4.5.3 Effect on Stress-Strain Distributions of LV Wall

The transmural distribution of fibre-stress was very sensitive to the change in fibre-angle specially near the base and the equatorial regions which supported the findings of Wang et al. (2013a). Close inspection suggested that the LV mid-wall became very stiff during passive inflation especially in the anterior, the lateral and the posterior regions when fibres were aligned more towards LV long axis. In contrast, LV endocardium surface became stiffer when the fibre angle was relatively small (i.e. for 30°-50°). This information will be useful whilst developing the procedure to predict fibre-distribution from in-vivo observation of LV motion or predicting LV deformation from known fibre-distribution. Also, it suggests that patient-specific fibre-distribution is important even for modelling normal diastolic mechanics of human heart.

For fibre angle 60°, it was clearly observed that the fibre and sheet stress and strain distribution of LV wall during passive inflation was changing when including the RV deformation. The changes were more notable in the basal and the equatorial areas in comparison to the apical location. This was quite natural as the effect of RV deformation reduced in the apical position due to the absence of RV pressure. The variation in fibre and shee stress-strain

distributions of LV wall was greater in BV model compared to the single LV model. Therefore, it is important to consider RV deformation whilst carrying out cardiac simulation in future studies. In addition, bi-ventricular model considers RV to provide structural support to the LV and thus, no artificial boundary condition at the ventricular septum would be required to provide the deformation experienced by it.

Effect of fibre-structure on stress-strain distribution of LV wall was investigated by Wang et al. (2013a) using only LV geometry. From current study, it was observed that the stress-strain distribution of LV wall during diastole would change due to the inclusion of RV deformation. Thus, the effect of fibre-structure on LV inflation shown here would be more realistic as compared to the results of Wang et al. (2013a). The surgeons could plan the surgery so that the mid wall of LV can endure the higher stresses after surgery if the fibre structure for that patient is orientated more towards LV longitudinal axis. For smaller helix angle (30° - 50°), the focuses should be on the endocardial wall of the LV.

4.5.4 Limitations of the Current Study

The material parameters, used in the study, were determined from the experimental data of porcine myocardium because the experimental data of human myocardium is not available. This limitation should not affect the conclusions drawn from the study. In Chapter 5, the material parameters will be calibrated for human myocardium. The same study (i.e. the effect of fibre structure) will then be accomplished with new material parameters for human myocardium to check whether the conclusion differs from the current study (Section 6.3.4B

of Chapter 6). The second limitation of the study was to use only one ventricular geometry. Therefore, the effect of fibre orientation will be investigated for two human hearts with their specific myocardium properties to ensure robust and generalise conclusions (Section 6.3.4B of Chapter 6). Finally, the current model used simplified boundary conditions without accounting the basal movement of the ventricles. The effect of such basal movement are addressed in detail in the Section 6.3.4A of Chapter 6.

4.6 Research Contributions

The key findings from this study are summarised below.

- **Effect of RV on LV passive inflation:**

  For the first time, the assumption of single LV model in the literature was interrogated, and the effect of RV deformation on LV diastole was investigated by comparing the results of BV and LV model of same heart. Results indicated considerable influence of RV deformation which led to additional LV passive inflation and increase in average fibre and sheet stress-strain of LV wall during diastole. Therefore, it is strongly suggests that RV deformation should be accounted for in computational modelling for improved understanding of the LV mechanics under normal and pathological conditions.

- **Effect of fibre orientation on EDPVRs of LV :**

  The effect of fibre orientation on EDPVRs was investigated for the first time. The sensitivity study of the fibre angle distribution indicated that any pathological remodelling of the fibre distribution that increased the amount of transmural fibre angle would lead to additional left ventricular inflation. Therefore, changes in the fibre direction in LV wall may also contribute to the heart failure with preserved ejection fraction (HFpEF) development. These findings will be helpful in medical practice to diagnose the condition of LV in diastole with known fibre structure. Besides, it can lead to development of new drugs which can alter fibre structure in order to control the inflation of the LV in diseased conditions.

- **Effect of fibre orientation on stress-strain distribution of LV**

wall :

The transmural distribution of the fibre stress and strain were very sensitive to the change in the fibre angle near the base and the equatorial regions. The LV mid-wall became stiffer during passive inflation especially in the anterior, the lateral and the posterior regions when fibre directions aligned more towards LV the longitudinal axis. This information will be useful whilst developing the procedure to predict fibre-distribution from in-vivo observation of LV motion or predicting LV deformation from known fibre-distribution. Also, it suggests that subject-specific fibre-distribution is important even for modelling normal diastolic mechanics of human heart.

4.7 Summary

This chapter addressed two research objectives (objective 1 and objective 2), and detailed the investigation procedures followed by the results, discussion and key findings. Anatomically realistic models of the human ventricle (BV and single LV), that employed rule based fibre orientation (LDRF algorithm) and a structure based orthotropic constitutive law (Holzapfel-Ogden law), were developed to simulate the passive diastolic mechanics of the LV (Section 4.3). The pressure-normalised volume (PV_n) relationship, calculated from BV and single LV model, agreed well with the published measurements, and served as a validation of the model (Section 4.4.2). The sensitivity study of the fibre angle distribution indicated that any pathological remodelling of the fibre distribution that increased the amount of transmural fibre angle would lead to additional LV inflation. Furthermore, the mid-wall of the myocardium would become stiffer when fibre direction aligned more towards LV longitudinal direction. These information will be useful in medical practice while developing new drug or planning for ventricular surgery. This highlights the use of personalised fibre orientation especially in pathological condition that involves remodelling of LV structure. The results from the BV model and the single LV model were compared, and it was observed that RV deformation increased LV wall stress-strain. These confirmed the effect of RV deformation on the passive inflation of LV. Future studies should consider RV whilst carrying out patient-specific modelling from in-vivo images to obtain improved understanding of the physiology of human hearts. All the above mentioned results were described in detail in Section 4.4 and 4.5. The reseach contributions from the study were highlighted in Section 4.6.

Chapter 5

Estimation of Passive Orthotropic Properties of Human Myocardium

5.1 Introduction

As mentioned in Chapter 4, one limitation of the study was the use of myocardium properties of pig due to the unavailability of human myocardial properties. In FE modelling, it is paramount to accurately use in-vivo passive biomechanical properties of the human myocardium and understand its microstructural effect on ventricular passive inflation, in order to mimic the cardiac mechanics properly (Wang et al., 2013a). Therefore, the flowing objective is addressed in this study as raised in Section 2.8 of Chapter 2.

Objective 3: To estimate the in-vivo passive orthotropic properties of healthy human myocardium using routinely used non-invasive clinical data, and to

explore the effect of geometry, fibre orientation, and end diastolic pressure (EDP) on the estimated properties.

A brief overview of the research gap, and subsequently, identification of the research objective is discussed in Section 5.2. The prerequisites to construct the FE modelling of ventricle were described briefly in Section 5.3.1 followed by a detailed investigation strategy in Section 5.3.2. The results and discussion about proposed methods are included in Section 5.4 and 5.5 respectively. The research contributions are addressed in Section 5.6.

5.2 Brief Literature Review

Traditionally, experimental studies were carried out to identify the myocardial properties through ex-vivo mechanical testing on myocardial tissue, harvested from a specific heart. Results from the biaxial tests of canine myocardium (Demer and Yin, 1983; Yin et al., 1987; Humphrey et al., 1990a; Novak et al., 1994) and simple shear test of pig myocardium (Dokos et al., 2002) clearly exhibited its orthotropic behaviour. These experimental data provided insights into defining the constitutive laws of the myocardium, and subsequently, determining the value of the constitutive parameters (Schmid et al., 2006, 2008). However, these traditional methods involved invasive ex-vivo operations, that resulted the destruction of the myocardium tissues (as a result of sectioning samples), and therefore, are not suitable for in-vivo clinical measurements (Dokos et al., 2000). Moreover, ex-vivo experiments using cadaver hearts may not be the true representative of the in-vivo passive properties (Wang et al., 2009) due to tissue homoeostasis . An extensive literature survey showed that

all ex-vivo experimental data were measured from animal heart, (except the recent publications by Sommer et al. (2015a,b)), and therefore, data for passive human myocardium were largely missing . As a result, the computational models of human LV, using those animal data, were unable to produce expected passive inflation for human heart (Wang et al., 2013a; Eriksson et al., 2013; Baillargeon et al., 2014).

FE modelling, in combination with cardiac magnetic resonance imaging (CMRI), was carried out by few researchers to estimate passive myocardial properties in a non-invasive manner (Walker et al., 2005; Wang et al., 2009; Xi et al., 2011b,a; Wenk et al., 2011b; Xi et al., 2013; Genet et al., 2014; Gao et al., 2015). Other work was accomplished to assess the passive material properties in isolated hearts with FE analysis (Omens et al., 1993; Emery et al., 1997; Okamoto et al., 2000; Augenstein et al., 2005, 2006; Nair et al., 2007). Most of them used Fung-type transversely isotropic constitutive model with animal heart (Guccione et al., 1991, 1995; Costa et al., 1996). In contrast, resent studies described the laminar architecture of the myocardium forming local orthotropic material axes within it (LeGrice et al., 1995b) (Section 2.3 of Chapter 2). This orthotropic behaviour of myocardium was also evident from the simple shear test of pig (Dokos et al., 2002) and human myocardium (Sommer et al., 2015a). Moreover, Schmid et al. (2008) reported that a transversely isotropic law would not be suitable for modelling orthotropic responses of passive myocardium under simple shear tests. Modified Fung-type law (Usyk et al., 2000; Costa et al., 2001) and pole-zero law (Nash and Hunter, 2000; Stevens et al., 2003) were introduced to incorporate such material orthotropy. However, in all the Fung-type material models, the material parameters were merely used

as weighting factors, rather than providing any physical importance (Goktepe et al., 2011). Besides, some of the material parameters were highly correlated in Fung-type and pole-zero law (Stevens et al., 2003; Remme et al., 2004; Wang et al., 2013a). Recently, Holzapfel and Ogden (2009) developed a constitutive law that considered the locally orthotropic tissue architecture and the parameters of this model were closely related to the characteristic micro-structure of myocardium. Due to the unavailability of experimental data for human myocardium, the parameters of the material model were fitted to the simple shear test results from pig myocardium (Dokos et al., 2002) to define fully orthotropic nature. The values of these fitted parameters (Table 5.1), used in existing literature, resulted in too stiff stress-strain relation in patient-specific model (Sommer et al., 2015a), and were therefore, unable to produce measured end-diastolic volume (EDV) of LV within the physiological end-diastolic pressure (EDP) (Wang et al., 2013a; Eriksson et al., 2013; Baillargeon et al., 2014). As discussed above and shown in Table 5.2, limited attempts have been made to determine in-vivo passive orthotropic material properties of human myocardium for the Holzapfel-Ogden material model.

Table 5.1: Values of Holzapfel-Ogden passive material parameters used in existing literature

Articles	Passive Material Parameters							
	a (kPa)	b	a_f (kPa)	b_f	a_s (kPa)	b_s	a_{fs} (kPa)	b_{fs}
Holzapfel and Ogden (2009)	0.059	8.023	18.472	16.026	2.481	11.12	0.216	11.436
Goktepe et al. (2011)	0.496	7.209	15.193	20.147	3.283	11.176	0.662	9.466
Wang et al. (2013a)	0.236	10.81	20.037	14.154	3.724	5.164	0.411	11.3
Eriksson et al. (2013)	0.333	9.242	18.535	15.972	2.564	10.446	0.417	11.602
Average	0.28	8.82	18.1	16.5	3.0	9.5	0.40	10.9

Table 5.2: A brief overview of the methods used to estimate constitutive parameters for myocardium

	Using mechanical test results of excised myocardium	Isolated heart with FE analysis	In-vivo estimation using FE analysis (Animal myocardium)	In-vivo estimation using FE analysis (Human myocardium)
Fung-type transversely isotropic	Schmid et al. (2006) Schmid et al. (2008)	Omens et al. (1993) Augenstein et al. (2005) Augenstein et al. (2006) Nair et al. (2007)	Walker et al. (2005) Wang et al. (2009)	Xi et al. (2011b) Xi et al. (2011a) Xi et al. (2013) Genet et al. (2014)
Pole-zero orthotropic		Stevens et al. (2003) Remme et al. (2004)		
Fung-type orthotropic	Schmid et al. (2006) Schmid et al. (2008)			
Holzapfel-Ogden orthotropic	Holzapfel and Ogden (2009) Goktepe et al. (2011) Wang et al. (2013a) Eriksson et al. (2013)			**Research Gap,** **addressed in the study Objective 3**

An inverse estimation method, which was typically formulated as a non-linear optimisation problem to minimise the differences in the measurements with respect to the unknown parameters, was used to quantify passive properties of human myocardium using Holzapfel-Ogden material law. Due to the highly non-linear nature of the inverse optimisation problem, large design space, and correlation amongst the material parameters, it was non-trivial to inversely estimate those parameters accurately and uniquely from limited clinical data. The trade-off was that, while fewer clinical data made the inverse problem more ill-posed, requirement of more subject-specific data (i.e. MRI tagging and in-vivo ventricular pressure) led to more complex and invasive clinical measurements with longer processing times, which was not always possible. Therefore, one of the major challenges, addressed in this study, was to extract the human myocardial stiffness instead of finding unique solution using only non-invasive routinely used clinical data rather than using invasive and computationally expensive clinical data (Objective 3).

5.3 Materials and Methods

5.3.1 FE Modelling of BV

In the present study, ECG gated, breath hold, steady state free precession (SSFP) cine CMRI was used to capture the images of five normal human ventricles at UHCW, UK. BSREC ethics approval (REGO-2012-032) was obtained to carry out the research on anonymised human data. The typical scanning protocol was summarised in Table 3.1 of Chapter 3. The image frame corresponding to early diastole (ErD), end diastole (ED) and end systole (ES) phase of cardiac cycle were identified by consulting with experienced radiologists (Section 3.2.2 of Chapter 3). BV mesh geometry, and subsequently, LV cavity geometry were constructed for each phase to calculate early diastolic volume (ErDV), end diastolic volume (EDV), end systolic volume (ESV) and, finally the Ejection Fraction (EF). The construction of BV and LV cavity geometries were described in Section 3.2.2 of Chapter 3. ErDV, EDV, ESV and EF, calculated from CMRI of five normal human hearts (BV1 to BV5), are shown in Figure 5.1. Each BV mesh geometry was composed of at least 750,000 linear tetrahedral elements (tet4) to achieve accurate results as identified from the mesh convergence study (Section 4.4.1 of Chapter 4). Detailed demographic information of the subjects are shown in Table 5.3.

Myocardial fibre structure was implemented using Laplace-Dirichlet-Region growing-FEM (LDRF) algorithm as detailed in Section 3.3 of Chapter 3. Based on previous histological studies (Streeter et al., 1969; Arts et al., 2001), the fibre direction was defined by a linear variation of helix angle from -70° in the sub-epicardium and right-ventricular septal endocardium to almost

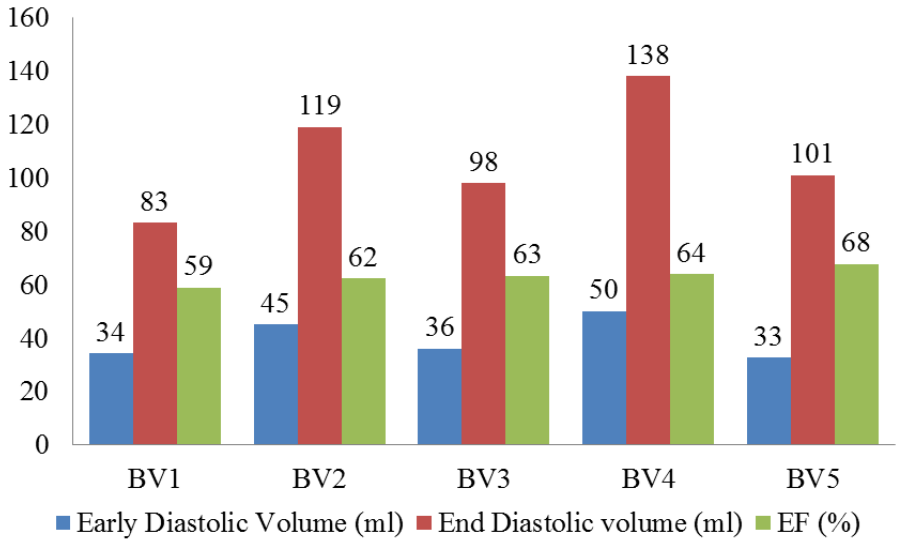

Figure 5.1: Early Diastolic Volume (ErDv), End Diastolic Volume (EDV) and Ejection Fraction (EF) extracted from CMRI for five normal hearts (BV1 to BV5)

Table 5.3: Demographic information of five subjects

	Sex	Age (years)
BV1	Female	39
BV2	Male	54
BV3	Male	28
BV4	Male	38
BV5	Male	36

0° in the mid-wall to $+70^\circ$ at sub-endocardium and right-ventricular free wall endocardium for all five ventricles. The sheet direction was assumed to be aligned with local radial direction (i.e. $\beta = 0^\circ$) as described in Section 3.3.1.

The Holzapfel-Ogden material law was described extensively in Holzapfel and Ogden (2009); Goktepe et al. (2011) and in Section 3.4 of Chapter 3. The key points are summarised here. There are eight non-negative material parameters (a, b, a_f, b_f, a_s, b_s, a_{fs}, b_{fs}) in the strain energy function along with

an extra bulk modulus (K) as shown in Eq. (3.17) where, a and b parameters represent the response of isotropic ground matrix; a_f and b_f characterise the response of myocardial fibres; a_s and b_s denote the contribution of sheet; and a_{fs} and b_{fs} account for the shear effects in the sheet-plane. All a_i and a represent the dimension of stress in kPa and the unit-less parameters b_i and b represent the non-linear behaviour of the corresponding structure. The bulk modulus (K) works as a penalty parameter for imposing incompressibility.

Holzapfel-Ogden constitutive law was implemented using a user-defined subroutine 'Hypela2' in MSC-Marc (MSC Software Corporation, California, US) utilising Total Lagrange framework as detailed in Section 3.4.2 of Chapter 3. The early-diastolic BV mesh geometry, composed of four node tetrahedral elements, was constructed from the early diastolic CMRI of human ventricle. According to state-of-the-art, early diastole is assumed as initial stress free configuration since the ventricular pressure is lowest at this point and therefore stress is minimum (Usyk et al., 2000; Sun et al., 2009; Wenk et al., 2011a,b; Genet et al., 2014). According to the previous mesh convergence study in Section 4.4.1 of Chapter 4, the number of tetrahedral elements in each ventricular mesh geometry was kept more than 750,000 to achieve reliable results. Due to the unavailability of subject-specific ventricular pressure which requires invasive measurement, LV EDP was assumed as 10 mmHg (Wang et al., 2013a; Lee et al., 2013a,b; Genet et al., 2014). One third of LV blood pressure was applied on the RV endocardium (Goktepe et al., 2011). The longitudinal movement of the base nodes and the circumferential displacement of epicardial wall at the base were suppressed in order to avoid undesirable rigid body displacement (Wenk et al., 2012; Eriksson et al., 2013; Wang et al., 2013a; Genet et al.,

2014). The rest of the ventricular wall including apex is left free (Wenk et al., 2012; Eriksson et al., 2013; Wang et al., 2013a; Genet et al., 2014). The following section describes the investigation strategies to estimate the value of the material parameters.

5.3.2 Investigation Strategies

As outlined by Xi et al. (2013) in the context of inverse estimation of material parameters, multiple sets of parameters were able to reproduce similar end-diastolic deformation states. Therefore, few strategic and logical assumptions were made as follows:

(A) Define Range of the Parameters

From the definition of the material law, all the eight parameters are positive real number (i.e. a , b, a_f, b_f, a_s, b_s, a_{fs}, $b_{fs} > 0$). On the other hand, it was reported that the human myocardium is less stiff than pig myocardium (Genet et al., 2014; Sommer et al., 2015a). As a result, the values of the material parameters, derived from harvested pig myocardium, could not produce expected EDV in computational model (Wang et al., 2013a; Eriksson et al., 2013; Baillargeon et al., 2014). Therefore, for each shear mode, the value of shear stress should be less for human myocardium compared to pig myocardium. Hence, the maximum value of each parameter would not be higher than the value estimated from the shear stress experiment of pig myocardium. In this study, the maximum value of each parameter was considered as the average value of the respective parameter, derived from the experimental data of pig myocardium shown in Table 5.1. Therefore, the range of parameters is as follows

$$\left.\begin{aligned} a^{max} &= 0.28, \quad b^{max} = 8.82 \\ a_f^{max} &= 18.1, \quad b_f^{max} = 16.5 \\ a_s^{max} &= 3.0, \qquad b_s^{max} = 9.5 \\ a_{fs}^{max} &= 0.40, \quad b_{fs}^{max} = 10.9 \end{aligned}\right\} \tag{5.1}$$

(B) Reduce the Design Space

Without changing the constitutive law, the design space of the problem was reduced by selecting fewer parameters for the inverse estimation using a method similar to the one described in Xi et al. (2013). It was observed from the experiment of pig myocardium that the stiffness in the **f**, **s** and **n** directions would be ordered according to $f > s > n$ so that the order of shear responses in six shear modes would follow as $\sigma^{(fs)} > \sigma^{(fn)} > \sigma^{(sf)} > \sigma^{(sn)} > \sigma^{(ns)}$, $\sigma^{(nf)}$ (where (ij) denoted the shear response in j direction of the plane containing i direction and $i \neq j \in f, s, n$ (Dokos et al., 2002; Holzapfel and Ogden, 2009) (Section 2.6 of Chapter 2 and Figure 2.10). The analytical expression of these shear stress modes, used to fit the parameters with the experimental data of pig myocardium, are shown by Eq. (5.2) to (5.7) (for details, see Section 3.4.2

of Chapter 3).

$$\sigma^{(fs)} = \gamma a \exp[\gamma^2 b] + 2\gamma^3 a_f \exp[\gamma^4 b_f] + \gamma a_{fs} \exp[\gamma^2 b_{fs}] \tag{5.2}$$

$$\sigma^{(fn)} = \gamma a \exp[\gamma^2 b] + 2\gamma^3 a_f \exp[\gamma^4 b_f] \tag{5.3}$$

$$\sigma^{(sf)} = \gamma a \exp[\gamma^2 b] + 2\gamma^3 a_s \exp[\gamma^4 b_s] + \gamma a_{fs} \exp[\gamma^2 b_{fs}] \tag{5.4}$$

$$\sigma^{(sn)} = \gamma a \exp[\gamma^2 b] + 2\gamma^3 a_s \exp[\gamma^4 b_s] \tag{5.5}$$

$$\sigma^{(nf)} = \gamma a \exp[\gamma^2 b] \tag{5.6}$$

$$\sigma^{(ns)} = \gamma a \exp[\gamma^2 b] \tag{5.7}$$

where, γ = amount of shear. From Eq. (5.2) to (5.7), it is evident that parameters a and b are present in all the shear mode responses. Therefore, the order of shear responses does not depend on parameters a and b (i.e. for any value of a and b, the order of shear responses would be maintained). The last six parameters are only responsible for maintaining the order of shear stiffness as is evident from Eq. (5.2) to (5.5). This can be maintained if $a_f : a_s : a_{fs}$ = constant and $b_f : b_s : b_{fs}$ = constant. Thus, in order to reduce the values of the parameters (derived from the experimental data of the pig myocardium) to make it less stiff, all the a_i and b_i would always be divided by Ka and Kb respectively so that Eq. (5.8) and (5.9) are maintained. Ka and Kb are positive real number.

$$\frac{a_f}{Ka} : \frac{a_s}{Ka} : \frac{a_{fs}}{Ka} = constant \tag{5.8}$$

$$\frac{b_f}{Kb} : \frac{b_s}{Kb} : \frac{b_{fs}}{Kb} = constant \tag{5.9}$$

Therefore, only four independent parameters (a, b, Ka, Kb) would be required

for inverse estimation to maintain the observed shear stiffness ordering (Dokos et al., 2002; Sommer et al., 2015a). The last six material parameters for human myocardium are then calculated using Eq. (5.1), (5.8) and (5.9), as

$$a_f^{human} = \frac{a_f^{max}}{Ka} = \frac{18.10}{Ka}, \tag{5.10}$$

$$a_s^{human} = \frac{a_s^{max}}{Ka} = \frac{3.00}{Ka}, \tag{5.11}$$

$$a_{fs}^{human} = \frac{a_{fs}^{max}}{Ka} = \frac{0.40}{Ka} \tag{5.12}$$

$$b_f^{human} = \frac{b_f^{max}}{Ka} = \frac{16.50}{Ka}, \tag{5.13}$$

$$b_s^{human} = \frac{b_s^{max}}{Ka} = \frac{9.50}{Ka}, \tag{5.14}$$

$$b_{fs}^{human} = \frac{b_{fs}^{max}}{Ka} = \frac{10.90}{Ka} \tag{5.15}$$

If it was assumed that the a_f and b_f values for human myocardium would not be less than 1, then the maximum values of Ka and Kb should not be greater than 18.10 and 16.50 respectively. On the other hand, the minimum values of Ka and Kb should not be less than 1 as $a_i^{human} <= a_i^{max}$ and $b_i^{human} <= b_i^{max}$ where, $i = f, s, fs$. The range of the parameters is defined by Eq. (5.20) to (5.23).

(C) Problem Formulation

The main goal of the optimisation problem was to estimate the values of four parameters (a, b, Ka, Kb) so that the passive inflation of LV could produce 'real' LV EDV at EDP where 'real' referred to the LV cavity volume measured from CMRI. Therefore, the objective function was to minimise the differences

between the FE predicted and 'real' LV cavity volume (Eq. 5.18). There would be various combinations of four parameters for each given set of LV EDV and EDP, although all the combinations might not provide the correct end-diastolic pressure volume relation (EDPVR) of LV. Moreover, subject-specific EDPVR can only be measured invasively which is not a routine clinical practice. Thus, the Klotz empirical relation (Klotz et al., 2006) was used in addition to match the measured LV EDV at EDP. The normalised volume can be calculated with respect to any pressure point, for example 10, 15, 20 or 30 mmHg etc. (Klotz et al., 2006). However, pressure point less than 15 mmHg was not preferred because the pressure-volume prediction was better when it was predicted by a point having EDP of more than 15 mmHg (Klotz et al., 2006). Therefore, the normalised LV volume in this study was calculated with respect to 20 mmHg scale as defined by Eq. (5.16), and there after measured the model predicted pressure-normalised volume (PV_{Sn}).

$$EDV_n = \frac{V - V_0}{V_{20} - V_0} \tag{5.16}$$

where, V_0 and V_{20} are LV volume at 0 mmHg and 20 mmHg respectively, V is the volume at a certain LV EDP. The empirical Klotz-curve was then derived by varying EDV_n from 0 to 1 in Eq. (5.17).

$$EDP = 20 \cdot EDV_n^{B_n} \tag{5.17}$$

where, EDV_n is normalised volume, and, $B_n = 2.76$. The closeness of the two curves (model predicted PV_{Sn} and PV_{Rn} i.e. Klotz curve) was then calculated using Eq. (5.19), which was solved by using 'trapz' function in Matlab (Figure 5.2). The closeness of the two curves was, therefore, used as a constraint

for the optimisation problem. The maximum value of this constraint was assumed from the initial feasibility study as indicated by Eq. (5.19). Hence, the optimisation problem formulation is defined as follows:

$$\begin{aligned} Minimise \quad & F_{obj}(a, b, Ka, Kb) \\ where, \quad & F_{obj} = [abs(V_{Rn} - V_{Sn})] \end{aligned} \tag{5.18}$$

subject to,

$$0 < abs\left[\int_{1}^{0} f(PV_{Rn})dV - \int_{1}^{0} f(PV_{Sn})dV\right] < 0.3 \tag{5.19}$$

$$a \in (0, 0.28) \tag{5.20}$$

$$b \in (0, 8.82) \tag{5.21}$$

$$Ka \in (1, 18.10) \tag{5.22}$$

$$Kb \in (1, 16.50) \tag{5.23}$$

where,

V_{Rn} = Real (MRI measured) normalised volume

$= 100 * (EDV_R - ErDV_R)/EDV_R$,

V_{Sn} = Simulated (FE generated) normalised volume

$= 100 * (EDV_S - ErDV_R)/EDV_S$,

EDV_R = Real End diastolic volume (EDV) measured from CMRI,

$ErDV_R$ = Real Early diastolic volume (ErDV) measured from CMRI,

EDV_S = Simulated End diastolic volume (EDV) generated from FE model,

PV_{Rn} = Empirical Klotz curve in 20 mmHg pressure scale (Eq. 5.17),

PV_{Sn} = Simulated Pressure-normalise volume curve generated from FE results in 20 mmHg pressure scale (Eq. 5.18),

abs = absolute value.

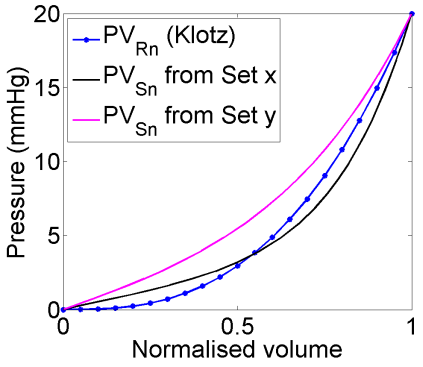

Figure 5.2: An exemplary graphical representation of the closeness between the empirical Klotz curve in 20 mmHg scale (PV_{Rn}) and model predicted pressure-normalised volume (PV_{Sn}) curve. 'Set x' predicted closer PV_{Sn} relation compare to 'Set y' (closeness values, calculated using Eq. (5.19), for 'Set x' and 'Set y' are 1.5 and 0.16 respectively). Each 'Set' is a unique combination of the four parameters within their respective range

(D) Optimisation

Initial sampling was carried out to create 50 sets of parameters using the range of the parameters, defined by Eq. (5.20) to (5.23). Each set is a unique combination of the four parameters within their respective range (Eq. (5.20) to (5.23)). In this study, Latin hypercube sampling (LHS) was used to generate uniformly distributed set of the parameters. Simulation of passive inflation for each set was then carried out using FE modelling and the boundary conditions, mentioned in Section 5.3. LV EDV and closeness of the PV_{Sn} to Klotz curve (PV_{Rn}) i.e. Eq. (5.19) (two outputs) were measured from each simulation. Empirical model of the two responses (Eq. (5.18) and (5.19)) with respect to four independent material parameters were developed using response surface

method (RSM). Genetic algorithm (GA) was then used to solve the optimisation problem to identify the optimum set of parameters (Appendix D). The GA optimised value of the parameters was again used in FE model to measure the LV EDV and Klotz curve closeness. If the absolute differences between GA optimised results and simulation results were greater than 3%, the new set with its simulation results was included in the sample to modify the response surface. The process continued until the simulation results matched with GA results with in 3% range. A flow chart of the proposed inverse optimisation procedure is depicted in Figure 5.3.

5.3.3 Sensitivity Analysis

Due to the unavailability of subject-specific ventricular pressure which required invasive measurement, population based LV EDP of 10 mmHg (Wang et al., 2013a; Lee et al., 2013a,b; Genet et al., 2014) was used in the study to estimate the value of the parameters. However, LV EDP might not always be 10 mmHg. Therefore, value of the material parameters were estimated using LV EDP as 8, 12 and 15 mmHg to identify the sensitivity of the material parameters due to the change in LV EDP. The study was conducted only for one ventricle (BV1).

In-vivo subject-specific measurement of fibre-orientation is still an open question (Bayer et al., 2012; Rohmer et al., 2007; Dorri, 2004; Geerts et al., 2002). Therefore, in this study, fibre-orientation was assumed to be varying from -70° in the sub-epicardium and RV septal endocardium to $+70^{\circ}$ at sub-endocardium and RV free wall endocardium with respect to local circumferential direction. However, it was observed in the previous study (Chapter

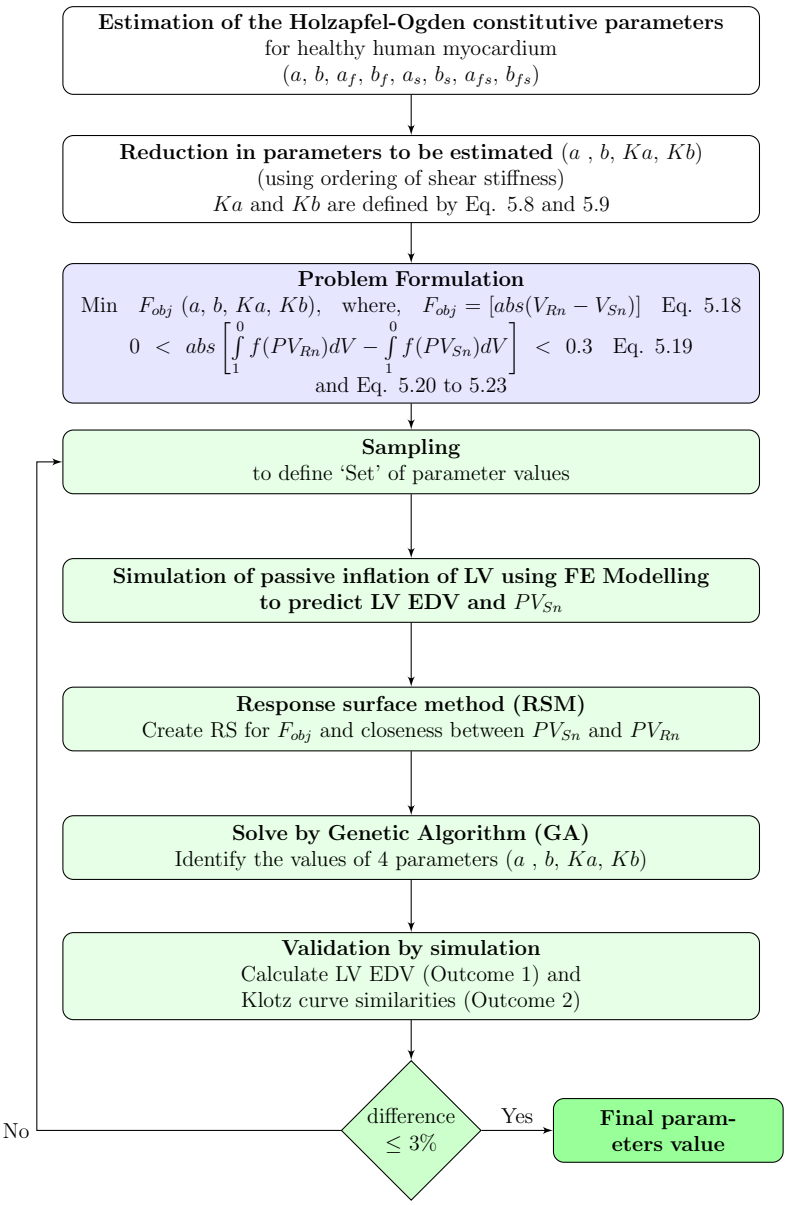

Figure 5.3: Work flow for estimating the parameters value of human myocardium using Holzapfel-Ogden material model

4) that fibre orientation has notable effect on EDPVR of LV and fibre stress distribution. Therefore, the estimation of parameters was also accomplished when helix angle was 50°, 60° and 80° for BV1.

5.4 Results

5.4.1 In-vivo Estimation of the Passive Properties

Table 5.4 shows the values of four material parameters (a, b, Ka, Kb) for five human BVs with LV EDP of 10 mmHg using the proposed inverse optimisation procedure, described in Section 5.3.2 and Figure 5.3. The six material parameters corresponding to fibre-sheet (a_f, a_s, a_{fs}, b_f, b_s and b_{fs}) were then derived using Eq. (5.10) to (5.13) (Section 5.3.2B) with the values of Ka and Kb, shown in Table 5.4. The values of all eight parameters are summarised in Table 5.5 assuming LV EDP of 10 mmHg.

Table 5.4: Subject-specific four material parameters of human myocardium with 10 mmHg LV EDP

	Passive Material Properties				LV EDV (ml)[a]	Klotz curve resemblances[b]
	a (kPa)	b	Ka	Kb		
BV1	0.080	6.00	6.10	2.8	83.01	0.09
BV2	0.092	4.80	6.80	3.1	118.89	0.20
BV3	0.089	4.76	6.98	3.3	98.08	0.15
BV4	0.060	4.45	7.20	3.4	138.03	0.16
BV5	0.048	4.38	7.30	3.3	101.04	0.12

[a]LV volume (EDV) in ml when EDP = 10 mmHg
[b]Klotz curve in 20 mmHg scale

It was observed that the values of each parameters were reduced with the increase in EF amongst the BVs. Moreover, the standard deviation for a particular parameter amongst the ventricles was not very high. A typical contour plot from the RSM and GA is shown in Figure 5.4.

Shear stresses for four shear modes [(fs), (fn), (sf), (sn)] were plotted (Figure 5.5) using the subject-specific value of the eight parameters (Table

Table 5.5: Subject-specific in-vivo passive orthotropic material parameters values of human myocardium with 10 mmHg LV EDP

	Passive Material Parameters							
	a (kPa)	b	a_f (kPa)	b_f	a_s (kPa)	b_s	a_{fs} (kPa)	b_{fs}
BV1	0.080	6.000	2.951	5.893	0.492	3.393	0.070	3.929
BV2	0.092	4.800	2.647	5.323	0.441	3.065	0.063	3.548
BV3	0.089	4.760	2.579	5.000	0.430	2.879	0.061	3.333
BV4	0.060	4.450	2.500	4.853	0.417	2.794	0.059	3.235
BV5	0.048	4.380	2.466	5.000	0.411	2.879	0.058	3.333
Average	0.081	4.696	2.628	5.214	0.438	3.002	0.062	3.476
SD[b]	0.028	0.288	0.193	0.417	0.032	0.240	0.005	0.278

[b]standard deviation

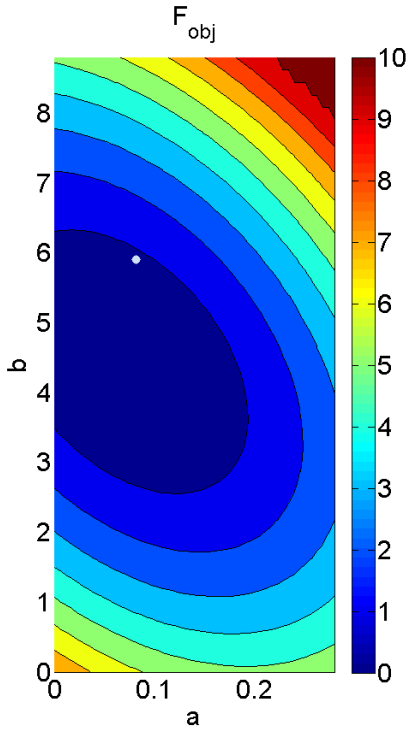

Figure 5.4: Landscape of objective function (F_{obj}) related to the parameter a and b for BV1 when LV EDP was assumed as 10 mmHg

5.5). It was observed that the predicted myofibre stress-strain relationships under different shear modes were reasonably similar for five subjects despite

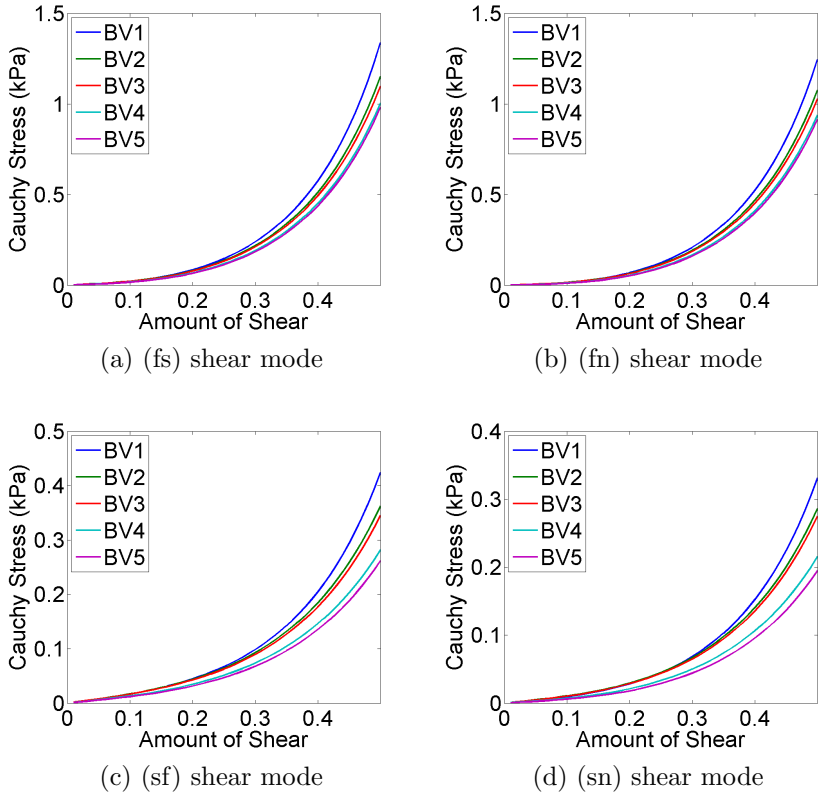

(a) (fs) shear mode (b) (fn) shear mode

(c) (sf) shear mode (d) (sn) shear mode

Figure 5.5: Comparison of shear stress-strain relationships for a cubic myocardial tissue under 4 different shear modes for five subjects (Table 5.5)

of the differences in predicted values. The similarities were more for shear in fs and fn plane compare to the shear in sf and sn plane.

5.4.2 Sensitivity Study

As mentioned in Section 5.3.3, LV EDP was assumed 10 mmHg during the estimation of the parameters. Therefore, a sensitivity study was carried out to explore the changes in parameters if EDP was varied to 8, 10 , 12 and 15 mmHg. The estimated values of material parameters are depicted in Table 5.6. It was observed that the variation in parameter b was comparatively higher due to the change in EDP.

Table 5.6: Estimated values of the parameters with different end diastolic pressures (EDPs) for BV1

EDP	Passive Material Parameters							
	a (kPa)	b	a_f (kPa)	b_f	a_s (kPa)	b_s	a_{fs} (kPa)	b_{fs}
8 mmHg	0.042	5.800	2.857	5.323	0.476	3.065	0.068	3.548
10 mmHg	0.080	6.000	2.951	5.893	0.492	3.393	0.070	3.929
12 mmHg	0.089	6.840	2.612	5.500	0.435	3.167	0.062	3.667
15 mmHg	0.120	8.200	3.600	7.174	0.600	4.130	0.085	4.783
Average	0.083	6.710	3.005	5.972	0.501	3.439	0.071	3.982
SD[b]	0.032	1.091	0.421	0.836	0.070	0.481	0.010	0.557

[b]standard deviation

Another sensitivity study was conducted to investigate the effect of different fibre orientations on parameter estimation. BV1 mesh geometry and LV EDP of 10 mmHg were utilised for the study. Table 5.7 shows the values of eight parameters when fibre angle was 50°, 60°, 70°, and 80°. In was observed that the effect of fibre orientation was comparatively greater on parameter b.

Table 5.7: Estimated values of the parameters with different fibre orientations with EDP = 10 mmHg for BV1

Fibre	Passive Material Parameters							
	a (kPa)	b	a_f (kPa)	b_f	a_s (kPa)	b_s	a_{fs} (kPa)	b_{fs}
fibre 50	0.060	4.090	2.647	5.500	0.441	3.167	0.063	3.667
fibre 60	0.086	4.900	2.769	5.500	0.462	3.167	0.066	3.667
fibre 70	0.080	6.000	2.951	5.893	0.492	3.393	0.070	3.929
fibre 80	0.114	8.010	2.951	5.500	0.492	3.167	0.070	3.667
Average	0.085	5.750	2.829	5.598	0.472	3.223	0.067	3.732
SD[b]	0.022	1.698	0.149	0.196	0.025	0.113	0.004	0.131

[b]standard deviation

Shear stresses for four shear modes ((fs), (fn), (sf), (sn)) were plotted (Figure 5.6) using the material parameters, predicted with different EDP

(Table 5.6) and with different fibre orientations (Table 5.7). It was noticed that the predicted (fs) and (fn) shear were quite similar except for 15 mmHg. When EDP was 15 mmHg, the myocardium became stiffer in fibre directions. The variation due to the fibre orientation was not notable in (fs) and (fn) shear modes. However, the variation was higher for (sf) and (sn) shear modes although the predicted stress values were in the range of 0.4 to 0.8 kPa only.

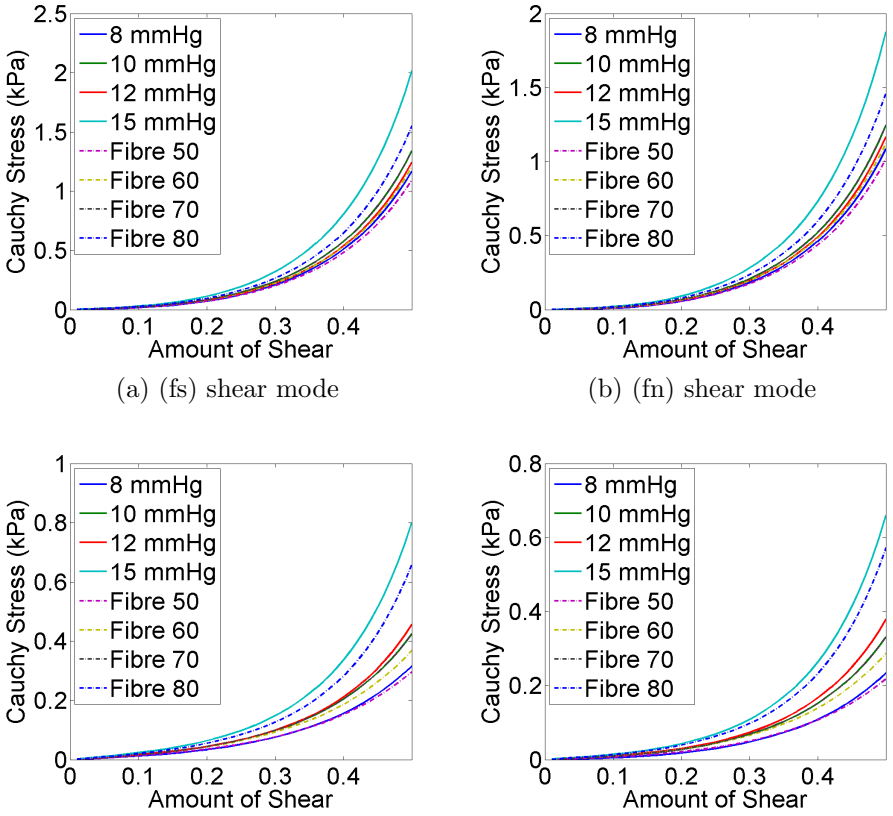

(a) (fs) shear mode

(b) (fn) shear mode

(c) (sf) shear mode

(d) (sn) shear mode

Figure 5.6: Compare shear stress-strain relationships for a cubic myocardial tissue under four different shear modes using the material parameter values, predicted with different EDP (Table 5.6) and with different fibre orientations (Table 5.7)

5.4.3 Comparison with State-of-the-Art

The shear stress-strain relations under six different shear modes of a cubic myocardium tissue were estimated using the value of the material parameters, identified in this study. The same shear stress-strain relations were measured with the material parameters, resulted from the study of Gao et al. (2015). The values of the parameters, identified with LV EDP of 10 mmHg, were selected from both the studies. The parameters for BV1 (Table 5.5) were used for this plot. Figure 5.7 shows that there is a good agreement between the predicted shear stress-strain relations. This highlighted that the estimated values of the parameters from both the studies were within a range. Clearly, it was observed that the shear stress-strain relations, measured from the traditional ex-vivo experiment on excised human myocardium tissue (Sommer et al., 2015b), were over-stiff. The (fs) and (fn) shear modes were in the range of 6 to 7 kPa from ex-vivo measurement whereas it was within the range of 1.2 to 1.8 kPa from in-vivo measurement when the amount of shear was 0.5. These discrepancies might be due to the tissue homoeostasis (Dokos et al., 2000)

Another study was carried out by comparing the stress-strain relation of cubic myocardial tissue under uniaxial stretch test using the estimated parameters in this study, with those from other studies, which inversely estimated human myocardial parameters. Xi et al. (2011a) estimated the values of four parameters for healthy human myocardium using transversely isotropic Fung-type law and LV EDP of 13.6 mmHg (1.81 kPa). Wang et al. (2013b) calibrated only the pressure scaling parameter (C_1) of transversely isotropic Fung-type law for healthy human myocardium with LV EDP of 11 mmHg, and the values of other three parameters were taken from the study of Wang et al.

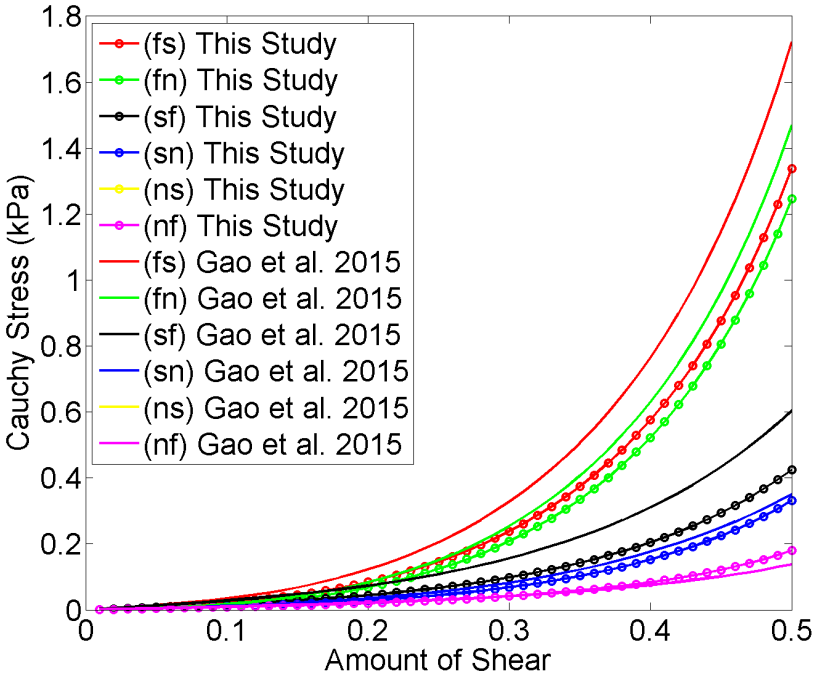

Figure 5.7: Comparison between shear stress-strain relationships for a cubic myocardial tissue under different shear modes using values of the material parameter, predicted in this study and the values predicted by Gao et al. (2015). The parameters value identified with LV EDP of 10 mmHg was selected from both the studies. The parameters value for BV1, shown in Table 5.5, were used for this plot

(2012). Krishnamurthy et al. (2013) reported the values of four parameters (a, b, a_f, b_f) using transversely isotropic part of Holzapfel-Ogden model for human LV with heart failure. Genet et al. (2014) reported the passive material properties of human myocardium using transversely isotropic Fung-type law with 9 mmHg LV EDP. Furthermore, the values of the Holzapfel-Ogden material parameters, estimated with different EDP in this study and by Gao et al. (2015), were also used for the comparison. Figure 5.8 summarises all the uniaxial stress-strain results, using the respective parameters. Although discrepancies existed amongst the plotted results due to the subject variety (geometry, fibre orientation, EF) and different constitutive laws, the overall

trend of the mechanical responses was reasonably similar.

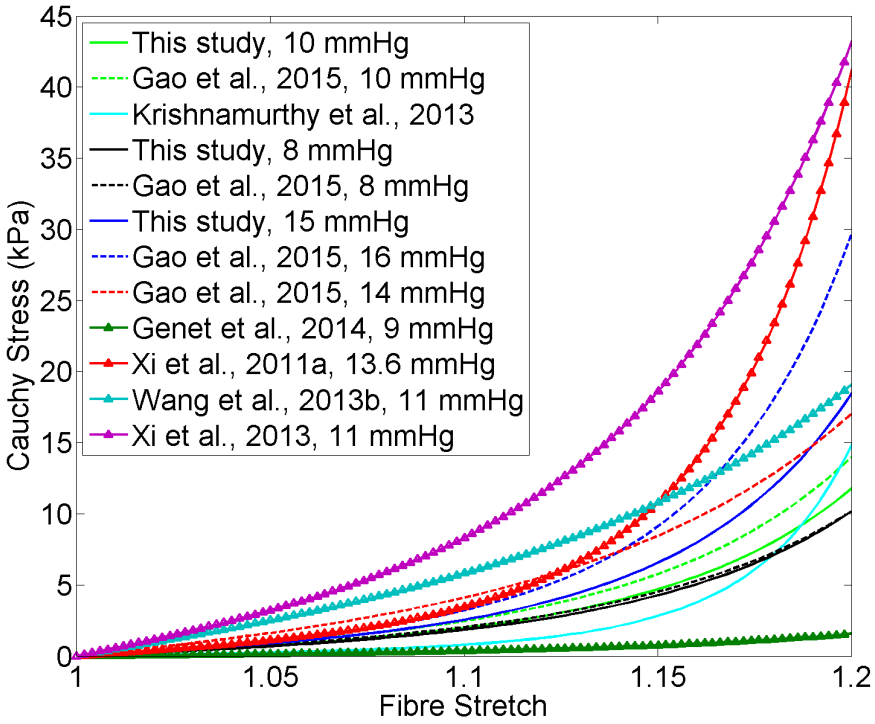

Figure 5.8: Comparison between stress-strain relationships for a cubic myocardial tissue under uniaxial stretch using the material parameter values, predicted in this study and in the literature

5.4.4 Difference in Model Predictions - Pig vs Human Myocardium Data

It was observed that true fibre strain in LV wall was more for human myocardium, because it was less stiff than pig myocardium, and therefore inflated more at diastole (Figure 5.9 and 5.10). However, close inspection indicated that the fibre strain and stress distribution patterns were almost similar for both data sets, even though quantitative differences existed. For human data, the lateral and posterior regions of endocardium experienced high fibre stress,

whereas for pig data, the same regions experienced high stress, but was in the middle of the wall (not exactly in endocardium) (Figure 5.9).

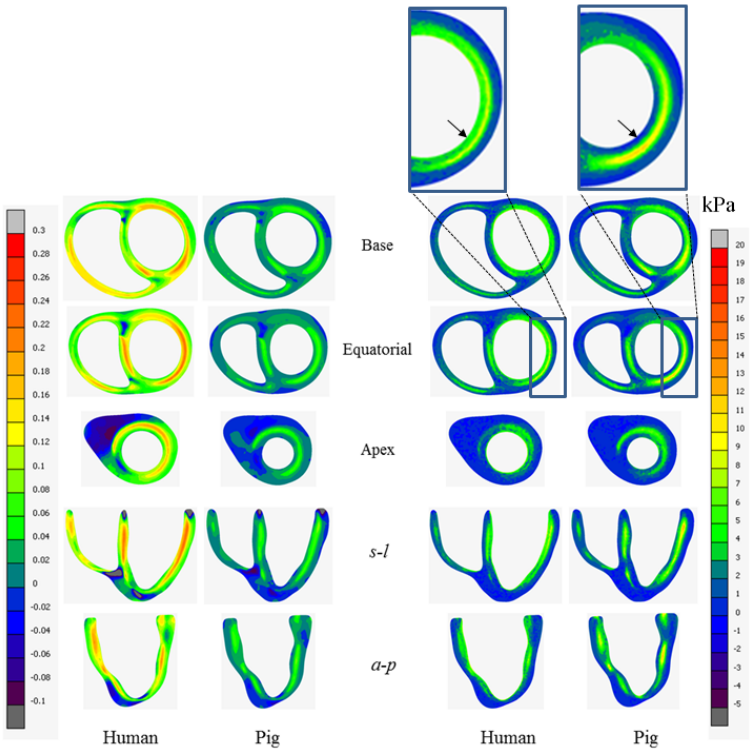

Figure 5.9: Comparison between the predicted true strain and stress (Cauchy stress) in fibre direction using the data set of pig and human myocardium

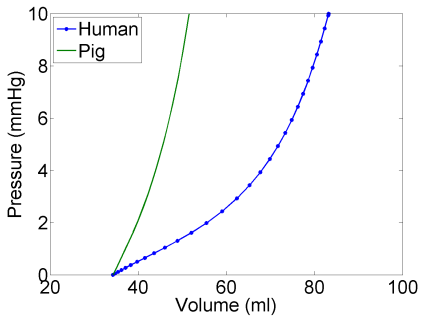

Figure 5.10: Comparison between EDPVRS of LV, predicted using the data set of pig and human myocardium

5.5 Discussion

The objective of the study was to estimate the subject-specific passive orthotropic properties of human myocardium using inverse optimisation. Inverse estimation of material parameters for a given constitutive law remains a major challenge in the field of cardiac biomechanics (Xi et al., 2013) due to the following reasons : (a) limited in-vivo clinical data due to the technical infeasibility, invasive measurements, and therefore, ethical issues, (b) highly non-linear nature of the inverse optimisation problem, (c) strong correlation amongst the material parameters, and (d) increase in material parameters due to the inclusion of fully orthotropic nature, and therefore, increase the design space of the optimisation problem. Different constitutive laws had been developed by many researchers over that past to define myocardium characteristics (Guccione et al., 1991; Costa et al., 1996; Stevens et al., 2003; Remme et al., 2004; Holzapfel and Ogden, 2009), and each law corresponded to different set of parameters and behaviours, and therefore, specific inverse optimisation approach was required. Structure-based, orthotropic Holzapfel-Ogden material law was used in this study to define myocardial characteristics as has several advantages over the other material laws (such as Fung-type transversely isotropic or orthotropic law) for heart modelling (Wang et al., 2013a; Gao et al., 2015). However, estimation of Holzapfel-Ogden material parameters for human myocardium from in-vivo measurement is still limited. Unique estimation of eight material parameters from limited in-vivo clinical data is not possible due to the ill-posed nature of the inverse problem. Therefore, in this study, human myocardial stiffness was extracted by identifying the normal range of the material parameters, rather than finding unique solutions.

Due to the insufficient clinical data, solving the inverse optimisation problem for fully orthotropic Hozapfel-Ogden law became very difficult. Therefore, various constraints were introduced to reduce the complexity of the problem. Inspired by previous studies (Xi et al., 2011b, 2013; Genet et al., 2014; Mojsejenko et al., 2015), the complexity of the problem was reduced by estimating a total of four parameters (a, b, Ka, Kb) instead of eight parameters. The decision was based (i.e. reduction in number of independent parameters) on the shear test results of myocardium (Dokos et al., 2002; Sommer et al., 2015a). It was observed from the experiment that the stiffness in the **f**, **s** and **n** directions would be ordered according to $f > s > n$ so that the order of shear responses in six shear modes would follow as $(fs) > (fn) > (sf) > (sn) > (ns), (nf)$ (where (ij) denoted the shear response in j direction of the plane containing i direction and $i \neq j \in f, s, n$ (Dokos et al., 2002; Holzapfel and Ogden, 2009). Comparing the analytical expression of these six shear modes, it was concluded that only four parameters would be enough to maintain such characteristics (Section 5.3.2B).

Even with the reduced set of parameters (a, b, Ka, Kb), it was not possible to find unique (globally minimum) solutions due to the ill-posed nature of the inverse problem. Also, subject-specific LV EDP and fibre-orientations were not available due to invasive measurement and technical infeasibility respectively as mentioned by Lee et al. (2013a,b); Wang et al. (2013a, 2009); Genet et al. (2014). Therefore, various studies were performed in order to identify the change in material parameters due to the change in LV EDP and fibre orientations (Section 5.4.2). The mechanical responses were similar (shear stress-strain) and within the physiological range even though the val-

ues of the parameters changed due to different EDPs and fibre-orientations. These observations agreed excellently with the sensitivity study of Wang et al. (2013a) using pig myocardium data and Holzapfel-Ogden model. One possible explanation for the similar stress-strain relationship from different parameter values of the same constitutive law is that the law is designed such a way so that I_{4f} and I_{4s} terms have major contributions in stress prediction. As the estimated parameters, that influenced these terms (I_{4f} and I_{4s}) in the Holzapfel-Ogden constitutive law, were relatively close for all the cases, the sets of the parameters yielded similar mechanical responses.

Validation of the inversely estimated parameters for each human ventricle is not feasible as it is impossible to perform mechanical tests on in vivo hearts. Therefore, stress-strain relations of a cubic myocardium under simple shear and uniaxial stretch were compared with previous studies (Wang et al., 2012; Xi et al., 2011a; Krishnamurthy et al., 2013; Genet et al., 2014). It was observed that the mechanical responses predicted using the estimated parameters (in this study) lie within the same range as in Wang et al. (2012); Xi et al. (2011a); Krishnamurthy et al. (2013) even with the differences in methods, material law, LV geometry, EDP, and fibre orientation. Gao et al. (2015) did not consider the effect of different fibre orientations on material parameters estimation. However, it was shown that the passive inflation of LV increased with the increase in helix-angle (Chapter 4). Also, the distribution of fibre stress altered due to the change in fibre structure (Chapter 4). In this study, the effect of different fibre orientations on estimated material parameters was also explored for the first time.

Although MRI tagging is able to provide in-vivo strain measurement,

this requires additional scanning time, and then perform complex image processing to calculate strain values. Moreover, MRI tagging is not a routine clinical procedure whereas performing SSFP cine CMRI is a clinical standard, and therefore readily available for any patient. Therefore, SSFP cine CMRI was used in this study. Although, LV strain can be measured even from 2D cine CMRI as described by Gao et al. (2015), it has several limitations such as difficulties in prediction out-of-plane motion, increase in uncertainties while estimating pixel-wise strain due to lack of motion tracking algorithm (Gao et al., 2015). Therefore, instead of using strain calculation, end diastolic pressure volume relation (EDPVR) of LV was used in this study. However, subject-specific measurement of EDPVR requires invasive measurement which is also not a regular clinical practice. Therefore, empirical Klotz curve was used in this study to yield pressure-volume relation of LV. The trade-off is that, while fewer data make the inverse problem more ill-posed, requirement of more subject-specific data leads to more complex and invasive clinical measurements with longer processing times, which is not always possible. Only necessary measurements (cine CMRI) are performed routinely for patients. Therefore, one of the major challenges in that study was to use standard clinical data to estimate human myocardium parameters. As shown in Section 5.4.3, the estimated value of the parameters yielded similar stress-strain results with those of other studies, which used MRI tagging and invasive measurements. However, in-vivo strain data and subject-specific EDPVR, if available in future, can easily be incorporated in the proposed method by adding new constraints.

5.6 Research Contributions

- **Development of a novel method for in-vivo estimation of passive orthotropic properties of human myocardium utilising routinely used non-invasive clinical data:**

  The study introduced a new method consisting of FE modelling, response surface method (RSM), and genetic algorithm (GA) to estimate the biomechanical properties of human myocardium using standard clinical data. However, the method is also capable of adding new subject-specific data (strain values, calculated from MRI tagging or personalised EDPVR, measured invasively) as a constraint to produce more unique solutions.

- **Reported normal range of the parameters under different conditions**

  The normal ranges of the parameters of holzapfel-Ogden model for human myocardium were estimated using routinely used clinical data. The changes in estimated parameters due to the change in ventricular geometry, end diastolic pressure and fibre orientation were also reported. It is observed that the material parameters of Holzapfel-Ogden model are highly correlated. The in-vivo estimation of human myocardium properties are less stiff compared to the traditional ex-vivo experimental results. The range of parameters could be used as a reference map for future study to accomplish subject-specific computational modelling.

5.7 Summary

In this study, subject-specific in-vivo passive material properties of human myocardium were estimated using inverse optimisation procedure. MRI measured EDV and empirical Klotz relation were used to scale the material parameters of the Holzapfel-Ogden model for five healthy human ventricles. Anatomically realistic subject-specific models of five human bi-ventricles (BVs), that employed rule based fibre-sheet orientation and a structure-based orthotropic constitutive law (Holzapfel-Ogden model), were used to simulate the passive diastolic mechanics (Section 5.3.1). FE modelling, Latin hypercube sampling (LHS), response surface method (RSM) followed by genetic algorithm (GA) based search optimisation procedures were applied to calibrate the material parameters from the original values, derived from the ex-vivo simple shear experiments of pig myocardium (Section 5.3.2D and Figure 5.3). Due to the limited clinical data, two different sensitivity studies were accomplished to identify the changes in values of the parameters with the change in EDP and fibre orientations (Section 5.4.2). Comparison of simple shear and uniaxial stress-strain relations with other studies, which inversely estimated human myocardial parameters based on different constitutive laws and EDP, showed that the estimated material parameters in this study generated similar stress-strain predictions (Section 5.4.3). The study provided the range of parameters due to the change in geometry (i.e. subject-specific), EDP, and fibre orientations. Such information could be useful for future computational study to identify the normal ranges of myocardial wall stress and strain during cardiac cycle.

Chapter 6

Modelling Passive Diastolic Mechanics of Human Ventricles

6.1 Introduction

Left ventricular (LV) remodelling, associated with diastolic heart failure (DHF), is driven by an increase in myocardial stress as mentioned in Chapter 1. Therefore, normalisation of LV wall stress is the cornerstone of many therapeutic treatments for DHF (Lee et al., 2014a; Wall et al., 2006). However, information regarding the normal ranges of the regional stress-strain distributions for human LV is still limited. Moreover, effects of LV base movement, which is more notable than the movement of apex, on diastolic model predictions were ignored in the literature. Therefore, the following research objective, detailed in Section 2.9 of Chapter 2, is addressed as follows.

Objective 4: To investigate the change in stress-strain distribution amongst the different wall locations and regions for five normal human ventricles at ED

due to the change in ventricular geometry and base movements, and subsequently, to provide a reference map of stress-strain values in healthy LV wall at ED for future computational studies.

A brief overview of the research gap and justification of setting objective 4 are discussed in Section 6.2. In addition to objective 4, objective 2 (see Section 2.5 of Chapter 2) is addressed here again to overcome the limitations of the study as detailed in Chapter 4. Personalised FE modelling of five normal human BV using subject-specific myocardium properties (identified in Chapter 5) is discussed in Section 6.3. The results and discussion are detailed in Section 6.4 and 6.5 respectively followed by the research contributions in Section 6.6.

6.2 Brief Literature Review

Majority of the passive diastolic FE models in the literature was based on either animal heart or idealised geometry of single LV (Guccione et al., 1995; Costa et al., 1996; Usyk et al., 2000; Vetter and McCulloch, 2000) (Table 6.1). With the advancement in MRI, personalised LV geometry was used for the simulation without considering RV deformation (Wang et al., 2013a, 2009; Genet et al., 2014). It was observed that the RV deformation had a significant effect on fibre stress-strain distribution of LV wall and should be considered in any ventricular modelling (Section 4.6 of Chapter 4). Furthermore, majority of the computational models used Fung-type transversely isotropic constitutive law (Guccione et al., 1995; Costa et al., 1996; Vetter and McCulloch, 2000; Wang et al., 2009; Genet et al., 2014). In contrast, simple shear test of pig (Dokos et al., 2002) and human myocardium (Sommer et al., 2015b,a) clearly exhibited

its fully orthotropic behaviour. Modified Fung-type (Usyk et al., 2000; Costa et al., 2001) and pole-zero law (Stevens et al., 2003) were used in diastolic simulation to incorporate such material orthotropy. However, the material parameters in those orthotropic models were merely used as weighting factors, rather than any physical significance (Goktepe et al., 2011), and some of these parameters were highly correlated (Wang et al., 2013a). Holzapfel and Ogden (2009) developed a constitutive law that considered the locally orthotropic tissue architecture and the parameters of this model were closely related to the characteristic micro-structure of myocardium. However, all the diastolic FE studies of human LV using Holzapfel-Ogden law used experimental data of animal myocardium, which resulted in too stiff stress-strain relation in patient-specific model, and thereby, unable to produce expected LV inflation through simulation (Wang et al., 2013a; Baillargeon et al., 2014). Moreover, all the previous diastolic simulation model of human LV used only one subject except the study conducted by Genet et al. (2014), which had the limitations of using single LV model and transversely isotropic material law (Table 6.1). Therefore, the effect of BV geometrical heterogeneity on the diastolic mechanics is still unexplored.

In majority of the FE models, kinematic constraints were typically used to fix longitudinal basal movement in order to avoid any rigid body displacement, and allowed the apex to move freely (Walker et al., 2008; Genet et al., 2014; Eriksson et al., 2013; Wang et al., 2013a). However, as suggested by Wang et al. (2009), the apex of the heart did not move considerably during diastole, as opposed to the mitral valve plane. Therefore, a comparative study was conducted to investigate the effect of base movement in diastolic model

Table 6.1: Previous work on passive diastolic modelling of LV with the key attributes and the limitations

	Single LV		Bi-ventricle (BV)		Effect of base movement
	Animal myocardium passive properties	Human myocardium passive properties	Animal myocardium passive properties	Human myocardium passive properties	
Animal ventricle/Idealised geometry	Humphrey and Yin (1989) Guccione et al. (1995) Costa et al. (1996) Vetter and McCulloch (2000) Usyk et al. (2000) Wang et al. (2009)		Stevens et al. (2003)		
Transversely isotropic	Humphrey and Yin (1989) Guccione et al. (1995) Costa et al. (1996) Vetter and McCulloch (2000) Wang et al. (2009)	Genet et al. (2014)			
Human ventricle	Wang et al. (2013a)	Genet et al. (2014)	Chapter 4	**Research Gap, addressed in this work**	
Orthotropic	Usyk et al. (2000) Wang et al. (2013a)		Stevens et al. (2003) Chapter 4		
More than one subject		Genet et al. (2014)			

predictions. As discussed above and to the best of our knowledge, no such diastolic modelling of human ventricle was conducted considering all the key attributes together mentioned in Table 6.1. Therefore, objective 4 was carried out in this study.

As explained in Chapter 4, the study regarding the effect of fibre orientation on LV diastolic mechanics (objective 2) had few limitations as follows - (a) the material parameters of porcine myocardium was used due to the unavailability of human myocardium data; (b) only one ventricular geometry was used, and therefore, the effect of geometrical heterogeneity could not be incorporated in the conclusions; and (c) the base movement was not included in the FE model. In-vivo passive orthotropic material parameters of human myocardium were identified in Chapter 5. Therefore, objective 2 was accomplished again with subject-specific human myocardium properties in order to explore the conclusions, which was obtained from the study in Chapter 4.

6.3 Materials and Methods

6.3.1 Construction of Subject-specific BV Mesh Geometry

ECG gated, breathe hold, steady state free precession (SSFP) cine CMRI was performed to capture the images of five normal human ventricles at UHCW, UK. BSREC ethics approval (REGO-2012-032) and patients' consents were obtained to carry out the research on anonymised human data. The typical scanning parameters were summarised in Table 3.1 of Chapter 3. The construction BV mesh geometry from CMRI, and subsequently, LV cavity geometry were described in Section 3.2 of Chapter 3. The ErDV, EDV, ESV and EF, calculated from CMRI of five normal human hearts (BV1 to BV5) are shown in Figure 5.1 of Chapter 5. Each BV mesh geometry composed of at least 750,000 linear tetrahedral elements (tet4) to achieve accurate results as identified from the mesh convergence study (Section 4.4.1 of Chapter 4).

The average longitudinal movement of base and apex from early (ErD) to end diastolic (ED) phase was measured from the LV cavity geometry (Figure 6.1). The LV cavity geometry at ErD and ED were extracted from their respective BV mesh geometries using the procedure detailed in Section 3.2.2 of Chapter 3. The longitudinal movement of base was then measured by calculating the distance between the planes located at the base of the ErD and ED LV cavity geometry (Figure 6.1). The same procedure was used to calculate the longitudinal movement of apex (Figure 6.1). It was observed that the longitudinal movement of base was considerably higher than the movement of apex for all five ventricles (Figure 6.2). Figure 6.3a, b and c show the early

diastolic (ErD) BV mesh geometries, early (ErD) and end diastolic (ED) LV cavity geometries respectively, constructed from subject-specific CMRI.

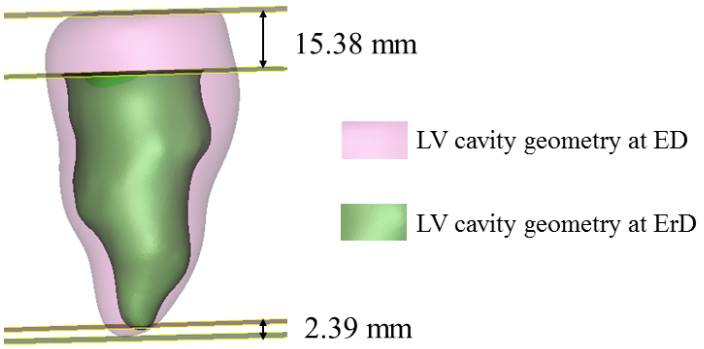

Figure 6.1: Graphical representation of the procedure to measure the average longitudinal movement of base and apex

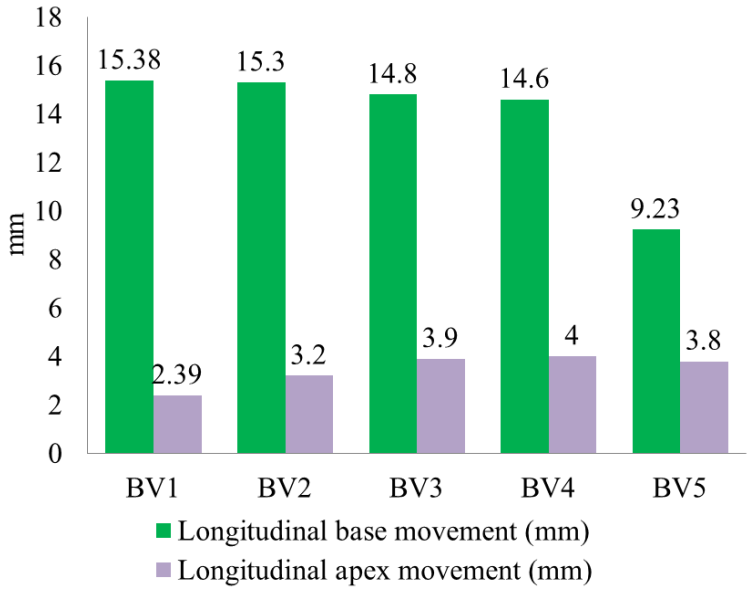

Figure 6.2: Longitudinal movement of base and apex measured for five ventricles (BV1 to BV5)

6.3.2 Construction of Rule-based Fibre Orientation

Myocardial fibre-sheet orientation was implemented by LDRF algorithm, detailed in Section 3.3 of Chapter 3. Based on the previous histological studies (Streeter et al., 1969; Arts et al., 2001), the fibre orientation was defined by a linear variation of helix angle from -70° in the sub-epicardium ($\partial\Omega_{epi}$) and RV septal endocardium ($\partial\Omega_{rvsep}$) to almost 0° in the mid-wall to $+70^{\circ}$ at sub-endocardium ($\partial\Omega_{lvendo}$) and RV free wall endocardium ($\partial\Omega_{rvfree}$) for all five ventricles (Figure 6.3d). In practice, mutually orthogonal fibre ($\mathbf{f}$), sheet ($\mathbf{s}$) and sheet-normal ($\mathbf{n}$) directions were defined at the centroid of each tetrahedral element in the mesh geometry using in-house Matlab script of LDRF algorithm. Furthermore, the local cardiac coordinates ($\mathbf{e_c}$, $\mathbf{e_z}$, $\mathbf{e_n}$), detailed in Section 3.3.1 and Figure 3.5, were defined for each element. The Green-Lagrange strain (GL) of LV wall at ED was calculated with respect to these local cardiac coordinates ($\mathbf{e_c}$, $\mathbf{e_z}$, $\mathbf{e_n}$).

6.3.3 FE Model of LV Passive Inflation

The early-diastolic BV mesh geometry, composed of four node tetrahedral elements, was constructed from the early diastolic CMRI of human ventricle. According to state-of-the-art, early diastole is assumed as initial stress free configuration since the ventricular pressure is lowest at this point, and therefore, stress is minimum (Usyk et al., 2000; Sun et al., 2009; Wenk et al., 2011a,b; Genet et al., 2014). According to previous mesh convergence study (Section 4.4.1 of Chapter 4), the number of tetrahedral elements in each ventricular mesh geometry was kept more than 750,000 to achieve reliable results. Due to the unavailability of subject-specific ventricular pressure, which required inva-

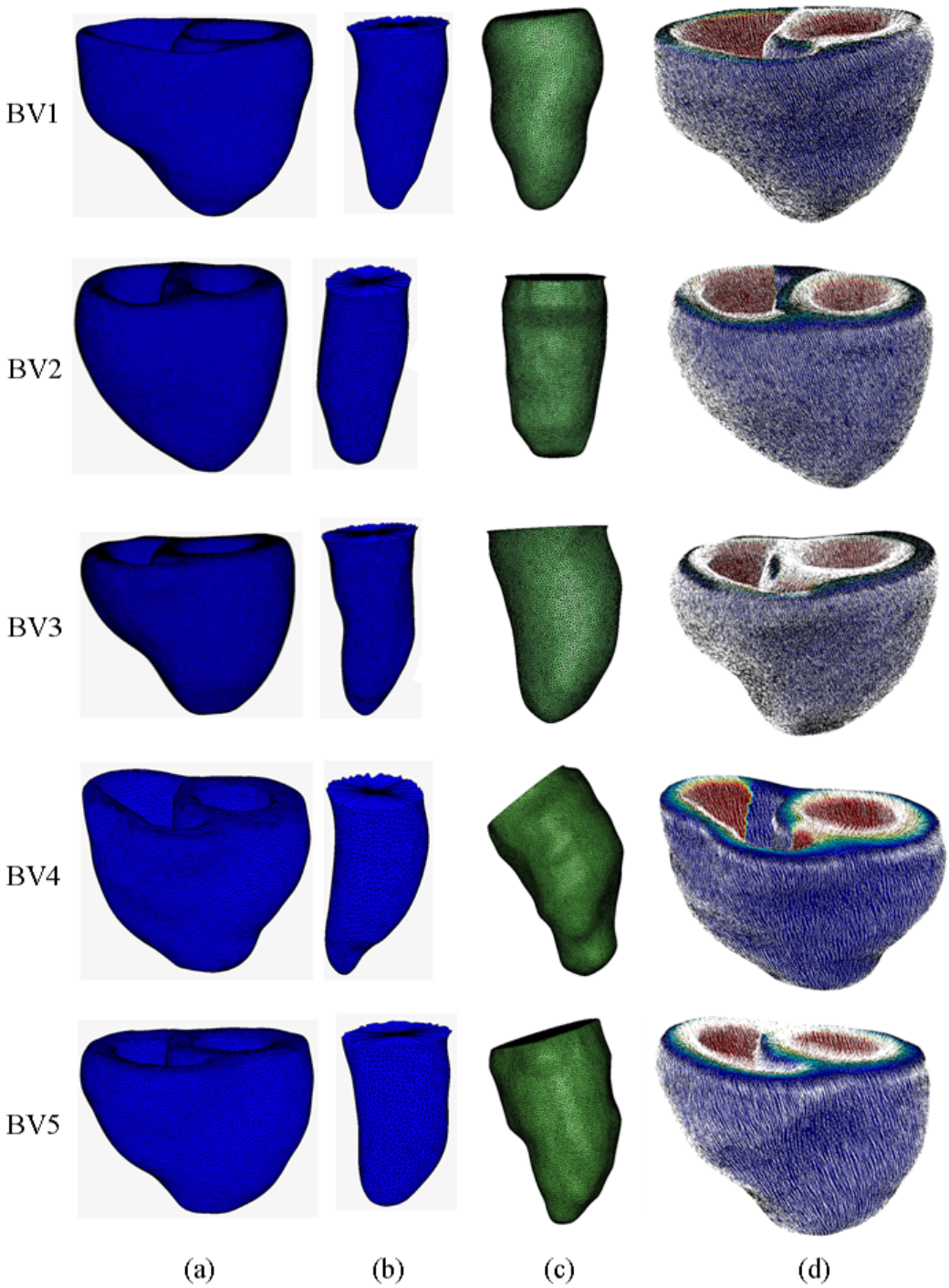

Figure 6.3: (a) Subject-specific BV mesh geometry; (b) LV cavity geometry at ErD; (c) LV cavity geometry at ED; (d) Fibre orientation using LDRF algorithm

sive measurement, LV EDP was assumed 10 mmHg (Wang et al., 2013a; Lee et al., 2013a,b; Genet et al., 2014). One third of the LV blood pressure was applied on the RV endocardium. Ventricular myocardium was characterised by Holzaphel-Ogden constitutive law (Eq. (3.17) in Chapter 3), which was implemented using a user-defined subroutine 'Hypela2' in MSC-Marc (MSC Software Corporation, California, US) utilising 'Total Lagrange' framework (Appendix B). Details of the constitutive law, FE implementation and validation procedures were discussed in Section 3.4.4 of Chapter 3. Subject-specific in-vivo passive orthotropic material parameters of human myocardium, which were already estimated in Chapter 5, were used to produce realistic LV inflation for human heart. The values of the parameters were summarised in Table 5.5 of Chapter 5.

6.3.4 Investigation Strategies

(A) Effect of Base Movement and Regional Stress-strain Distribution of LV at ED

In the natural state, the LV is surrounded by different anatomic structures such as RV, atria, pericardium, aorta and other tissues. Quantitative information on these boundary conditions is not available, yet, in order to avoid undesirable rigid body displacement, appropriate kinematic boundary conditions must be chosen in FE formulation (Dorri, 2004; Wang et al., 2009). Traditionally, the longitudinal movement of the base nodes and the circumferential displacement of epicardial wall at the base were suppressed whereas apex was set free (Genet et al., 2014; Wang et al., 2013a; Eriksson et al., 2013; Wenk et al., 2011b; Dorri et al., 2006; Lee et al., 2014a). However, as reported by

Wang et al. (2009) and observed from CMRI (Figure 6.1 and 6.2), the base movement was notably greater compared to the movement of apex during diastole. Therefore, in order to explore the effect of base movement, two cases were considered for all five BVs. Case 1 used the traditional method of constraining the longitudinal movement of base and allowing the apex to move free (Lee et al., 2014a; Wang et al., 2013a; Genet et al., 2014; Eriksson et al., 2013; Dorri, 2004; Wenk et al., 2011b). Case 2 followed the method of Wang et al. (2009) in order to include the base movement to match the data from the CMRI. Average longitudinal displacement, measured from the LV cavity geometry (Figure 6.1), was prescribed in all the basal nodes except the basal endocardial nodes. The movement of apex and the circumferential displacement of epicardial wall at base were suppressed in order to avoid any rigid body displacement (Wang et al., 2009). The accuracy in model prediction of the two cases was investigated by comparing both LV EDV and geometrical shape-volume of the LV cavity, resulting from simulation and from the CMRI data.

In order to study the stress-strain distribution of the LV wall during passive inflation, three short-axis slices were considered as follows: (a) basal (B) slice positioned 10 mm below the base; (b) equatorial (E) slice located 20 mm below the basal slice; and (c) apical (A) slice positioned 20 mm above the apex. In addition, two long axis slices were defined for the study. The s-l slice, passing through the septum and lateral wall, divided both RV and LV in the middle. The a-p slice, passing through anterior and posterior wall, divided the LV cavity in the middle. The locations of the short and long axis slices were depicted in Figure 4.4 in Chapter 4. In addition, each short-axis location (i.e.

B, E and A) was divided into four regions such as: (a) anterior (A), (b) lateral (L), (c) posterior (P), and (d) septum (S). The averages of stress-strain values along with standard deviations were measured for each short-axis location as well as for each region of a particular location of LV wall at ED.

(B) Effect of Fibre Orientation on LV Diastolic Mechanics

Two human hearts (BV1 and BV2) were selected in the study. Eight different fibre-structures were considered as follows: fibre [$\alpha 1$ - $\alpha 2$] represented a linear variation of helix angle from $-\alpha 1^{\circ}$ in the sub-epicardium ($\partial\Omega_{epi}$) and RV septal endocardium ($\partial\Omega_{rvsep}$) to $+\alpha 2^{\circ}$ at sub-endocardium ($\partial\Omega_{lvendo}$) and RV free wall endocardium ($\partial\Omega_{rvfree}$) for both BV1 and BV2, where [$\alpha 1$ - $\alpha 2$] = [30 - 30], [40 - 40], [50 - 50], [60 - 60], [70 - 70], [80 - 80], [50 - 80], [80 - 50]. Explicit definitions of each fibre set are summarised in Table 6.2.

Table 6.2: Different types of fibre orientation used in this study

	$\partial\Omega_{epi}$ and $\partial\Omega_{rvsep}$	$\partial\Omega_{lvendo}$, $\partial\Omega_{rvfree}$
fibre [30 - 30]	-30°	$+30^{\circ}$
fibre [40 - 40]	-40°	$+40^{\circ}$
fibre [50 - 50]	-50°	$+50^{\circ}$
fibre [60 - 60]	-60°	$+60^{\circ}$
fibre [70 - 70]	-70°	$+70^{\circ}$
fibre [80 - 80]	-80°	$+80^{\circ}$
fibre [50 - 80]	-50°	$+80^{\circ}$
fibre [80 - 50]	-80°	$+50^{\circ}$

As mentioned in Section 4.3.4 of Chapter 4, the sheet-normal was assumed to be aligned with local radial direction (i.e. $\beta = 0^{\circ}$) in all cases because it has very little effect on passive stress-strain distribution (Wang et al., 2013a). Each of the above mentioned fibre-orientation was assigned in early diastolic geometry of BV1 and BV2. The subject-specific material parameters for BV1

and BV2, identified in Chapter 5 (Table 5.5), were used along with the respective base movement shown in Figure 6.2. Simulation of passive inflation of LV was carried out for each set of fibre orientations while keeping the mesh geometry, boundary and loading conditions same. The end diastolic pressure volume relation (EDPVR) and fibre stress (Cauchy) were measured for each simulation to identify the variation amongst them due to the change in fibre orientation.

6.3.5 Model Validation Strategies

In order to validate the modelling approach in the study, various comparative studies were carried out. First the construction of subject-specific mesh geometry at early diastole and ED were validated by comparing the LV cavity volume from the 3D geometry with the volume calculated by radiologists. Implementation of Holzapfel-Ogden material model in FE analysis was validated by conducting standard unit and multi-element tests (Section 3.4.4 of Chapter 3). The diastolic simulation was validated by comparing the subject-specific pressure-normalise volume of LV with empirical Klotz curve (Klotz et al., 2006) (Chapter 5). Moreover, a shape-volume based validation procedure was introduced, for the first time, instead of comparing only LV EDV. Mesh geometry of LV cavity at ED, constructed from CMRI, was considered as 'original' shape. The intersected volume between 'original' and simulated geometry of LV cavity at ED was calculated in order to incorporate the geometrical-shape relevancy, and subsequently, to check the accuracy of the model predictions.

6.4 Results

6.4.1 Model Validations

The differences in LV cavity volume calculated by radiologist and from the 3D mesh geometry in the study were in the range of 3-5%. This was due to the partial volume error induced by the base movement of LV, which was not considered by radiologists during volume calculation (Section 3.2.3 of Chapter 3). Besides, a semi-automatic segmentation and wrapping operations for generating usable FE mesh approximated the LV volume calculation as explained in Section 3.2.3 of Chapter 3. The validation tests of the implementation of Holzapfel-Ogden material law in FE framework were detailed in Section 3.4.4 of Chapter 3. The passive inflation of each ventricle produced expected LV EDV at EDP (i.e. 10 mmHg) along with maintaining empirical Klotz-curve, which was measured with respect to 20 mmHg pressure point as shown in Chapter 5. Furthermore, Figure 6.6 shows that the passive inflation of LV, predicted in the study, is able to produce 85.91±2.84% shape-volume similarities when compared with the original LV cavity at ED.

6.4.2 Effects of Base Movement

For each normal BV, two separate simulations (case 1 and case 2) were carried out (as explained in Section 6.3.4A) to investigate the effect of base movement in model predictions. Three different comparisons were conducted as follows.

First, the EDV was compared by plotting the LV EDPVR for both the cases (Figure 6.4). It was observed that the base movement did not affect the EDPVR of LVs, and therefore, both cases achieved same EDV as measured

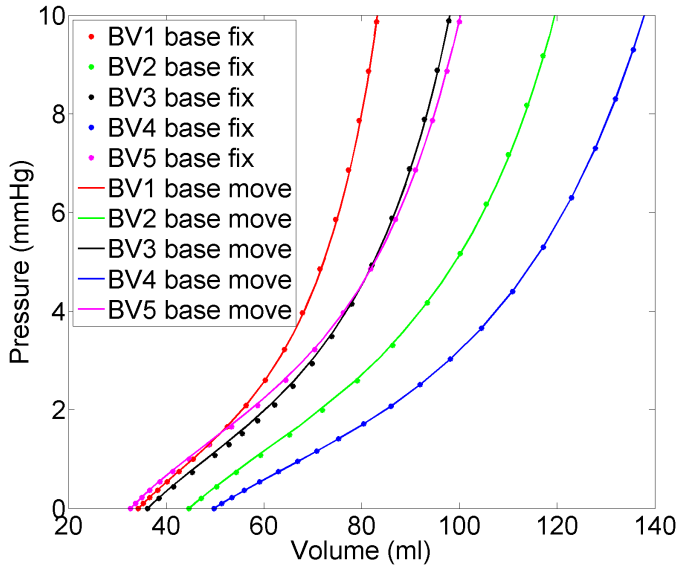

Figure 6.4: Effect of base movement on diastolic model prediction. Predicted EDPVRs of LV for each subject and for both cases (i.e. base fix vs base move) were identical

from CMRI (Figure 6.4).

Second, a shape-volume based comparison was accomplished as explained in Section 6.3.5, to compare not only the EDV but also the geometrical relevancy of the model predicted LV cavity. 'Original' mesh geometry of LV cavity at ED, constructed from CMRI, was compared with the LV ED cavity geometry, resulted from the simulation. As shown in Figure 6.5, the shape-volume comparison was carried out by calculating the intersected volume between 'original' and simulated LV cavity at ED for both the cases. Although both the cases produced same LV EDPVR (Figure 6.4), the percentage of intersected volume was more for case 2 for each subject (Figure 6.6). The higher percentage of intersected volume with respect to 'original' LV cavity geometry (85.91±2.84% in case 2 compared to 70.72±4.05% in case 1) indicated that the inclusion of the base movement in FE model resulted better shape-volume

prediction.

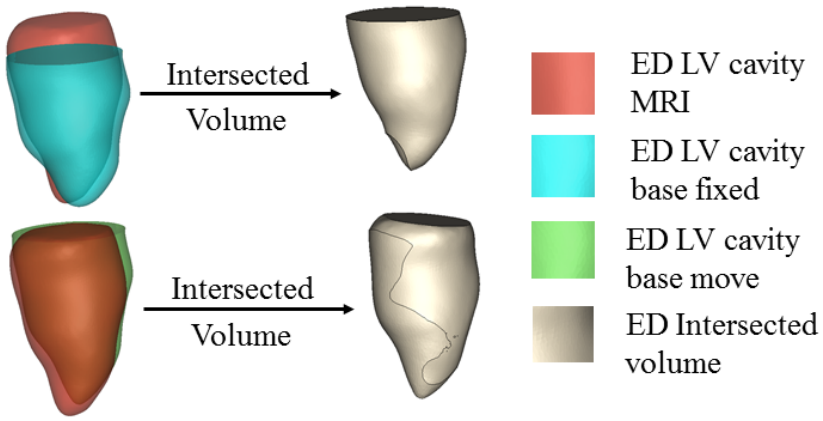

Figure 6.5: Procedure to calculate intersected volume to incorporate the shape-volume relevancy of LV cavity at ED

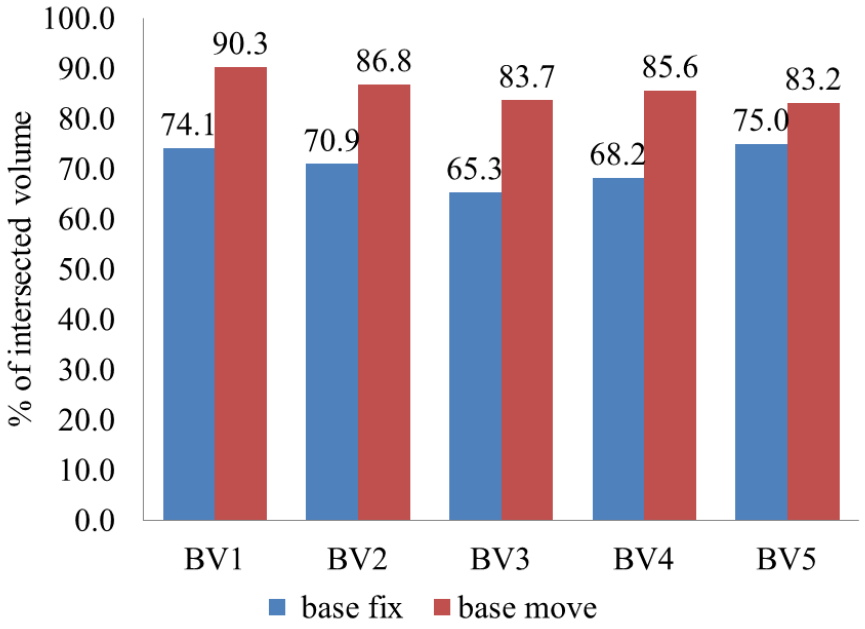

Figure 6.6: Percentage of intersected volume between original and model predicted LV cavity at ED for all fire BVs

Third, a qualitative comparison in fibre stress-strain distribution in LV wall (BV1) at ED for both cases was carried out (Figure 6.7). It was identified

that the fibre stress distribution pattern was almost same for both the cases in basal and equatorial locations. However, close inspection indicated that the anterior region of basal and equatorial locations and LV endocardium were experienced higher fibre stress in case 2 than case 1. The fibre stress distribution at apical location was completely different between the cases as evident from apex, s-l and a-p locations of Figure 6.7. Moreover, the entire LV wall experienced higher fibre strain in case 2 although the strain distribution patterns were almost similar in basal and equatorial locations.

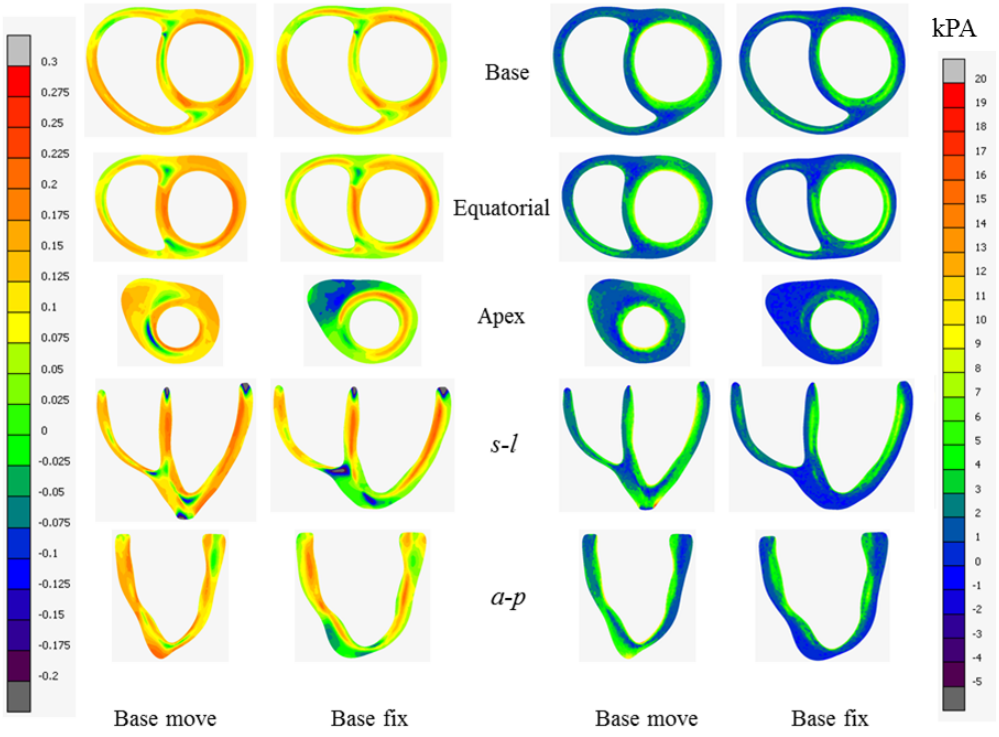

Figure 6.7: Comparison between the model predictions (fibre stress and strain), generated by two cases (base move vs base fix) for BV1. The location of the images were described in Figure 4.4

6.4.3 Stress-strain Amongst the Different Wall Locations

Figure 6.8 shows the distribution of fibre stress (Cauchy) in three short-axis (B, E and A) and two long-axis (*s-l* and *a-p*) locations. It was observed that the LV endocardium experienced high fibre stress compare to epicardium. Although the stress distribution patterns almost similar, regional differences existed amongst them.

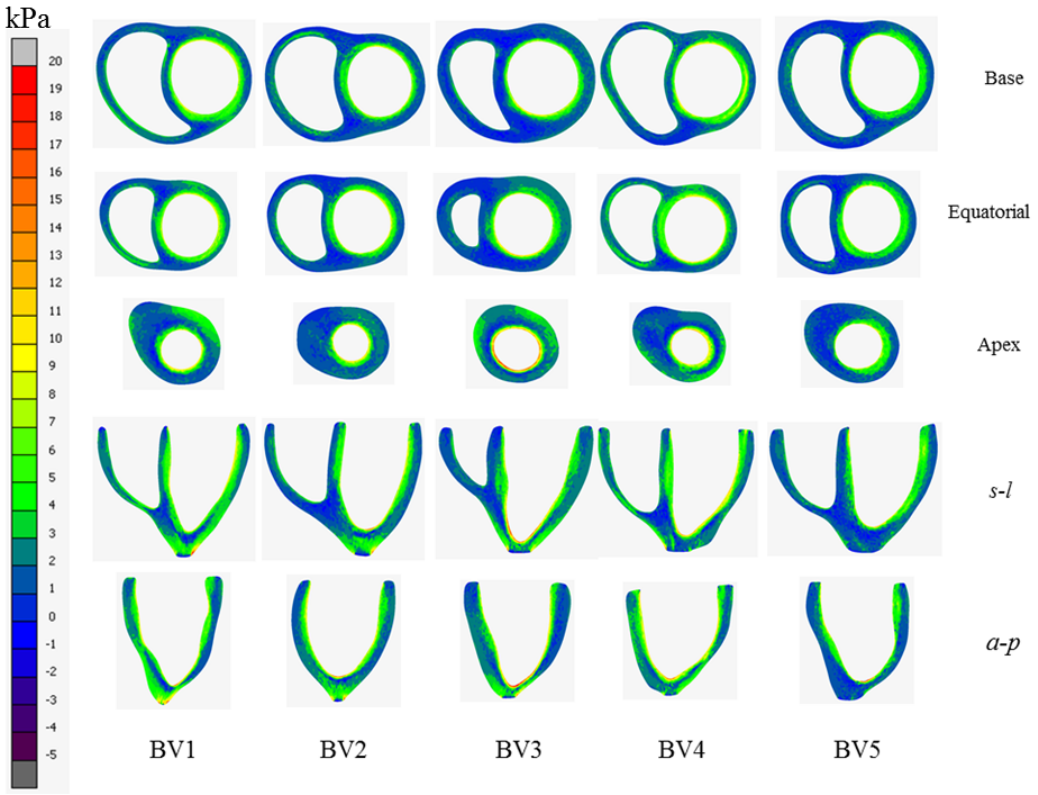

Figure 6.8: Subject-specific fibre stress (Cauchy stress) at three short axis and two long-axis locations described in Section 6.3.4A

For more detailed analysis, mean Cauchy stresses and Green-Lagrange (GL) strains in each location were calculated for all five ventricles (Figure 6.9 and 6.10). The average fibre stress (ff) was slightly higher in the equato-

rial location compared to the basal and the apical locations (except for BV3) although the differences amongst them were not considerable (Figure 6.9a). Both sheet (ss) sheet-normal (nn) stresses were greater in the basal location and minimum in the apical location for all five ventricles (Figure 6.9). Variations (or range) in fibre (ff) and sheet (ss) stress distributions in the apical location were higher compared to the basal and the equatorial locations (Figure 6.9b). In contrast, the variation in sheet-normal (nn) stress was more in the basal location. The average fibre stress (ff) at ED was greater in comarison with sheet (ss) and sheet-normal (nn) stresses in all the locations. The range of fibre, sheet and sheet-normal stresses were approximately in the range of 0 to 6 kPa, -1.5 to 1.5 kPa and -1 to 5 kPa respectively for all locations (Figure 6.9b). fs, sn and fn shear stresses were in the range of -1 to 1 kPa, -0.4 to 0.4 kPa and -0.05 to 1 kPa respectively (not shown in figure).

Figure 6.10 shows the average Green-Lagrange (GL) strain with standard deviation with respect to the local cardiac coordinate ($\mathbf{e_c}$, $\mathbf{e_z}$, $\mathbf{e_n}$) in three short-axis locations. The definition of local cardiac coordinate ($\mathbf{e_c}$, $\mathbf{e_z}$, $\mathbf{e_n}$) or ($\mathbf{c}$, $\mathbf{l}$, $\mathbf{r}$) was described in Section 3.3.1 and Figure 3.5. The circumferential (cc) and radial (rr) strains were higher in the base and the equatorial locations in comparison with the apical location for all five ventricles, whereas the longitudinal (ll) strain was higher in apical location and lowest in equatorial location (Figure 6.10a). The circumferential GL strain, ranged in between -0.1 to 0.5, was greater in all the locations compared to longitudinal (ll) and radial (rr) strain, both of which were in the range between 5% to 30% (Figure 6.10b).

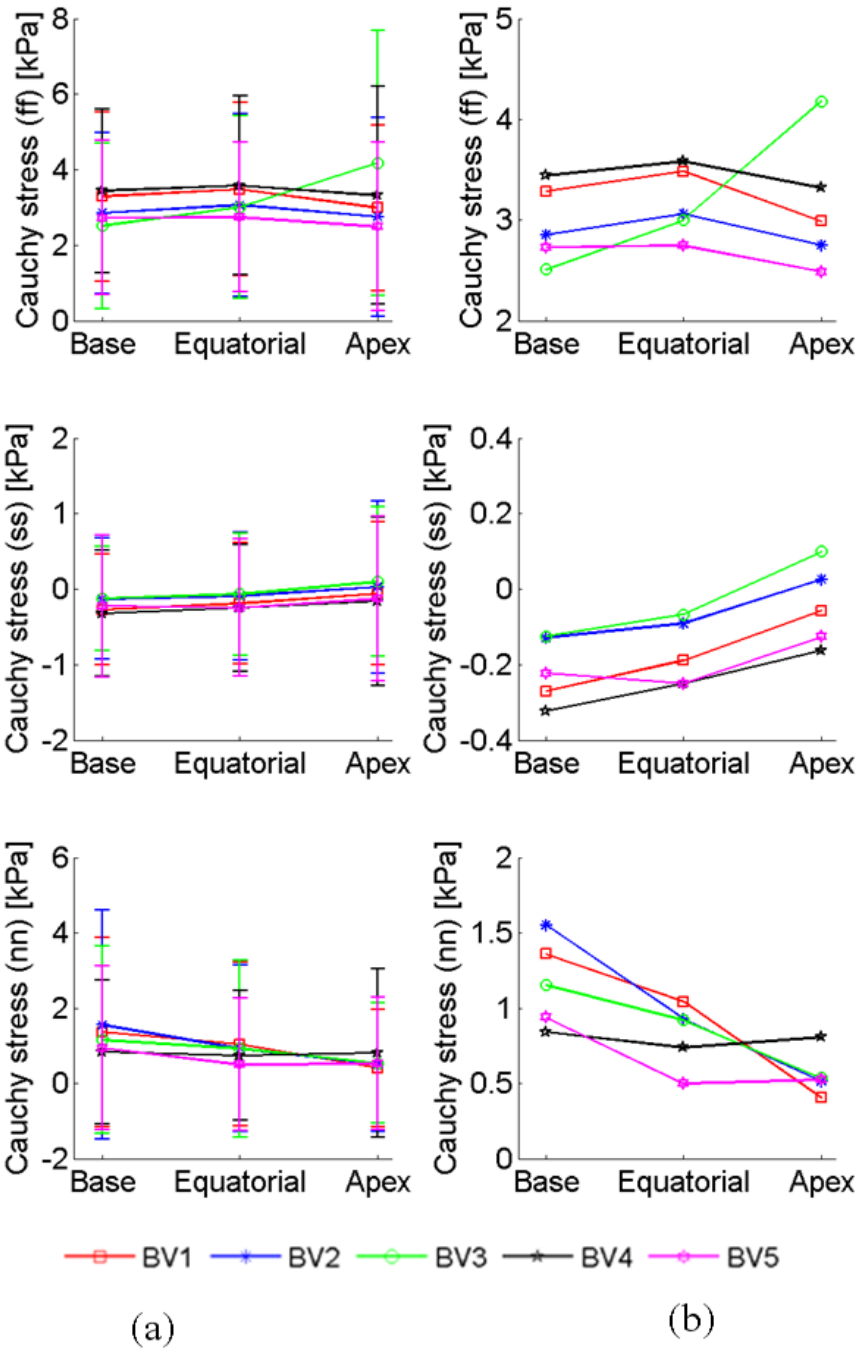

Figure 6.9: (a) Average values with standard deviations, and (b) average values only of the fibre (ff), sheet (ss) and sheet-normal (nn) stresses at base, equatorial and apical locations of each BV

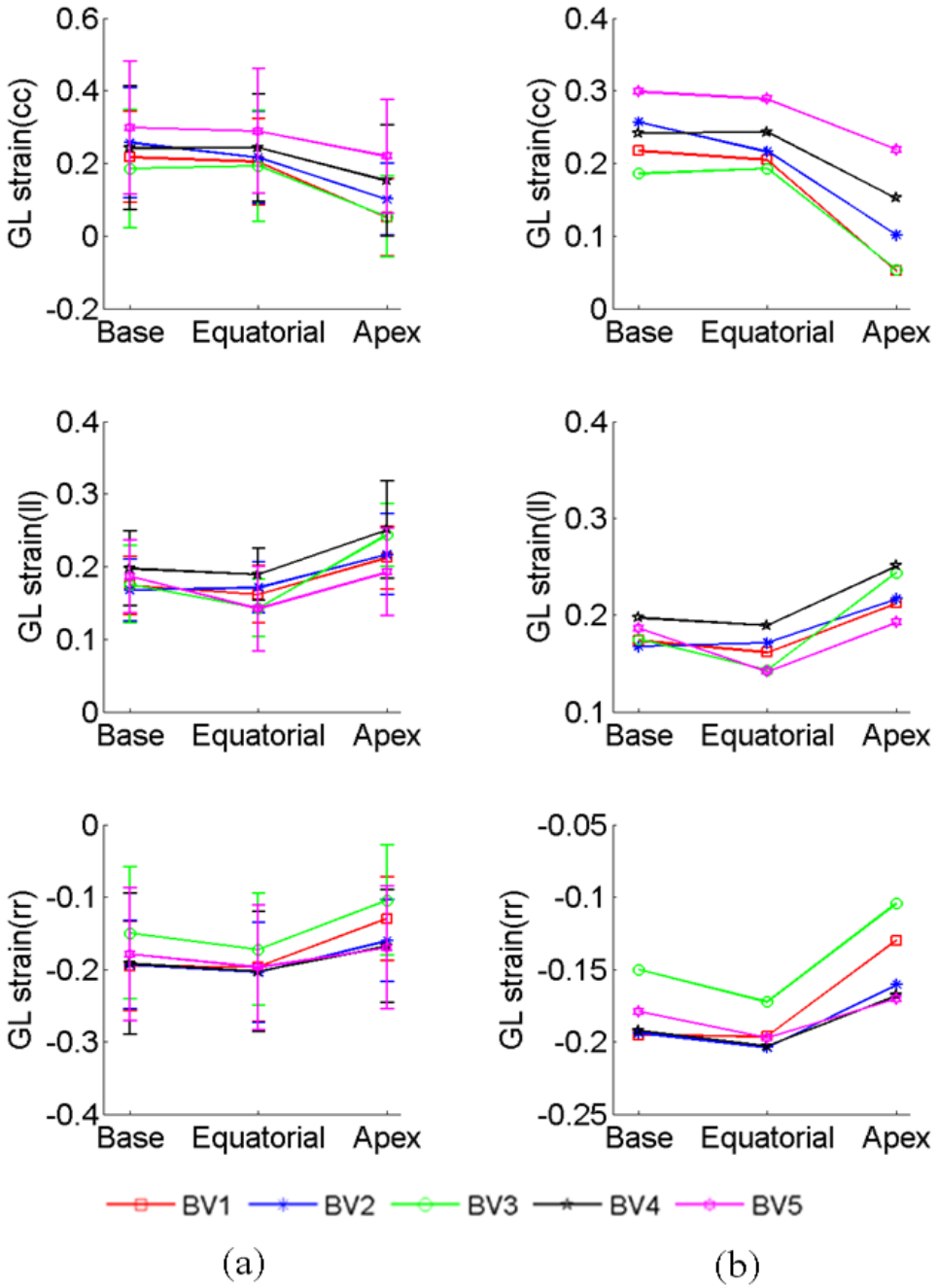

Figure 6.10: (a) Average values with standard deviations; and (b) average values only of the circumferential (cc), longitudinal (ll) and radial (rr) strains at base, equatorial and apical locations of each BV

6.4.4 Stress-strain Amongst the Different Wall Regions

The average stress-strain values with standard deviations were measured (Figure 6.11 to 6.14) in each of the four regions (A, L, P, S) for each short-axis location (B, E, A) to identify the regional variation amongst them (see Section 6.3.4 for the definition of regions and locations).

The lateral (L) region of LV in all the short-axis locations experienced comparatively higher fibre stress (ff) for all five ventricles (except BV4 in the equatorial location) whereas the septum wall (S) in the apical location experienced lower fibre-stress. Compressive sheet stress (ss) was greater in the lateral (L) region of the equatorial and the apical locations (Figure 6.12). Sheet-normal (nn) stress was higher in the posterior (P) region of the equatorial location, whereas the lateral (L) wall experienced comparatively lower sheet-normal stresses for all the ventricles (except BV3). The variations in sheet and sheet-normal stresses amongst the regions in the basal location for different ventricles were considerably higher. Moreover, the variation in fibre-stress amongst the regions was less in the base and the equatorial locations compared to the variation in the apical location. The ranges of stress values experienced by different regions of LV wall in different short-axis locations are shown in Figure 6.11.

High circumferential (cc) GL strain was experienced by the lateral wall at the basal location, and the posterior region of the equatorial and the apical locations (Figure 6.14). The anterior and the septum wall received comparatively lower circumferential GL strain. The longitudinal (ll) GL strain was less in the posterior region of the base and the equatorial locations. Compar-

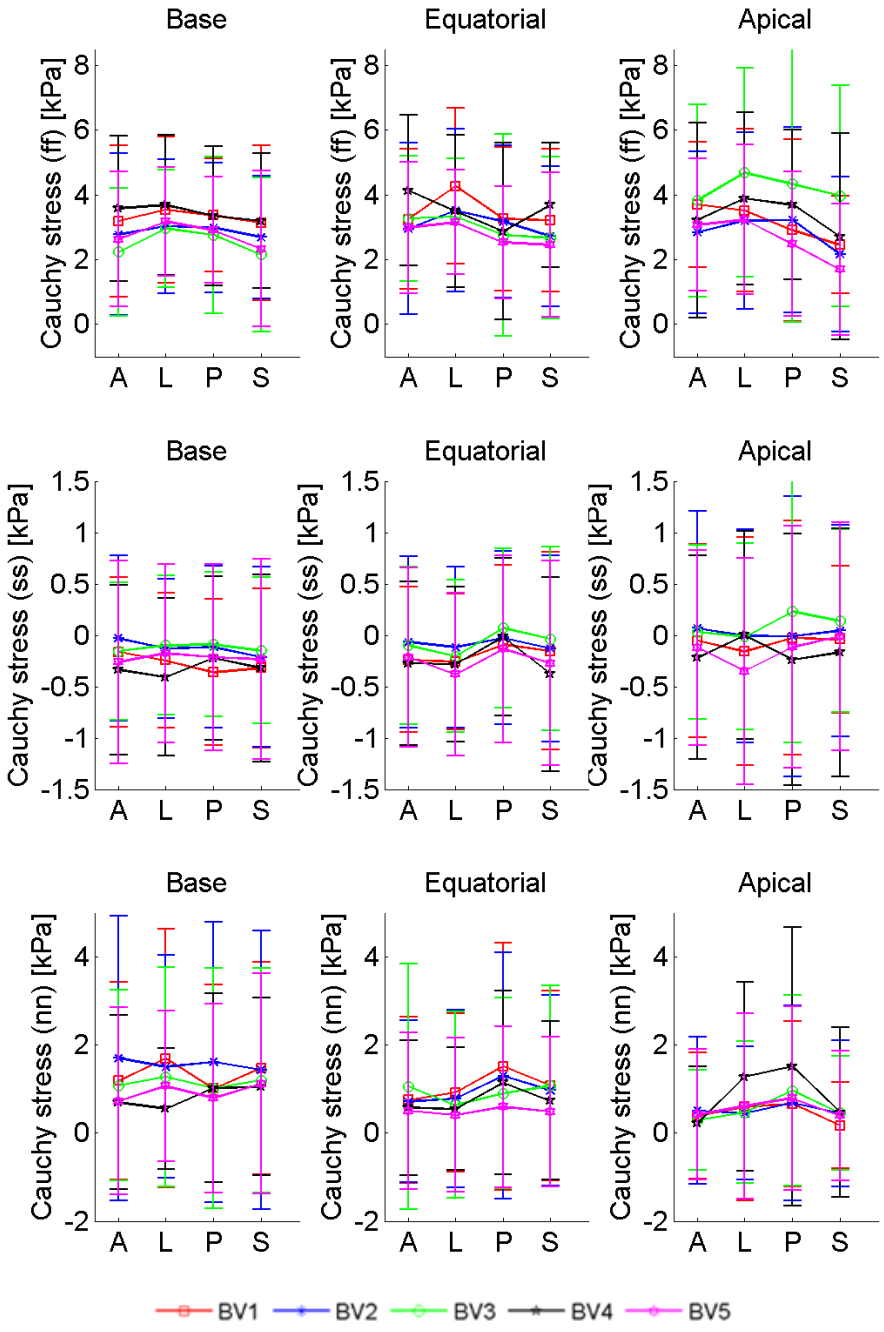

Figure 6.11: Average values with standard deviations of the fibre (ff), sheet (ss) and sheet-normal (nn) stresses at anterior (A), lateral (L), posterior (P) and septum (S) regions of each locations (i.e. base, equatorial and apical) of each BV

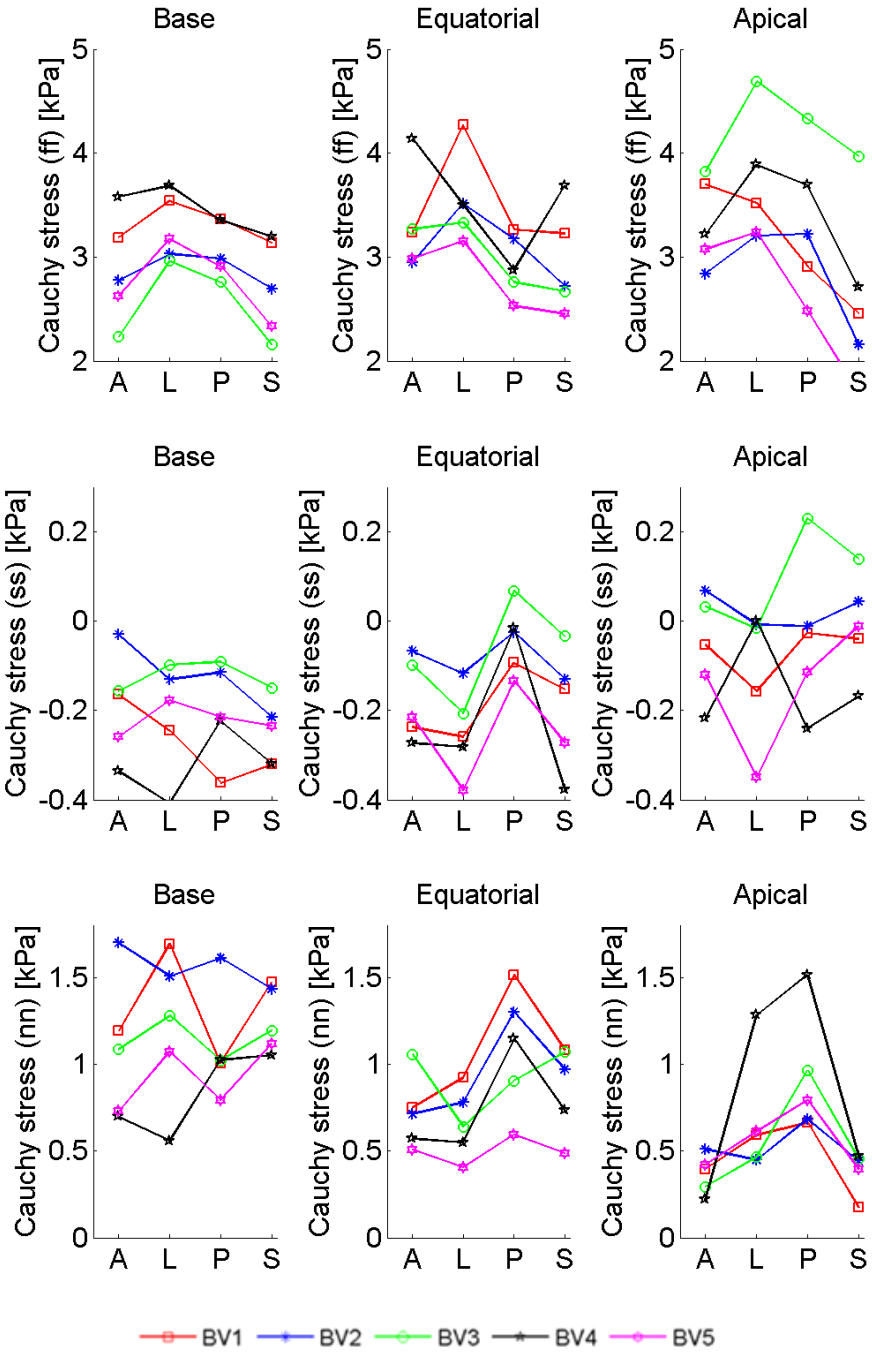

Figure 6.12: Average values only of the fibre (ff), sheet (ss) and sheet-normal (nn) stresses at anterior (A), lateral (L), posterior (P) and septum (S) regions of each locations (i.e. base, equatorial and apical) of each BV

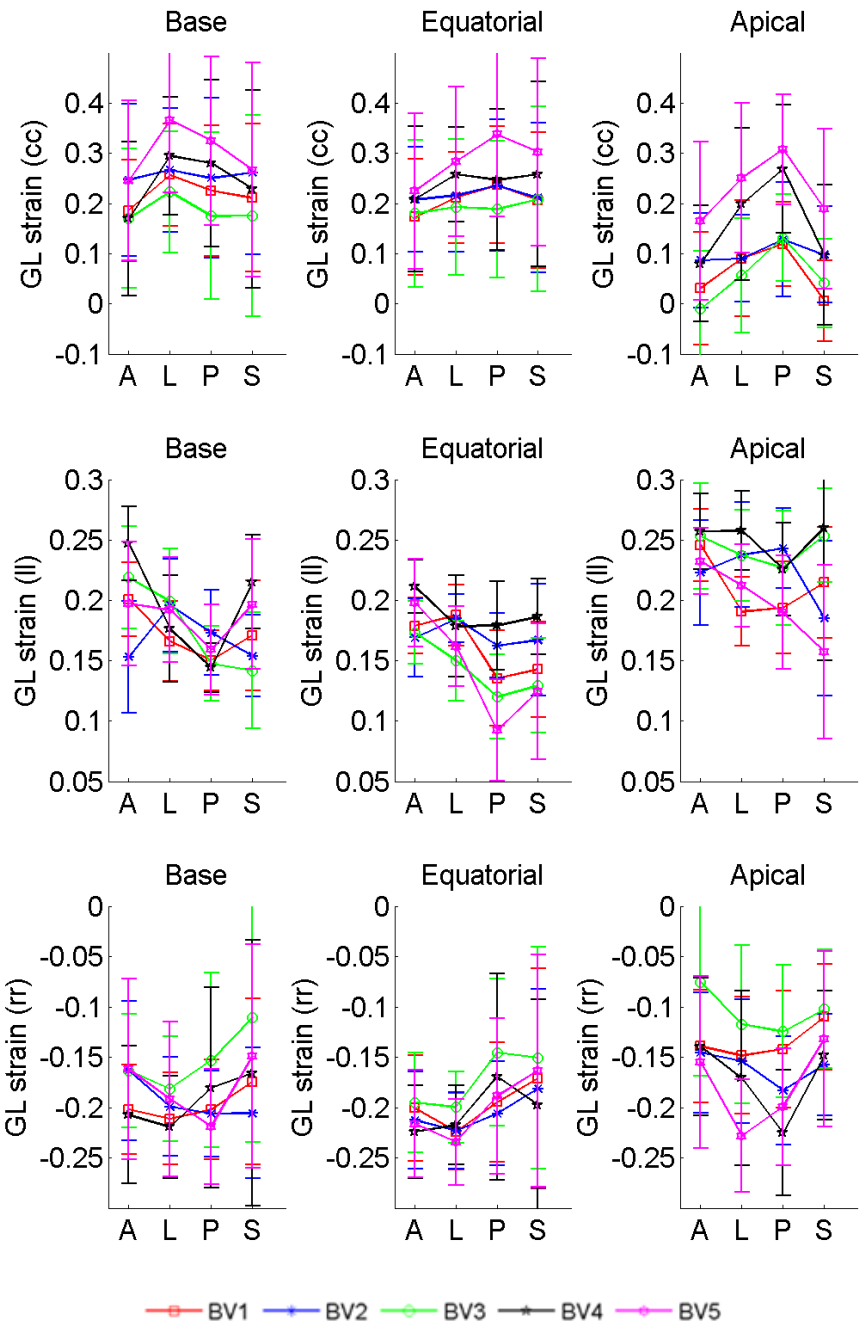

Figure 6.13: Average values with standard deviations of the fibre (ff), sheet (ss) and sheet-normal (nn) strains at anterior (A), lateral (L), posterior (P) and septum (S) regions of each locations (i.e. base, equatorial and apical) of each BV

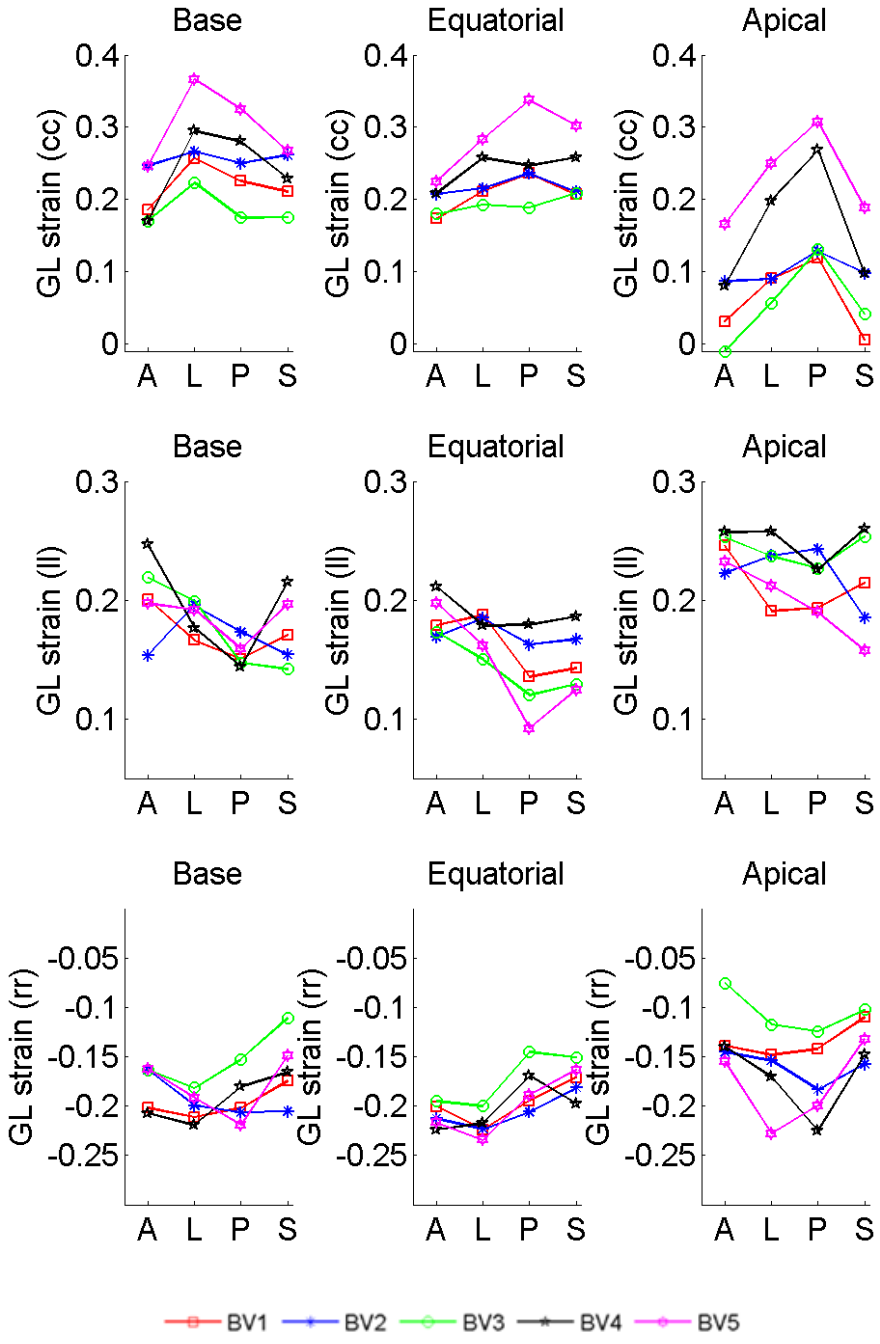

Figure 6.14: Average values only of the fibre (ff), sheet (ss) and sheet-normal (nn) strains at anterior (A), lateral (L), posterior (P) and septum (S) regions of each locations (i.e. base, equatorial and apical) of each BV

atively less radial (rr) GL strain was experienced in the septum region of all the locations for all five ventricles (except BV4 in equatorial). The ranges of different GL strain components are plotted in Figure 6.13.

6.4.5 Effect of Fibre Orientation on LV Diastolic Mechanics

Effect of fibre orientation on (A) EDPVRS of LV and (B) fibre stress distribution of LV wall was investigated again. Details of the results are shown in the following sections.

(A) Effect of Fibre Orientations on EDPVRs of LV

When $\alpha 1 = \alpha 2$, the LV EDV increased with the increase in fibre angle [$\alpha 1$ - $\alpha 2$] for same LV EDP (Figure 6.15a and 6.15c) . Figure 6.15b and 6.15d show the effect on EDPVRs of LV when the fibre angles in epicardium and endocardium are different (i.e. $\alpha 1 \neq \alpha 2$). It was observed that the EDV was always less for fibre angle [50-80] compared to the EDV for [80-50] (Fig. 6.15b and 6.15d). In addition, the EDVs achieved for [50-80] and [80-50] were in between the EDVs produced for [50-50] and [80-80]. However, the EDPVR for [50-80] was very close to the EDPVR of LV when fibre angle was 50° (i.e. when $\alpha 1 = \alpha 2 = 50°$). Although, the EDPVRs were different for BV1 and BV2, the effects of fibre orientation on EDPVRs were similar.

Figure 6.16 shows the percentage change in LV EDV with respect to actual EDV, measured from CMRI. The actual EDV was achieved for both ventricles when fibre angle was assumed 70° (i.e. [70-70]) while calibrating the human myocardium parameters (Chapter 5). The absolute value of percent-

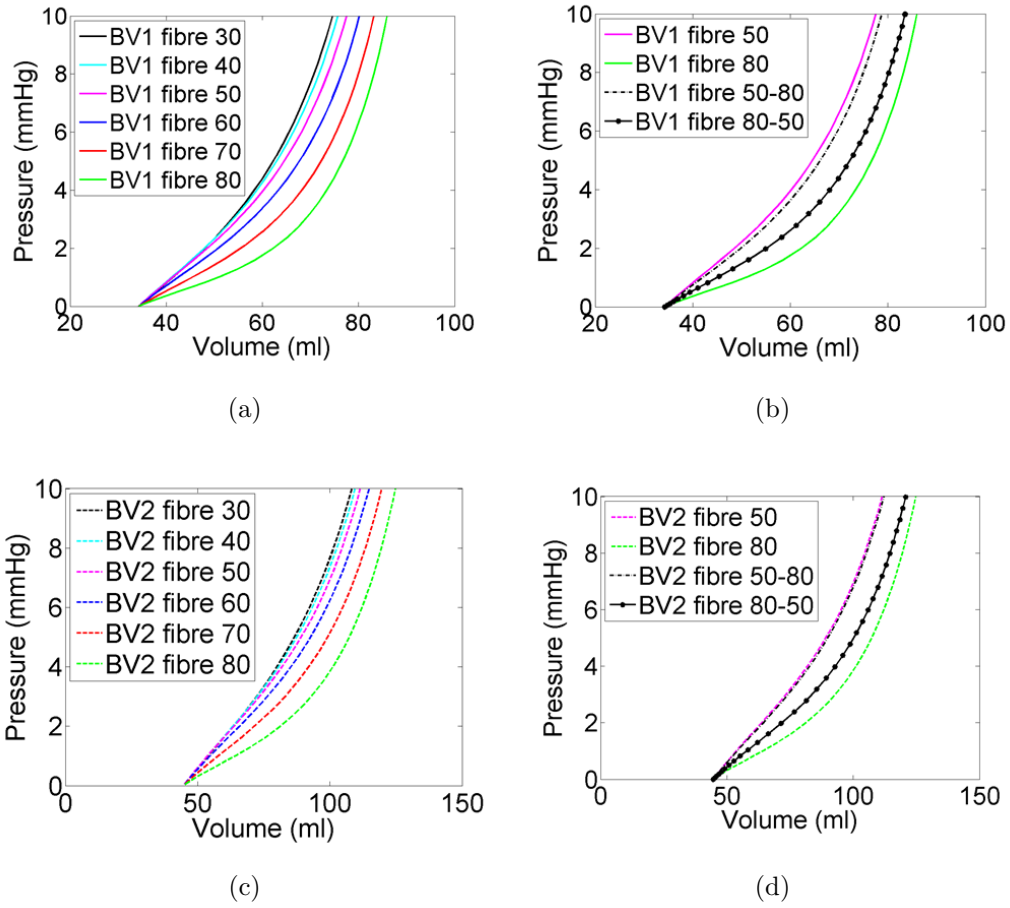

Figure 6.15: Change in EDPVRs of LV for BV1 and BV2 with the change in fibre orientations

age change in LV EDV was more when fibre angle increased to 10° (i.e. 80°) compare to the same decrease (i.e. 60°) from 70° (Figure 6.16). It was observed that [50-80] fibre-angle reduced the LV EDV whereas [80-50] increased it. The results were further explored for LV pressure of 20 mmHg as LV filling pressure reaches to this level in HF and similar effects of fibre orientation on LV EDPVRs were observed.

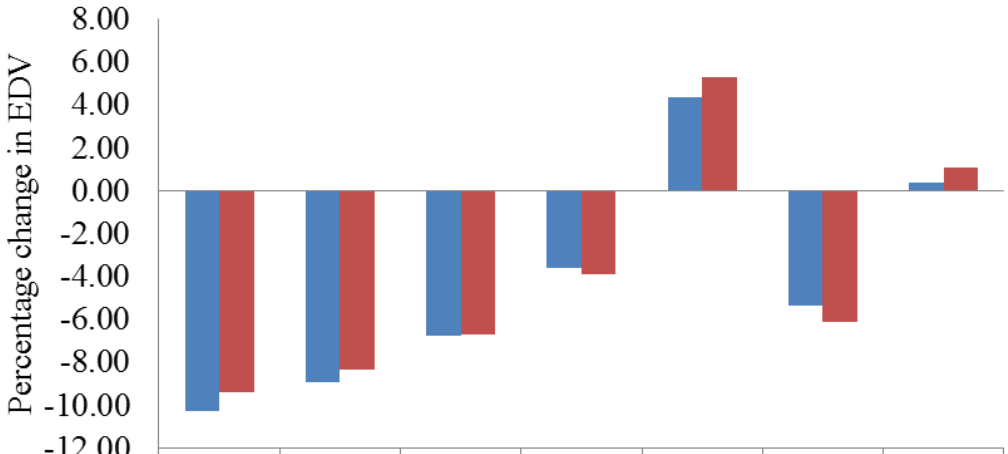

	fibre 30-30	fibre 40-40	fibre 50-50	fibre 60-60	fibre 80-80	fibre 50-80	fibre 80-50
BV1	-10.29	-8.98	-6.76	-3.60	4.32	-5.36	0.38
BV2	-9.40	-8.36	-6.70	-3.89	5.29	-6.15	1.08

Figure 6.16: The percentage change in EDV with respect to the actual EDV, measured from CMRI, due to the change in fibre angle. The actual EDV was achieved for both ventricles when fibre angle was assumed [70-70] (Chapter 5)

(B) Effect of Fibre Orientations on Fibre Stress Distribution of LV Wall

From Figure 6.17, it is observed that the transmural distribution of fibre stress from the base to the apex changes considerably for higher fibre orientation (i.e. for 60° to 80°) compared to such changes for small fibre angle (i.e. for 30° to 50°). The fibre stress in the endocardium was higher in comparison with the epicardium for all fibre orientations. However, the mid-wall to the endocardium experienced higher fibre stress for fibre angle 60° to 80° (i.e. for [60 -60], [70 - 70] and [80 - 80]), and the regions of high fibre stress were gradually confined to near endocardium with the decrease in fibre angle below 50° (i.e. for [30 - 30], [40 - 40], and [50 - 50]). These changes were more prominent for the equatorial location. Also, the anterior and the lateral wall

of the equatorial and the apical locations experienced higher fibre stress for fibre angle more than 70° (i.e. for [70 - 70] and [80 - 80]) (Figure 6.17A, a-p, s-l). The fibre stress were mostly in the range of 0 to 7 kPa for all fibre orientations. Similar results were also observed for BV2, and therefore, are not shown here.

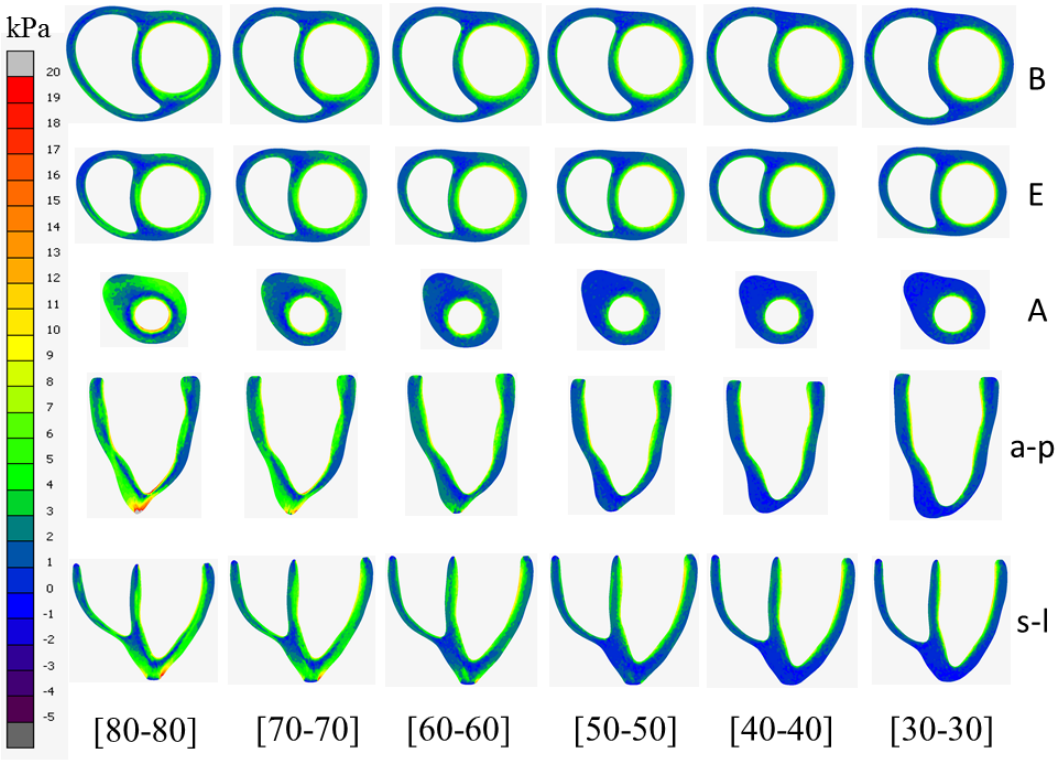

Figure 6.17: Effect of different fibre orientations on the fibre stress (Cauchy) distribution patterns of LV wall at 10 mmHg LV cavity pressure for BV1; B : Basal, E : Equatorial, A : Apical, a-p : Anterior-Posterior, s-l : septum-lateral; the definition of the locations are described in Section 6.3.4A

The fibre stress distributions for [50-80] and [80-50] are shown in Figure 6.18. For comparison, the results from the fibre orientations [80-80] and [50-50] are also included in Figure 6.18. For [50-80], the anterior and the lateral regions of the LV wall were experienced higher fibre stress compared to the results from [80-50]. The fibre stress distribution for [50-80] was similar to the

[80-80] whereas the results for [80-50] and [50-50] were close.

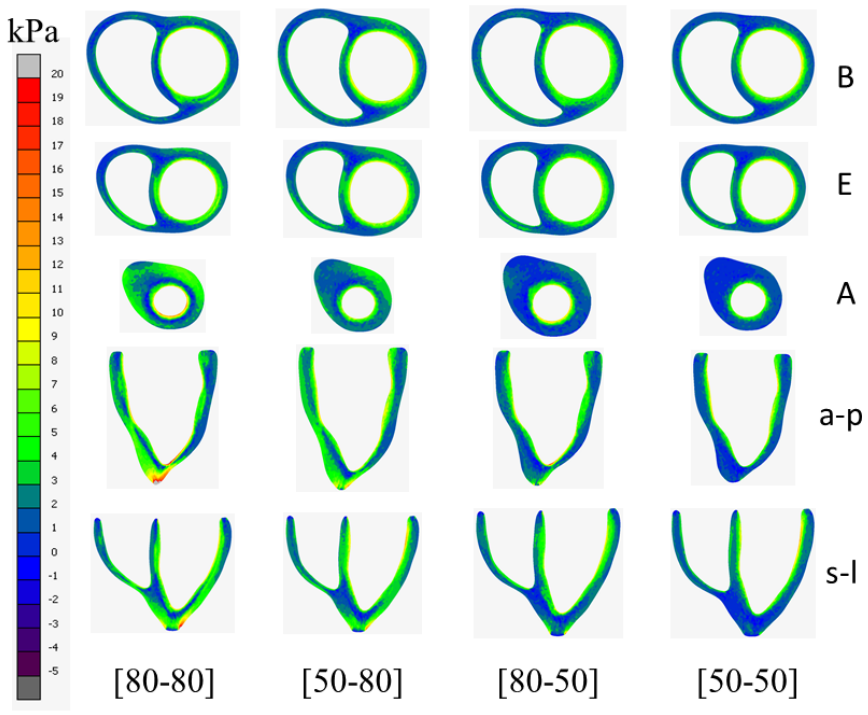

Figure 6.18: Effect of different fibre orientation on the fibre stress (Cauchy) distribution patterns of LV wall during passive inflation at LV EDP for BV1

6.5 Discussion

6.5.1 Comparison with State-of-the-Art

For the first time, subject-specific passive diastolic modelling of human LV was carried out using subject-specific passive orthotropic material properties of human myocardium and bi-ventricular model. The diastolic simulation was accomplished for five human ventricles in order to investigate the effect of base movement and geometrical heterogeneity on the regional variation in stress-strain distribution of LV wall. Several improvements were incorporated in the present study over state-of-the-art to provide more accurate model prediction. Firstly, right-ventricle (RV) was included in the model by using BV geometries in order to consider the effect of RV deformation. As reported in our previous study in Chapter 4, inclusion of RV deformation in the computational model not only changed the stress-strain distribution pattern (especially for fibre and sheet stress-strain) but also increased average values of stress-strain in LV wall during diastole. The changes were more significant near the basal and the equatorial locations compared to the apical location (Figure 4.16 of Chapter 4). Most of the previous studies of diastolic modelling (Wang et al., 2009, 2013a; Genet et al., 2014) used only single LV geometry, and therefore, the effects of RV deformation were not considered. Secondly, fully orthotropic in-vivo passive material properties for human myocardium were used instead of transversely isotropic properties used previously (Genet et al., 2014). The passive material properties, used in this study, were consistent with the observed shear stiffness characteristics of myocardium and empirical EDPVR (Klotz-curve) of LV as detailed in Chapter 5. Thirdly, the base movement was included in the model to predict more accurate shape-volume changes of LV

cavity during diastole. Although Wang et al. (2009) included base movement in their model, the effect of base movement was first investigated in this study. Fourthly, a new shape-volume based validation procedure was introduced to explore the model prediction accuracy. It was found that only volume based validation of computational diastolic model, as used in previous studies (Genet et al., 2014; Walker et al., 2005; Lee et al., 2013a), would not be sufficient and therefore, shape relevancy must be considered during model validation. Finally, for the first time, the distributions and variations of the fibre (ff), sheet (ss) and sheet-normal (nn) stresses and related shear components amongst different wall regions and locations of the five ventricles were reported. Also, each component of GL strain (with respect to local cardiac coordinate) in LV wall at ED was presented in the study. Such values of different stress-strain components could be used as a target for in-silico design of new surgical patch or passive constraint for heart failure patients.

The effects of different fibre orientations on diastolic mechanics of human LV were investigated again to overcome the limitations of our previous study as detailed in Chapter 4. The improvement of this study compared to the previous drawbacks as follows. Firstly, subject-specific material properties of human myocardium were used instead of pigs material properties as described in Chapter 5. Secondly, the effect of base movement, indispensable for physiologically realistic deformation (Section 6.4.2 and Figure 6.6), was included in this study. This movement was not considered in the previous study. Thirdly, the effect of fibre orientation was investigated for two human hearts with their specific myocardium properties to ensure robust and generalise conclusions. Finally, two more fibre orientation sets ([50 - 80] and [80 -

50]) were considered to investigate whether the effect of the fibre orientation depends on the locations.

6.5.2 Effect of Base Movement

In this study, a detailed comparison was carried out to identify the effect of the base movements, which was not considered in the majority of previous computational studies on diastolic mechanics (Genet et al., 2014; Wang et al., 2013a). The EDPVRs of LV did not alter due to the inclusion of the longitudinal base movement, and therefore, same subject-specific EDV was achieved for both the cases. However, from shape-volume based comparison, it was observed that the model prediction matched better (85.91±2.84% compared to 70.72±4.05%) with MRI derived 'original' geometry, when the longitudinal movement of the base was included in the model. In addition, including the base movement increased the average fibre strain in the LV wall, and introduced high fibre stress in the endocardium and the apical locations. These observations indicated two aspects which should be incorporated in future computational studies of cardiac mechanics. Firstly, the longitudinal base movement should be included in the model, otherwise the model would provide accurate volume estimation with inaccurate geometrical shape. Furthermore, the systolic simulation, based on the results of ED, would also lead to inconsistent geometrical shape and inaccurate stress-strain estimation if base movement was not considered. Any surgical simulation with such inconsistency could lead to inaccurate model prediction, and thereby, lead to the selection of wrong surgical treatment. Secondly, the traditional method of validating diastolic model prediction by comparing only LV EDV (Genet et al., 2014; Lee et al.,

2013a), measured from MRI, would not be sufficient enough to generate accurate model estimation. Future studies should compare the geometrical shape as well to provide more precise model estimation for diastole and systole.

6.5.3 Stress-strain Amongst the Different Wall Locations and Regions

It was identified that the endocardium region experienced high fibre stress compared to the epicardium of LV wall. The observation was consistent with the results reported by Genet et al. (2014). In contrast, the mid-wall of the LV underwent greater fibre stress in comparison with the epicardium and the endocardium wall as reported by Wang et al. (2013a) and in Section 4.4.4 of Chapter 4, which was predicted using pig's myocardium properties and when fibre angle was $\pm 70^{\circ}$ or more. This inconsistency indicated the requirement of subject-specific myocardium properties in a computational model in order to predict accurate stress-strain distribution of ventricular wall. There was no evidence of any correlation between the stress-strain distributions with the increase of EF . Although the average fibre stress was comparatively higher in the equatorial location compared to the base and the apical locations, the differences were not considerable. Furthermore, the sheet and sheet-normal stresses and circumferential strain were higher in the base location in comparison with the equatorial and the apical locations of LV. Therefore, it was concluded that the LV wall near the basal location experienced higher stress-strain. In addition, a detailed analysis of regional stress-strain distribution was carried out to identify the highly stressed regions of LV wall during diastole. It was identified that the lateral wall of LV experienced higher fibre and sheet

stress as well as circumferential strain, although the sheet-normal stress was lower in the lateral wall compared to the other regions. Those results were mostly consistent for all five normal human ventricles. Three way ANOVA test was performed in SPSS statistical packages (IBM Corporation) to determine the significance of the differences in each stress/strain component amongst the three factors (i.e. 5 BV Geometries, 4 regions and 3 locations of each geometry). The nodal stress-strain values, extracted from MSC Marc, were used in this study. However, due to the large number of nodes (≥ 800) in each region and location, the sample size became very high for ANOVA test. As a result, all the tests led to significant differences at 95% and 99% confidence level even with small variations. Therefore, the ranges of stress-strain values for each region and location are illustrated in Figures 6.9 to 6.14 instead of showing statistical significance. Such information can be used as a reference map for diastolic stress-strain distribution patterns for healthy LV wall. Any alteration in such distribution patterns amongst the regions could lead to diastolic heart failure, and consequently, ventricular remodelling. In addition, the LV remodelling process is thought to be driven by an increase in ventricular wall stress (Lee et al., 2014a; Wall et al., 2006). The surgical interventions, which include the use of hydrogel injection (Lee et al., 2013a), anisotropic reinforcement (Fomovsky et al., 2012), Cardiokinetix Parachute device (Lee et al., 2014a) , and Cardiac Support Device (Wenk et al., 2013), aim to reduce the stress in LV wall and bring it back to the normal range at ED and ES. The study not only identified the fibre stress, but also reported the different components of stress and strain amongst the different locations and regions of the LV wall at ED for five normal hearts. These stress and strain values could be used as targets for in silico design of new instruments/devices for heart failure treatments.

6.5.4 Effect of Fibre Orientation on LV Diastolic Mechanics

The study indicated that the fibre-angle distribution had substantial impact on the EDPVRs of LV during passive inflation. When fibre directions were aligned more towards LV longitudinal axis, the LV wall became less stiff, resulting increment in LV EDV. In addition, increase in fibre angle towards the endocardium wall made the LV less stiff, resulting higher LV EDV, compared to the effect of fibre angle increment towards the epicardium wall. The change in volume was very close to each other when the fibre angle varied in the range of 30° to 50°. This suggests that any pathological remodelling of the fibre structure, which increases the volume change more than the normal condition, indicates increment in fibre angle and vice versa. The results in the current study was consistent with our previous work in Chapter 4 except for fibre angle below 40°. This was due to the change in myocardium properties from pig to human.

The endocardium experienced higher fibre stress for all kind of fibre orientations which was consistent with the diastolic fibre stress distributions, identified using [60-60] fibre orientation in Genet et al. (2014). In contrast, our previous study with pigs data (Chapter 4) identified that the endocardium was not experienced high fibre stress for fibre [80-80] and [70-70]. This was due to the change in myocardium properties from pig to human (Section 5.4.4 of Chapter 5). The high fibre stress regions from the endocardium to the midwall were gradually reduced and shifted more towards the endocardium with the reduction in fibre angle. When fibre orientations aligned more towards the LV longitudinal axis, the anterior and the lateral wall of the equatorial and

the apical locations experienced higher fibre stress.

Increases in the LV mass, LV fibrosis, and cardiomyocyte stiffness had been shown to contribute to heart failure with preserved ejection fraction (HFpEF) (Paulus and Tschpe, 2013). The present results suggested that changes in the fibre direction in LV wall may also contribute to the HFpEF development. These findings will be helpful in medical practice to diagnose the condition of LV in diastole with known fibre structure. Besides, it can lead to the development of new drugs which can alter fibre-structure in order to control the inflation of LV in diseased conditions.

6.6 Research Contributions

The key findings from this study are summarised below.

- **Effect of base movement in FE model prediction :**
  Inclusion of longitudinal base movement of ventricle in FE model improved the shape-volume relevancy of the predicted LV cavity with the original one, which was constructed from CMRI. However, the EDPVRs of LV did not alter due to the inclusion of longitudinal base movement, and therefore, same subject-specific EDV was achieved. In addition, including base movement increased the average fibre strain in the LV wall and introduced high fibre stress in endocardium, epicardium and apical locations. Hence, future computational studies should consider subject-specific longitudinal base movement in EF model to improve the model predictions. Furthermore, the shape-volume relevancy should be accomplished to account the geometrical aspects of the predicted results. Only EDV based validation would not be sufficient enough to provide accurate model estimation.

- **Regional stress-strain distribution of LV wall at ED :**
  Endocardium region experienced higher fibre stress compared to the epicardium of LV wall. The LV wall near base location received greater stress and strain with respect to the middle and apical locations. In general, the lateral LV wall underwent higher stress distribution (fibre and sheet stress) in comparison to the other three regions. This information could be used to optimise diastolic heart failure treatments or design new therapeutic interventions/devices.

- **Reference map of normal ranges of ventricular wall stress-strain for future study :**

  A detailed measurement of end diastolic (ED) stress-strain components in three short-axis locations (base, equatorial and apical) as well as four regions (anterior, posterior, lateral and septum) of LV wall was reported for five healthy ventricles. This detailed information is reported for the first time using subject-specific passive orthotropic myocardium parameters, respective base movement, and especially for five healthy hearts. These could be used as a reference map for future computational studies or could serve as targets for in-silico design of therapeutic interventions for diastolic heart failure treatments.

- **Effect of fibre orientation on diastolic mechanics for human ventricle:**

  Any pathological remodelling of the fibre distribution that increased the amount of transmural fibre angle led to additional LV inflation. Such effects was more notable if the fibre angle was higher towards the endocardium. The regions of high fibre stress was gradually reduced from the endocardium to the mid-wall and shifted more towards the endocardium with the reduction in fibre angle, especially near the equatorial location. The study indicates that change in fibre orientation may contribute to the heart failure with preserved ejection fraction (HFpEF) development. This study may be useful for predicting fibre distribution from in-vivo observations of LV motion or diagnosing the diastolic conditions of LV with known fibre structure. It also highlights the importance of subject-specific fibre orientation in computational model.

6.7 Summary

In the present study, personalised passive diastolic modelling of human LV was carried out using subject-specific passive orthotropic material properties of human myocardium and base movement of LV in order to identify regional stress-strain distributions in LV wall at ED (objective 4). The uniqueness of the current study compared to state-of-the-art as follows.

1. Bi-ventricular model was considered to include RV deformation instead of single LV model (Section 6.3.1 and Figure 6.2).

2. Subject-specific in-vivo passive orthotropic material properties of human myocardium was used for better model predictions, instead of previously used animal myocardium data with transverse isotropic properties (Section 6.3.3).

3. Personalised computational models of five healthy human ventricles were carried out instead of using single human heart (Sections 6.3.3 and 6.3.4), and therefore, the conclusions from the study were more general and robust.

4. A new shape-volume based validation procedure was introduced along with EDV based comparison (Section 6.3.5).

5. Subject-specific base movement, which was not considered by most of the previous studies, was included, and subsequently, the effect of such movement on model prediction was explored (Section 6.4.2).

6. High stress-strain regions in LV wall during ED for normal human LV were identified (Sections 6.4.3 and 6.4.4).

7. Normal range of stress-strain distribution in LV wall at ED was reported from the results of five normal ventricles (Figures 6.11 to 6.13).

Results indicated that only EDV based validation, used in all the previous studies of LV diastolic model, was not sufficient for accurate model prediction, and therefore, shape-volume relevancy should be compared (Section 6.4.2). Including base movement in computational model increased the shape-volume relevancy of LV cavities, and led to improved model predictions (Sections 6.4.2 and 6.5.2). The endocardium of LV wall experienced higher fibre stress compared to the epicardium wall. The LV wall near base location received greater stress and strain with respect to middle and apical locations. In general, the lateral region of LV wall underwent higher stress (especially fibre and sheet stress) and strains distributions in comparison to the other three regions (Section 6.5.3). A detailed measurement of different stress-strain components amongst different locations as well as amongst different regions of LV wall was also reported for five healthy ventricles. The effect of fibre orientation on LV diastolic mechanics (objective 2) was reinvestigated (Section 6.5.4) to overcome the limitation of our previous study (Chapter 4). The research contributions were explicitly summarised in Section 6.6. This information could be used as a reference map for future computational studies or could serve as targets for in-silico design of heart failure treatments.

Chapter 7

Summary and Conclusions

7.1 Introduction

The study presented in the thesis set out to achieve the following research goal

" To predict the normal range of LV wall stress-strain at end diastole and to identify the influence of ventricular geometry, myocardial fibre-orientation, and myocardium material properties on passive inflation of healthy human ventricle."

Four research objectives were raised (Sections 2.4, 2.5, 2.8 and 2.9 of Chapter 2) in order to answer the research question. Before highlighting the main research contributions and conclusions obtained from this study (Section 7.3), it is worth summarising the methods and techniques used in relevance to the research goal (Section 7.2). Recommendation for future work is addressed in Section 7.6.

7.2 Summary of Research Methodology

A brief overview of the research question and objectives was highlighted in Chapter 1. The detailed description of these research objectives, derived from the limitation in current literature through critical review process, was addressed in Chapter 2. Moreover, the thorough literature review helped to identify the research framework, methods and techniques to be used in this study. CMRI was used in this work to construct the BV geometry of human heart as it has good spacial and temporal resolution (Section 2.4). Mimics and 3-matic were used to read the CMRI data in DICOM format and to construct the mesh geometry of the ventricle (Chapter 3). As outlined in Section 2.5, Poisson interpolation (PI) based algorithm, proposed by Wong and Kuhl (2014), was selected, and modified to LDRF algorithm to assign fibre orientation on ventricular mesh geometry (Chapter 3). Passive LV human myocardium is considered as non-linear hyperelastic, orthotropic, quasi-incompressible, and homogeneous as identified though the literature (Section 2.6). Structure based orthotropic Holzapfel-Ogden material law was selected for modelling human myocardium as it has few advantages than other orthotropic laws (Fung-type and pole-zero) as detailed in Section 2.7. Holzapfel-Ogden constitutive law was implemented, using a user-defined subroutine Hypela2, in MSC-Marc (MSC Software Corporation, California, US) utilising Total Lagrange framework (Chapter 3). FE modelling, response surface method (RSM) and genetic algorithm (GA) were used to non-invasively calibrate the average values of the Holzapfel-Ogden constitutive parameters for human myocardium. More detailed investigation strategies for each objective were outlined in corresponding Chapters 4, 5, and 6.

7.3 Research Contributions

This section summarises the key contributions to the knowledge obtained from the research. These finding have come from all stages of the research, from establishing the modelling framework through to meeting the requirements of all the research objectives. Impact and implications of the research findings are discussed in a separate section (Section 7.4).

- **Effect of RV on LV passive inflation:**

  For the first time, the assumption of single LV model in the literature was validated by identifying the effect of RV deformation on LV diastole (Objective 1). (a) Inclusion of RV deformation in computational model increases average fibre and sheet stress of the LV wall during diastole. (b) RV deformation also leads to additional LV passive inflation. It shows that that RV deformation plays important role in LV diastolic mechanics, and therefore, it should be accounted for in computational modelling for improved understanding of the LV mechanics under normal and pathological conditions. Details of the results was included in Chapter 4.

- **Effect of fibre orientation on LV diastolic mechanics:**

  The influence of fibre orientation on LV wall stress and EDPVR was investigated for the first time in the study (Objective 2). (a) The region of high fibre stress gradually reduces from the endocardium to the midwall and shifts more towards the endocardium with the reduction in fibre angle, especially near equatorial location. (b) The fibre distribution that increases the amount of transmural fibre angle leads to additional LV inflation. This effect is more notable when the fibre angle is higher

towards the endocardium. The findings are similar for two different subjects, and therefore, the effect of fibre orientation are independent of ventricular geometry, myocardium properties and base movements. The study also indicates that the change in fibre structure may contribute to the heart failure with preserved ejection fraction (HFpEF) development. These finding was obtained from the study detailed in Chapter 4 and 6.

- **Development of a novel method for in-vivo estimation of passive orthotropic properties of human myocardium utilising routinely used non-invasive clinical data:**

  The study introduced a new method consisted of FE modelling, response surface method (RSM) and genetic algorithm (GA) to estimate the biomechanical properties of human myocardium using standard clinical data. The method was developed in order to achieve research objective 3. Although limited clinical data is used in the study, the method is capable of utilising additional subject-specific data as a constraint to produce more unique solutions. The detail description of the proposed method was outlined in Chapter 5.

- **Reported normal ranges of the parameters under different conditions:**

  The normal ranges of the parameters of holzapfel-Ogden model, which was used to define human myocardium behaviour, were estimated using the standard non-invasive clinical data (Objective 3). The change in estimated parameters due to the change in ventricular geometry, end diastolic pressure (EDP) and fibre orientation were also reported. Conclusions from the study are as follows. (a) The variations in estimated

values of the parameters due to the change in geometry, fibre orientations and EDP are not considerably high. As a results, the estimated values produces similar stress-strain relation within a range. (b) The material parameters of Holzapfel-Ogden model are highly correlated, and additional subject-specific clinical data are required to estimate unique solutions. (c) The proposed inverse optimisation method is capable of estimating in-vivo human myocardium properties, which are less stiff compared to the traditional ex-vivo experimental results. All the estimated values were shown in Chapter 5.

- **Effect of base movement in FE model predictions**

  Inclusion of longitudinal base movement of LV affects various aspects of FE model predictions as follows. (a) The inclusion of LV base movement improves the shape-volume relevancy of the predicted LV cavity with the original one, constructed from CMRI. (b) However, the EDPVRs of LV does not alter due to the inclusion of longitudinal base movement, and therefore, same subject-specific EDV will be achieved. (c) In addition, including the base movement increases the average fibre strain in the LV wall, and introduces high fibre stress in the endocardium, epicardium and apical locations. (d) Furthermore, the shape-volume relevancy should be accomplished to account the geometrical aspects of the model predicted results. Only EDV based validation of the FE model would not be sufficient enough to provide accurate model estimation. Future computational studies should consider subject-specific longitudinal base movement to improve the model predictions. The study was carried out to achieve objective 4 and details of the results were included

in Chapter 6 .

- **Regional stress-strain distribution of LV wall at ED:**

  Although the stress-strain distribution of the LV wall is highly heterogeneous amongst the subjects due to the geometrical heterogeneity, it is observed that the endocardium region experiences high fibre stress compared to the epicardium of the LV wall. The LV wall near the base location experiences high stress and strain compared to the middle and apical locations. In general, the lateral LV wall undergoes greater stress distribution (fibre and sheet stress) in comparison with the other three regions. The results were achieved to address objective 4, and were detailed in Chapter 6.

- **Reference map of normal ranges of ventricular wall stress-strain for future study:**

  A detailed measurement of end diastolic (ED) stress-strain components in three short-axis locations (base, equatorial and apical) as well as four regions (anterior, posterior, lateral and septum) of LV wall was reported for five healthy ventricles (Chapter 6). These could be used as a reference map for future computational studies or could serve as targets for in-silico design of therapeutic interventions for diastolic heart failure treatments.

- **Development of LDRF algorithm to automatically assign fibre map on ventricular mesh geometry:**

  A novel Laplace-Dirichlet-Region growing-FEM (LDRF) based algorithm was developed to assign the fibre orientation on computational ventricular mesh geometry (Chapter 3). The algorithm was developed based on the method suggested by Wong and Kuhl (2014) with the major

amendment in identifying the RV and LV surface domains automatically to define the Dirichlet boundary conditions. The identification of different surface domains, required to assign boundary values, was carried out using the region growing algorithm (Franciosa and Gerbino, 2008) and distance based approach. With three inputs and three functions, the algorithm can generate fibre and sheet orientations on either LV or BV mesh geometries automatically which can be used in FE modelling. Details of the method was described in Section 3.3 of Chapter 3.

- **Summarised all the analytical expressions required for the validation of FE implementation of Holzapfel-Ogden law:**
  The complete expressions of the stress tensor and related mathematical descriptions of Holzapfel-Ogden constitutive law for the passive myocardium under various test cases were elaborately summarised in Chapter 3. Such analytic expressions are very useful to validate the FE implementation of Holzapfel-Ogden material model, and therefore, could be useful in future computation study.

7.4 Implications of Research Contributions

The research findings, highlighted in Section 7.3, have several contributions to the knowledge. The implications of the knowledge have impacts in two areas of the research - computational cardiac biomechanics and clinical cardiac physiology.

7.4.1 Computational Cardiac Biomechanics

- The majority of FE models assumed single LV geometry, and the validity of this assumption is investigated for the first time. Inclusion of RV in computational model not only alters the stress-strain distribution but also increases average values of fibre and sheet stress of LV wall. Although RV provides additional geometrical constraint against LV, it actually helps LV to inflate more as detailed in Chapter 4. The reason is that the pressure on RV free wall supports the LV to expand more compared to the pressure acted on RV septum, which tries to suppress the LV inflation. In addition, the previous studies simplified the effect of RV by providing RV pressure only on the septum wall for single LV model, which was not suitable to identify the overall effect of RV deformation on LV diastolic mechanics. Some single LV model tried to match the model predicted strain with the strain values calculated from MRI tagging (which considers RV deformations). In absence of the RV geometry, it is difficult to define proper boundary conditions in those single LV models to include the effect of RV deformation to improve model predictions. Inclusion of RV geometry in FE model helps to define proper boundary conditions to improve the match between the model predicted and MRI measured strain values, specially in septum wall. Hence it is concluded that RV geometry, and its deformation should be considered in future LV modelling studies.

- A fully automatic rule-based algorithm (LDRF) is developed in this study (Section 3.3 of Chapter 3). The algorithm combines Poisson interpolation (PI), region growing algorithm and FE method to assign

histologically observed fibre orientation on ventricular mesh geometry without manual intervention (using three inputs). The method can also be used in conjunction with DTI derived fibre map to construct smooth fibre structure. This algorithm can be useful for future computational model of ventricle.

- Although it was identified by many researchers (see Chapter 2) that fibre-structure is important for cardiac biomechanics, the influences of fibre orientation on LV EDPVR and fibre stress distribution pattern during diastole are explicitly identified in this study for the first time (Section 7.3). These effects are independent of human subjects (i.e. the effect is same for different geometry and myocardium properties). The study shows the requirement of subject-specific fibre orientation in computational model, and therefore, the future work should focus on identifying personalised in-vivo fibre orientation using diffusion tensor imaging (DTI).

- A novel method was developed by combining FE model, response surface (RS) and genetic algorithm (GA) to estimate the Holzapfel-Ogden constitutive parameters for healthy human myocardium. This method can be used in future with additional subject-specific data, which could be used as a constraint in this method to produce more personalised solution.

- The average value of Holzapfel-Ogden constitutive parameters for human myocardium (healthy) was reported. The variations in estimated values of the parameters due to the change in ventricular geometry, fibre orientations and EDP are not considerably high (Section 7.3). These av-

erage values (fully orthotropic passive properties of human myocardium) could be used directly in future computational study without implementing complex computational method to estimate the parameters. Previous computational study used human ventricular geometry with pig myocardium properties due to unavailability of human myocardium properties. As a consequence, the model resulted in too stiff stress-strain relation in subject-specific model. The study enables the future computational study to use average healthy human myocardium properties to provide better model predictions. Moreover, the values can be used to design new patch or injectable material for the treatments of HF patients.

- Inclusion of longitudinal base movement of LV, ignored in computational model of ventricle, improves the FE model predictions. Besides, inclusion of base movement increases the average fibre strain in the LV wall and introduces high fibre stress in the endocardium, epicardium and apical locations. The model would provide accurate LV volume estimation with inaccurate geometrical shape if base movement is not included. As a result, the systolic simulation, which is based on the results of ED, would also produce inaccurate geometrical shape and stress-strain estimation. Any surgical simulation with such inconsistency could lead to inaccurate model prediction, and therefore, could lead to the selection of wrong surgical treatment. This highlights the importance of including subject-specific base movement in computational model of LV.

- The majority of previous LV diastolic models was validated by using only LV EDV. In this study, it is identified that inclusion of base movement does not alter the LV EDPVR, and therefore, same LV EDV is achieved.

However, from shape-volume based comparison, it was observed that the model prediction matched better with MRI derived 'original' geometry when longitudinal movement of base was included in the model. Only EDV based validation of the FE model would not be sufficient enough to provide accurate model estimation. MRI tagging is used to calculate the LV wall strain to validate the FE model prediction. Although this validation improves the model prediction accuracy, still it does not take care of LV cavity shape. Moreover, the shape-volume validation is easy to incorporate in computational model compared to strain validation, which involves complex image analysis and takes more time.

- The normal range of stress-strain values for three short-axis locations (base, equatorial and apical) as well as four regions (anterior, posterior, lateral and septum) of LV wall was reported. This information was obtained from 5 healthy human ventricles using subject-specific passive orthotropic myocardium properties for the first time. Such information can be used as a reference map for diastolic stress-strain distribution patterns for healthy LV wall. LV remodelling process due to heart failure is thought to be driven by an increase in stress in the LV wall (Lee et al., 2014a; Wall et al., 2006). The surgical intervention, which includes the use of hydrogel injection (Lee et al., 2013a), anisotropic reinforcement (Fomovsky et al., 2012), Cardiokinetix Parachute device (Lee et al., 2014a) or Cardiac Support Device (Wenk et al., 2013), aims to reduce the stress in LV wall and brings it back to the normal range at ED and ES. This study not only identified the fibre stress, but also different components of stress-strain amongst the different locations and regions of the

LV wall at ED for five normal hearts. These stress and strain values could serve as targets for in silico design of such instruments/devices for heart failure treatments.

- The complete expressions of the stress tensor and related mathematical descriptions of Holzapfel-Ogden constitutive law for the passive myocardium under various test cases were elaborately summarised in Chapter 3. Such analytic expressions are very useful to validate the FE implementation of Holzapfel-Ogden material model, and therefore, could be useful in future computation study.

7.4.2 Clinical Cardiac Physiology

- When fibre directions align more towards LV longitudinal axis, the LV wall becomes less stiff, resulting increment in LV EDV. In addition, the increase in fibre angle towards endocardium wall produces higher LV EDV, compare to the effect of fibre angle increment towards epicardium wall. The region of high fibre stress gradually reduces from the endocardium to the mid-wall and shifts more towards the endocardium with the reduction in fibre angle, especially near the equatorial location. This illustrates the change in fibre orientation has substantial impact on the EDPVRs of LV and fibre stress. Increases in the LV mass, LV fibrosis, and cardiomyocyte stiffness had been shown to contribute to heart failure with preserved ejection fraction (HFpEF) (Paulus and Tschpe, 2013). The present study suggests that changes in the fibre direction in LV wall may also contribute to the heart failure with preserved ejection fraction (HFpEF) development. These findings will be helpful in med-

ical practice to diagnose the condition of left-ventricle in diastole with known fibre structure. Besides, it can lead to development of new drugs which can alter fibre-structure in order to control the inflation of LV in diseased conditions.

- Although the stress-strain distribution of the LV wall is highly heterogeneous due to the geometrical heterogeneity, it is observed that the endocardium region experiences high fibre stress compare to the epicardium of the LV wall during diastole. The LV wall near the base location and the lateral region experiences high stress and strain. This information could be useful for future diagnosis of heart failure.

7.5 Limitations of the Research

There were few limitations associated with the approach presented in this study. First of all, rule-based fibre orientation was used instead of subject-specific fibre structure. Precise fibre-sheet orientation can be measured only ex-vivo, and feasibility of in-vivo DTI for subject-specific fibre orientation is still an open question (Wang et al., 2009; Genet et al., 2014). The LV EDP was considered 10 mmHg due to the unavailability of subject-specific EDP, which requires invasive measurements using micromanometer-tipped catheters. Due to such ethical and technical limitations, studies regarding human ventricular mechanics assumed physiologically reasonable values of ventricular pressure in computational model (Lee et al., 2013a,b; Wang et al., 2013a; Genet et al., 2014). However, small change within physiological EDP would not change the conclusions of the study considerably (Lee et al., 2013a). The third limitation was the assumption of an initial stress-free state, which was present in all

previous simulations of the heart based on in-vivo images (Usyk et al., 2000; Sun et al., 2009; Wenk et al., 2011a,b; Genet et al., 2014). Therefore, this is the state-of-the-art due to limited clinical data (Sun et al., 2009). Not all blood in the ventricles is ejected during systole, the remaining blood creates a small amount of residual stress on the heart in early diastole (Sun et al., 2009). Using computational model study, Guccione et al. (2001a) reported that the residual stress produced by surgical remodelling has little effect on ventricular function and regional mechanics. Besides, Wang et al. (2014) reported that the effects of such initial (residual) stresses are relatively small in late diastole when pressure is higher. In contrast, a recent study observed measurable effect (reduce the LV stiffness by 40% during passive filling) of pre-stress during diastole (Genet et al., 2015). Therefore, it is still an open question and future studies will be carried out to compute personalised diastolic mechanics by taking into account physiological pre-stress condition to identify the effect of residual stress. The model developed in this study used the method of Wang et al. (2009) to include the base movement in computational model extracted from the CMRI. However, the ventricles are also surrounded by pericardium sac and other anatomical structures. Interaction between them would enforce challenges in predicting physiologically realistic diastolic mechanics. Due to the limited information, it is still an open question (Hunter et al., 2003).

From the perspective of myocardial physiology and ventricular blood pressure, the structure-functional relations of normal human heart are very complex. It is not claimed that the personalised computational model of bi-ventricles being able to realistically simulate all those coupled phenomena with inadequate clinical data. However, the model can realistically simulate

only a limited scope of local LV diastolic mechanics, and within that scope, the models are state-of-the-art in their pragmatism and consistent with which they have been validated.

7.6 Future Scope

This current FE modelling framework did not take residual stress or strain into account. The assumption of an initial stress-free state, which was present in all previous simulations of the heart, based on in-vivo images (Usyk et al., 2000; Sun et al., 2009; Wenk et al., 2011a,b; Genet et al., 2014; Palit et al., 2015a). Using computational model study, Guccione et al. (2001a) reported that the residual stress produced by surgical remodelling has little effect on ventricular function and regional mechanics. Besides, Wang et al. (2014) reported that the effects of such initial (residual) stresses are relatively small in late diastole when pressure is higher. In contrast, a recent study observed measurable effect (reduce the LV stiffness by 40% during passive filling) of pre-stress during diastole (Genet et al., 2015). Therefore, it is still an open question and future studies will be carried out to compute personalised diastolic mechanics by taking into account physiological pre-stress condition to identify the effect of residual stress.

The ventricles are also surrounded by pericardium sac and other anatomical structures. Interaction between them would enforce challenges in predicting physiologically realistic diastolic mechanics. Inclusion of pericardium in computational modelling involves contact mechanics problem. Few researchers tried to include a pericardial constraint into the FE models to prevent the LV

from excessive deformation in a prolate spheroidal coordinate system (Nash, 1998; Wong et al., 2009). However, due to the limited information, it is still an open question (Hunter et al., 2003). A better approach would involve the construction of 3D geometry from MRI to represent the pericardium, and to add contact constraints between the ventricular epicardium and pericardium to the FE models to produce more realistic diastolic mechanics.

Due to the limited clinical data, DTI derived fibre and MRI tagging derived strain values were not used in this study. When such data become available, they could be straightforwardly incorporated into the existing modelling framework. A similar study could then be performed to compare the change in mechanical responses from the current results due to the utilisation of more realistic fibre and strain values.

In summary, FE modelling of LV was constructed to predict the passive inflation mechanics of the ventricle using routinely used clinical data. The study provided insight into regional distributions of myocardial stress and strain in healthy hearts, and identified the effects of fibre orientation and geometric heterogeneity on such stress-strain distribution pattern. Comparing models of healthy and diseased states will enable investigation into the underlying mechanisms for LV dysfunction.

Bibliography

Arts, T., Costa, K. D., Covell, J. W., and McCulloch, A. D. (2001). Relating myocardial laminar architecture to shear strain and muscle fiber orientation. *American Journal of Physiology - Heart and Circulatory Physiology*, 280:H2222–H2229.

Arts, T., Veenstra, P. C., and Reneman, R. S. (1982). Epicardial deformation and left ventricular wall mechanics during ejection in the dog. *American Journal of Physiology - Heart and Circulatory Physiology*, 243:H379–H390.

Augenstein, K., Cowan, B., LeGrice, I., and Young, A. (2006). *Estimation of Cardiac Hyperelastic Material Properties from MRI Tissue Tagging and Diffusion Tensor Imaging*, volume 4190 of *Lecture Notes in Computer Science*, book section 77, pages 628–635. Springer Berlin Heidelberg.

Augenstein, K. F., Cowan, B. R., LeGrice, I. J., Nielsen, P. M., and Young, A. A. (2005). Method and apparatus for soft tissue material parameter estimation using tissue tagged magnetic resonance imaging. *Journal of Biomechanical Engineering*, 127(1):148–57.

Axel, L. (2002). Biomechanical dynamics of the heart with mri. *Annual Review of Biomedical Engineering*, 4(1):321–347.

Baillargeon, B., Rebelo, N., Fox, D. D., Taylor, R. L., and Kuhl, E. (2014). The living heart project: A robust and integrative simulator for human heart function. *European Journal of Mechanics - A/Solids*, 48:38–47.

Bayer, J. D., Blake, R. C., Plank, G., and Trayanova, N. A. (2012). A novel rule-based algorithm for assigning myocardial fiber orientation to computational heart models. *Annals of Biomedical Engineering*, 40(10):2243–2254.

Bernabeu, M. O., Bishop, M. J., Pitt-Francis, J., Gavaghan, D. J., Grau, V., and Rodriguez, B. (2008). High performance computer simulations for the study of biological function in 3d heart models incorporating fibre orientation and realistic geometry at para-cellular resolution. In *Computers in Cardiology, 2008*, pages 721–724.

Bishop, M., Hales, P., Plank, G., Gavaghan, D., Scheider, J., and Grau, V. (2009). *Comparison of Rule-Based and DTMRI-Derived Fibre Architecture in a Whole Rat Ventricular Computational Model*, volume 5528 of *Lecture Notes in Computer Science*, book section 10, pages 87–96. Springer Berlin Heidelberg.

Bishop, M. J., Plank, G., Burton, R. A., Schneider, J. E., Gavaghan, D. J., Grau, V., and Kohl, P. (2010). Development of an anatomically detailed mri-derived rabbit ventricular model and assessment of its impact on simulations of electrophysiological function. *American Journal of Physiology - Heart and Circulatory Physiology*, 298(2):H699–718.

Bottini, P. B., Carr, A. A., Prisant, L. M., Flickinger, F. W., Allison, J. D., and Gottdiener, J. S. (1995). Magnetic resonance imaging compared to echocardiography to assess left ventricular mass in the hypertensive patient. *American Journal of Hypertension*, 8(3):221–228.

Bovendeerd, P. H., Arts, T., Huyghe, J. M., Campen, D. H. v., and Reneman, R. S. (1992). Dependence of local left ventricular wall mechanics on myocardial fiber orientation: a model study. *Journal of Biomechanics*, 25(10):1129–1140.

Bovendeerd, P. H., Huyghe, J. M., Arts, T., van Campen, D. H., and Reneman, R. (1994). Influence of endocardial-epicardial crossover of muscle fibers on left ventricular wall mechanics. *Journal of Biomechanics*, 27(7):941–951.

Buckberg, G., Hoffman, J. I., Mahajan, A., Saleh, S., and Coghlan, C. (2008). Cardiac mechanics revisited the relationship of cardiac architecture to ventricular function. *Journal of American Heart Association*, 118:2571–2587.

Burch, G. E., Ray, C. T., and Cronvich, J. A. (1952). Certain mechanical peculiarities of the human cardiac pump in normal and diseased states. *Circulation*, 5(4):504–13.

Chuong, C. J. and Fung, Y. C. (1986). *Residual stress in arteries*, pages 117–129. Springer New York.

Cleland, J., Dargie, H., S., H., McDonagh, T., and Mitchell, P. (2010). National health service., 2010. national heart failure audit 2010. Report, The NHS Information Centre ,The British Society for Heart Failure. UK heart failure data of 2010.

Costa, K. D., Holmes, J. W., and McCulloch, A. D. (2001). Modelling cardiac mechanical properties in three dimensions. *The Royal Society*, 359:1233–1250.

Costa, K. D., Hunter, P. J., Rogers, J. M., Guccione, J. M., Waldman, L. K., and McCulloch, A. D. (1996). A three-dimensional finite element method for large elastic deformations of ventricular myocardium: Icylindrical and spherical polar coordinates. *Journal of Biomechanical Engineering*, 118(4):452–463.

Costa, K. D., May-Newman, K., Farr, D., ODell, W. G., McCulloch, A. D., and H.Omens, J. (1997). Three-dimensional residual strain in midanterior canine left ventricle. *American Journal of Physiology - Heart and Circulatory Physiology*, 273:H1968–H1976.

Dang, A. B. C., Guccione, J. M., Mishell, J. M., Zhang, P., Wallace, A. W., Gorman, R. C., III, J. H. G., and Ratcliffe, M. B. (2005a). Akinetic myocardial infarcts must contain contracting myocytes: finite-element model study. *American Journal of Physiology - Heart and Circulatory Physiology*, 288:H1844 – H1850.

Dang, A. B. C., Guccione, J. M., Zhang, P., Wallace, A. W., Gorman, R. C., III, J. H. G., and Ratcliffe, M. B. (2005b). Effect of ventricular size and patch stiffness in surgical anterior ventricular restoration: A finite element model study. *The Annals of Thoracic Surgery*, 79:185 – 193.

Demer, L. L. and Yin, F. C. (1983). Passive biaxial mechanical properties of isolated canine myocardium. *The Journal of Physiology*, 339:615630.

Dokos, S., LeGrice, I. J., Smaill, B. H., Kar, J., and Young, A. A. (2000). A triaxial-measurement shear-test device for soft biological tissues. *Journal of Biomechanical Engineering*, 122(5):471–478.

Dokos, S., Smaill, B. H., Young, A. A., and LeGrice, I. J. (2002). Shear properties of passive ventricular myocardium. *American Journal of Physiology - Heart and Circulatory Physiology*, 283:H2650–H2659.

Dorri, F. (2004). *A Finite element model of the human left ventricular systole, taking into account the fibre orientation pattern.* Phd, Swiss Federal Institute Of Technology, Zurich.

Dorri, F., Niederer, P. F., and Lunkenheimer, P. P. (2006). *A finite element model of the human left ventricular systole.* PhD thesis, Swiss Federal Institute Of Technology, Zurich.

Emery, J. L., Omens, J. H., and McCulloch, A. D. (1997). Biaxial mechanics of the passively overstretched left ventricle. *American Journal of Physiology - Heart and Circulatory Physiology*, 272:H2299–H2305.

Eriksson, T. S. E., Prassl, A. J., Plank, G., and Holzapfel, G. A. (2013). Influence of myocardial fiber/sheet orientations on left ventricular mechanical contraction. *Mathematics and Mechanics of Solids*, 18(6):592–606.

Fomovsky, G. M., Clark, S. A., Parker, K. M., Ailawadi, G., and Holmes, J. W. (2012). Anisotropic reinforcement of acute anteroapical infarcts improves pump function. *Circulation: Heart Failure*, 5(4):515–522.

Fonseca, C. G. (2004). *Assessment of left ventricular diastolic function with three dimensional cardiac magnetic resonance imaging*. PhD thesis, In Department of Anatomy, The University of Auckland.

Franciosa, P. and Gerbino, S. (2008). A cad-based methodology for planar and cylindrical features recognition. In *4th CIRP International Conference on Intelligent computation in manufacturing engineering*.

Gao, H., Li, W. G., Cai, L., Berry, C., and Luo, X. Y. (2015). Parameter estimation in a holzapfelogden law for healthy myocardium. *Journal of Engineering Mathematics*, pages 1–18.

Geerts, L., Bovendeerd, P., Nicolay, K., and Arts, T. (2002). Characterization of the normal cardiac myofiber field in goat measured with mr-diffusion tensor imaging. *American Journal of Physiology - Heart and Circulatory Physiology*, 283(1):H139–45.

Genet, M., Lee, L. C., Nguyen, R., Haraldsson, H., Acevedo-Bolton, G., Zhang, Z., Ge, L., Ordovas, K., Kozerke, S., and Guccione, J. M. (2014). Distribution of normal human left ventricular myofiber stress at end diastole and end systole: a target for in silico design of heart failure treatments. *Journal of applied physiology*, 117(2):142–152.

Genet, M., Rausch, M. K., Lee, L. C., Choy, S., Zhao, X., Kassab, G. S., Kozerke, S., Guccione, J. M., and Kuhl, E. (2015). Heterogeneous growth-induced prestrain in the heart. *Journal of Biomechanics*, 48(10):2080–2089.

Ghista, D. N. and Sandler, H. (1969). An analytic elastic-viscoelastic model for the shape and the forces in the left ventricle. *Journal of Biomechanics*, 2(1):35–47.

Gilbert, S. H., Benson, A. P., Li, P., and Holden, A. V. (2007). Regional localisation of left ventricular sheet structure: integration with current models of cardiac fibre, sheet and band structure. *European Journal of Cardio-thoracic Surgery*, 32:231–249.

Go, A. S., Mozaffarian, D., Roger, V. L., Benjamin, E. J., Berry, J. D., Blaha, M. J., Dai, S., Ford, E. S., Fox, C. S., Franco, S., Fullerton, H. J., Gillespie, C., Hailpern, S. M., Heit, J. A., Howard, V. J., Huffman, M. D., Judd, S. E., Kissela, B. M., Kittner, S. J., Lackland, D. T., Lichtman, J. H., Lisabeth, L. D., Mackey, R. H., Magid, D. J., Marcus, G. M., Marelli, A., Matchar, D. B., McGuire, D. K., Mohler, E. R., Moy, C. S., Mussolino, M. E., Neumar, R. W., Nichol, G., Pandey, D. K., Paynter, N. P., Reeves, M. J., Sorlie, P. D., Stein, J., Towfighi, A., Turan, T. N., Virani, S. S., Wong, N. D., Woo, D., and Turner, M. B. (2013). Heart disease and stroke statistics 2014 update: A report from the american heart association. *Circulation*.

Goktepe, S., Acharya, S. N. S., Wong, J., and Kuhl, E. (2011). Computational modeling of passive myocardium. *International Journal for Numerical Methods in Biomedical Engineering*, 27(1):1–12.

Gould, P., Ghista, D. N., Brombolich, L., and Mirsky, I. (1972). In vivo stresses in the human left ventricular wall: analysis accounting for the irregular 3d geometry and comparison with idealised geometry analyses. *Journal of Biomechanics*, 5(5):521–539.

Grewal, B. S. (1988). *The Mechanical Behaviour of the Left Ventricle of the Human Heart in Diastole*. PhD thesis, Department of Mechanical Engineering, Brunel University.

Guccione, J. M., Costa, K. D., and McCulloch, A. D. (1995). Finite element stress analysis of left ventricular mechanics in the beating dog heart. *Journal of Biomechanics*, 28(10):1167–1177.

Guccione, J. M., McCulloch, A. D., and Waldman, L. K. (1991). Passive material properties of intact ventricular myocardium determined from a cylindrical model. *Journal of Biomechanical Engineering*, 113(1):42–55.

Guccione, J. M., Moonly, S. M., Moustakidis, P., Costa, K. D., Moulton, M. J., Ratcliffe, M. B., and Pasque, M. K. (2001a). Mechanism underlying mechanical dysfunction in the border zone of left ventricular aneurysm: A finite element model study. *The Annals of Thoracic Surgery*, 71:652 – 654.

Guccione, J. M., Scott M. Moonly, B., Wallace, A. W., and Ratcliffe, M. B. (2001b). Residual stress produced by ventricular volume reduction surgery has little effect on ventricular function and mechanics: A finite element model study. *Surgery for Acquired Cardiovascular Disease*, 122:592 –599.

Guyton, A. C. and Hall, J. E. (c2011). *Textbook of medical physiology*. Elsevier Saundres.

Hafner, J., Sachse, F. B., Sansour, C., Seemann, G., and Dssei, O. (2002). Hyperelastic description of elastomechanic properties of the heart: a new material law and its application. *Biomedizinische Technik*, 47:770–773.

Holzapfel, G. A. and Ogden, R. W. (2009). Constitutive modelling of passive myocardium: a structurally based framework for material characterization. *Philosophical Transactions of the Royal Society A*, 367:3445–3475.

Horowitz, A., Perl, M., Sideman, S., and Ritman, E. (1986). Comprehensive model for the simulation of left ventricle mechanics part2 implementation and results analysis. *Medical and Biological Engineering and Computing*, 24:150–156.

Huisman, R. M., Elzinga, G., Westerhof, N., and Sipkema, P. (1980). Measurement of left ventricular wall stress. *Cardiovascular Research*, 14(3):142–153.

Humphrey, J. D., Strumpf, R. K., and Yin, F. C. (1990a). Biaxial mechanical behavior of excised ventricular epicardium. *American Journal of Physiology - Heart and Circulatory Physiology*, 259:H101–8.

Humphrey, J. D., Strumpf, R. K., and Yin, F. C. (1990b). Determination of a constitutive relation for passive myocardium: I. a new functional form. *Journal of Biomechanical Engineering*, 112:333–339.

Humphrey, J. D. and Yin, F. C. (1987a). A new constitutive formulation for characterizing the mechanical behavior of soft tissues. *Biophysical Journal*, 52(4):563–570.

Humphrey, J. D. and Yin, F. C. (1987b). On constitutive relations and finite deformations of passive cardiac tissue. part i. a pseudo-strain energy function. *Journal of Biomechanical Engineering*, 109(4):298–304.

Humphrey, J. D. and Yin, F. C. (1989). Constitutive relations and finite deformations of passive cardiac tissue ii: stress analysis in the left ventricle. *Circulation Research*, 65:805–817.

Hunter, P. J. (1975). *Finite Element Analysis of Cardiac Muscle Mechanics*. PhD thesis, University of Oxford,.

Hunter, P. J., McCulloch, A. D., and ter Keurs, H. E. D. J. (1998). Modelling the mechanical properties of cardiac muscle. *Progress in Biophysics and Molecular Biology*, 69(23):289–331.

Hunter, P. J., Pullan, A. J., and Smaill, B. H. (2003). Modeling total heart function. *Annual Review of Biomedical Engineering*, 5:147–77.

Huyghe, J. M., Arts, T., van Campen, D. H., and Reneman, R. (1992). Porous medium finite element model of the beating left ventricle. *American Journal of Physiology - Heart and Circulatory Physiology*, 262:H1256–67.

Huyghe, J. M., van Campen, D. H., Arts, T., and Heethaar, R. M. (1991a). The constitutive behaviour of passive heart muscle tissue. a quasi-linear viscoelastic formulation. *Journal of Biomechanics*, 24:841–849.

Huyghe, J. M., van Campen, D. H., Arts, T., and Heethaar, R. M. (1991b). A two-phase finite element model of the diastolic left ventricle. *Journal of Biomechanics*, 24:527–538.

Janz, R. F. (1980). Effect of chamber eccentricity on equatorial fiber stress during systole. *Fed Proc*, 39(2):183–7.

Janz, R. F. and Grimm, A. F. (1972). Finite-element model for the mechanical behavior of the left ventricle. prediction of deformation in the potassium-arrested rat heart. *Circulation Research*, 30(2):244–52.

Janz, R. F. and Grimm, A. F. (1973). Deformation of the diastolic left ventricle. nonlinear elastic effects. *Biophysical Journal*, 13(7):689–704.

Janz, R. F., Kubert, B. R., Moriarty, T. F., and Grimm, A. F. (1974). Deformation of the diastolic left ventricle: Ii. nonlinear geometric effects. *Journal of Biomechanics*, 7(6):509–516.

Jhun, C.-S., Wenk, J. F., Zhang, Z., Wall, S. T., Sun, K., Sabbah, H. N., Ratcliffe, M. B., and Guccione, J. M. (2010). Effect of adjustable passive constraint on the failing left ventricle: A finite element model study. *The Annals of Thoracic Surgery*, 89(1):132 – 137.

Kerckhoffs, R. C. P., Bovendeerd, P. H. M., Kotte, J. C. S., Prinzen, F. W., Smits, K., and Arts, T. (2003). Homogeneity of cardiac contraction despite physiological asynchrony of depolarization: a model study. *Annals of Biomedical Engineering*, 31:536–547.

Klotz, S., Hay, I., Dickstein, M. L., Yi, G.-H., Wang, J., Maurer, M. S., Kass, D. A., and Burkhoff, D. (2006). Single-beat estimation of end-diastolic pressure-volume relationship: a novel method with potential for noninvasive application. *American Journal of Physiology - Heart and Circulatory Physiology*, 291(1):H403–H412.

Krishnamurthy, A., Villongco, C. T., Chuang, J., Frank, L. R., Nigam, V., Belezzuoli, E., Stark, P., Krummen, D. E., Narayan, S., Omens, J. H., McCulloch, A. D., and Kerckhoffs, R. C. P. (2013). Patient-specific models of cardiac biomechanics. *Journal of Computational Physics*, 244(0):4–21.

Krumholz, H. M., Chen, Y. T., Wang, Y., Vaccarino, V., Radford, M. J., and Horwitz, R. I. (2000). Predictors of readmission among elderly survivors of admission with heart failure. *American Heart Journal*, 139(1 Pt 1):72–7.

Lee, L., Ge, L., Zhang, Z., Pease, M., Nikolic, S., Mishra, R., Ratcliffe, M., and Guccione, J. M. (2014a). Patient-specific finite element modeling of the cardiokinetix parachute () device: effects on left ventricular wall stress and function. *Medical and Biological Engineering and Computing*, 52(6):557–566.

Lee, L., Genet, M., Dang, A. B., Ge, L., Guccione, J. M., and Ratcliffe, M. B. (2014b). Applications of computational modeling in cardiac surgery. *Journal of Cardiac Surgery*, 29(3):293–302.

Lee, L. C., Wall, S. T., Klepach, D., Ge, L., Zhang, Z., Lee, R. J., Hinson, A., Gorman, J. H., r., Gorman, R. C., and Guccione, J. M. (2013a). Algisyl-lvr with coronary artery bypass grafting reduces left ventricular wall stress and improves function in the failing human heart. *International Journal of Cardiology*, 168(3):2022–8.

Lee, L. C., Wenk, J. F., Zhong, L., Klepach, D., Zhang, Z., Ge, L., Ratcliffe, M. B., Zohdi, T. I., Hsu, E., Navia, J. L., Kassab, G. S., and Guccione, J. M. (2013b). Analysis of patient-specific surgical ventricular restoration: importance of an ellipsoidal left ventricular geometry for diastolic and systolic function. *J Appl Physiol (1985)*, 115(1):136–44.

LeGrice, I., Takayama, Y., and Covell, J. (1995a). Transverse shear along myocardial cleavage planes provides a mechanism for normal systolic wall thickening. *Circulation Research*, 77(1):182–193.

LeGrice, I. J., Hunter, P. J., A.Young, A., and Smaill, B. H. (2001). The architecture of the heart: a data-based model. *Philosophical Transactions of the Royal Society London*, 359:1217–1232.

Legrice, I. J., Hunter, P. J., and Smaill, B. H. (1997). Laminar structure of the heart: a mathematical model. *American Journal of Physiology - Heart and Circulatory Physiology*, 272:H2466–H2476.

LeGrice, I. J., Smaill, B. H., Chai, L. Z., Edgar, S. G., Gavin, J. B., and Hunter, P. J. (1995b). Laminar structure of the heart: ventricular myocyte arrangement and connective tissue architecture in the dog. *American Journal of Physiology - Heart and Circulatory Physiology*, 269:H571–H582.

Lin, D. H. S. and Yin, F. C. (1998). A multiaxial constitutive law for mammalian left ventricular myocardium in steady-state barium contracture or tetanus. *Journal of Biomechanical Engineering*, 120:504–517.

Mojsejenko, D., McGarvey, J. R., Dorsey, S. M., Gorman, J. H., r., Burdick, J. A., Pilla, J. J., Gorman, R. C., and Wenk, J. F. (2015). Estimating passive mechanical properties in a myocardial infarction using mri and finite element simulations. *Biomechanics and Modeling in Mechanobiology*, 14(3):633–47.

Moustakidis, P., Maniar, H. S., Cupps, M. B. P., Absi, T., Zheng, J., Guccione, J. M., Sundt, T. M., and Pasque, M. K. (2002). Altered left ventricular geometry changes the border zone temporal distribution of stress in an experimental model of left ventricular aneurysm: A finite element model study. *Circulation*, 106:I –168 – I –175.

Nair, A. U., Taggart, D. G., and Vetter, F. J. (2007). Optimizing cardiac material parameters with a genetic algorithm. *Journal of Biomechanics*, 40(7):1646–50.

Nash, M. P. (1998). *Mechanics and material properties of the heart using an anatomically accurate mathematical model*. PhD thesis, University of Auckland, New Zealand.

Nash, M. P. and Hunter, P. J. (2000). Computational mechanics of the heart. *Journal of Elasticity*, 61:113–141.

Nichols, M., Townsend, N., Luengo-Fernandez, R., Leal, J., Gray, A., Scarborough, P., and et al. (2012). European cardiovascular disease statistics. Report, European Heart Network, European Society of Cardiology.

Nielsen, P. M., Le Grice, I. J., Smaill B, H., and Hunter, P. J. (1991). Mathematical model of geometry and fibrous structure of the heart. *The American Journal of Physiology*, 260:H1365–H1378.

Nikou, A., Dorsey, S. M., McGarvey, J. R., Gorman, J. H., r., Burdick, J. A., Pilla, J. J., Gorman, R. C., and Wenk, J. F. (2015). Computational modeling of healthy myocardium in diastole. *Annals of Biomedical Engineering*, pages 1–13.

Novak, V. P., Yin, F. C., and Humphrey, J. D. (1994). Regional mechanical properties of passive myocardium. *Journal of biomechanics*, 27(4):403–412.

Okamoto, R. J., Moulton, M. J., Peterson, S. J., Li, D., Pasque, M. K., Pasque, M. K., and Guccione, J. M. (2000). Epicardial suction: a new approach to mechanical testing of the passive ventricular wall. *Journal of Biomechanical Engineering*, 122:479–487.

Omens, J. H. and Fung, Y. C. (1990). Residual strain in rat left ventricle. *Circulation Research*, 66:37–45.

Omens, J. H., MacKenna, D. A., and McCulloch, A. D. (1993). Measurement of strain and analysis of stress in resting rat left ventricular myocardium. *Journal of Biomechanics*, 26(6):665–676.

Palit, A., Bhudia, S. K., Arvanitis, T. N., Turley, G. A., and Williams, M. A. (2015a). Computational modelling of left-ventricular diastolic mechanics: Effect of fibre orientation and right-ventricle topology. *Journal of Biomechanics*, 48(4):604–612.

Palit, A., Bhudia, S. K., Arvanitis, T. N., V., S., Wayte, S., and Turley, G. A. Williams, M. A. (2015b). Effect of fibre orientation on diastolic mechanics of human ventricle. In *IEEE Engineering in Medicine and Biology Society (EMBC) 2015*.

Palit, A., Bhudia, S. K., Arvanitis, T. N., and Williams, M. A. (2015c). Modelling passive diastolic mechanics of human ventricles. (under review).

Palit, A., Franciosa, P., Bhudia, S. K., Arvanitis, T. N., Turley, G. A., and Williams, M. A. (2015d). The estimation of passive orthotropic properties of human myocardium. (under review in Computer Methods in Biomechanics and Biomedical Engineering).

Palit, A., Turley, G. A., Bhudia, S. K., Wellings, R., and Williams, M. A. (2014). Assigning myocardial fibre orientation to a computational biventricular human heart model. In Goh, J., editor, *The 15th International Conference on Biomedical Engineering*, volume 43 of *IFMBE Proceedings*, pages 144–147. Springer International Publishing.

Panda, S. C. and Natarajan, R. (1977). Finite-element method of stress analysis in the human left ventricular layered wall structure. *Medical and Biological Engineering and Computing*, 15:67–71.

Pao, Y. C., Robb, R. A., and Ritman, E. L. (1976). Plane-strain finite-element analysis of reconstructed diastolic left ventricular cross section. *Annals of Biomedical Engineering*, 4(3):232–249.

Paulus, W. J. and Tschpe, C. (2013). A novel paradigm for heart failure with preserved ejection fractioncomorbidities drive myocardial dysfunction and remodeling through coronary microvascular endothelial inflammation. *Journal of the American College of Cardiology*, 62(4):263–271.

Perl, M., Horowitz, A., and Sideman (1986). Comprehensive model for the simulation of left ventricle mechanics. part1 model description and simulation procedure. *Medical and Biological Engineering and Computing*, 24:145–149.

Peters, J., Ecabert, O., Schmitt, H., Grass, M., and Weese, J. (2009). *Local Cardiac Wall Motion Estimation from Retrospectively Gated CT Images*, volume 5528 of *Lecture Notes in Computer Science*, book section 21, pages 191–200. Springer Berlin Heidelberg.

Petitjean, C. and Dacher, J. N. (2011). A review of segmentation methods in short axis cardiac mr images. *Medical Image Analysis*, 15:169–184.

Pope, A. J., Sands, G. B., Smaill, B. H., and LeGrice, I. J. (2008). Three-dimensional transmural organization of perimysial collagen in the heart. *American Journal of Physiology - Heart and Circulatory Physiology*, 295:H1243–H1252.

Potse, M., Dube, B., Richer, J., Vinet, A., and Gulrajani, R. M. (2006). A comparison of monodomain and bidomain reaction-diffusion models for action potential propagation in the human heart. *Biomedical Engineering, IEEE Transactions on*, 53(12):2425–2435.

Remme, E. W., Hunter, P. J., Smiseth, O., Stevens, C., Rabben, S. I., Skulstad, H., and Angelsen, B. (2004). Development of an in vivo method for determining material properties of passive myocardium. *Journal of Biomechanics*, 37(5):669–678.

Rijcken, J., Bovendeerd, P. H. M., Schoofs, A. J. G., Van-Campen, D. H., and Arts, T. (1999). Optimization of cardiac fiber orientation for homogeneous fiber strain during ejection. *Annals of Biomedical Engineering*, 27:289–297.

Rohmer, D., Sitek, A., and Gullberg, G. T. (2007). Reconstruction and visualization of fiber and laminar structure in the normal human heart from ex vivo diffusion tensor magnetic resonance imaging (dtmri) data. *Investigative Radiology*, 42(11):777–789.

Sandler, H. and Dodge, H. T. (1963). Left ventricular tension and stress in man. *Circulation Research*, 13(2):91–104.

Schmid, H., Nash, M. P., Young, A. A., and Hunter, P. J. (2006). Myocardial material parameter estimationa comparative study for simple shear. *Journal of Biomechanical Engineering*, 128:742–750.

Schmid, H., OCallaghan, P., Nash, M. P., Lin, W., LeGrice, I. J., Smaill, B. H., Young, A. A., and Hunter, P. J. (2008). Myocardial material parameter estimation: a non-homogeneous finite element study from simple shear tests. *Biomechanics and Modeling in Mechanobiology*, 7:161–173.

Smaill, B. H., LeGrice, I. J., Hooks, D. A., Pullan, A. J., Caldwell, B. J., and Hunter, P. J. (2004). Cardiac structure and electrical activation: models and measurement. *Clin Exp Pharmacol Physiol*, 31(12):913–9.

Sommer, G., Haspinger, D. C., Andra, M., Sacherer, M., Viertler, C., Regitnig, P., and Holzapfel, G. A. (2015a). Quantification of shear deformations and corresponding stresses in the biaxially tested human myocardium. *Annals of Biomedical Engineering*, 43:2334–2348.

Sommer, G., Schriefl, A. J., Andr, M., Sacherer, M., Viertler, C., Wolinski, H., and Holzapfel, G. A. (2015b). Biomechanical properties and microstructure of human ventricular myocardium. *Acta Biomaterialia*, 24:172–192.

Spencer, A. (1984). *Continuum theory of the mechanics of fibre-reinforced composites*. Wien: Springer.

Stevens, C., Remme, E., LeGrice, I., and Hunter, P. (2003). Ventricular mechanics in diastole: material parameter sensitivity. *Journal of Biomechanics*, 36(5):737–748.

Streeter, D. D., Ramesh, J. R., Vaishnav, N., Patel, D. J., Spotnitz, H. M., Ross, J., and Sonnenblick, E. H. (1970). Stress distribution in the canine left ventricle during diastole and sstok. *Biophysical Journal*, 10:345–363.

Streeter, D. D. J. and Basset, D. L. (1966). An engineering analysis of myocardial fibre orientation in pig's left ventricle in systole. *The Anatomical Record*, 155:503–511.

Streeter, D. D. J. and Hanna, W. L. (1973). Engineering mechanics for successive states in canine left ventricular myocardium : Ii.fiber angle and sarcomere length. *Circulation Research*, 33:656–664.

Streeter, D. D. J., Spotnitz, D. P. P., Ross, J. J., and Sonnenblick, E. H. (1969). Fiber orientation in the canine left ventricle during diastole and systole. *Circulation Research*, 24:339–347.

Stuckey, D. J., Carr, C. A., Tyler, D. J., and Clarke, K. (2008). Cine-mri versus two-dimensional echocardiography to measure in vivo left ventricular function in rat heart. *NMR in Biomedicine*, 21(7):765–772.

Sun, K., Stander, N., Jhun, C.-S., Zhang, Z., Suzuki, T., Wang, G.-Y., Saeed, M., Wallace, A. W., Tseng, E. E., J.Baker, A., Saloner, D., Einstein, D. R., Ratcliffe, M. B., and M.Guccione, J. (2009). A computationally efficient formal optimization of regional myocardial contractility in a sheep with left ventricular aneurysm. *Journal of Biomechanical Engineering*, 131:111001/1 – 111001/10.

Sun, K., Zhang, Z., Suzuki, T., Wenk, J., Stander, N., Einstein, D. R., Saloner, D. A., Wallace, A. W., Guccione, J. M., and Ratcliffe, M. B. (2010). Dor procedure for dyskinetic anteroapical myocardial infarction fails to improve contractility in the borderzone. *The Journal of Thoracic and Cardiovascular Surgery*, 140(1):233 –239.

Takayama, K., Ashihara, T., Ijiri, T., Igarashi, T., Haraguchi, R., and Nakazawa, K. (2008). A sketch-based interface for modeling myocardial fiber orientation that considers the layered structure of the ventricles. *The Journal of Physiological Sciences*, 58(7):487–492.

Tang, D., Yang, C., Geva, T., Gaudette, G., and Nido, P. J. d. (2010). Effect of patch mechanical properties on right ventricle function using mri-based two-layer anisotropic models of human right and left ventricles. *Computer Modeling in Engineering & Sciences*, 56(2):113–130.

Tang, D., Yang, C., Geva, T., Gaudette, G., and Nido, P. J. d. (2011). Multi-physics mri-based two-layer fluidstructure interaction anisotropic models of human right and left ventricles with different patch materials:cardiac function assessment and mechanical stress analysis. *Computers and Structures*, 89:1059–1068.

Thiele, H., Paetsch, I., Schnackenburg, B., Bornstedt, A., Grebe, O., Wellnhofer, E., Schuler, G., Fleck, E., and Nagel, E. (2002). Improved accuracy of quantitative assessment of left ventricular volume and ejection fraction by geometric models with steady-state free precession. *J Cardiovasc Magn Resonance*, 4(3):327–39.

Toussaint, N., Stoeck, C. T., Schaeffter, T., Kozerke, S., Sermesant, M., and Batchelor, P. G. (2013). In vivo human cardiac fibre architecture estimation using shape-based diffusion tensor processing. *Medical Image Analysis*, 17(8):1243–1255.

Tozeren, A. (1983). Static analysis of the left ventricle. *Journal of Biomechanical Engineering*, 105(1):39–46.

Usyk, T. P., Mazhari, R., and McCulloch, A. D. (2000). Effect of laminar orthotropic myofiber architecture on regional stress and strain in the canine left ventricle. *Journal of Elasticity*, 31:143–164.

Vetter, F. J. and McCulloch, A. D. (2000). Three-dimensional stress and strain in passive rabbit left ventricle: A model study. *Annals of Biomedical Engineering*, 28:781 – 792.

Vinson, C. A. (1977). *Analysis of Stress and Deformation in the Human Left Ventricle*. PhD thesis, Department of Mechanical Engineering, Brunel University.

Vinson, C. A., Gibson, D. G., and Yettram, A. L. (1979). Analysis of left ventricular behaviour in diastole by means of finite element method. *British Heart Journal*, 41:60–67.

Vossoughi, J., Vaishnav, R. N., and Patel, D. J. (1980). Compressibility of the myocardial tissue.

Walker, J. C., Ratcliffe, M. B., Zhang, P., Wallace, A. W., Fata, B., Hsu, E. W., Saloner, D., and Guccione, J. M. (2005). Mri-based finite-element analysis of left ventricular aneurysm. *American Journal of Physiology - Heart and Circulatory Physiology*, 289:H692–H700.

Walker, J. C., Ratcliffe, M. B., Zhang, P., Wallace, A. W., Hsu, E. W., Saloner, D. A., and Guccione, J. M. (2008). Magnetic resonance imaging-based finite element stress analysis after linear repair of left ventricular aneurysm. *The Journal of Thoracic and Cardiovascular Surgery*, 135(5):1094 – 1102.

Wall, S. T., Walker, J. C., Healy, K. E., Ratcliffe, M. B., and Guccione, J. M. (2006). Theoretical impact of the injection of material into the myocardium: a finite element model simulation. *Circulation*, 114(24):2627–35.

Wallen, W. J. and Rao, V. (2010). Surgical remodeling of the left ventricle in heart failure. *Annals of Thoracic and Cardiovascular Surgery*, 16(2):72–77. overview and problem realted to surgical remodeling.

Wang, H. M., Gao, H., Luo, X. Y., Berry, C., Griffith, B. E., Ogden, R. W., and 1, T. J. W. (2013a). Structure-based finite strain modelling of the human left ventricle in diastole. *International Journal for Numerical Methods in Biomedical Engineering*, 29:83–103.

Wang, H. M., Luo, X. Y., Gao, H., Ogden, R. W., Griffith, B. E., Berry, C., and Wang, T. J. (2014). A modified holzapfel-ogden law for a residually stressed finite strain model of the human left ventricle in diastole. *Biomechanics and Modeling in Mechanobiology*, 13(1):99–113.

Wang, J. and Nagueh, S. F. (2009). Current perspectives on cardiac function in patients with diastolic heart failure. *Circulation*, 119(8):1146–1157.

Wang, V., Ennis, D., Cowan, B., Young, A., and Nash, M. (2012). *Myocardial Contractility and Regional Work throughout the Cardiac Cycle Using FEM and MRI*, volume 7085 of *Lecture Notes in Computer Science*, book section 15, pages 149–159. Springer Berlin Heidelberg.

Wang, V., Lam, H., Ennis, D., Cowan, B., Young, A., and Nash, M. (2010). *Cardiac Active Contraction Parameters Estimated from Magnetic Resonance Imaging*, volume 6364 of *Lecture Notes in Computer Science*, book section 20, pages 194–203. Springer Berlin Heidelberg.

Wang, V., Young, A., Cowan, B., and Nash, M. (2013b). *Changes in In Vivo Myocardial Tissue Properties Due to Heart Failure*, volume 7945 of *Lecture Notes in Computer Science*. Springer Berlin Heidelberg.

Wang, V. Y., Lam, H. I., Ennis, D. B., Cowan, B. R., Young, A. A., and Nash, M. P. (2009). Modelling passive diastolic mechanics with quantitative mri of cardiac structure and function. *Medical Image Analysis*, 13(5):773–784.

Weiss, J. A. (1994). *A constitutive model and finite element representation for transversely isotropic soft tissue*. Thesis, Swiss Federal Institute of Technology Zurich.

Weiss, J. A., Makerc, B. N., and Govindjeed, S. (1996). Finite element implementation of incompressible, transversely isotropic hyperelasticity. *Computer Methods in Applied Mechanics and Engineering*, 135:107–128.

Wenk, J. F., Eslami, P., Zhang, Z., Xu, C., Kuhl, E., III, J. H. G., Robb, J. D., Ratcliffe, M. B., MD, R. C. G., and Guccione, J. M. (2011a). A novel method for quantifying the in-vivo mechanical effect of material injected into a myocardial infarction. *The Annals of Thoracic Surgery*, 92:935 – 941.

Wenk, J. F., Ge, L., Zhang, Z., Mojsejenko, D., Potter, D. D., Tseng, E. E., Guccione, J. M., and Ratcliffe, M. B. (2013). Biventricular finite element modeling of the acorn corcap cardiac support device on a failing heart. *The Annals of Thoracic Surgery*, 95(6):2022–2027.

Wenk, J. F., Ge, L., Zhang, Z., Soleimani, M., Potter, D. D., Wallace, A. W., Tseng, E., Ratcliffe, M. B., and Guccione, J. M. (2012). A coupled biventricular finite element and lumped-parameter circulatory system model of heart failure. *Computer Methods in Biomechanics and Biomedical Engineering*, 16:807–818.

Wenk, J. F., Sun, K., Zhang, Z., Soleimani, M., Ge, L., Saloner, D., Wallace, A. W., Ratcliffe, M. B., and Guccione, J. M. (2011b). Regional left ventricular myocardial contractility and stress in a finite element model of posterobasal myocardial infarction. *Journal of Biomechanical Engineering*, 133(4):044501–1 – 044501–6.

Wong, A. Y. K. and Rautaharju, P. M. (1968). Stress distribution within the left ventricular wall approximated as a thick ellipsoidal shell. *American Heart Journal*, 75(5):649–662.

Wong, J. and Kuhl, E. (2014). Generating fibre orientation maps in human heart models using poisson interpolation. *Computer Methods in Biomechanics and Biomedical Engineering*, 17(11):1217–26.

Wong, K. L., Wang, L., and Shi, P. (2009). *Active Model with Orthotropic Hyperelastic Material for Cardiac Image Analysis*, volume 5528 of *Lecture Notes in Computer Science*, book section 25, pages 229–238. Springer Berlin Heidelberg.

Xi, J., Lamata, P., Niederer, S., Land, S., Shi, W., Zhuang, X., Ourselin, S., Duckett, S. G., Shetty, A. K., Rinaldi, C. A., Rueckert, D., Razavi, R., and Smith, N. P. (2013). The estimation of patient-specific cardiac diastolic functions from clinical measurements. *Medical Image Analysis*, 17(2):133–46.

Xi, J., Lamata, P., Shi, W., Niederer, S., Land, S., Rueckert, D., Duckett, S., Shetty, A., Rinaldi, C. A., Razavi, R., and Smith, N. (2011a). *An Automatic Data Assimilation Framework for Patient-Specific Myocardial Mechanical Parameter Estimation*, volume 6666 of *Lecture Notes in Computer Science*, book section 50, pages 392–400. Springer Berlin Heidelberg.

Xi, J., Lamataa, P., Leeb, J., Moireauc, P., Chapellec, D., and Smitha, N. (2011b). Myocardial transversely isotropic material parameter estimation from in-silico measurements based on a reduced-order unscented kalman filter. *Journal of the Mechanical Behavior of Biomedical Materials*, 4:1090–1102.

Yang, C., Tang, D., Geva, T., and Nido, P. J. d. (2008). Mri-based patient-specific computational modeling of right ventricular response to pulmonary valve insertion surgery: a passive anisotropic fsi model with fiber orientation. pages 160 – 167. IEEE Computer Society.

Yettram, A. L., Vinson, C. A., and Gibson, D. G. (1983). Effect of myocardial fiber architecture on the behavior of the human left ventricle in diastole. *Journal of Biomedical Engineering*, 5:321–328.

Yin, F. C., Chan, C. C., and Judd, R. M. (1996). Compressibility of perfused passive myocardium. *American Journal of Physiology - Heart and Circulatory Physiology*, 271(5 Pt 2):H1864–70.

Yin, F. C. P., Strumpf, R. K., Chew, P. H., and Zeger, S. L. (1987). Quantification of the mechanical properties of noncontracting canine myocardium under simultaneous biaxial loading. *Journal of Biomechanics*, 20:577–589.

Appendix A

BSREC Ethics Approval

Biomedical and Scientific Research Ethics Committee (BSREC) ethics approval was obtained to carry out the research on anonymised patient data. The project proposal underwent through a light touch review process by BSREC as the project only used anonymised MRI data of human heart.

The BSREC ethic approval for the project is attached in the next page.

11th April 2013

Warwick Medical School

PRIVATE
Arnab Palit
WMG
University of Warwick
Coventry
CV4 7AL

Dear Arnab,

Study Title and BSREC Reference: *3D Modelling and Analysis of the Human Heart's Ventricle for Designing Patient-Specific Optimal Surgical Plan,* **REGO-2012-032**

Thank you for submitting the above-named project to the University of Warwick Biomedical and Scientific Research Ethics Sub-Committee for Chair's approval.

I am pleased to confirm that your application meets the required standard which means that full approval is granted and your study may commence.

I take this opportunity to wish you success with the study and to remind you any substantial amendments require approval from the committee before they can be made. Please keep a copy of the original signed version of this letter with your study documentation.

Yours sincerely,

Dr David Davies
Chair
Biomedical and Scientific
Research Ethics Sub-Committee

Copy: Mark Williams

Biomedical and Scientific Research Ethics Subcommittee
Enquiries: Amy Ismay
B032 Medical School Building
Warwick Medical School,
Coventry, CV4 7AL.
Tel: 02476-151875
Email: A.C.Ismay@warwick.ac.uk

THE UNIVERSITY OF WARWICK

Appendix B

FE Code for Material Model using Hypela2

```
      subroutine hypela2(d,g,e,de,s,t,dt,ngens,m,nn,kcus,matusx,ndi,
     2              nshear,disp,dispt,coord,ffn,frotn,strechn,eigvn,ffn1,
     3                     frotn1,strechn1,eigvn1,ncrd,itel,ndeg,ndm,
     4                     nnode,jtype,lclassx,ifr,ifu)
c
c
c *************   user subroutine for defining material behavior  **************
c
CAUTION : Due to calculation of the Deformation gradients, Stretch Tensors and
c         Rotation tensors at previous and current states, the analysis can be
c         computationally expensive. Please use the user subroutine >  hypela
c         if these kinematic quantities are not needed in the constitutive model
c
c IMPORTANT NOTES :
c
c (1) F,R,U are only available for continuum and membrane elements (not for
c     shells and beams).
c
c (2) For total Lagrangian formulation use the > 'Elasticity,1' card(=
c     total Lagrange with large disp) in the parameter section of input deck.
c     For updated Lagrangian formulation use the > 'Plasticity,3' card(=
c     update+finite+large disp+constant d) in the parameter section of
c     input deck.
c
c     d             stress strain law to be formed
c     g             change in stress due to temperature effects
c     e             total elastic strain
c     de            increment of strain
c     s             stress   should be updated by user
c     t             state variables (comes in at t=n, must be updated
c                                    to have state variables at t=n+1)
c     dt            increment of state variables
c     ngens         size of stress   strain law
c     m(1)          user element number
c     m(2)          internal element number
c     nn            integration point number
c     kcus(1)       layer number
c     kcus(2)       internal layer number
c     matus(1)      user material identification number
c     matus(2)      internal material identification number
c     ndi           number of direct components
c     nshear        number of shear components
c     disp          incremental displacements
c     dispt         displacements at t=n   (at assembly,        lovl=4) and
c                   displacements at t=n+1 (at stress recovery, lovl=6)
c     coord         coordinates
```

```
c      ncrd          number of coordinates
c      ndeg          number of degrees of freedom
c      itel          dimension of F and R, either 2 or 3
c      nnode         number of nodes per element
c      jtype         element type
c      lclass(1)     element class
c      lclass(2)     Herrmann element flag (1) lower order, (2)  higher order
c      ifr           set to 1 if R has been calculated
c      ifu           set to 1 if strech has been calculated
c
c      at t=n   :
c
c      ffn           deformation gradient
c      frotn         rotation tensor
c      strechn       square of principal stretch ratios, lambda(i)
c      eigvn(i,j)    i principal direction components for j eigenvalues
c
c      at t=n+1 :
c
c      ffn1          deformation gradient
c      frotn1        rotation tensor
c      strechn1      square of principal stretch ratios, lambda(i)
c      eigvn1(i,j)   i principal direction components for j eigenvalues
c
c      The following operation obtains U (stretch tensor) at t=n+1 :
c
c      call scla(un1,0.d0,itel,itel,1)
c      do 3 k=1,3
c       do 2 i=1,3
c        do 1 j=1,3
c         un1(i,j)=un1(i,j)+sqrt(strechn1(k))*eigvn1(i,k)*eigvn1(j,k)
c1      continue
c2     continue
c3     continue
c
       implicit none

c      Inbuilt or Marc defined common block
       include '../common/concom'
       include '../common/array2'
       include '../common/heat'
       include '../common/space'
       include '../common/creeps'
       include '../common/BCLABEL'

c      user defined common block
       include 'common_matdat'

c      Marc defined variable
       real*8 coord, d, de, disp, dispt, dt, e, eigvn, eigvn1, ffn, ffn1
       real*8 frotn, frotn1, g
       real*8 s, strechn, strechn1, t

       integer ifr, ifu, itel, jtype, kcus, lclassx, matusx, m, ncrd,ndeg
       integer ndi, ndm, ngens, nn, nnode, nshear
c
       dimension e(*),de(*),t(*),dt(*),g(*),d(ngens,*),s(*)
       dimension m(2),coord(ncrd,*),disp(ndeg,*),matusx(2),
     *           dispt(ndeg,*),ffn(itel,*),frotn(itel,*),
     *           strechn(itel),eigvn(itel,*),ffn1(itel,*),
     *           frotn1(itel,*),strechn1(itel),eigvn1(itel,*),
     *           kcus(2),lclassx(2)

c      user defined variable
       real*8  detf, getotal, rcgdtotal, rcgdtotalinv, rcgddev,
      1 strain, rsumm, rabs, gg, aa, totaltime, volchange, volchnageratio
       integer iopen, nr, kl, ierrfl, il, i2, i3, il, gausspoint
       integer mint, ielint, lporient, irrfl,firstflag

       dimension getotal(ngens), strain(ngens)
       dimension rcgdtotal(3,3), rcgdtotalinv(3,3), rcgddev(3,3)
       dimension gg(ndi,ndi),aa(ndi,ndi)

c      define local parameters
       save iopen
       logical there
       data iopen/1/
       data firstflag/1/

c      nr = element number
       nr = m(1)

c      ~~~~~~~~~~~~~~~~~~~~~~~~~~~~~~~~~~~~~~~~~~~~~~~~~~~~~~~~~~~~~~~~~~~~~~~
c      read input file

       if(iopen.eq.1)then
           iopen = 0
```

```
          if(readfileflag.eq.1) then
c             read material coefficient from input data file 'matcoeff'
              inquire(file='matcoeff',exist=there)
              if(.not.there) goto 9005
              open(200,file='matcoeff',status='old')
c             read passive material parameter
              read(200,*,end=9012,err=9012)a,b,af,bf,as,bs,afs,bfs,d1
c             read active stress values
              read(200,*,end=9012,err=9012)fact, sact, nact, snact
              read(200,*,end=9012,err=9012) Cp, Cprv, Cao, Rao, Cpa, Rpa
              read(200,*,end=9012,err=9012) edp,diap, sysp
              read(200,*,end=9012,err=9012) edv, esv
              open (unit = 1234, file = "material_patameter.txt")
              close(200)
          end if

c     ~~~~~~~~~~~~~~~     end of reading file 'matcoeff'     ~~~~~~~~~~~~~~~~~~~~
c     ~~~~~~~~~~~~~~      start of reading orientation'     ~~~~~~~~~~~~~~~~~~~~

c         read orientation vector from fibre_orientation file

          inquire(file='fibre_orientation.txt',exist=there)
          if(.not.there) goto 9002
          open(201,file='fibre_orientation.txt',status='old')
          do 10 i1=1,nelm
              read(201,*,err=9011,end=9003)
     1            raniso(i1,1), raniso(i1,2), raniso(i1,3),
     2            raniso(i1,4), raniso(i1,5), raniso(i1,6),
     3            raniso(i1,7), raniso(i1,8), raniso(i1,9)

            do 25 i2=1,9
                raniso1(i1,i2)=raniso1(i1,i2)
25          continue
c           check for orthogonality of orientation vectors in raniso
            rsumm=0.0d0
            do 5 i2=1,3
                rsumm=rsumm+raniso(i1,i2)*raniso(i1,i2+3)
5           continue
            if(dabs(rsumm).gt.1.0d 6)then
                ierrfl=1
                goto 9004
            end if

            rsumm=0.0d0
            do 6 i2=1,3
                rsumm=rsumm+raniso(i1,i2)*raniso(i1,i2+6)
6           continue
            if(dabs(rsumm).gt.1.0d 6)then
                ierrfl=2
                goto 9004
            end if

            rsumm=0.0d0
            do 7 i2=1,3
                rsumm=rsumm+raniso(i1,i2+3)*raniso(i1,i2+6)
7           continue
            if(dabs(rsumm).gt.1.0d 6)then
                ierrfl=3
                goto 9004
            end if
c           make orientation vectors in raniso unit vectors and double check again
            il=0
            do 50 i3=1,3
                rabs=0.0d0
                do 60 i2=1,3
                    rabs=rabs+raniso(i1,i2+il)*raniso(i1,i2+il)
60              continue
                rabs=dsqrt(rabs)
                rsumm=0.0d0
                do 70 i2=1,3
                    raniso(i1,i2+il)=raniso(i1,i2+il)/rabs
                    rsumm=rsumm+raniso(i1,i2+il)*raniso(i1,i2+il)
70              continue
                rsumm=dabs(dsqrt(rsumm) 1.0d0)
                if(rsumm.gt.1.0d 4)goto 9006
                il=il+3
50          continue
10        continue
          close(201)

          open(202,file='fibre_orientation_deformed.out',
     +          form='formatted',status='unknown')
          close(202,status='delete')
          open(202,file='fibre_orientation_deformed.out',
     +       form='formatted',status='new')

c         read local cradiac coordinate for each element
```

```
      inquire(file='local_cardiac_coordinate.txt',exist=there)
      if(.not.there) goto 9018
      open(203,file='local_cardiac_coordinate.txt',status='old')
      do 100 i1=1,nelm
          read(203,*,err=9011,end=9003)
     1         loccardsys(i1,1), loccardsys(i1,2), loccardsys(i1,3),
     2         loccardsys(i1,4), loccardsys(i1,5), loccardsys(i1,6),
     3         loccardsys(i1,7), loccardsys(i1,8), loccardsys(i1,9)
c       check for orthogonality of orientation vectors in loccardsys

          rsumm=0.0d0
          do 105 i2=1,3
              rsumm=rsumm+loccardsys(i1,i2)*loccardsys(i1,i2+3)
105         continue
          if(dabs(rsumm).gt.1.0d 6)then
              ierrfl=1
              goto 9004
          end if

          rsumm=0.0d0
          do 106 i2=1,3
              rsumm=rsumm+loccardsys(i1,i2)*loccardsys(i1,i2+6)
106         continue
          if(dabs(rsumm).gt.1.0d 6)then
              ierrfl=2
              goto 9004
          end if

          rsumm=0.0d0
          do 107 i2=1,3
              rsumm=rsumm+loccardsys(i1,i2+3)*loccardsys(i1,i2+6)
107         continue
          if(dabs(rsumm).gt.1.0d 6)then
              ierrfl=3
              goto 9004
          end if
c         make orientation vectors in loccardsys unit vectors and double check again
          il=0
          do 350 i3=1,3
              rabs=0.0d0
              do 360 i2=1,3
                  rabs=rabs+loccardsys(i1,i2+il)*
     1                loccardsys(i1,i2+il)
360           continue
              rabs=dsqrt(rabs)
              rsumm=0.0d0
              do 370 i2=1,3
                  loccardsys(i1,i2+il)=loccardsys(i1,i2+il)/rabs
                  rsumm=rsumm+loccardsys(i1,i2+il)*
     1                loccardsys(i1,i2+il)
370           continue
              rsumm=dabs(dsqrt(rsumm) 1.0d0)
              if(rsumm.gt.1.0d 4)goto 9006
              il=il+3
350       continue
100     continue
        close(203)
      endif
c     ~~~~~~~~~~~~~~~~~~~~~~~~~~~~~~~~~~~~~~~~~~~~~~~~~~~~~~~~~~~~~~~~~~~~~~~~~~~~
      open (unit = 12345, file = "volume.txt")
      open (unit = 11111, file = "volumechange.txt")

c     total time of the job
      totaltime = cptim+timinc

c     lv cavity volume change
      volchange = lvolc   lvolp
      volchnageratio = abs(volchange/lvolp)

c     call to activepart in loadcase2 (isovolumic_contraction) i.e. when totaltime of job
     >= 1.0
      !if(ncycle.eq.0 .and. totaltime.ge.1.0d0)then
      if(totaltime.ge.1.0d0)then
          call activepart(nr,nn,firstflag)
          firstflag = 0
      end if

c      for nycyle = 0, getotal = e()
c      for ncycle > 0, getotal = e + de
      if(ncycle.eq.0)then
          do k1 = 1,ngens
              getotal(k1) = e(k1)
          end do
      else
          call gmadd (e,de,getotal,ngens,1)
      end if
```

```
c      calcuulate ight cauchy green deformation tesnor from Green Lagrange strain
       call greenLangstrain(getotal, nr, nn, ngens, detf, rcgdtotal,
     1                      rcgdtotalinv, rcgddev)

c      Calculate 2PK stress
       call secondpkstress(nr,nn, ndi, nshear, ngens, detf, rcgdtotal,
     1                     rcgdtotalinv, rcgddev, s)

c      Calculate material stiffness using finite difference method
       call stiffness(nr, nn, ndi, nshear, ngens, getotal, d)

c     ~~~~~~~~~~~~~~~~~~~~~~~~~~~~~~~~~~~~~~~~~~~~~~~~~~~~~~~~~~~~~~~~~~~~~~~~~~~~
c      calculate rotation of the fibre
       if(lovl.eq.6)then

c          initialize rrotat; as only one averaged rotation matrix will be computed per
     element, do it only once per elemnte (nn=1)
           if(nn.eq.1)then
               do 150 i1=1,3
                   do 151 i2=1,3
                       rrotat(i1,i2)=0.0d0
151                continue
150            continue
           end if

c          add current rotation matrix at integration point to rrotat
           do 155 i1=1,3
               do 156 i2=1,3
                   rrotat(i1,i2)=rrotat(i1,i2)+frotn1(i1,i2)
156            continue
155        continue
           gausspoint = 0
           if(jtype.eq.134) then
               gausspoint = 1
           elseif (jtype.eq.157) then
               gausspoint = 4
           end if
           if(nn.eq.gausspoint)then
               !  if (nr.eq.1 .or. nr.eq.2) then
               !    write(12345,*) 'jtype, gauus point',jtype,gausspoint
               !end if
               do 160 i1=1,3
                   rsumm=0.0d0
                   do 161 i2=1,3
                       rsumm=rsumm+rrotat(i2,i1)*rrotat(i2,i1)
161                continue
                   rsumm=dsqrt(rsumm)
                   do 162 i2=1,3
                       rrotat(i2,i1)=rrotat(i2,i1)/rsumm
162                continue
160            continue

               do 200 i1=1,3
                   do 202 i2=1,3
                       gg(i1,i2)=0.0d0
202                continue
200            continue
               il=0
               do 205 i2=1,3
                   do 210 i1=1,3
                       gg(i1,1)=raniso(nr,i1+il)
210                continue
c                  rotate orientation vector in original configuration raniso to the
     current configuration raniso1
                   call tjrrotat(gg,aa,rrotat,2,1)
                   do 220 i1=1,3
                       raniso1(nr,i1+il)=aa(i1,1)
220                continue
                   il=i1+3
205            continue
               if (nr.eq.1 .or. nr.eq.2) then
                   write(202,*)'~~~~~~~~~~~~~~~~~~~~~~~~~~~~~~~~~~~~~~~~~~~~~~~~~~~',
                   write(202,*)
     1             raniso1(nr,1), raniso1(nr,2), raniso1(nr,3),
     2             raniso1(nr,4), raniso1(nr,5), raniso1(nr,6),
     3             raniso1(nr,7), raniso1(nr,8), raniso1(nr,9)
                   write(202,*)'~~~~~~~~~~~~~~~~~~~~~~~~~~~~~~~~~~~~~~~~~~~~~~~~~~~',
               end if
         end if
       end if
       goto 9999

c*********************************************************************************c
c      error messages                                                             c
c *********************************************************************************c
9002   write(6,*)' '
```

```
      write(6,*)'****************************************'
      write(6,*)'error message from hypela.f:'
      write(6,*)'fibre_orientation.txt'
      write(6,*)'does not exist!'
      write(6,*)'****************************************'
      write(6,*)' '
      call quit(9002)

9003  write(6,*)' '
      write(6,*)'****************************************'
      write(6,*)'error message from hypela.f:'
      write(6,*)'orientation vector file fibre_orientation.txt'
      write(6,*)'has not enough entries for all elements!'
      write(6,*)'****************************************'
      write(6,*)' '
      call quit(9003)

9005  write(6,*)' '
      write(6,*)'************************************************'
      write(6,*)'Error message from hypela.f:'
      write(6,*)'material input data does not exist!'
      write(6,*)'define material input data "matcoeff"'
      write(6,*)'************************************************'
      write(6,*)' '
      call quit(9005)

9004  write(6,*)' '
      write(6,*)'****************************************'
      write(6,*)'error message from hypela.f:'
      write(6,*)'orientation vectors in fibre_orientation.txt'
      write(6,*)'are not orthogonal!                    '
      write(6,*)'element: ',nelm
      if(irrfl.eq.1)then
        write(6,*)'vector 1 and 2'
      else if(irrfl.eq.2)then
        write(6,*)'vector 1 and 3'
      else if(irrfl.eq.3)then
        write(6,*)'vector 2 and 3'
      end if
      write(6,*)'****************************************'
      write(6,*)' '
      call quit(9004)

9006  write(6,*)' '
      write(6,*)'****************************************'
      write(6,*)'Error message from hypela.f:'
      write(6,*)'Anisotropy vector is not a unit vector!'
      write(6,*)'Element number: ',nr
      write(6,*)'Integr. Point: ',nn
      write(6,*)'****************************************'
      write(6,*)' '
      call quit(9006)

9008  write(6,*)' '
      write(6,*)'****************************************'
      write(6,*)'Error message from hypela.f:'
      write(6,*)'Largest element number is greater than     '
      write(6,*)'parameter nelm in common_matdat! Increase  !'
      write(6,*)'nelm and recompile the program!      '
      write(6,*)'****************************************'
      write(6,*)' '
      call quit(9008)

9011  write(6,*)' '
      write(6,*)'********************************************'
      write(6,*)'error message from hypela2.f:'
      write(6,*)'error while reading vectors defining anisotropy!'
      write(6,*)'********************************************'
      write(6,*)' '
      call quit(9011)

9012  write(6,*)' '
      write(6,*)'************************************************'
      write(6,*)'error message from hypela2.f:'
      write(6,*)'error while reading material input data  '
      write(6,*)'file matcoeff.dat . please check the file input!'
      write(6,*)'************************************************'
      write(6,*)' '
      call quit(9012)
9018  write(6,*)' '
      write(6,*)'************************************************'
      write(6,*)'error message from hypela2.f:'
      write(6,*)'error while reading local cardiac coordinate file'
      write(6,*)'file . please check the file input!'
      write(6,*)'************************************************'
      write(6,*)' '
      call quit(9018)
```

```
c**********************************************************************c

9999  return
      end


      subroutine greenLangstrain(getotal, nr, nn, ngens, detf,
     1                           rcgdtotal, rcgdtotalinv, rcgddev)


c     input

c     getotal          total elastic strain   Green Lagrange strain
c     nr               element number
c     nn               gauss point
c     ngens            size of stress   strain law

c     output

c     rcgdtotal        total right cauchy green deformation tesnor
c     detf             determinant of rcgdtotal
c     rcgdtotalinv     invariance of rcgdtotal
c     rcgddev          deviatoric right cauchy green deformation tesnor
c                      = J(-2/3).rcgdtotal


      implicit none

      real*8 rcgdtotal, rcgdtotalinv, rcgddev, rcgddet,
     1       detf, j, jfact, getotal, rcgddet1
      integer nr, nn, k1, k2, ngens
      dimension rcgdtotal(3,3), rcgdtotalinv(3,3), rcgddev(3,3),
     1          getotal(ngens)


c     determine total right cauchy green deformation tesnor (Please check attcahed
     derivation Pdf)


      rcgdtotal(1,1) = 1.0d0 + 2.0d0 * getotal(1)
      rcgdtotal(2,2) = 1.0d0 + 2.0d0 * getotal(2)
      rcgdtotal(3,3) = 1.0d0 + 2.0d0 * getotal(3)

      rcgdtotal(1,2) = getotal(4)
      rcgdtotal(2,1) = getotal(4)

      rcgdtotal(2,3) = getotal(5)
      rcgdtotal(3,2) = getotal(5)

      rcgdtotal(1,3) = getotal(6)
      rcgdtotal(3,1) = getotal(6)


c     detremine inverse of total right cauchy green deformation and its determinent
c     rcgddet = I3 = Det(rcgdtotal) = jacobian*jacobian
c     inv3x3 = utility routine in Marc

      call inv3x3 (rcgdtotal, rcgdtotalinv, rcgddet, 2)

      if (rcgddet.eq.0.0d0) goto 9013
      if (rcgddet.lt.0.0d0) goto 9014

c     determinant of deformation gradinet
      detf = dsqrt(abs(rcgddet))

      jfact = detf**(-2.0d0/3.0d0)

      do k1 = 1,3
          do k2 = 1,3
              rcgddev(k1,k2) = jfact * rcgdtotal(k1,k2)
          end do
      end do


      goto 9998

9013  write(6,*)' '
      write(6,*)'****************************************'
      write(6,*)'Error message from greenLangstrain.f:'
      write(6,*)'determinant is zero      '
      write(6,*)'rcgdtotal becomes singular  !'
      write(6,*)'      '
      write(6,*)'****************************************'
      write(6,*)' '
      call quit(9013)
```

```
9014  write(6,*)' '
      write(6,*)'****************************************'
      write(6,*)'Error from hypela: negative determinant'
      write(6,*)'of right cauchy green tensor in element',nr
      write(6,*)'integration point',nn
      write(6,*)'and rcgddet', rcgddet
      write(6,*)'****************************************'
      write(6,*)' '
      call quit(9014)

9998  return
      end


      subroutine secondpkstress(nr,nn, ndi, nshear, ngens, detf,
     1                          rcgdtotal, rcgdtotalinv, rcgddev, s)


c     input

c     nr            element number
c     nn            gauss point
c     ndi           number of direct components
c     nshear        number of shear components
c     ngens         size of stress   strain law
c     rcgdtotal     total right cauchy green deformation tesnor
c     detf          determinant of rcgdtotal
c     rcgdtotalinv  invariance of rcgdtotal
c     rcgddev       deviatoric right cauchy green deformation tesnor
c                   = J(-2/3).rcgdtotal

c     output

c     s             stress   updated by user




      implicit none
      include '../common/concom'

c     user defined common block
      include 'common_matdat'

      real*8 detf, rcgdtotal, rcgdtotalinv, rcgddev, s, j, jfact, dudj
      real*8 rinv1, rinv1dt
      real*8 rinv4f, rinv4s, rinv8fs, rinv4fdt, rinv4sdt, rinv8fsdt
      real*8 rinv1dtDEV, rinv4fdtDEV, rinv4sdtDEV, rinv8fsdtDEV
      real*8 w1, w4f, w4s, w8fs, stress

      integer nr, ndi, nshear, ngens, k1, k2, nn, idim

      dimension rcgdtotal(3,3), rcgdtotalinv(3,3), rcgddev(3,3),
     1          s(ngens), stress(3,3)
      dimension  rinv1dt(3,3), rinv4fdt(3,3), rinv4sdt(3,3),
     1           rinv8fsdt(3,3), rinv1dtDEV(3,3), rinv4fdtDEV(3,3),
     2           rinv4sdtDEV(3,3), rinv8fsdtDEV(3,3)



      idim = ndi


c     Calculate first invariant and its derivative  with respect to rcgdtotal
      call invar1(rcgddev,idim,rinv1,rinv1dt,1)

c     Calculate 4th and 8th invariant nd its derivative  with respect to rcgdtotal
      call invar4invar8(nr,nn, rcgddev, idim, rinv4f, rinv4s, rinv8fs,
     1                  rinv4fdt, rinv4sdt, rinv8fsdt, 1)


c     this is coming from strain energy function (please see attcahed pdf)
      w1  = a  * exp(b * (rinv1  - 3.0d0))
      w4f=2.0d0 *af* (rinv4f  - 1.0d0)*exp(bf * (rinv4f  - 1.0d0)**2.0d0)
      w4s=2.0d0 *as* (rinv4s  - 1.0d0)*exp(bs * (rinv4s  - 1.0d0)**2.0d0)
      w8fs=2.0d0*afs* rinv8fs * exp(bfs * rinv8fs**2.0d0)

c     Deviatoric projection : DEV(.) = (.)  - 1/3 * [(.):c]c^(-1)

      call DEV(rinv1dt,rcgdtotal,rcgdtotalinv, rinv1dtDEV )
      call DEV(rinv4fdt,rcgdtotal,rcgdtotalinv,rinv4fdtDEV)
      call DEV(rinv4sdt,rcgdtotal,rcgdtotalinv,rinv4sdtDEV)
      call DEV(rinv8fsdt,rcgdtotal,rcgdtotalinv,rinv8fsdtDEV)

      if (rinv4f.lt.1.0d0) then
          w4f = 0.0d0
```

```
      end if

      if (rinv4s.lt.1.0d0) then
          w4s = 0.0d0
      end if

      j = detf
      jfact = j**( 2.0d0/3.0d0)

c     volumetric part of stress comes from volumetric part of strain energy (see attached
     pdf)
      dudj = ( (1.0d0/j) + j )* d1

      do k1 = 1,3
          do k2 = 1,3
              stress(k1,k2) = dudj * j * rcgdtotalinv(k1,k2)
     1                      + jfact * w1 * rinv1dtDEV(k1,k2)
     2                      + jfact * w4f * rinv4fdtDEV(k1,k2)
     3                      + jfact * w4s * rinv4sdtDEV(k1,k2)
     4                      + jfact * w8fs * rinv8fsdtDEV(k1,k2)
          end do
      end do


      s(1) = stress(1,1) + sactive(nr,1)
      s(2) = stress(2,2) + sactive(nr,2)
      s(3) = stress(3,3) + sactive(nr,3)
      s(4) = stress(1,2) + sactive(nr,4)
      s(5) = stress(2,3) + sactive(nr,5)
      s(6) = stress(1,3) + sactive(nr,6)



      return
      end
```

Appendix C

Matlab Code for LDRF

```
clc
clear
close all

tstart = tic;

% import original *.inp file
filename='BV2_normal.inp';
fibre_angle_endo_input = 70;
fibre_angle_epi_input = 70;
 % read and store Vertex and element. each row of vertex and element corresponds to vertex
       number and element number erspectively
[vertex, element]=importAbaqusMesh(filename);

nnode = size(vertex,1);

% calculate stifness matrix of the whole geomtry
L_sym_fem = getAssembledKe(element, vertex);

% to get the boundary faces,node, node normal and connectivity
[Nnode,bface,bnode,Connectivity] = getNode_normal_boundary (element, vertex);

% read 3 points in for creating cutting plane parallel to tops surface
[Nplane, Pplane] = readfile_create_top_plane('early_BV2_basal_plane.asc');
% disp ('top plane created');

%get the surface excluding top
bfacecrop=setCropPlane(bface, Connectivity, vertex, bnode, Pplane, Nplane);
% disp ('top surface removed');

point_on_bfacecrop =  bfacecrop(1,1);
vertex_point_bface= vertex(point_on_bfacecrop,:);
vec1 = vertex_point_bface   Pplane;
dist = dot(Nplane, vec1);

if(dist > 0)
    Nplane =   Nplane;
end

% get connected domains
domain=growingComponents(bfacecrop);
% disp('lv, rv and outer shell seperated');

if length(domain) == 3
%get the rvdomain and apex point
%for all case, domain_each(1) = lv, domain_each(2) = rv,domain_each(3) = outepi
[domain_each, Papex, rvbottom, dis]= checkRV_findapexpoint(domain,bfacecrop,vertex,Pplane,
      Nplane);
% split right ventricular
[rv_epi_vertex, rv_epi_node, rv_endo_vertex, rv_endo_node] = splitrvdomain(domain,
     domain_each,bfacecrop,vertex,Papex,rvbottom,Nplane);

disp('rv surface seperated into epi and endo');

disp('apex point and each domain number identified');
elseif length(domain) == 2
    %for all case, domain_each(1) = lv, domain_each(2) = outepi
    if length(domain{1}) > length(domain{2})
        lv_inner_endo_1 = 2;
```

```
        lv_outer_epi_1 = 1;
        domain_each = [lv_inner_endo_1,lv_outer_epi_1];
    else
        lv_inner_endo_1 = 1;
        lv_outer_epi_1 = 2;
        domain_each = [lv_inner_endo_1,lv_outer_epi_1];
    end
%     Papex=0;
    rvbottom = 0;
    rv_epi_vertex = 0;
    rv_epi_node = 0;
    rv_endo_vertex = 0;
    rv_endo_node = 0;
end

disp('calculate f,s,n on boundary');
% get the node normal to the corresponding node for particular domain
[lv_endo_node,lv_endo_N_node, rv_epi_N_node, rv_endo_N_node, out_epi_node, out_epi_N_node]
     = getnode_normal_each_domain(domain,bfacecrop,bnode,Nnode,domain_each,rv_epi_node,
    rv_endo_node);

% calculate circumferencial direction
[lv_endo_C_node, rv_endo_C_node, rv_epi_C_node, out_epi_C_node] =
    calculate_Circum_direction(lv_endo_N_node, rv_endo_N_node, rv_epi_N_node,
    out_epi_N_node,Nplane);

% calculating fiber orienation f and sheet normal s
[lv_endo_f_node,lv_endo_s_node, rv_endo_f_node, rv_endo_s_node, rv_epi_f_node,
    rv_epi_s_node, out_epi_f_node, out_epi_s_node] = calculate_f_s_direction(
    fibre_angle_endo_input,fibre_angle_epi_input,lv_endo_C_node, rv_endo_C_node,
    rv_epi_C_node, out_epi_C_node,lv_endo_N_node,rv_endo_N_node, rv_epi_N_node,
    out_epi_N_node, Nplane);

% get all boundary value together
disp('get all boundary value together');
[boundary_f, boundary_s, boundary_ang, L_sym_fem] = get_all_boundary_value(
    fibre_angle_endo_input,fibre_angle_epi_input, L_sym_fem, lv_endo_node,lv_endo_f_node,
    lv_endo_s_node,rv_endo_node, rv_endo_f_node,rv_endo_s_node, rv_epi_node,
    rv_epi_f_node, rv_epi_s_node, out_epi_node, out_epi_f_node,out_epi_s_node, nnode);

% get interpolation
disp('calculating interpolation');
[interploated_f, interpolated_s, interploated_ang, interplolated_N_fs] = interpolation(
    L_sym_fem, boundary_f,boundary_s, boundary_ang);

% [interploated_f, interpolated_s, interploated_ang, interpolated_orthonormal_s,
    interplolated_N_fs] = interpolation(L_sym_fem,boundary_f,boundary_s, boundary_ang);
disp('interpolation calculation done, writing in txt file in msc fromat');
[interpolated_f_element,interpolated_s_element,centroid, interpolated_n_element,
    dot_product] = element_f_s(element,vertex,interploated_f,interpolated_s);


s = [interpolated_f_element interpolated_s_element interpolated_n_element];
dlmwrite('fibre_orientation.txt',s,'precision',9);

lv_inner = bfacecrop(domain{domain_each(1)},:);
% disp('lv_inner =', domain_each(1));
if  max(domain_each) == 3
    rv_inner = bfacecrop(domain{domain_each(2)},:);
%     disp('rv_inner =', domain_each(2));
    out_epi = bfacecrop(domain{domain_each(3)},:);
%     disp('out =', domain_each(3));
else
    rv_inner = 0;
    out_epi = bfacecrop(domain{domain_each(2)},:);
end

disp('wrting done, identifying lv endo boundary node');
% identify the lv_endo_boundary
[edgeLoop, meshclosure, nodebnd, cnt, vertex1] = get_node_lv_endo(vertex, lv_inner);

circum_point = edgeLoop{1};
fid = fopen('circum_point_endo.txt', 'w');
fprintf(fid, '%d  \n',circum_point);
fclose(fid);

disp('wrting done, identifying outer epi boundary node');
% identify the lv_endo_boundary
[edgeLoop1, meshclosure1, nodebnd1, cnt1, vertex2] = get_node_lv_endo(vertex, out_epi);

circum_point1 = edgeLoop1{1};
fid = fopen('circum_point_outer_epi.txt', 'w');
fprintf(fid, '%d  \n',circum_point1);
fclose(fid);

%identify base node
bfacecropnode =  unique(bfacecrop);
```

```
base_node = setdiff(bnode,bfacecropnode);

fid = fopen('base_point.txt', 'w');
fprintf(fid, '%d \n',base_node);
fclose(fid);

[edgeLoop2, meshclosure2, nodebnd2, cnt2, vertex3] = get_node_lv_endo(vertex, rv_inner);

circum_point = edgeLoop2{1};
fid = fopen('rv_circum_point_endo.txt', 'w');
fprintf(fid, '%d \n',circum_point);
fclose(fid);

% calcule local cardiac coordinate system
ele_num = length(interpolated_s_element);
N_plane_ele = repmat(Nplane,[ele_num,1]);

local_radial_element = interpolated_s_element;
local_circumferential_element_1 = cross(N_plane_ele,local_radial_element);
local_longitudinal_element_1 = cross(local_radial_element,local_circumferential_element_1)
    ;

norm_c_1 = sqrt(sum(local_circumferential_element_1.^2,2));
norm_l_1 = sqrt(sum(local_longitudinal_element_1.^2,2));


norm_c = repmat(norm_c_1,[1,3]);
norm_l = repmat(norm_l_1,[1,3]);

local_circumferential_element = local_circumferential_element_1./norm_c;
local_longitudinal_element = local_longitudinal_element_1./norm_l;

s_local_cardiac = [local_circumferential_element local_longitudinal_element
    local_radial_element];
dlmwrite('local_cardiac_coordinate.txt',s_local_cardiac,'precision',9);

%%
% ele_num = length(interpolated_s);
% N_plane_ele = repmat(Nplane,[ele_num,1]);
%
% local_radial_element = interpolated_s;
% local_circumferential_element = cross(N_plane_ele,local_radial_element);
% local_longitudinal_element = cross(local_radial_element,local_circumferential_element);

%%
% base = setdiff(bface,bfacecrop,'rows');
% [edgeLoop2, meshclosure2, nodebnd2, cnt2, vertex3] = get_node_lv_endo(vertex, base);
%
% circum_point2 = edgeLoop2{1};
% fid = fopen('circum_point_epi.txt', 'w');
% fprintf(fid, '%d \n',circum_point2);
% fclose(fid);

%%
disp('writing lv and rv faces in msc format');
% Write lv and rv inner faces
flag_1 = write_faces(element, lv_inner, rv_inner);

% [all_traingular_faces,x_data,y_data,z_data]= calculate_faces(element,vertex);
% elementid = 1:length(element);
% s = [elementid',interpolated_f_element interpolated_s_element];
% dlmwrite('fibre_direction_element.txt',s,'precision',6);
% save('interpolated_f_s_element.txt','s',' ASCII')
% toc;

%%
%post processing results
hold all
%
for i=1:length(domain)
    col=rand(1,3);
    f=bfacecrop(domain{domain_each(i)},:);
    patch('faces',f,'vertices',vertex,'facecolor',col,'edgecolor','k','facealpha',1)
end

patch('faces',bfacecrop,'vertices',vertex,'facecolor','r','edgecolor','y','facealpha
    ',0.9,...
          'FaceVertexCData',interploated_ang(:,1),...
          'EdgeColor','k',...
          'FaceColor','inter',...
          'FaceLighting','phong',...
          'EdgeLighting','phong')

quiver3(vertex(:,1),vertex(:,2),vertex(:,3),...
        local_radial_element(:,1),local_radial_element(:,2),local_radial_element(:,3),'
            color', 'r')
quiver3(vertex(:,1),vertex(:,2),vertex(:,3),...
```

```
        local_circumferential_element(:,1),local_circumferential_element(:,2),
            local_circumferential_element(:,3))
quiver3(vertex(:,1),vertex(:,2),vertex(:,3),...
        local_longitudinal_element(:,1),local_longitudinal_element(:,2),
            local_longitudinal_element(:,3))

axis equal
view(3)
axis tight
toc;

telapse = toc(tstart);
disp ('        complete              ')
disp(telapse);


% apply a growing procedure to group connected components
function Domain=growingComponents(element)

% INPUT
% element: element connections [Nele, Nnode_x_element]

% OUTPUT
% Domain: [1xndom]. entry {i}=[list of connected elements]

% set initial output
Domain=[];

%
nele=size(element,1);
nnode=max(element(:));

nodetag=false(nnode,1);
eletag=false(nele,1);

% update connectivity matrix
connectivity=element2Node(element, nnode);

nDom=1;
while true

    % get initial seed
    [idparent, nodetag]=getParentNode(nodetag, connectivity, nDom);

    if isempty(idparent)
        break
    end

    st=sprintf('... growing Component ID: %d', nDom);
    disp(st)

    % set default fields
    Domain{nDom}=[];

    % grow domain "nDom" locally
    while true

        nparent=length(idparent);
        idEle=[];
        for i=1:nparent
          [Domain, eletag, temp]=getNode2Element(Domain, eletag, idparent(i), connectivity
              , nDom);

          idEle=[idEle,temp];
        end

        % check if a new domain has been filled
        if isempty(idEle)
            nDom=nDom+1;
            break
        end

        nElec=length(idEle);
        idparent=[];
        for i=1:nElec
         [nodetag, temp]=getChildrenNode(nodetag, element, idEle(i), nDom);

         idparent=[idparent,temp];
        end

    end

end

% get seed Node
function [idseed, nodetag]=getParentNode(nodetag, connectivity, nDom)
```

```
idseed=[];

nnode=length(nodetag);

for i=1:nnode
    if nodetag(i)==0 && ~isempty(connectivity{i}) % never visited
        idseed=i;

        nodetag(i)=nDom; % now this node is taged as visited

        return
    end
end

% get child nodes
function [nodetag, idchild]=getChildrenNode(nodetag, element, idele, nDom)

idchild=[];

temp=element(idele,:);

n=length(temp);
for i=1:n

    if nodetag(temp(i))==0 % never visited
        idchild=[idchild,temp(i)];

        nodetag(temp(i))=nDom;  % now this element is taged as visited

    end

end


% get elements connected to parent
function [Domain, eletag, idEle]=getNode2Element(Domain, eletag, idnode, connectivity,
    nDom)

idEle=[];

temp=connectivity{idnode};

n=length(temp);
for i=1:n

    if eletag(temp(i))==0 % never visited
        idEle=[idEle, temp(i)];

        eletag(temp(i))=nDom;  % now this element is taged as visited

        Domain{nDom}=[Domain{nDom},temp(i)];

    end

end
```

Appendix D

Matlab Code for Estimation of Material Parameters

```
clc
clear
close all

% load data
Xraw=importdata('X.txt');
Yraw=importdata('Y.txt');

% define parameters' range
dataRegression.Parameter.X.Range=[0  0.28
                                  0  8.8
                                  3  10
                                  3  10];

dataRegression.Parameter.Y.Range=[0.0  10
                                  0.0  0.3];

dataRegression.Parameter.Y.Target=[0.0  0.0]; % target values

dataRegression.Solver.PopulationSize=3000;

% set parameters
degreeSM=2; % max degree
numFolds=1000; % no. of foldings
numToLeaveOut=3; % no. of leave out

%%
% STEP 1: calculate RS
[dataRegression.Model, flag]=run_calculate_regression_fnc(Xraw, Yraw,...
                                                          degreeSM,...
                                                          numFolds,...
                                                          numToLeaveOut);

%%
% STEP 2: run optimisation
idfitting=1;
idcon=2;
optResult=solveOptimisationProblem(dataRegression,...
                                   idfitting,...
                                   idcon,...
                                   Xraw);

%%
% STEP 3: plot RS
figure()

% set parameters
res=50; % resolution
Xid=1; % b a
Yid=2; %
Cid=[3  4]; % k1, k2
Cval=optResult.X(Cid);
XYmin=dataRegression.Parameter.X.Range([Xid, Yid],1);
XYmax=dataRegression.Parameter.X.Range([Xid, Yid],2);
```

```
tx={'F_{obj}', 'Klotz curve closeness'};
xyla={'a', 'b', 'Ka', 'Kb'};
for i=1:2

    Zmin=dataRegression.Parameter.Y.Range(i,1);
    Zmax=dataRegression.Parameter.Y.Range(i,2);


    ax=subplot(1,2,i);
    hold all

    % plot regression
    runPlotRegression(dataRegression.Model{i}, Cid, Cval, Xid, Yid, XYmin, XYmax, Zmin,
        Zmax, res, ax);

    % plot opt point
    plot(optResult.X(Xid),optResult.X(Yid),'s', 'parent',ax)

    st=sprintf('a: %f\n b: %f\n k1: %f\n k2: %f\n fitting: %f\n constraint: %f',...
                optResult.X(1), optResult.X(2), optResult.X(3), optResult.X(4), optResult.
                    Y(1), optResult.Y(2));

    text(optResult.X(Xid),optResult.X(Yid), st,...
         'HorizontalAlignment','center',...
         'BackgroundColor','w',...
         'EdgeColor','k')



    ti = title(tx{i});

    fontsiz = 24;
    x_label = xlabel(ax, xyla{Xid});
    y_label = ylabel(ax, xyla{Yid});
%     h_legend = legend('show', 0, 'Location','NorthWest');
    % set(h_legend,'FontSize',fontsiz,'Fontname','Timesnewroman' );
    set(x_label,'FontSize',fontsiz, 'Fontname','Timesnewroman');
    set(y_label,'FontSize',fontsiz, 'Fontname','Timesnewroman');
    set(ti, 'FontSize',fontsiz, 'Fontname','Timesnewroman');
    set(gca, 'FontSize', fontsiz, 'Fontname','Timesnewroman')

set(gcf, 'PaperPosition',[0,0,30,20]);
saveas(gcf,'contour_plot.png');



end

function [polymodel, flag]=run_calculate_regression_fnc(Xraw, Yraw,...
                                                        degreeSM,...
                                                        numFolds,...
                                                        numToLeaveOut)

% data: data structure
% degreeSM: max polynomial degree
% numFolds: no. of cross validations
% numToLeaveOut: no. of point to leave out

% modelSM.
    % Model=polymodel

flag=true;

% calculate surrogate models
nkpi=size(Yraw,2);
polymodel=cell(1,nkpi);
for i=1:nkpi
    polymodel{i} = getPolynomialModel(Xraw, Yraw(:,i), [0 degreeSM],...
                                        numFolds,...
                                        numToLeaveOut);

    if isempty(polymodel{i})
        flag=false;
        break
    end
end

function polymodel=getPolynomialModel(X, Y, degree,...
                                      numFolds,...
                                      numToLeaveOut)

% INPUT:
% X: independent variables [nsample, nvars]
% Y: dependent variables [nsample, 1]
% degree: [min max] polynomial degree
```

```
% numFolds: no. of cross validations
% numToLeaveOut: no. of point to leave out

% OUTPUT
% polymodel
%         polymodel.ModelTerms = list of terms in the model
%         polymodel.Degree = polynomial degree
%         polymodel.Coefficients = regression coefficients
%         polymodel.R2 = coefficient of determination (R^2)
%         polymodel.RMSE = Root mean squared error

polymodel=[];

% check inputs
if degree(1)<0 || degree(2)<0
    fprintf('Polynomial fitting: degree must be bigger than zero!\n')
    return
end

if isempty(X) || isempty(Y)
    fprintf('Polynomial fitting: data set must be not empty!\n')
    return
end

if numToLeaveOut>=size(X,1)
    fprintf('Polynomial fitting: no. of leave out too large!\n')
    return
end

if size(X,1)~=size(Y,1)
    fprintf('Polynomial fitting: data set not consistent!\n')
    return
end

if numFolds<0
    fprintf('Polynomial fitting: no. of cross validations must be bigger than 0!\n')
    return
end


% run...
fprintf('Polynomial fitting: running...\n')

% get size of the data set
[nsample, nvars]=size(X);

orders=degree(1):degree(2);
count=length(orders);

R2=zeros(1,count);
polymodel=cell(1,count);
c=1;
for iord=orders

    fprintf('   polynomial degree: %g\n',iord)

    % STEP 1: build the prediction model
    polymodel{c} = getPolyFit(X, Y, iord);

    % check
    if isnan(norm(polymodel{c}.Coefficients))

        polymodel{c}.R2 = 0;
        R2(c)=polymodel{c}.R2;

        polymodel{c}.RMSE=inf;

    else
        % ... now run cross validation to check the accuracy
        Ytest=zeros(1,numFolds*numToLeaveOut);
        Ym=zeros(1,numFolds*numToLeaveOut);
        ce=0;
        for k = 1:numFolds

            % STEP 2: split data into training and testing data
            [train, test] = crossvalind('LeaveMOut',nsample, numToLeaveOut);

            % STEP 3: calculate model
            Xtrain=X(train,:);
            Ytrain=Y(train,:);
            polymodelk = getPolyFit(Xtrain, Ytrain, iord);

            % STEP 4: calculate residuals
            Xtest=X(test,:);
            tYtest=Y(test,:);

            cs=ce+1;
```

```
            ce=ce+length(tYtest);

            Ytest(cs:ce)=tYtest;

            Ym(cs:ce)=evalPolyFit(polymodelk, Xtest);

        end

        %
        if numFolds==0
            R2(c)=polymodel{c}.R2;
        else

            % evaluate R^2
            SSr = norm(Ytest   Ym)^2;
                            % SSt=norm(Ytest mean(Ytest))^2; % centered
            SSt=norm(Ytest)^2; % not centered

            polymodel{c}.R2 = max(0,1    SSr/SSt);
            R2(c)=polymodel{c}.R2;

            % get root mean square error
            polymodel{c}.RMSE = sqrt(mean((Ytest   Ym).^2));

        end

    end

    % plot outcomes
    fprintf('       R2: %f\n',polymodel{c}.R2)
    fprintf('       RMS   Root Mean Square: %f\n',polymodel{c}.RMSE)

    c=c+1;

end

% get final model
[~, iord]=max(R2);
polymodel = polymodel{iord};

% plot outcomes
fprintf('                    \n')
fprintf('Polynomial fitting: summary\n')
fprintf('       polynomial degree: %g\n',polymodel.Degree)
fprintf('       no. of cross validation: %g\n',numFolds)
fprintf('       no. of leave out points: %g\n',numToLeaveOut)
fprintf('       no. of independent variables: %g\n',nvars)
fprintf('       no. data points: %g\n',nsample)
fprintf('       R2: %f\n',polymodel.R2)
fprintf('       RMS   Root Mean Square: %f\n',polymodel.RMSE)
fprintf('                    \n')


% solve optimisation problem
function optResult=solveOptimisationProblem(dataRegression,...
                                                    idfitting,...
                                                    idcon,...
                                                    Xraw)

% INPUT
% dataRegression: regression data set
% idfitting: fitting function (ID)
% idcon: list of constraints

% OUTPUT
% optResult.X=best x
% optResult.Y=best y

optResult.X=[];
optResult.Y=[];

% no. of variables
nvars=size(dataRegression.Parameter.X.Range,1);

% define solver options
options = gaoptimset('PopulationSize',dataRegression.Solver.PopulationSize, 'UseParallel',
      'Always',...
          'initialpopulation', Xraw);

% get ranges
LBx=dataRegression.Parameter.X.Range(:,1); % min
UBx=dataRegression.Parameter.X.Range(:,2); % max
ytarget=dataRegression.Parameter.Y.Target(idfitting);

% define constraints
LBy=dataRegression.Parameter.Y.Range(idcon,1);
UBy=dataRegression.Parameter.Y.Range(idcon,2);
```

```
con.Type={'>=', '<='};
con.b=[LBy, UBy];

% solve problem
xbest=ga(@(X)localFittingFnc(X, dataRegression.Model{idfitting}, ytarget), nvars,...
         [], [], [], [], LBx, UBx,@(X)localConstraintFnc(X, dataRegression.Model{idcon},
              con), options);


% get final outcomes
y(1)=localFittingFnc(xbest, dataRegression.Model{idfitting}, ytarget);
y(2)=evalPolyFit(dataRegression.Model{idcon}, xbest);

% store output
optResult.X=xbest;
optResult.Y=y;

 %
% define fitting function
function y=localFittingFnc(x, polymodel, ytarget)

% INPUT
% polymodel: model

% OUTPUT
% y: dependent variable

y=abs(evalPolyFit(polymodel, x)    ytarget);


 %
% define constraint function
function [c, ce]=localConstraintFnc(x, polymodel, con)

% INPUT
% polymodel: model
% con: constraints
% con{id}.Type: ">=", "<="
% con{id}.b
%      con{id}.Type{i} of con{id}.b(i)

% listcon: list of constraint ids

% OUTPUT
% c: constraints
% ce: equalities

% set intial
ce=[];

 %
c=[];

% get value
zij=evalPolyFit(polymodel, x);
for k=1:length(con.b)

      %
      ck=con.b(k);

      % check
      if strcmp(con.Type{k},'<=')
         c=[c, zij ck];
      elseif strcmp(con.Type{k},'>=')
         c=[c,  zij+ck];
      end
end
```